TESIS DE LA UNIVERSIDAD DE ZARAGOZA

2024 304

Marcos Rubin Osanz

Pump-probe experiments on superconducting resonators coupled to molecular spins

Director/es
Luis Vitalla, Fernando
Zueco Láinez, David

ISSN 2254-7606

Prensas de la Universidad
Universidad Zaragoza

Universidad de Zaragoza
Servicio de Publicaciones

ISSN 2254-7606

Universidad Zaragoza
1542

Tesis Doctoral

PUMP-PROBE EXPERIMENTS ON SUPERCONDUCTING RESONATORS COUPLED TO MOLECULAR SPINS

Autor

Marcos Rubin Osanz

Director/es

Luis Vitalla, Fernando
Zueco Láinez, David

UNIVERSIDAD DE ZARAGOZA
Escuela de Doctorado

Programa de Doctorado en Física

2024

Universidad Zaragoza
1542

Tesis Doctoral

PUMP-PROBE EXPERIMENTS ON SUPERCONDUCTING RESONATORS COUPLED TO MOLECULAR SPINS

Autor

Marcos Rubín Osanz

Directores

Fernando Luis Vitalla
David Zueco Láinez

Universidad de Zaragoza
Escuela de Doctorado

Programa de Doctorado en Física

2023

Pump-probe Experiments on Superconducting Resonators Coupled to Molecular Spins

Arrakis teaches the attitude of the knife – chopping off what's incomplete and saying: "Now, it's complete because it's ended here."

Frank Herbert, "Dune"

A mis padres.

Contents

Resumen

La evolución de la computación clásica en las últimas décadas ha estado marcada por el desarrollo de componentes cada vez más pequeños y rápidos. Sin embargo, este proceso de miniaturización tiene un límite en las escalas en las que los efectos cuánticos empiezan a ser relevantes. Este problema es una oportunidad para desarrollar un nuevo tipo de computación, la *computación cuántica*, que toma precisamente como elemento básico un sistema con propiedades cuánticas. Este elemento básico es el bit cuántico o *qubit*, el análogo cuántico del bit clásico. Mientras un bit clásico solo puede estar en uno de dos estados, o 0 o 1, un qubit puede estar en cualquier superposición $|\psi\rangle := \alpha\,|0\rangle + \beta\,|1\rangle$ de dos estados base $|0\rangle$ y $|1\rangle$, donde α y β son dos números complejos. Esta propiedad de superposición permite de manera natural hacer operaciones paralelas. Además, también son posibles los estados de superposición de más de un qubit, conocidos como estados entrelazados. De esta manera, un conjunto de qubits tiene acceso a un número de estados exponencialmente mayor que el mismo número de bits clásicos. Las posibilidades de procesamiento de información que introducen los estados de superposición permitirían a un futuro ordenador cuántico resolver ciertos problemas complejos como la factorización de números primos muy grandes, la búsqueda en grandes bases de datos o la simulación de sistemas cuánticos. Algunos de estos problemas están lejos de las capacidades de los ordenadores clásicos en tiempo y recursos finitos.

Desde finales del siglo pasado se han propuesto diversos sistemas cuánticos como realizaciones físicas del concepto de qubit. A día de hoy, el abanico de sistemas es amplio: circuitos superconductores, defectos de espín en semiconductores, fotones, átomos ultrafríos, y más, cada uno con sus ventajas y sus incovenientes. Uno de los retos más importantes a los que se enfrenta cualquiera de estos dispositivos es el fenómeno de *decoherencia*, en el que la interacción del qubit con su entorno destruye la información que éste almacena, generando errores de computación. Incluso los ordenadores cuánticos más avanzados y sofisticados están limitados por errores al manipular un número considerable de qubits. Una solución para mitigar estos errores es la implementación de códigos de corrección de errores basados en un almacenamiento redundante de

la información. Para cada qubit lógico protegido frente a errores se necesitan qubits físicos adicionales, lo que genera un nuevo problema asociado a tener que controlar un número mucho mayor de qubits. Una alternativa prometedora es pasar de la lógica binaria de los qubits, con dos estados base, a sistemas cuáticos más complejos con $d > 2$ estados base, conocidos como *qudits*. Los estados adicionales de los que dispone un qudit se han propuesto como una plataforma para codificar una unidad de correción de errores.

Los espines presentes en las moléculas magnéticas pueden codificar tanto qubits como qudits. Como unidades básicas de un ordenador cuántico, las moléculas magnéticas destacan por su pureza y reproducibilidad, ya que las caracteríticas de todas quedan definidas por las mismas propiedades químicas. La principal fuente de decoherencia en estos sistemas es la interacción dipolar magnética, ya que los espines son relativamente inmunes a las fluctuaciones del campo eléctrico. Esto hace que los tiempos de coherencia de los qubits de espín puedan ser mucho más largos que en otros tipos de qubits, con valores récord de más de 30 segundos. El reto de desarrollar un procesador cuántico basado en qubits de espín molecular es diseñar una plataforma escalable en la que el estado de espín de cada molécula magnética puede ser inicializado, controlado y medido con pulsos de microondas. Una propuesta prometedora, basada en la electrodinámica cuántica de circuitos (*Circuit Quantum Electrodynamics* o *circuit-QED*), integra los qubits de espín molecular en circuitos superconductores, donde el espín interacciona con el campo magnético de microondas generado por fotones individuales confinados en resonadores.

Un elemento crucial en la manipulación del estado del espín es la frecuencia de Rabi, Ω_R, que establece la velocidad a la que se produce el cambio de estado. Esta frecuencia, que depende de la potencia de los pulsos de microondas, debe ser lo suficientemente alta como para controlar el estado del espín antes de que la coherencia de é decaiga (con tiempo característico T_2). Esta condición viene dada por $\Omega_R T_2 \gg 1$. De la misma forma, el acoplo espín-resonador G_1 también debe cumplir $G_1 T_2 \gg 1$. Por desgracia, conseguir detectar moléculas individuales acopladas a resonadores es todavía una tarea desafiante, tanto por la depósición como por la detección de estás (G_1 es demasiado pequeño). Los avances más recientes en este aspecto exploran la fabricación de una nanoconstricción en el inductor del resonador superconductor, la cual concentra y amplifica el campo magnético de microondas en un pequeño volumen en el que se depositan moléculas con nanolitrografía 'dip pen' (DPN).

Los hitos experimentales en el camino hacia un procesador cuántico basado en qubits o qudits de espín molecular pueden resumirse en:

- Acoplar moléculas individuales a resonadores individuales. Este requisito, como ya se ha comentado, es bastante complicado actualmente, pero

los experimentos de prueba de concepto pueden realizarse con muestras con volúmenes cada vez más pequeños.

- Controlar coherentemente el estado de los qubits/qudits de espín molecular con pulsos de microondas. Caracterizar el efecto del acoplo de los qubits/qudits a resonadores en sus tiempos de relajación y coherencia.

- Leer el estado de los qubits/qudits tras modificar su estado. Esto puede hacerse a través de su acoplo a resonadores superconductores, trabajando en el régimen dispersivo en el que las frecuencias asociadas a qubit y resonador son suficientemente distintas. En concreto, su diferencia de frecuencias debe ser mucho mayor que el acoplo espín-fotón.

- Explorar moléculas magnéticas capaces de codificar qudits y con un buen acoplo a campos de microondas generados por resonadores.

- Caracterizar el efecto de las interacciones entre espines en el acoplo de éstos a los fotones de microondas en los circuitos superconductores. Mientras no se llegue al límite de trabajar con moléculas individuales, estas interacciones estarán presentes, y pueden ser muy relevantes en algunos sistemas al disminuir la temperatura para inicializar los qubits/qudits en el estado fundamental ($T \ll 1$ K).

- Diseñar y fabricar distintos tipos de resonadores superconductores. En concreto, los resonadores de elementos concentrados (Lumped-element resonators o LERs) son interesantes por sus propiedades de multiplexación en frecuencia y su libertad de diseño. Integrar un SQUID en el inductor de estos resonadores para tener una inductancia modulable.

A continuación se resumen los experimentos presentados en esta tesis, los cuales constituyen los primeros pasos hacia la realización de algunos de los hitos descritos arriba.

Acoplo fuerte de conjuntos de qubits de espín molecular basados en radicales orgánicos a LERs

El radical libre DPPH, con espín electrónico 1/2, es un marcador común en experimentos de resonancia paramágnética. El régimen de acoplo fuerte de muestras en polvo de DPPH a resonadores coplanares, fabricados a partir de una línea de transmisión superconductora, se había conseguido ya previamente. Este régimen se obtiene gracias a que el acoplo colectivo de N espines idénticos escala con $\sqrt{N}$ respecto del acoplo de un único espín. Se ha depositado el mismo tipo de muestras sobre LERs para comprobar que este nuevo diseño de resonador también permite acceder al régimen de acoplo fuerte.

Lectura del estado de qubits de espín molecular basados en radicales orgánicos con la técnica de lectura dispersiva. Primeros experimentos de manipulación coherente de qubits de espín molecular acoplados a circuitos superconductores.

La técnica de lectura dispersiva del estado de un qubit molecular de espín consiste en inferir este estado a partir de su efecto en la resonancia de un LER al que está acoplado. El sistema híbrido qubit-resonador debe estar en el régimen dispersivo, en el que la diferencia $\Delta = \omega_q - \omega_r$ entre la frecuencia de operación del qubit, ω_q, y la frecuencia del resonador, ω_r, es mucho mayor que el acoplo colectivo entre ambos subsistemas, G_N ($\Delta \gg G_N$). Los experimentos excitación-lectura ('pump-probe') están compuestos de un pulso de manipulación del qubit con frecuencia cercana a ω_q ('pump pulse') y uno varios pulsos con frecuencias cercanas a ω_r que reconstruyen el cambio en la resonancia del LER ('probe pulse(s)'). Los primeros experimentos excitación-lectura con qubits moleculares de espín se han realizado con muestras de PTM_r, un radical libre con espín electrónico 1/2.

Estudio del complejo [^{173}Yb(trensal)] como qudit electronuclear con 12 estados. Alta cooperatividad en transiciones nucleares acopladas a fotones en resonadores superconductores.

El complejo [^{173}Yb(trensal)], una molécula con un ion Yb^{3+} con espín electrónico $S = 1/2$ y el espín nuclear $I = 5/2$ del isótopo ^{173}Yb. Este sistema puede codificar un qudit electronuclear con $d = (2S + 1) \times (2I + 1) = 12$ estados. El diseño de resonadores con frecuencias de resonancia cercanas a las frecuencia de resonancia de las transiciones nucleares permite estudiar si la presencia del espín electrónico optimiza el acoplo del espín nuclear a campos magnéticos de microondas.

Competición entre interacciones espín-espín y espín-fotón en conjuntos de radicales libres (moleculas con espín 1/2) acopladas a líneas de transición superconductoras. Efecto de introducir anisotropía magnética al sustituir los radicales por [Ni(2-Imdipa)], con espín 1

A muy baja temperatura, las interacciones entre espines en muestras concentradas pueden cambiar las propiedades de la interacción de la muesta con fotones en circuitos superconductores. Se ha estudiado este efecto con dos tipos de moléculas: DPPH, con espín 1/2, y [Ni(2-Imdipa)], con espín 1. Esta última molécula, con $S > 1/2$, añade un ingrediente adicional, la anisotropía magnética. La transición entre su estado fundamental y su primer estado excitado es una 'transición de reloj', más robusta frente a fluctuaciones del campo magnético que una transición normal. De esta manera, el acoplo de [Ni(2-Imdipa)] a circuitos superconductores permite explorar la competición entre interacciones entre espines y el gap de enería asociado a la transición de reloj.

Chapter 1

Introduction

Since the development of the transistor in 1947 [1], the evolution of classical computation has been driven by the constant development of smaller and faster components. The corresponding exponential growth of computational power was predicted by Gordon Moore in 1965 [2]. Remarkably, his prediction has held true for decades, but eventually it may run into fundamental size limitations and the emerging quantum effects in very small physical systems. Quantum computing aims to transform this threat into an opportunity.

In 1982, Richard Feynman proposed the concept of a quantum generalization of classical computing, addressing the challenge of efficiently simulating quantum systems [3]. In a quantum computer, the classical bit is replaced by the quantum bit or *qubit*. The former can be only in one of two classical states, either 0 *or* 1, while a qubit can exist in any superposition state $|\psi\rangle := \alpha\,|0\rangle + \beta\,|1\rangle$ of two quantum states $|0\rangle$ and $|1\rangle$, enabling natural parallel operations. Moreover, multiple qubits can form collective superposition states known as entangled states. A collection of qubits has therefore access to an exponentially larger set of states than the same number of classical bits. The additional possibilities that superposition states introduce to process information allow a quantum computer to efficiently solve certain complex problems such as the prime factorization of large numbers with Shor's algorithm [4], data search in large databases with Grover's algorithm [5], and the aforementioned simulation of real quantum systems proposed by Feynman. Some of these tasks are beyond the capability of classical computers in reasonable times and with finite resources.

Cold trapped ions were the first proposed physical system to encode qubits able to perform universal quantum operators, back in 1995 [6]. Nowadays, various contenders for qubits exist, such as superconducting circuits, spin defects in semiconductors, photons, ultracold atoms, and more, each presenting

distinct strengths and weaknesses. A significant challenge in quantum computation is the phenomenon of decoherence [7], in which the interaction of the qubit with its environment destroys the information encoded in its quantum state and generates errors in the computation. Even the most advanced quantum computers, e.g. those based on superconducting circuits, are limited by unavoidable errors in manipulating a substantial number of qubits [8]. Thus, the realization of a universal, error-corrected hardware still remains distant from current capabilities.

A solution to mitigate errors is the implementation of error correction codes, which are based on redundancy. Fault-tolerant quantum computing requires additional physical qubits to encode each single logical qubit. For example, the implementation of Shor's algorithm with the surface code, a robust error correction code based on encoding logical qubits with nearest-neighbors superposition states of physical qubits in a 2-D lattice, would require as many as 10^8 physical qubits [9]. A promising alternative involves transitioning from binary qubit logic to the utilization of multilevel logical units known as *qudits* [10]. The additional quantum states in a qudit (with d quantum states) have been proposed as a suitable platform to encode an error correction unit [11].

Microscopic spins found in molecular magnets are capable of encoding both qubits and qudits [12, 13]. In addition, they are interesting due to their easily controllable purity and reproducibility, as the individual qubit/qudit properties are governed by chemistry. In the context of spin qubits, the magnetic dipolar interaction is the main source of decoherence, as spins are relatively immune to electric field fluctuations. This makes spin qubits distinct from other qubit candidates like superconducting circuits [14] or trapped ions [15], where decoherence is mainly due to their coupling to electric fields. As a result, spin qubits can exhibit much longer coherence times, with record values > 30 s [16].

The challenge of developing a quantum processor based on molecular spin qubits is designing a scalable platform where the spin of each individual molecule can be initialized, controlled, and read out. A promising approach, based on circuit quantum electrodynamics (circuit-QED), involves coupling molecular spin qubits to individual photons confined within on-chip superconducting resonators [17–19]. A proposal for the most basic quantum processor based on molecular spin qudits coupled to superconducting circuits is shown in figure 1.1 [10]. Two GdW_{30} molecules [20], each encoding a qudit with $d = 8$ states, are coupled to a lumped-element resonator with a tunable inductance $L(\Phi)$. The tuning of $L(\Phi)$, which modulates the photon-mediated coupling between the two qudits, is introduced by changing the magnetic flux Φ through a SQUID with an auxiliary transmission line. Each qudit has an excitation line that

inputs the microwave pulses that control the qudit state, whereas its coupling to the resonator inductor allows reading out the results and introduces an effective communication channel between different qudits.

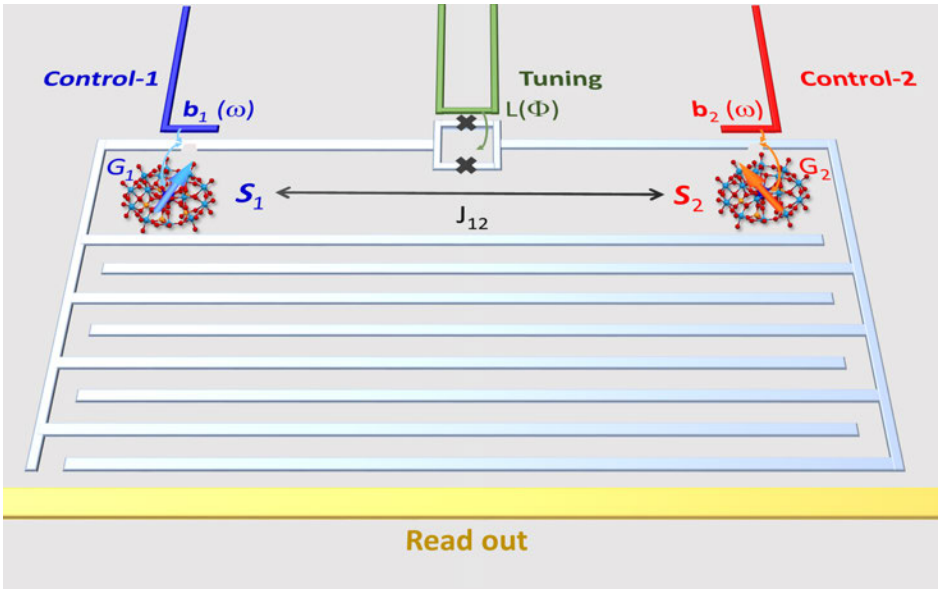

Figure 1.1: Scheme of a proposal for the most basic quantum processor based on molecular spin qudits coupled to superconducting circuits.

The crucial element is to establish a Rabi frequency Ω_R, which depends on the microwave power of control pulses, and a qubit-resonator (or qudit resonator) coupling G_1 significantly exceeding the inverse of the spin coherence time T_2. This ensures that the spin state is changed sufficiently fast ($\Omega_R T_2 \gg 1$) and that the resulting state can be readout ($G_1 T_2 \gg 1$). Unfortunately, pushing the boundaries from molecular ensembles to single molecules remains a challenging task. Recent advancements explore the fabrication of a nano-constriction in the inductor [21], which concentrates and enhances the microwave magnetic field in a very small volume, combined with small molecular deposits with Dip Pen Nanolithography (DPN) [22].

An alternative to enhance both the spin-photon coupling and the coherence time is based on chemical design, tailoring the spin wavefunctions encoding the qubit/qudit states to enhance their coupling to electromagnetic radiation and protect the spin states from decoherence. An interesting case is that of 'clock transitions' between spin superposition states that can arise in molecular spin systems with integer electronic spin and/or non-zero nuclear spin, which show a remarkable stability against magnetic field fluctuations [23].

Several experimental milestones are still in the way towards a physical realization of the proposal in figure 1.1:

- Coupling single molecular spin qubits/qudits to superconducting resonators.
- Controlling the state of molecular spin qubits/qudits.
- Reading the state of molecular spin qubits/qudits through their coupling to superconducting resonators.
- Exploring other magnetic molecules encoding molecular spin qudits.
- Characterizing the light-mediated spin-spin interactions.
- Fabricating and testing lumped-element resonators with an integrated SQUID.

In this thesis, I take the first steps towards realizing the basic ingredients of the hybrid scheme in figure 1.1. For this, I study experimentally some of these requirements. The outline of this work is:

- First, the experimental techniques used throughout this work are presented in chapter 2.
- Chapters 3 and 4 introduce the theoretical framework that describes the elements of the quantum processor, namely the molecular spins and the superconducting resonators, their coupling, and their measurement with microwave experiments.
- The coupling of free radical molecules with $S = 1/2$ to superconducting lumped-element resonators (LERs) is studied in chapters 5 and 6. In chapter 5, the coupling of DPPH ensembles to LERs is characterized with continuous wave experiments. Chapter 6 focuses instead on pulsed experiments on PTM_r in the dispersive regime. In these experiments, first the state of the molecular spin state is controlled with pump pulses, then the resulting state is read out by measuring the LER resonance frequency, which depends on the qubit state.
- Chapter 7 generalizes the experiments in chapters 5 and 6 to molecular spin qudits, with $d > 2$ spin states. In particular, the [Yb(trensal)] complex with ^{173}Yb, with electronic spin $S = 1/2$ and nuclear spin $I = 5/2$ is studied as an electro-nuclear qudit with $d = 12$ states.
- Finally, chapter 8 explores the competition of spin-spin interactions, inherent to spin ensembles unless diamagnetically samples are used, with the interaction of spins with photons travelling through a waveguide and with clock transitions.

In addition to the conclusions of each individual chapter, a summary of the general conclusions is included at the end.

References

[1] J. Bardeen and W. H. Brattain, Physical Review **74**, 230 (1948).

[2] G. E. Moore, Electronics **38(8)**, 114 (1965).

[3] R. P. Feynman, International Journal of Theoretical Physics **21(6/7)**, 467 (1982).

[4] P. W. Shor, in *Proceedings 35th Annual Symposium on Foundations of Computer Science* (1994), pp. 124–134.

[5] L. K. Grover, Physical Review Letters **79(2)**, 325 (1997).

[6] J. I. Cirac and P. Zoller, Applied Physics Letters **74(20)**, 4091 (1995).

[7] W. H. Zurek, Reviews of Modern Physics **75**, 715 (2003).

[8] J. Preskill, Quantum **2**, 79 (2018).

[9] A. G. Fowler, M. Mariantoni, J. M. Martinis, and A. N. Cleland, Physical Review A **86**, 032324 (2012).

[10] A. Chiesa, S. Roca, S. Chicco, M. de Ory, A. Gómez-León, A. Gomez, D. Zueco, F. Luis, and S. Carretta, Physical Review Applied **19**, 064060 (2023).

[11] M. Chizzini, L. Crippa, L. Zaccardi, E. Macaluso, S. Carretta, A. Chiesa, and P. Santini, Physical Chemistry Chemical Physics **24(34)**, 19979 (2022).

[12] A. Gaita-Ariño, F. Luis, S. Hill, and E. Coronado, Nature Chemistry **11**, 301 (2019).

[13] I. Gimeno, A. Urtizberea, a. J. Romáan-Roche, D. Zueco, A. Camón, P. J. Alonso, O. Roubeau, and F. Luis, Chemical Science **12**, 5621 (2021).

[14] M. H. Devoret and R. J. Schoelkopf, Science **339**, 1169 (2003).

[15] C. Monroe and J. Kim, Science **339**, 1164 (2013).

[16] J. T. Muhonen, J. P. Dehollain, A. Laucht, F. E. Hudson, R. Kalra, T. Sekiguchi, K. M. Itoh, D. N. Jamieson, J. C. McCallum, A. S. Dzurak, et al., Nature Nanotechnology **9**, 986 (2014).

[17] A. Wallraff, D. I. Schuster, A. Blais, L. Frunzio, R.-S. Huang, J. Majer, S. Kumar, S. M. Girvin, and R. J. Schoelkopf, Nature **431**, 162 (2004).

[18] J. Majer, J. M. Chow, J. M. Gambetta, J. Koch, B. R. Johnson, J. A. Schreier, L. Frunzio, D. I. Schuster, A. A. Houck, A. Wallraff, et al., Nature **449**, 443 (2007).

[19] J. Schoelkopf and S. M. Girvin, Nature **451**, 664 (2008).

[20] M. D. Jenkins, Y. Duan, B. Diosdado, J. J. García-Ripoll, A. Gaita-Ariño, C. Giménez-Saiz, P. J. Alonso, E. Coronado, and F. Luis, Physical Review B **95**, 064423 (2017).

[21] I. Gimeno, W. Kersten, M. C. Pallarés, P. Hermosilla, M. J. Martínez-Pérez, M. D. Jenkins, A. Angerer, C. Sánchez-Azqueta, D. Zueco, J. Majer, et al., Physical Review Applied **20**, 044070 (2020).

[22] R. D. Piner, J. Zhu, F. Xu, S. Hong, and C. A. Mirkin, Science **283**, 661 (1999).

[23] M. Shiddiq, D. Komijani, Y. Duan, A. Gaita-Ariño, E. Coronado, and S. Hill, Nature **531**, 348 (2016).

Chapter 2

Experimental setup and techniques

This chapter presents the experimental setup and techniques used throughout this work. Most experiments here are focused on manipulating and reading molecular spin qubits and qudits coupled to superconducting resonators. The setup for these experiments consists of a superconducting chip with the molecular samples inside a dilution refrigerator, which is probed with microwaves. A transmission line and several lumped-element resonators (LERs) are patterned on the surface of the chip, on top of which the molecular spin qubits/qudits are deposited. This is the quantum processor (see section 2.1).

A dilution refrigerator cools down the processor to as low as 7 mK. Inside, a superconducting magnet generates the DC magnetic field that tunes the frequencies of the molecular spin qubits to match those of the resonators (see section 2.2). Section 2.3 introduces the microwave setup for pulse generation and detection, comprising all instruments needed to control and read the molecular spin qubit state through the LERs with microwave photons. Other complementary experimental techniques used throughout this thesis can be found in section 2.4.

2.1 Superconducting chip

Electronic Paramagnetic Resonance (EPR) is a well-established control and characterization technique of molecular electronic spins coupled to 3D cavities [1]. However, in the context of quantum computation this 3D cavity poses a problem of scalability, and it is more interesting to use instead 2D microwave integrated circuits in superconducting chips as cavities [2]. Single photons

can be confined in these systems, increasing the spin-photon coupling. This enhancement of the coupling moves the hybrid spin-photon system away from the weak coupling regime characteristic of EPR experiments, into the strong coupling regime that is achieved in circuit-QED.

The first proposals for coupling molecular spin qubits to superconducting circuits were based on coplanar resonators [3, 4]. These are fabricated by interrupting the transmission line of a superconducting chip with gap capacitors so that the dimensions match the wavelength of microwave modes. However, with this design is not possible to have several resonators with slightly different frequencies in the same transmission line. Each resonator is essentially a filter that reflects any microwaves with frequencies out of its bandwidth. Then, the first resonator from the input port hinders the transmission of microwaves probing the rest of resonators. Also, the design of a coplanar resonator is constrained to an interrupted line: its capacitance and inductance must be tailored so that the resonator impedance $Z = \sqrt{L/C}$ match the impedance of the transmission line, Z_0. This last condition limits the tunability of the frequency of the resonator, which is given by $\omega_r = 1/\sqrt{LC}$.

A different chip design in which all resonators can be measured through a single transmission line is desired. This would allow, for example, the characterization of a qudits in a single chip by matching different resonators to the different transition frequencies of the qudit. The property of probing resonators with different ω_r inside the same chip is known as frequency multiplexing. A proposal for a quantum processor with this property is coupling the molecular spin qubits/qubits to lumped-element resonators (LERs). LERs are side coupled to the transmission line, which makes them transparent to microwaves out of their bandwidth and allows frequency multiplexing. They consist of an inductive meander and an inter-digitated capacitor patterned in the surface of a superconducting chip (figure 2.1). The inductance L and capacitance C of the LER can be tuned independently by changing the design of each of the two parts of the circuit. On top, they achieve very high quality factors ($Q \sim 10^4$ to 10^5) and, therefore, long coherence times ($\kappa^{-1} > \mu$s) [5].

Resonance frequencies are usually in the range of 1-10 GHz, matching the frequencies of the electronic spin transitions in our molecules. Inductor and capacitor are clearly separated in space in each resonator (figure 2.1). This potentially allows choosing either magnetic or electric spin-photon coupling in resonance depending on where the sample is deposited.

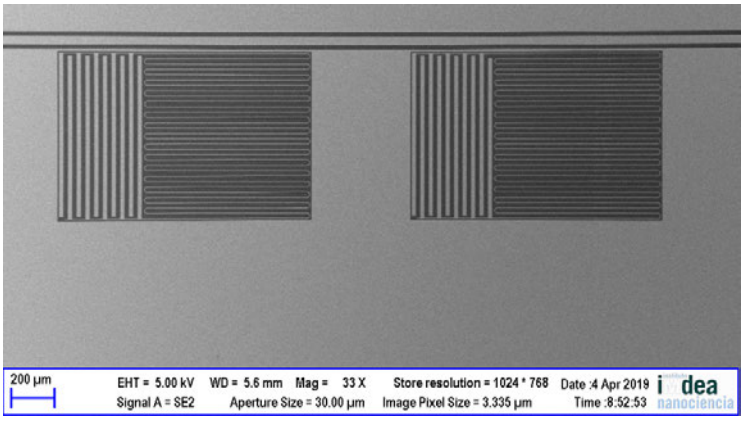

Figure 2.1: Two lumped element resonators (LERs) side coupled to a transmission line in a superconducting chip, each with two distinct parts: an inter-digitated capacitor on the left and an inductor on the right.

2.1.1 Design and fabrication

Each superconducting chip is composed of a transmission line with several side-coupled LERs (figure 2.2). These chips were designed by Alicia Gomez and Marina Calero, from CAB (Centro de Astrobiología de Madrid), and then fabricated by Maite Magaz at Center for Nanofabricaction of IMDEA-Nanoscience [6]. They are made on 100 nm thick niobium (Nb) films deposited on top of 350 μm thick Si substrate wafers. Niobium is a superconductor below $T_c = 9.26$ K, with low dielectric losses.

First, the geometries of the transmission line and lumped-element resonators are designed with CAD software. The output vector files with the design are fed to the commercial software Sonnet for the RF simulations. In these simulations the Nb film has no thickness, but the Si substrate thickness is included. With the combination of these two software tools it is possible to tailor the parameters and characteristics of the resonators (resonance frequency, quality factors, size and shape of inductor and capacitor) so that they suit best the experiments.

The fabrication process begins with the deposition of the Nb film on the Si substrate by means of DC magnetron sputtering. The transmission line and the LERs are then patterned in the Nb film by ultra-violet (UV) laser lithography and reactive ion etching (RIE) techniques. UV laser lithography is a maskless circuit fabrication technique to pattern a photosensitive polymer or photoresist on top a substrate with laser UV irradiation. In this case, a 405 nm wavelength laser is used to irradiate a negative photoresist deposited on top of the Nb film. The laser is fed with the vector files containing the design

of the transmission line and the lumped-elements resonators.

The non-irradiated areas of the photoresist are removed with acetone, exposing areas of the Nb film below that are then removed by RIE (Reactive Ion Etching). A beam of accelerated ions composed of a mix of SF_6 and argon gases is sent to the sample, and provides energy to drive a chemical etching reaction in the exposed Nb film. The combination of physical and chemical etching of RIE confers both good selectivity and directionality to the etching process [7]. Once the pattern is transferred to the Nb film, the remaining photoresist is removed with successive cleanings with acetone, isopropyl alcohol (IPA) and pressurized N_2 gas. The final device is then tested at room and low temperatures to check the expected properties.

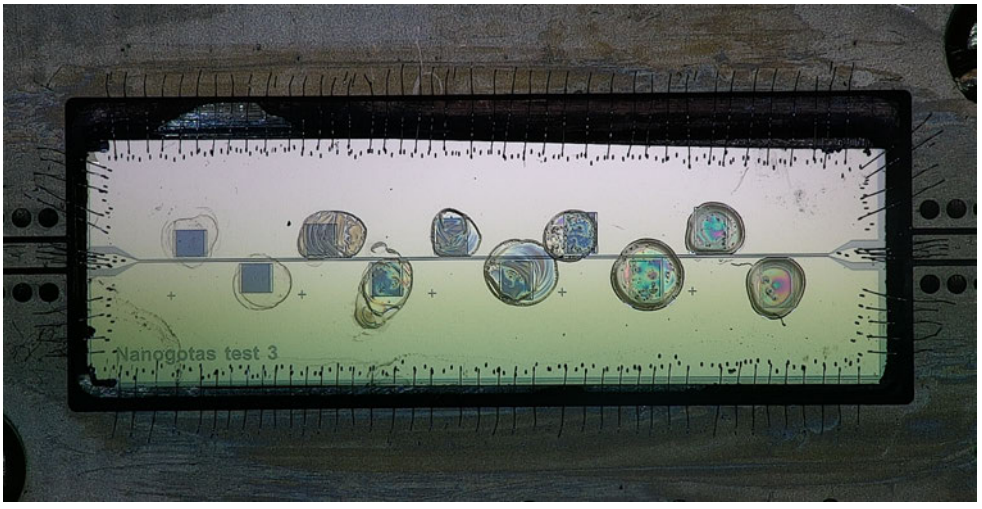

Figure 2.2: Example of a superconducting chip with side-coupled LERs. On top of each LER there is a sample of magnetic molecules. The chip is connected to a PCB with the wire bonding technique detailed in section 2.1.2.

2.1.2 Interface with microwave coaxial lines: PCBs and wire bonding

The transmission line in the superconducting chip is interfaced with the input and output microwave lines inside the cryostat with a PCB (Printed Circuit Board). The PCB consists of several layers of electrical conductors separated by an insulating material, with its conducting surface patterned so that it has a central line and two ground plates as in a transmission line.

The superconducting chip is placed in a rectangular hole in the centre of the PCB, with its central line and grounds electrically connected to those of the

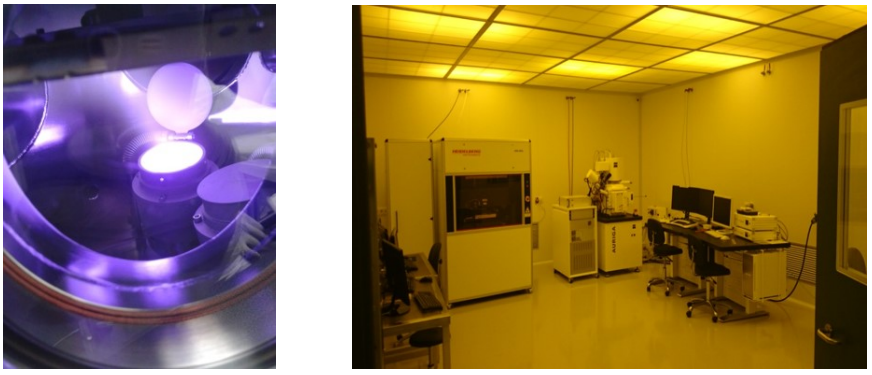

(a) (b)

Figure 2.3: AJA Orion-5 DC magnetron sputtering system (a) and Heidelberg Maskless DWL66fs laser lithography system (b) at Center for Nanofabricaction of IMDEA-Nanoscience.

PCB using $\varnothing 25$ μm 1% SiAl wires (see figure 2.2). These wires are bonded to the chip surface and PCB with a Hybond model 572A wire bonding machine at INMA (Instituto de Nanociencia y Materiales de Aragón) based on the wedge bonding technique. The clamped wire is first welded to the PCB and then to the chip applying ultrasounds and pressure. The capillary that holds the wire can be moved between the two bonding sites in the three spatial directions with three independent controllers.

The interface of the PCB to the coaxial lines inside the cryostat are two female SMA adapters (input and output). SMA are used instead of SMP adapters, as the former are more robust against tensions in the coaxial cables and temperature changes. These adapters are placed far from the superconducting chip, with the PCB being much larger in size than the chip. This large design keeps ground voltage inhomogeneities away from the central line and reduces their effect on the transmission.

2.2 Cryogen-free dilution refrigerator

A qubit is initialized in its ground state by cooling it far below $\hbar\omega/k_{\mathrm{B}}$, where ω is the qubit operation frequency. From this initial state, the qubit state is controlled with different quantum gates. Similarly, an ensemble of quantum systems cooled to temperatures below $\Delta E/k_{\mathrm{B}}$, where ΔE is the energy difference between the initial and final states, is initialized in the sense that different populations in equilibrium are obtained according to the Boltzmann distribution ($\propto 1 - e^{-\Delta E/k_{\mathrm{B}}T}$). Without this non-negligible difference in pop-

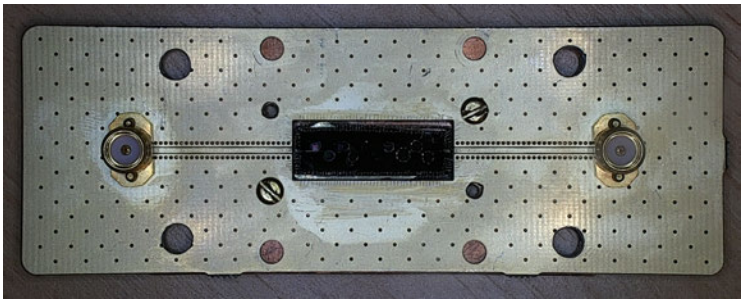

Figure 2.4: PCB with the superconducting chip placed in the rectangular hole in its centre. Figure 2.2 is a close up of this image. All the PCB acts as a ground plate, except the patterned transmission line that connects the line of the chip with two female SMA adapters. First, the chip is placed on top of a oxygen-free copper holder with GE low temperature varnish to ensure good a thermal connection. Then the PCB is screwed to the holder as shown in the image. Finally, chip and PCB are electrically connected with wire bonding.

ulation there is no significant change in the system: according to the detailed balance of absorption and stimulated emission in thermodynamic equilibrium, the rates of the two processes are the same for any transition in our quantum system if its initial and final states have the same degeneracy. [8, 9]

The energy differences in a magnetic molecule, when converted to transition frequencies, range from tenths of MHz in nuclear splittings to a few GHz in electronic Zeeman and zero-field splittings. [10] This demands cooling temperatures ranging from a few mK to hundreds of mK for initialization. That is, temperatures which can only be provided continuously by ^{3}He-^{4}He dilution refrigerators.

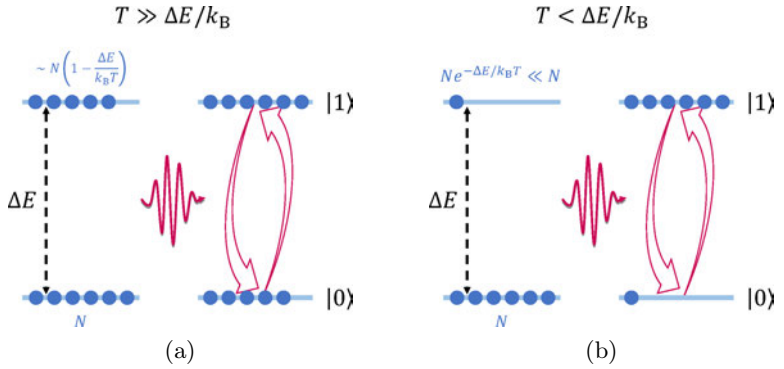

Figure 2.5: Population inversion with resonant microwave radiation at high (a) and low temperatures (b). The absorption and stimulated emission rates are the same, so it is the difference between the initial populations of the states that makes the population inversion non negligible. This difference is enhanced when $T < \Delta E/k_B$.

2.2.1 Operating principle of a ^{3}He-^{4}He dilution refrigerator

A dilution refrigerator is based on the cooling properties of the phase separation of a mixture of the two stable helium isotopes, ^{3}He and ^{4}He, at very low temperatures. To start the cooling cycle, an auxiliary cooling mechanism is needed to get the mixture around the temperature of liquid helium (4.2 K) or below. In a standard, not cryogen-free dilution refrigerator, this temperature is obtained by inserting the dilution circuit inside a vacuum can surrounded by a liquid helium bath. The mixture is cooled to 4.2 K with small volumes of liquid helium from the bath, and then it can be cooled further by using a 1 K pot.

The dilution refrigerator used in this work is a BlueFors LD250 Dilution Refrigerator System (figure 2.6), managed as a service by the Servicio de Apoyo a la Investigación (SAI) of the University of Zaragoza and accessible to all researchers [11]. It is a cryogen-free dilution refrigerator that does not need a liquid helium bath. All cooling stages of the cryostat are inside a vacuum can in order to suppress heat conduction and convection, and to thermally isolate the circuit from the environment. The vacuum can is also enclosed by a radiation shell that protects the stages from incident radiation that would otherwise heat them.

The different stages are separated by a stainless steel tubes with poor thermal conductivity, and heat switches filled with helium gas and active carbon. While the heat switch heaters are on, the helium gas thermally connects the stages. When they are turned off, helium gas is absorbed by active carbon and the stages are isolated.

To attain liquid helium temperatures, the outer stage (50 K plate) is cooled by a Cryomech Inc. Pulse Tube (PT) cooler. In this process, all cooling stages of the cryostat, from the 50 K plate to the mixing chamber, are thermally connected by heating the heat switches. After 20 hours, or 30 if the superconducting magnet is installed, a temperature of around 4.2 K si reached in the still and the mixing chamber. The heaters of the heat switches are then turned off to isolate the different stages.

After this pre-cooling process is completed, the ^{3}He-^{4}He mixture starts flowing through the dilution circuit. The incoming mixture is pre-cooled below 4.2 K by different heat exchangers, and then compressed 2 bar to condense it. This compression is needed in cryo-free systems because ^{3}He has a condensation temperature below 4 K at atmospheric pressure. The liquid mixture fills the circuit up to the still, with the gaseous phase of the mixture being constantly pumped out it. This evaporative cooling process lowers the temperature below 800 mK.

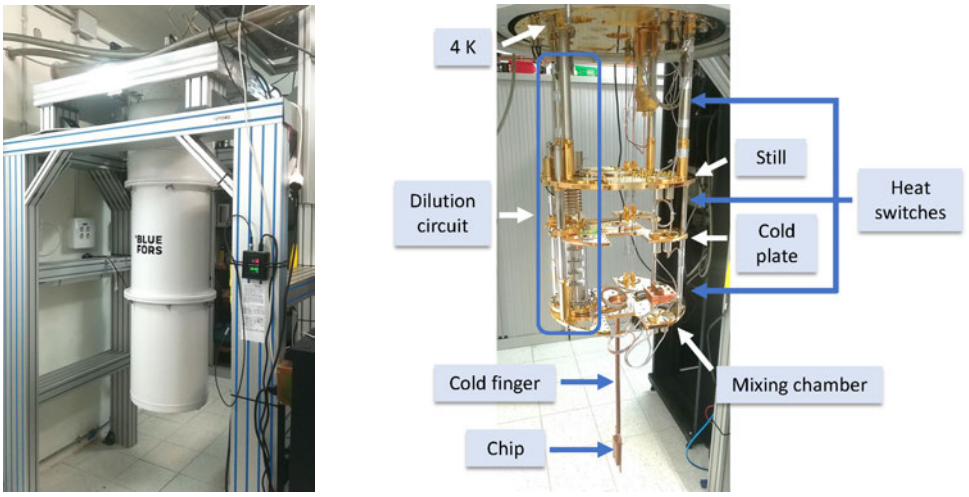

(a) (b)

Figure 2.6: BlueFors LD250 Dilution Refrigerator System closed (a) and open (b) to see its different cooling stages (or plates). These stages are, from warmer to colder, the 50 K plate (not visible), the 4 K plate, the still, the cold plate and the mixing chamber.

Below that temperature, the mixture is separated into a ^{4}He-rich (or dilute) phase and an almost pure ^{3}He gaseous phase. As ^{4}He is heavier than ^{3}He, the dilute phase remains at the bottom of the mixing chamber, while ^{3}He gas continues to flow through the dilution circuit (see figure 2.7). When ^{3}He gas is pumped into the mixing chamber, it is forced to go through the phase boundary with the diluted phase to complete the circuit, taking some energy from the mixing chamber and cooling it along our samples to as low as 7 mK.

2.2.2 Superconducting magnet

The cryostat has an uniaxial superconducting magnet by American Magnetics mounted below the mixing chamber, which applies magnetic fields up to 1 T parallel to the vertical axis of the cryostat with a resolution of 10^{-4} T. The magnet is thermally connected to the 4.2 K plate and isolated from the mixing chamber. An oxygen-free copper cold finger extends below the mixing chamber and into space inside the magnet coils, which allows us to place our chip in the center of the magnet while thermalising our sample with the mixing chamber. A 430 power supply programmer controlling a 4Q06125PS-430 power supply outputs the current in the magnet. This programmer can be controlled from the computer.

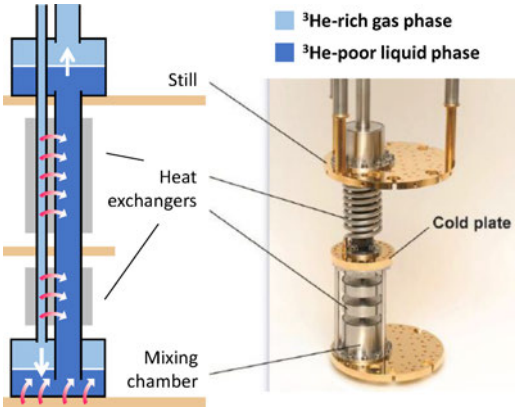

Figure 2.7: Scheme and close-up of the dilution circuit in figure 2.6. The temperature of the incoming ^{3}He-rich gas flow in the condensing line decreases as it transfers heat to the ^{3}He-poor column between the mixing chamber and the still. At the mixing chamber, ^{3}He atoms borrow energy from the mixing chamber structure to cross the phase boundary. The main limitation to the cooling power of the circuit are the heat exchangers. This is due to the thermal boundary resistance between liquid helium and the exchanger walls, known as Kapitza resistance, which increases with decrease temperature [12, 13].

2.2.3 Microwave coaxial lines and cryogenic amplifier

The input and output semi-rigid coaxial lines inside the cryostat send the input microwave signals to the chip and receive its transmission. The input coaxial lines are made of stainless steel down to the 4 K plate, and then of a CuNi alloy down to the mixing chamber. 10 dBm attenuators are installed in each cooling stage, limiting the input power that reaches the chip.

The output coaxial lines connecting the mixing chamber and the 4 K plate are made of a superconducting NbTi alloy. At the latter stage, they are connected to a LNF 0.3-14 GHz cryogenic Low Noise Amplifier (LNA) [14]. Superconducting coaxial lines allow a close to perfect propagation of the often very weak output signals while maintaining a proper thermal isolation. The LNA then amplifies these signals by 30 dBm at cryogenic temperatures, when the thermal noise is still low. The rest of the output coaxial lines is made of a metallic CuNi alloy.

2.3 Microwave setup for pump-probe experiments

In pump-probe experiments, two pulses are sent to the chip: a short, high-power pulse (pump pulse) which excites a transition in our spin system, and a long, low-power pulse (probe pulse) to read the resonator frequency shift due

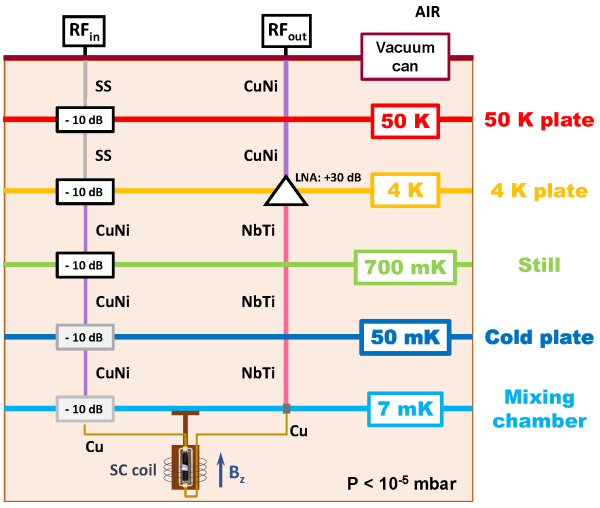

Figure 2.8: Input and output microwave coaxial lines inside the dilution refrigerator. The LNA in the output line is thermally anchored to the 4 K plate.

to its strong coupling to the excited spins. This method of reading the states of our spins by measuring the coupled resonator is known as dispersive readout. Our microwave setup for these experiments has changed in the course of this thesis work, the latest setup being shown in figure 2.9. It consists of two parts: a pulse generation stage and a readout stage.

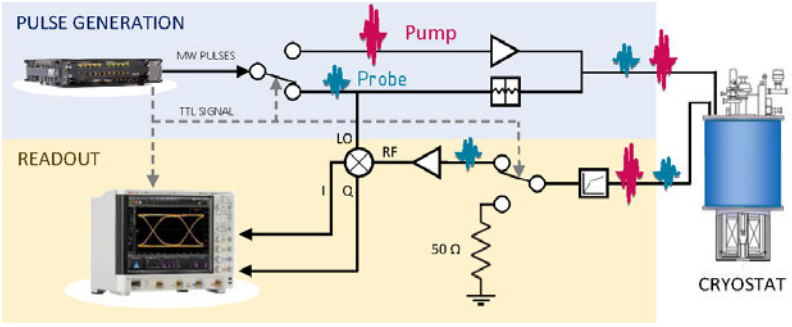

Figure 2.9: Microwave setup for pump-probe experiments

2.3.1 Characterization with continuous wave experiments

Before we start any dispersive readout experiment we need to characterize our resonators and the ensemble-resonator coupling with continuous wave experiments. For this purpose we use a vector network analyser (VNA), which measures the effect of frequency-swept or power-swept radio-frequency and microwave signals on the amplitude and phase of the transmission through our

chip. In particular, we use a Rohde & Schwarz ZVB14 model (figure 2.10a) provided by the Electronic Engineering and Communications Department of the University of Zaragoza, which can send and measure signals ranging from 10 MHz to 14 GHz [15].

The ZVB14 model has four ports. In each measurement we can decide which port sends a signal to our system and which ports are set to receive and measure transmitted or reflected signals. We define the complex quantities S_{ij} as the ratio between the measured signal at port i and the signal sent from port j while the other ports are decoupled from the system (figure 2.10b):

$$S_{ij} = \left.\frac{(V_{\text{out}})_i}{(V_{\text{in}})_j}\right|_{(V_{\text{in}})_{k\neq j}=0} . \tag{2.1}$$

In a simple transmission experiment with two ports with input signal at port 1, the transmission and reflection of the system are given by S_{21} and S_{11}. An example of these measurements is shown in figure 2.11a.

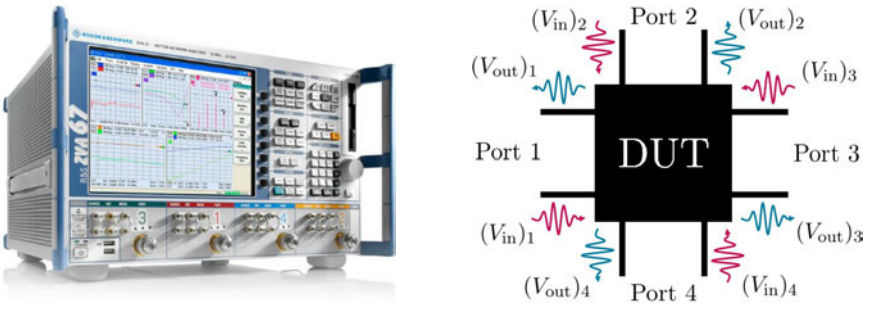

(a) (b)

Figure 2.10: Rohde & Schwarz ZVB14 model vector network analyser (a) and definition of the inputs and outputs of its 4 ports (b) from the point of view of the DUT (Device Under Test): $(V_{\text{in}})_i$ is the input wave from port i into the DUT, $(V_{\text{out}})_i$ is the output wave from the DUT into port i.

2.3.2 Pulse generation

The pulse generation stage is a Keysight M9180A Arbitrary Waveform Generator (AWG) with an amplifying stage [16]. It generates arbitrary pulses with a bandwidth of 5 GHz and a maximum amplitude of 1 V (10 dBm). The pulses are generated as a digital signal in the computer and then converted to an analog signal by the DAC (Digital-Analog Converter) of the AWG with a sampling rate of 12 GSa/s ($12 \cdot 10^9$ samples per second).

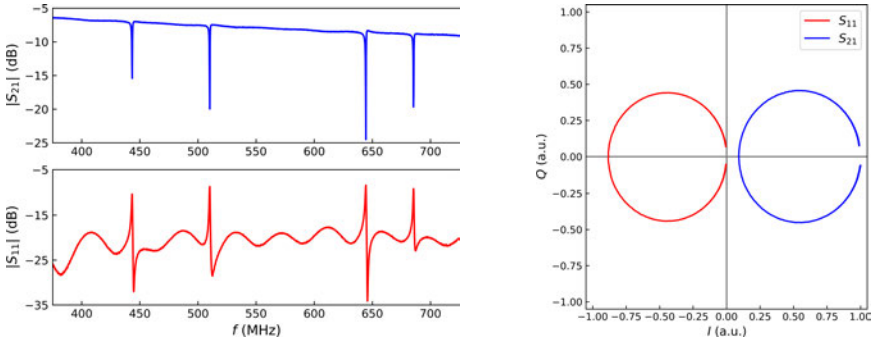

(a) (b)

Figure 2.11: (a) Module of the transmission S_{21} and reflection S_{11} scattering parameters of a transmission line with four lumped-element resonators. S_{11} and S_{21} are complex quantities that can be expressed by their module and phase or by their in-phase (I) and quadrature (Q) components (real and imaginary components). It is common to write the scattering parameters in dB units, defined as $20\log_{10}(S_{ij})$. (b) IQ plot of the calibration of the resonator at 443 MHz from figure 2.11a.

The AWG also sends, with the same sampling rate, a pulsed TTL signal that can be used to trigger other instruments. In particular, this signal controls the microwave switch that routes the pump pulse to an additional amplifying stage, while the probe pulse is routed to an IQ mixer as the local oscillator (LO) signal and then attenuated. Both pulses are combined again in a single line before entering the cryostat.

2.3.3 Readout

After the high power excitation pulse and the low power readout pulse interact with the spins and resonators in the chip, their transmission exits the cryostat and arrives at the detection stage. Before this stage, a second microwave switch separates the transmitted high power excitation pulses from the low power readout pulses. The latter are routed to the IQ mixer again, now as the RF signal.

The IQ mixer outputs two signals, I and Q (in-phase and quadrature), which are the product of the RF and LO signals, the latter shifted by 90° for the Q channel. Each of the I and Q channels outputs the sum of two signals: a high-frequency signal which oscillates with the sum of the RF and LO frequencies, and a low-frequency signal which oscillates with their absolute difference. The high-frequency signal is filtered by the bandwidth of the mixer, leaving only the low-frequency or 'demodulated' signal.

The I and Q outputs of the mixer were measured with a Keysight MSOS404A

oscilloscope. This instrument has a bandwidth of 8 GHz and is triggered by the pulsed TTL signal generated by the AWG [17]. The raw acquired data can be processed and averaged in the oscilloscope before sending it to the computer. All microwave instruments described above, from characterization and pulse generation to measurement and data acquisition, are controlled from the computer with homemade Python scripts (see section **??**).

2.4 Complementary experimental techniques

Characterizing a new molecule in a microwave setup is not always a straightforward process. First, there is a limitation in frequency, as only spin transitions in the frequency range of the microwave instruments can be probed. In addition, the coupling between microwaves and the target spin system depends on the orientation of the microwave field generated by the resonator or transmission line. These limitations do not pose a problem when dealing with simple non-interacting $S = 1/2$ systems, but they are very relevant in the case spin systems with magnetic anisotropy or when spin-spin interactions are relevant.

This section, details some experimental techniques that complement microwave experiments. Heat capacity and magnetic properties measurements were performed in services provided by the SAI (Servicio General de Apoyo a la Investigación) of the University of Zaragoza.

2.4.1 SQUID magnetometry

Magnetic measurements down to 1.9 K were carried out in a Magnetic Properties Measurement System (MPMS) by Quantum Design [18] operated by the Servicio de Apoyo a la Investigación (SAI) of the University of Zaragoza. The MPMS is a commercial magnetometer based on a dc-SQUID (Superconducting Quantum Interference Device) detector, which acts as a very sensitive magnetic flux to voltage transducer that allows the determination of the magnetization M of small samples at very low temperatures. Its operation is based on two quantum properties of superconductor materials: the quantization of the magnetic flux and the Josephson effect [19]. The sample is placed inside superconductor coils that couple the magnetic flux of the sample to the superconductor ring of the SQUID. The MPMS has a sensitivity better than 10^{-7} emu (1 emu $\leftrightarrow 10^{-3}$ A/m^2). The system has a liquid Helium cryostat that hosts the sample chamber, which allows varying temperature between 1.8 K and 350 K, and a superconducting magnet, which can generate DC magnetic fields up to 5 T.

(a) (b) (c)

Figure 2.12: (a) MPMS-XL at SAI. (b) PPMS-9T at SAI. (c) Measurement probe of the PPMS-9T.

A dc-SQUID consists of two superconductors connected in parallel by two Josephson junctions, forming a ring (see figure 2.13a). Both junctions have almost the same critical intensity I_c. In the presence of a magnetic field, a magnetic flux ϕ goes through the ring, causing the phase of each junction to evolve differently. If the SQUID is polarized with an external electric current $I_b > 2I_c$, a difference of electric potential V appears between its ends, which is modulated by the net current in the ring due to phase imbalance generated by ϕ. V is an oscillating function of ϕ with a period ϕ_0, the magnetic flux quantum ($\phi_0 = h/2e \simeq 2 \cdot 10^{-15}$ Wb). In order to measure the magnetic flux ϕ generated by the sample, a feedback loop introduces an external magnetic flux $\phi_V \propto V$ opposite to ϕ which tries to maintain $\phi + \phi_V = 0$. Provided that the feedback loop keeps this condition, by measuring V gives the magnetic flux $\phi = -\phi_V \propto V$. The proportionality constant $G := \phi/V$, which depends on the geometry of the SQUID, is a known calibration parameter.

In this thesis I carried out DC magnetic measurements, in which the MPMS applies a constant magnetic field so that sample gets a net magnetization M and generates a dipolar field. If the sample is moved across the SQUID pick-up coils, the magnetic flux changes and can be distinguished from that originated by other sources.

2.4.2 Micro-Hall magnetometry

Micro-Hall magnetometry experiments were carried out in a Physical Properties Measurement System (PPMS). The PPMS is a commercial system by Quantum Design [18] that allows performing measurements of different phys-

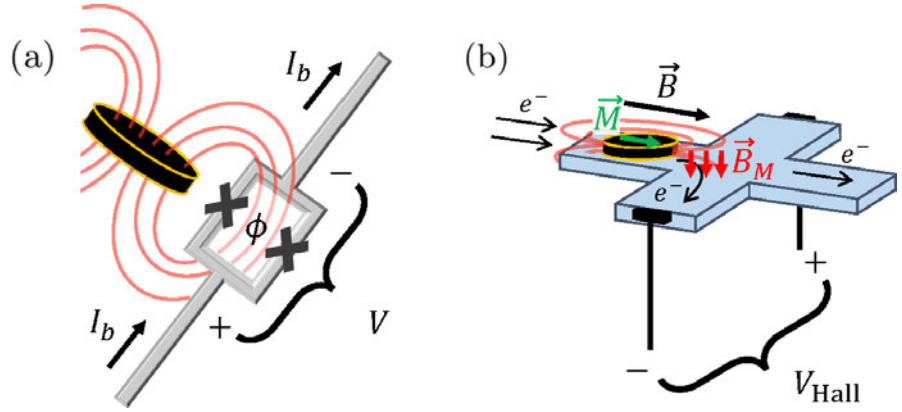

Figure 2.13: (a) Scheme of a SQUID. (b) Scheme of 'cross' magnetometer device designed to measure the Hall voltage induced by a magnetic sample.

ical properties in a wide range of temperatures (down to 350 mK) and fields (up to 9 or 14 T, depending on the model). In order to reach these low temperatures and high fields, the main body of the PPMS is a liquid helium dewar with a superconducting magnet, in which a measurement probe with the sample chamber and a ^{3}He cryostat is inserted.

The Micro-Hall magnetometry technique is based on the Hall effect [20]. Electrons in an electric current are deviated by a magnetic field $\vec{B}$ perpendicular to their propagation direction (defined by their velocity $\vec{v}$) via the (magnetic) Lorentz force $\vec{F} = q\vec{v} \times \vec{B} = -|e|\vec{v} \times \vec{B}$. This generates a electric current perpendicular to both $\vec{v}$ and $\vec{B}$ with an associated voltage V_{Hall}, which is the quantity that is measured.

The Micro-Hall magnetometer, sketched in figure 2.13b, consists of two layers of semiconductors, GaAs and $Al_{1-\alpha}Ga_\alpha As$, shaped in the form of a cross [21]. A two dimensional electron gas is confined at the interface between the two materials. The electrons behave as high-mobility charge carriers, which increases the Hall coefficient and the measured signal, reduces the resistivity of the device and improves the sensitivity. A current flow is introduced between two ports of the 'cross' magnetometer, with a magnetic field $\vec{B}$ applied parallel to the direction of propagation of the electrons. This field does not produce a Hall voltage, as it is parallel to $\vec{v}$. Its role is to generate a magnetization $\vec{M}$ in a magnetic sample deposited on top of the magnetometer, which in turn generates an additional magnetic field $\vec{B}_M$. Part of this field is perpendicular to the device (and $\vec{v}$), producing a Hall voltage V_{Hall} proportional to the induced magnetization $\vec{M}$ in the sample.

2.4.3 Heat capacity experiments

Heat capacity experiments were carried out in the PPMS described in the previous section. The measurements are performed with controlled pressure conditions in the sample chamber, that is, the PPMS measures the constant-pressure heat capacity, C_p:

$$C_p := \frac{dU}{dT}\Big|_p. \tag{2.2}$$

The sample chamber hosts a calorimeter for low-temperature heat capacity measurements [22] that consists of a sapphire disc (the sample holder), on which the sample is placed, with an integrated heater and thermometer. Sample and holder are put in mutual thermal contact with apiezon N grease. The holder is connected to a thermal reservoir with constant temperature T_0 by thin gold wires (see figure 2.14).

The heat capacity of the sample is measured using a relaxation technique [23]. A controlled quantity of heat power P_0 is introduced through the heater for a time t_0, which increases the temperature T_1 of both the holder and the sample. Part of the heat is transferred through the gold wires, modeled with a thermal conductivity K_1, to the thermal reservoir. The whole process is governed by the following differential equation relating the heat and temperature variation rates:

$$\frac{\partial Q(t)}{\partial t} := P_0\theta(t-t_0) = C_{\text{total}}\frac{\partial T_1(t)}{\partial t} + K_1\left[T_1(t) - T_0\right], \tag{2.3}$$

where $C_{\text{total}} = C_{\text{holder}} + C_{\text{sample}}$ is the combined heat capacity of the holder and the sample, and $\theta(t)$ is the step function.

Figure 2.14c shows the solution to equation 2.3. It consists of an increase in the sample temperature T_1 during the heat pulse, followed by a relaxation to T_0. Both the increase and decrease are exponential functions with a time constant $\tau_1 = C_{\text{total}}/K_1$. Knowing K_1 from calibration experiments, the total heat capacity C_{total} is calculated from the measurement of τ_1. The different holders are regularly calibrated, that is, measured without sample, so that their heat capacity C_{holder} can be subtracted from C_{total} to obtain the sample heat capacity.

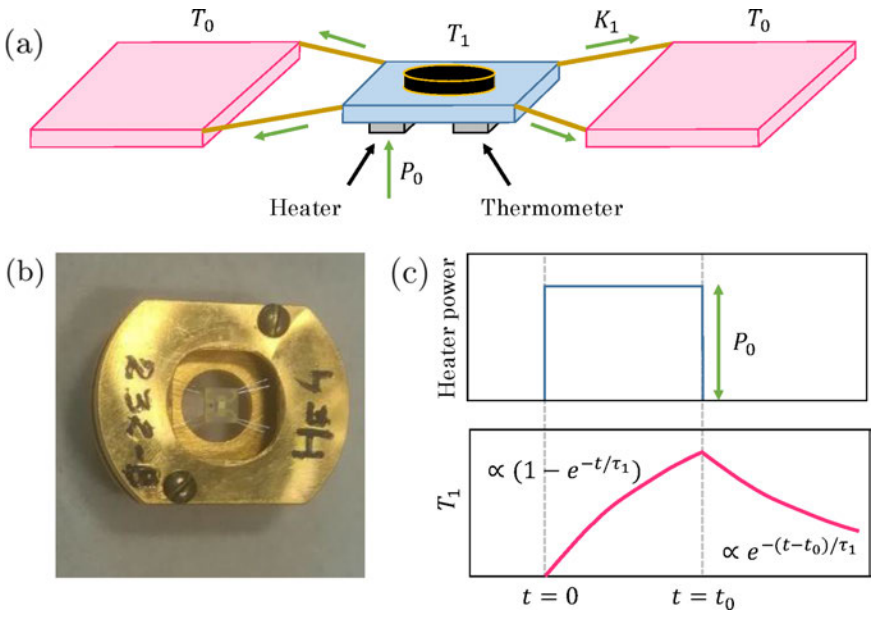

Figure 2.14: (a) Scheme of the sample holder (blue) connected to the reservoir (magenta) by thin gold wires. (b) Photo of the bulk of the calorimeter (the reservoir) with the square sample holder suspended in its centre. (c) Response of the temperature T_1 of the sample to a heat pulse at constant power P_0.

2.4.4 Electron Paramagnetic Resonance

Electron Paramagnetic Resonance (EPR) is a spectroscopy technique in which an oscillating magnetic field induces magnetic dipole transitions between energy levels of a system of spins in a paramagnetic sample [1, 10, 24]. EPR experiments were performed in a commercial Elexsys E-580 by Brucker Corporation [25] operating in the X-band, property of the INMA (see figure 2.15a). The spectrometer consists of a resonant cavity that is irradiated with a microwave source. X-band cavities, which are the most common setup, have a resonance frequency around 9.8 GHz. The paramagnetic sample is placed inside the cavity, which in turn is located at the center of an electromagnet. The external DC magnetic field generated by the magnet tunes the spin transitions in the sample to the cavity frequency, which results in a resonant absorption of microwave power by the paramagnetic sample.

In continuous wave EPR (cw-EPR) experiment, the cavity is continuously irradiated while the DC magnetic field is swept slowly. Around each resonance condition where a spin transition frequency of the sample matches the cavity frequency, the incoming microwave radiation is absorbed by the sample. The absorption signal is obtained with a field-modulation detection, in which a set of small coils apply a radio-frequency (RF) magnetic field modulation that

results in derivative-like lineshape for each absorption signal (figures 2.15b-c). The cw-EPR spectrum of the sample gives information about the energies and states in the spin system and about the effective spin Hamiltonian that generates them.

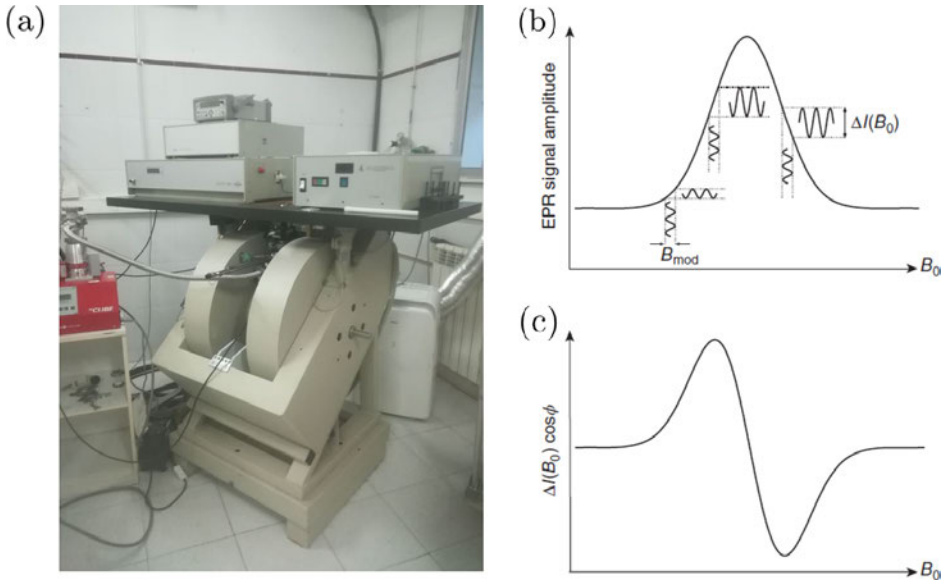

Figure 2.15: (a) Elexsys E-580 spectrometer. The bulk of the device are the magnet coils. (b) A Gaussian absorption line, measured as a function of the DC magnetic field B_0. The relation between the intensity $I(B_0)$ of the absorption line and the change $\Delta I(B_0)$ induced by the modulation field B_{mod} is shown for three fields. (c) The derivative-like lineshape that is obtained by detecting $\Delta I(B_0)$ with a lock-in amplifier. Figures (b) and (c) were taken from [1, Ch.1].

A complementary technique is pulsed EPR, which measures the signal emitted by a spin system after interacting with a series of microwave pulses. This gives information on the relaxation and coherence of the spin system, as the detected signal depends on the dynamics of the spin state prepared by the pulses. The simplest pulsed EPR experiment is the measurement of the Free Induction Decay (FID), which is the signal that the spin system generates in the cavity after a microwave pulse that generates a coherence between the two spin states of a given transition. This signal decays with a characteristic time T_2^* that is shorter that the phase memory time T_m of the individual spins if there is a distribution of Larmor frequencies at which the spins precess around the DC magnetic field B_0. This effect, pictured in figure 2.16a, is known as inhomogeneous broadening. The FID measurement is usually limited by a dead time of the spectrometer after the pulse, which is needed to protect the detection circuit from the high power signal.

The two-pulse echo, or Hahn-echo, sequence adds a second pulse that refocuses the FID signal after removing the effect of inhomogeneous broadening (see figure 2.16). If the second pulse is delayed by a time τ, the revival of the FID signal happens at a time τ after the second pulse (2τ from the first pulse). This revival is known as the echo signal, which decays with the single spin memory time $T_\mathrm{m} > T_2^*$ (if spin-spin interactions are neglected). This time is obtained by measuring the echo for different delay times τ between the two pulses. The limitation of the dead time of the spectrometer is removed by choosing a long enough τ.

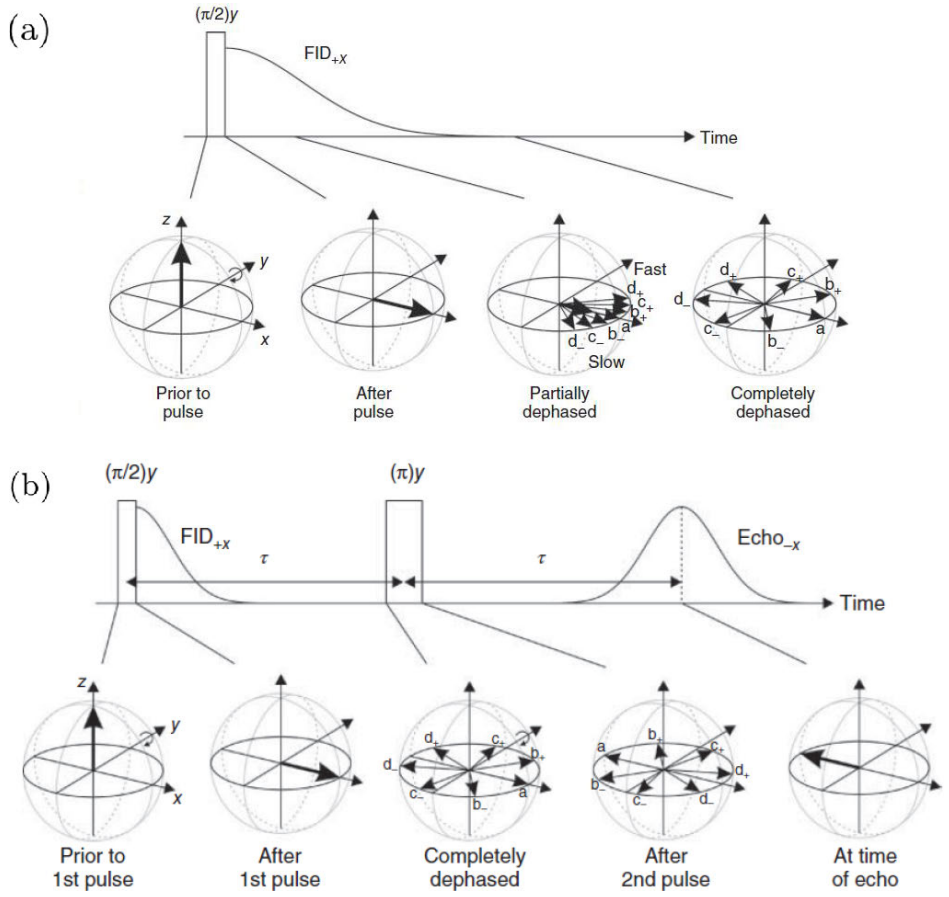

Figure 2.16: (a) FID measurement. (b) Hanh-echo experiment. Figures were taken from [1, Ch.11].

References

[1] D. Goldfarb and S. Stoll, *EPR spectroscopy: fundamentals and methods* (Wiley, 2018).

[2] A. Blais, R.-S. Huang, A. Wallraff, S. M. Girvin, and R. J. Schoelkopf, Physical Review A **69**, 062320 (2004).

[3] M. D. Jenkins, T. Hümmer, M. J. Martínez-Pérez, J. J. García-Ripoll, D. Zueco, and F. Luis, New Journal of Physics **15**, 095007 (2013), URL 10.1088/1367-2630/15/9/095007.

[4] M. D. Jenkins, D. Zueco, O. Roubeau, G. Aromi, J. Majer, and F. Luis, Dalton Transactions **45**, 16682 (2016).

[5] S. Doyle, P. Mauskopf, J. Naylon, A. Porch, and C. Duncombe, Journal of Low Temperature Physics **151**, 530 (2008).

[6] B. Aja, M. C. de Ory, L. de la Fuente, E. Artal, J. P. Pascual, M. T. Magaz, D. Granados, and A. Gomez, IEEE Transactions on Microwave Theory and Techniques **69**, 578 (2020).

[7] C. Mack, *Introduction to semiconductor lithography: the science of microfabrication* (Wiley-Interscience, 2008).

[8] A. Einstein, Physikalische Zeitschrift **8**, 121 (1917).

[9] C. Cohen-Tannoudji, B. Diu, and F. Laloë, *Quantum mechanics (Second edition)* (Wiley-VCH, 2020).

[10] A. Abragam and B. Bleaney, *Electron paramagnetic resonance of transition ions* (Oxford University Press, 1970).

[11] Bluefors, *BF-LD-Series user manual* (2016).

[12] P. L. Kapitza, Physical Review **60**, 354 (1941).

[13] G. L. Pollack, Reviews of Modern Physics **41(1)**, 48 (1969).

[14] LNF, *LNF-LNC0.3_14B - Datasheet* (2022).

[15] Rohde & Schwarz, *ZVB Vector Network Analyzers - Datasheet* (2011).

[16] Keysight, *M8190A Arbitrary Waveform Generator - Datasheet* (2021).

[17] Keysight, *Infiniium S-Series - Datasheet* (2022).

[18] Quantum Design, *Quantum design*, https://qd-europe.com.

[19] B. D. Josephson, Physics Letters **1(7)**, 251 (1962).

[20] H. Hall, E, American Journal of Mathematics **2**, 287 (1879).

[21] A. D. Kent, S. von Molnár, S. Gider, and D. D. Awschalom, Journal of Applied Physics **76(10)**, 6656 (1994).

[22] M. Evangelisti, F. Luis, L. J. de Jongh, and M. Affronte, Journal of Materials Chemistry **16**, 2534 (2006).

[23] G. R. Stewart, Review of Scientific Instruments **54**, 1 (1983).

[24] A. Schweiger and G. Jeschke, *Principles of pulse electron paramagnetic resonance* (Oxford University Press, 2001).

[25] Bruker Corporation, *Bruker corporation*, `https://www.bruker.com`.

Chapter 3

Background on spin systems coupled to superconducting resonators

This chapter summarizes the theoretical framework needed to describe our quantum processor. We will define an effective Hamiltonian for our molecular spin qubits and describe their decoherence and relaxation processes (see section 3.1). We need as well a model of the lumped-element resonator that we use to read, drive/excite and control these qubits (see section 3.2).

These two quantum systems are not isolated, but coupled and entangled. The nature of this coupling and the implications of its strength compared to the qubit and resonator relaxation rates are discussed in section 3.3. Finally, in section 3.4 we discuss the theory of the dispersive regime, when the detuning between the transition frequencies of the spin system and the resonator frequency is larger than the coupling between the two systems.

3.1 Molecular spin systems

When using molecular spin systems, we encode the qubit/qudit states in the low energy spin states of a magnetic molecule. At very low temperatures, these are the only relevant populated states in our system. Therefore, we need an effective spin Hamiltonian which accounts only for the low energy level structure and spin states of the molecular ground spin multiplet of the molecule.

3.1.1 The ground multiplet

The core of a magnetic molecule is composed of one or several transition metal or lanthanide magnetic ions. The ground multiplet of an isolated ion is determined by the Coulomb interaction of its electrons with the electric field of the nucleus and the repulsive interaction between electrons. We have to consider as well the spin-orbit coupling between the orbital angular momentum and the spin of each electron.

In a molecule, the magnetic core is surrounded by non-magnetic ligands that stabilize it and isolate from neighbouring molecules in the same crystal. The local coordination of each ion generates an electric field, known as crystal field, which splits the atomic orbitals and modifies the wavefunctions. The competition between crystal field and spin-orbit interactions gives rise to a different character of the ground multiplet for transition metal and lanthanide ions.

The crystal field is the dominant interaction in transition metal ions [1, Ch.7]. The orbital contribution to the angular momentum $\mathbf{L}$ in these ions is largely quenched due to the crystal field splittings, which leads to a small magnetic anisotropy. In most cases, this means that the total spin S is a good quantum number for the ground multiplet, so the effective spin vector operator is just $\mathbf{S}$. The ligand field does not affect these spin states directly, but it manifests itself through spin-orbit coupling.

Lanthanide ions have large orbital angular momentum ($L = 3$), and therefore a strong spin-orbit coupling and large magnetic anisotropy. In addition, the crystal field interaction is relatively small, as the 4f orbitals are close to the nucleus. Following Hund's rules, the ground electronic state of a free lanthanide ion is a multiplet with a well defined total angular momentum $\mathbf{J} = \mathbf{L} + \mathbf{S}$. We treat $\mathbf{J}$ as an effective spin, which we will label $\mathbf{S}$ in what follows keeping in mind that it has an orbital angular momentum component.

3.1.2 Effective spin Hamiltonian

The effective Hamiltonian H_S describes the (?) of a molecular spin within its orbital ground state. It comprises the electronic Zeeman interaction $H_{el,Z}$, the magnetic anisotropy contribution arising from the crystal field, H_{ma}, and, if the nuclear spin I of the ion is non zero, the hyperfine (H_{hf}), nuclear Zeeman ($H_{nu,Z}$) and quadrupolar (H_{qp}) interactions (though the latter two are usually

negligible). The resulting Hamiltonian is [1, Ch.3]:

$$\begin{aligned} H_S &= H_{el,Z} + H_{ma} + H_{hf} + H_{nu,Z} + H_{qp} \\ &= \mu_{\mathrm{B}} \boldsymbol{B} \cdot \boldsymbol{g} \cdot \hat{\boldsymbol{S}} + \sum_{k,\,q} B_{kq} \hat{O}_k^q + \hat{\boldsymbol{S}} \cdot \boldsymbol{A} \cdot \hat{\boldsymbol{I}} - \mu_N g_I \boldsymbol{B} \cdot \hat{\boldsymbol{I}} + P_{\parallel} \left(\hat{I}_z^2 - \tfrac{1}{3} I(I+1) \right), \end{aligned} \tag{3.1}$$

with the meaning of the quantities and parameters detailed below.

At high magnetic fields, the electronic Zeeman interaction between the magnetic moment of the electronic shell and the external magnetic field is the dominant term in the Hamiltonian. In a free ion, this term is $\mu_{\mathrm{B}} g_e \boldsymbol{B} \cdot \hat{\boldsymbol{S}}$, where μ_{B} is the Bohr magneton and $g_e \simeq 2.0$ is the free electron g-factor.[1] The effect of the magnetic anisotropy is included by replacing g_e with a 'tensor' $\boldsymbol{g}$.[2] In the most general case this gives all the different products of the components of $\boldsymbol{B}$ and $\hat{\boldsymbol{S}}$:

$$H_{el,Z} = \mu_{\mathrm{B}} \boldsymbol{B} \cdot \boldsymbol{g} \cdot \hat{\boldsymbol{S}} \equiv \mu_{\mathrm{B}} \begin{pmatrix} B_x & B_y & B_z \end{pmatrix} \begin{pmatrix} g_{xx} & g_{xy} & g_{xz} \\ g_{yx} & g_{yy} & g_{yz} \\ g_{zx} & g_{zy} & g_{zz} \end{pmatrix} \begin{pmatrix} \hat{S}_x \\ \hat{S}_y \\ \hat{S}_z \end{pmatrix} \tag{3.2}$$

In most cases the cross terms can be eliminated if we work in a suitable frame of reference — the principal axes — and it is enough to describe the interaction using only the diagonal terms:

$$H_{el,Z} = \mu_{\mathrm{B}} \left(g_x B_x \hat{S}_x + g_y B_y \hat{S}_y + g_z B_z \hat{S}_z \right). \tag{3.3}$$

The deviation of $g_x = g_{xx}$, $g_y = g_{yy}$ and $g_z = g_{zz}$ from g_e depends on the strength of magnetic anisotropy. If there is axial symmetry, which is usually assigned to the principal axis z, we may distinguish between the parallel g-factor $g_{\parallel} \equiv g_z$ and the perpendicular g-factor $g_{\perp} \equiv g_x = g_y$.

If the nucleus of the ion has a magnetic moment, there is also a nuclear Zeeman interaction between this moment and the magnetic field:

$$H_{nu,Z} = -\mu_N g_I \boldsymbol{B} \cdot \hat{\boldsymbol{I}} = -\mu_N g_I \left(B_x \hat{I}_x + B_y \hat{I}_y + B_z \hat{I}_z \right). \tag{3.4}$$

[1] The Bohr magneton is proportional to the electron charge, and therefore a negative quantity. However, it is common practice to cancel out the negative sign of μ_{B} with the negative sign of the Zeeman interaction and define μ_{B} as positive. Note that we do not do this with the nuclear magneton μ_N, which we define to be positive (with g_I positive or negative depending on the nucleus).

[2] Although $\boldsymbol{g}$ is usually called a tensor, it is not a tensor in general. The same can be said for the hyperfine 'tensor' $\boldsymbol{A}$. The only thing that matters is whether we can use the same choice of principal axes and basis states to keep only the diagonal terms in both $\boldsymbol{g}$ and $\boldsymbol{A}$ [1, Ch.15].

Here μ_N is the nuclear magneton and g_I, the g-factor of the nucleus, is a dimensionless constant of the order of unity which can be positive or negative. The nuclear Zeeman interaction is much smaller than the electronic Zeeman, as the nucleus is much heavier than the electron: $\frac{\mu_N}{\mu_\mathrm{B}} \propto \frac{m_e}{m_N} \sim 10^{-3}$.

At low fields, and in particular at zero field, magnetic anisotropy is the dominant term in the Hamiltonian. This term groups together the effects coming from the crystal field and the spin-orbit coupling. It is written as a combination of the Stevens operators $\hat{O}_k^q$, which take into account the several symmetries in the coordination sphere and how they affect the spin states, with coefficients B_{kq}:

$$H_{ma} = \sum_{k,\,q} B_{kq}\hat{O}_k^q \equiv \sum_{k=2,4,6} \left(\sum_{-k\leq q\leq k} B_{kq}\hat{O}_k^q \right). \tag{3.5}$$

Each Stevens operator $\hat{O}_k^q$ is a combination of powers of the spin operators $\hat{S}_x$, $\hat{S}_y$ and $\hat{S}_z$ up to order k (see table 3.1).

For an effective spin S, only operators with $k \leq 2S$ have non-zero matrix elements. If S is small and with low symmetry we can describe H_{ma} with only two $k = 2$ terms:

$$H_{ma} = B_{20}\hat{O}_2^0 + B_{22}\hat{O}_2^2 \equiv D\left(\hat{S}_z^2 - \tfrac{1}{3}S(S+1)\right) + E\left(\hat{S}_x^2 - \hat{S}_y^2\right), \tag{3.6}$$

where $D = 3B_{20}$ and $E = B_{22}$ are the tetragonal and orthorhombic distortion parameters.

According to Kramers theorem, at zero magnetic field, systems with half-odd electronic spin form doublets of spin states related by time-reversal symmetry [1, Ch.15]. This degeneracy, which can not be lifted by magnetic anisotropy, can be lifted in turn by the hyperfine interaction between the electronic and nuclear magnetic moments of the ion. It is in this situation when the hyperfine interaction becomes more relevant. Due to magnetic anisotropy, this interaction is mediated by a 'tensor' $\boldsymbol{A}$:[3]

$$H_{el,Z} = \hat{\boldsymbol{S}} \cdot \boldsymbol{A} \cdot \hat{\boldsymbol{I}} \equiv \begin{pmatrix} \hat{S}_x & \hat{S}_y & \hat{S}_z \end{pmatrix} \begin{pmatrix} A_{xx} & A_{xy} & A_{xz} \\ A_{yx} & A_{yy} & A_{yz} \\ A_{zx} & A_{zy} & A_{zz} \end{pmatrix} \begin{pmatrix} \hat{I}_x \\ \hat{I}_y \\ \hat{I}_z \end{pmatrix} \tag{3.7}$$

In most cases the principal axes for the hyperfine interaction are the same as those for the electronic Zeeman interaction, and we can describe our system

[3] We will obtain products of electronic and nuclear spin operators, which belong to different subspaces. The product of these operators is then a tensor product that we are omitting from the notation: $\hat{S}_i\hat{I}_j \equiv \hat{S}_i \otimes \hat{I}_j$.

k	q	$\hat{O}_k^q$
2	0	$3\hat{S}_z^2 - s\mathbb{I}$
	±1	$c_\pm \{\hat{S}_z,\, \hat{S}_+ \pm \hat{S}_-\}_+$
	±2	$c_\pm (\hat{S}_+^2 \pm \hat{S}_-^2)$
4	0	$35\hat{S}_z^4 - (30s-25)\,\hat{S}_z^2 + \left(3s^2-6s\right)\mathbb{I}$
	±1	$c_\pm \{7\hat{S}_z^3 - (3s+1)\,\hat{S}_z,\, \hat{S}_+ \pm \hat{S}_-\}_+$
	±2	$c_\pm \{7\hat{S}_z^2 - (s+5)\,\mathbb{I},\, \hat{S}_+^2 \pm \hat{S}_-^2\}_+$
	±3	$c_\pm \{\hat{S}_z,\, \hat{S}_+^3 \pm \hat{S}_-^3\}_+$
	±4	$c_\pm (\hat{S}_+^4 \pm \hat{S}_-^4)$
6	0	$231\hat{S}_z^6 - (315s-735)\,\hat{S}_z^4 + \left(105s^2-525s+294\right)\hat{S}_z^2 -$ $- \left(5s^3-40s^2+60s\right)\mathbb{I}$
	±1	$c_\pm \{33\hat{S}_z^5 - (30s-15)\,\hat{S}_z^3 + \left(5s^2-10s+12\right)\hat{S}_z,\, \hat{S}_+ \pm \hat{S}_-\}_+$
	±2	$c_\pm \{33\hat{S}_z^4 - (18s+123)\,\hat{S}_z^2 + \left(s^2+10s+102\right)\mathbb{I},\, \hat{S}_+^2 \pm \hat{S}_-^2\}_+$
	±3	$c_\pm \{11\hat{S}_z^3 - (3s+59)\,\hat{S}_z,\, \hat{S}_+^3 \pm \hat{S}_-^3\}_+$
	±4	$c_\pm \{11\hat{S}_z^2 - (s+38)\,\mathbb{I},\, \hat{S}_+^4 \pm \hat{S}_-^4\}_+$
	±5	$c_\pm \{\hat{S}_z,\, \hat{S}_+^5 \pm \hat{S}_-^5\}_+$
	±6	$c_\pm (\hat{S}_+^6 \pm \hat{S}_-^6)$

Table 3.1: Stevens operators from *EasySpin* documentation [2]. $\{A,B\}_+$ indicates the symmetrized product $(AB+BA)/2$, and $s = S(S+1)$, $c_+ = 1/2$, $c_- = 1/2i$.

only with the diagonal terms:

$$H_{hf} = A_x \hat{S}_x \otimes \hat{I}_x + A_y \hat{S}_y \otimes \hat{I}_y + A_z \hat{S}_z \otimes \hat{I}_z, \tag{3.8}$$

with $A_x \equiv A_{xx}$, $A_y \equiv A_{yy}$ and $A_z \equiv A_{zz}$. For axial symmetry, following the notation used in the electronic Zeeman interaction, we have $A_\parallel = A_z$ for the principal axis and $A_\perp = A_x = A_y$ for its orthogonal directions.

Finally, if both $S \geq 1$ and $I \geq 1$ we have also the quadrupolar nuclear term:

$$H_{qp} = P_\parallel \left(\hat{I}_z^2 - \tfrac{1}{3} I(I+1)\right). \tag{3.9}$$

3.1.3 Decoherence and relaxation processes

The molecule is surrounded by an environment that interacts with it. Then, the full Hamiltonian must include additional degrees of freedom from the environment. The decoherence and relaxation rates of the spin system are obtained by including all relevant interactions in the Hamiltonian and then tracing out all degrees of freedom except those of the spins [3, Ch.8].

Let us consider the simplest case: a single spin with $S = 1/2$. We can write its state at a given time t as:

$$|\psi(t)\rangle = \cos(\theta(t))\,|0\rangle + e^{i\phi(t)}\sin(\theta(t))\,|1\rangle \tag{3.10}$$

where $|0\rangle$ and $|1\rangle$ are eigenstates of $\hat{S}_z$. $|0\rangle$ is the ground state and $|1\rangle$ is the excited state, with a energy difference of $\hbar\omega_q$. The states described by equation 3.10 can be plotted in the Bloch sphere, as shown in figures 3.1a and 3.1b: $|0\rangle$ is the north pole of the sphere, $|1\rangle$ its south pole. The state of a single spin rotates around the z-axis of its Bloch sphere at a rate ω_q.

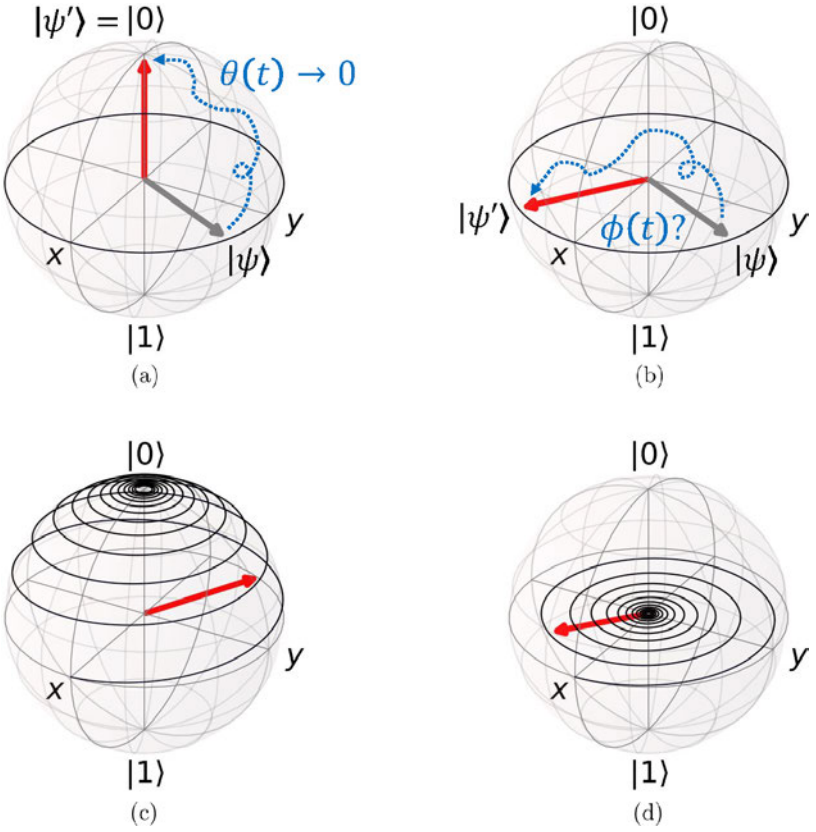

Figure 3.1: Relaxation and decoherence processes in the Bloch sphere. In the top row (a,b), the single spin description. (a) Longitudinal relaxation, where the state $|\psi\rangle$ jumps to the ground state $|\psi'\rangle = |0\rangle$. That is, $\theta(t) \to 0$, and we lose as well the information in $\phi(t)$. (b) Transverse relaxation, where the state $|\psi\rangle$ jumps to another state $|\psi'\rangle$ with the same $\theta(t)$ but different $\phi(t)$. The information in $\phi(t)$ is lost. In the bottom row (c,d), the ensemble description. Now we have a mixed state described by a Bloch vector. (c) Longitudinal relaxation, where the z component of the Bloch vector decays with T_1. Note that the x and y components also decay (see equation (3.11)). (d) Transverse relaxation, where the x and y components decay with T_2'.

Longitudinal spin relaxation is the relaxation process between different

energy states of the Hamiltonian of the isolated spin system. As the total energy changes, energy conservation requires that the same energy is absorbed or provided by the environment. In a single spin $S = 1/2$, this means a jump from the state $|\psi(t)\rangle$ to the ground state $|0\rangle$ at an arbitrary time (see figure 3.1a).

Transverse spin relaxation is the loss of coherence of the spin system, that is, the decay of the non-diagonal terms of the density matrix $\rho(t) = |\psi(t)\rangle \langle\psi(t)|$, where $\langle\psi(t)|$ is the Hermitian conjugate of the state $|\psi(t)\rangle$. In a single spin $S = 1/2$, this means a jump to another state $|\psi'(t)\rangle$ with the same $\theta(t)$ but different $\phi(t)$ at an arbitrary time (see figure 3.1b). We do not need an energy exchange between the spin system and the environment in transverse spin relaxation, although an interaction with the environment is still needed.

There is a probability for these processes to occur at a given time. We can recover this probability by either measuring the same qubit multiple times or having several identical copies of it. If we measure ensemble averages of $\hat{S}_x$, $\hat{S}_y$ or $\hat{S}_z$ we recover exponential decays. These three averages form the Bloch vector: $(\langle\hat{S}_x\rangle, \langle\hat{S}_y\rangle, \langle\hat{S}_z\rangle)$. We can trace the evolution of this vector in the Bloch sphere for the two types of relaxation processes (see figures 3.1c and 3.1d).

Longitudinal spin relaxation is quantified by T_1, the decay time of $\langle\hat{S}_z\rangle$, or, alternatively, its relaxation rate T_1^{-1}. In solids, the dominant contribution to T_1^{-1} is spin-lattice relaxation, driven by the interaction between the spins and electric field fluctuations caused by lattice vibrations (phonons). Besides, if the spin system is strongly coupled to a resonator, it is possible that T_1^{-1} is enhanced by the spin-photon interaction at energies (or frequencies) close to the spin-resonator resonance. This is known as the Purcell effect [4, Ch.4].

Transverse spin relaxation is quantified by the decay rate of $\langle\hat{S}_x\rangle$ and $\langle\hat{S}_y\rangle$. One mechanism is provided by the energy conserving flip-flop process: two spins exchange states, destroying phase ($\phi(t)$) correlation. The contribution by flip-flop processes is measured by T_2'. The total transverse spin relaxation rate T_2^{-1} includes also the contribution from longitudinal spin relaxation, which is half as efficient in destroying coherence than flip-flop processes as it only involves one spin:[4]

$$\frac{1}{T_2} = \frac{1}{T_2'} + \frac{1}{2T_1}\,. \tag{3.11}$$

In solid state systems T_2 is often not well defined, as the number of coherently coupled spins can change depending on the experiment we perform.

[4]Note in figure 3.1c that the longitudinal spin relaxation process implies a decay in $\langle\hat{S}_x\rangle$ and $\langle\hat{S}_y\rangle$.

Instead of using T_2, it is common practice to define characteristic transverse decay times associated to each experiment. One of these parameters is the phase memory time T_m, the inverse of the homogeneous half-width of the spin transition. It is measured as the decay time of the echo signal after a Hahn echo sequence ($\pi/2$ and π pulses) as we increase the separation time τ between the two pulses.[5] Another relevant parameter is T_2^*, which is the inverse of the inhomogeneous half-width of the transition and can be measured directly from the spectrum.

3.1.4 The molecular spin qubit

The Hamiltonian of a two-level system encoding a qubit with a frequency of operation ω_q is:

$$H_q = \frac{\hbar\omega_q}{2}\hat{\sigma}_z. \tag{3.12}$$

Here $\hat{\sigma}_z$ is one of the three Pauli matrices:

$$\hat{\sigma}_x = \begin{pmatrix} 0 & 1 \\ 1 & 0 \end{pmatrix}, \qquad \hat{\sigma}_y = \begin{pmatrix} 0 & -i \\ i & 0 \end{pmatrix}, \qquad \hat{\sigma}_z = \begin{pmatrix} 1 & 0 \\ 0 & -1 \end{pmatrix}, \tag{3.13}$$

which obey $\hat{\sigma}_j\hat{\sigma}_k = \delta_{jk}\mathbb{I} + i\epsilon_{jkl}\hat{\sigma}_l$.[6]

The simplest physical system with this Hamiltonian is the spin of a free electron biased with an static magnetic field $\boldsymbol{B}$. The isotropic Zeeman interaction of its spin 1/2 with the magnetic field gives the Hamiltonian:

$$H_q = \mu_\mathrm{B} g_e B \hat{S}_z = \frac{\mu_\mathrm{B} g_e B}{2}\hat{\sigma}_z, \tag{3.14}$$

where g_e is the g-factor of the free electron and we defined $\hat{z}$ as the orientation of the magnetic field ($\boldsymbol{B} := B\,\hat{z}$). We used the adimensional spin operator $\hat{S}_z = \hat{\sigma}_z/2$.[7] The frequency of operation of the free electron qubit is then $\omega_q = \mu_\mathrm{B} g_e B/\hbar$.

Free-radicals provide the closest example of a free electron in an organic molecule. One atom in these molecules loses an electron, leaving an unpaired electron with spin 1/2 with almost no anisotropy. We can use then Hamiltonian (3.14) with a g-factor that will be very similar to but not exactly g_e.

[5] T_m is often called T_2, but in general T_m is a lower bound to T_2 as it includes the instantaneous diffusion effect during the pulses.

[6] ϵ_{jkl} is the Levi-Civita symbol.

[7] The true spin operators $\hat{S}_j = \hbar\hat{\sigma}_j/2$ (with $j = x,\ y,\ z$) fulfill the angular momentum algebra and represent a spin 1/2. Using adimensional spin operators (dividing by $\hbar$) is just a convention to have the spin Hamiltonian parameters in units of energy

In a more complex molecule, like an organic ligand hosting a magnetic ion with effective spin 1/2, we will have an anisotropic Zeeman interaction with the magnetic field. Here we have to be careful with the different frames of reference in our experiment: the principal axes of the magnetic anisotropy of the molecule ($\hat{x}_{mol}$, $\hat{y}_{mol}$ and $\hat{z}_{mol}$) in which we write the spin Hamiltonian and the laboratory axes defined by the magnetic field ($\hat{x}_{lab}$, $\hat{y}_{lab}$ and $\hat{z}_{lab}$, where $\hat{z}_{lab}$ is parallel to the $\boldsymbol{B}$).

The only effect of the magnetic anisotropy on the spin Hamiltonian for a spin 1/2 is that we may have different g-values for the three principal axes in the diagonal tensor $\boldsymbol{g}$ of the Zeeman interaction. The simplest setup is then applying the magnetic field along one of the principal axes, and we just have to replace g_e by the corresponding g-value in equation (3.14). If the magnetic field is applied in any other direction, we need to either write $\boldsymbol{g}$ in the laboratory frame of reference (which will be non-diagonal) or $\hat{z}_{lab}$ in the frame of reference of the principal axes to find the effective g-value for $\hat{z}_{lab}$.

3.1.5 The molecular spin qudit

In a molecular spin qudit we need a magnetic molecule with more than two spin states. This can be achieved by using a magnetic ion with electronic spin greater than 1/2 and/or using a magnetic ion with non-zero nuclear spin. For each value of the magnetic field $\boldsymbol{B}$ we will have a set of d eigenstates $\{|\alpha\rangle\}$. In this basis, the qudit Hamiltonian (the spin Hamiltonian of the magnetic molecule, with all necessary terms) takes the simple diagonal form:

$$H_q = \sum_{\alpha=0}^{d-1} E_\alpha \hat{X}^{\alpha,\alpha}, \tag{3.15}$$

Here $\hat{X}^{\alpha,\alpha} \equiv |\alpha\rangle \langle\alpha|$ is the projector onto the eigenstate $|\alpha\rangle$ with energy eigenvalue E_α. We label the states in increasing order in energy so that $E_\beta > E_\alpha$ if $\beta > \alpha$. The indices α and β run from 0 to $d-1$.

3.2 Lumped-element resonators

Lumped-element resonators or LERs can be seen as superconducting LC circuits, with two well defined parts: an inductor and a capacitor (see figure 2.1 in chapter 2, and figure 3.2). The inductor is composed of several turns in one side of the resonator, which give rise to an inductance L. On the other side, we have an inter-digitated capacitor with capacitance C. The resonance

frequency of the system is given by:

$$\omega_r = \frac{1}{\sqrt{LC}}. \tag{3.16}$$

The quantization of a LER as an LC circuit is obtained starting at classical circuit theory, expressed in terms of flux Φ or charge q, from which we construct an effective Lagrangian and derive a Hamiltonian and quantize it using canonically conjugate variables [5].

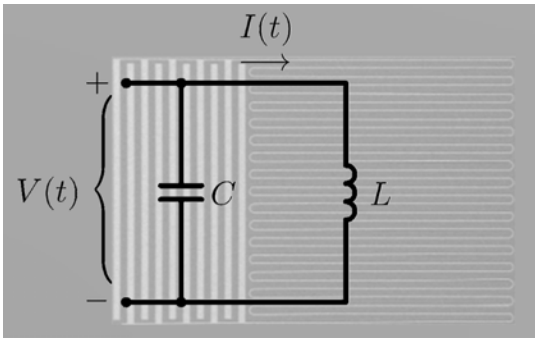

Figure 3.2: Parallel LC circuit representing a lumped-element resonator. $V(t)$ is the voltage in the capacitor and in the inductor. If we take $I(t)$ as the current in the inductor, then the current in the capacitor is $-I(t)$.

3.2.1 The classical LC resonator

The Kirchhoff's voltage and current laws for the LC resonator are (see figure 3.2):

$$\begin{aligned} V(t) - L\dot{I}(t) &= 0\,, \\ I(t) + C\dot{V}(t) &= 0\,. \end{aligned} \tag{3.17}$$

We can integrate in time the voltage law and combine it with the current law into a single equation in terms of the flux ϕ, which is related to V as $\dot{\phi} = V$:

$$\ddot{\phi}(t) = -\omega_r^2 \phi(t). \tag{3.18}$$

This is the equation of motion of a resonator with frequency ω_r. It can be derived from the classical Lagrangian for the LC circuit:

$$L_R = \frac{1}{2}C\dot{\phi}^2 - \frac{1}{2L}\phi^2, \tag{3.19}$$

or the associated Hamiltonian:

$$H_R = q\dot{\phi} - L_S = \frac{1}{2C}q^2 + \frac{1}{2L}\phi^2, \tag{3.20}$$

where the charge $q = \partial L_S / \partial \dot{\phi}$, defined in terms of current as $\dot{q} = I$, is the canonical conjugate variable of ϕ.[8]

3.2.2 Quantization of the LC resonator

The LC circuit can be quantized as the harmonic oscillator. The canonical conjugate variables ϕ and q are now two non-commuting operators $\hat{\phi}$ and $\hat{q}$, with $[\hat{\phi}, \hat{q}] = i\hbar$.[9] We define the annihilation $\hat{a}$ and creation $\hat{a}^\dagger$ operators in terms of $\hat{\phi}$ and $\hat{q}$ as:

$$\hat{a} := \sqrt{\frac{1}{2\hbar Z}} \left(\hat{\phi} + iZ\hat{q} \right) \quad , \quad \hat{a}^\dagger := \sqrt{\frac{1}{2\hbar Z}} \left(\hat{\phi} - iZ\hat{q} \right). \tag{3.21}$$

Here $Z = \sqrt{L/C}$ is the impedance of the resonator and the operators obey bosonic rules $[\hat{a}, \hat{a}^\dagger] = 1$. Using $\hat{a}$ and $\hat{a}^\dagger$ we obtain the textbook Hamiltonian of the quantum harmonic oscillator:

$$H_R = \hbar\omega_r \, \hat{a}^\dagger \hat{a} + \text{constant}. \tag{3.22}$$

We are interested in the time evolution of the expectation value of $\hat{a}$, given by $\langle \hat{a} \rangle = \langle \psi | \, a \, | \psi \rangle$, where $|\psi\rangle$ is the wavefunction of the resonator. We can also write it as $\langle \hat{a} \rangle = \langle \psi | \, a \, | \psi \rangle = \operatorname{Tr} \hat{a} \rho$, where $\rho = |\psi\rangle \langle \psi|$ is the density matrix.[10] Then, the time evolution of $\langle \hat{a} \rangle$ reads:

$$\frac{\mathrm{d}}{\mathrm{d}\, t} \langle \hat{a} \rangle = -\frac{i}{\hbar} \operatorname{Tr} \hat{a} \, [H_R, \rho] = -i\omega_r \langle \hat{a} \rangle \quad \Rightarrow \quad \langle \hat{a} \rangle (t) = \langle \hat{a} \rangle (0) e^{-i\omega_r t}. \tag{3.23}$$

where only the density matrix is time dependent, obeying von Neumann equation $\dot{\rho} = -i \, [H_R, \rho] / \hbar$.[11] If the resonator is not completely isolated there will be a leaking of photons to the environment. We model this with a decay rate κ for $\langle \hat{a} \rangle$ (and $\langle \hat{a}^\dagger \rangle$):[12]

$$\frac{\mathrm{d}}{\mathrm{d}\, t} \langle \hat{a} \rangle = -i\omega_r \langle \hat{a} \rangle - \kappa \langle \hat{a} \rangle \quad \Rightarrow \quad \langle \hat{a} \rangle (t) = \langle \hat{a} \rangle (0) e^{-(i\omega_r + \kappa)t}. \tag{3.24}$$

[8] The Poisson bracket of ϕ and q gives $\{\phi, q\}_{\mathrm{PB}} = 1$. The bracket is defined, for any pair of variables $A(\phi, q)$ and $B(\phi, q)$ that are functions of the canonical conjugate variables ϕ and q, as $\{A(\phi, q), B(\phi, q)\}_{\mathrm{PB}} = \dfrac{\partial A}{\partial \phi} \dfrac{\partial B}{\partial q} - \dfrac{\partial A}{\partial q} \dfrac{\partial B}{\partial \phi}$.

[9] The Poisson bracket of two canonical conjugate variables is promoted to the commutator of the operators that represent them (with a factor $i\hbar$): $\{\phi, q\}_{\mathrm{PB}} = 1 \rightarrow [\hat{\phi}, \hat{q}] = i\hbar$

[10] Given a matrix A, $\operatorname{Tr} A$ is the sum of its diagonal elements: $\operatorname{Tr} A = \sum_i A_{ii}$.

[11] $\frac{\mathrm{d}}{\mathrm{d}\, t} \langle \hat{a} \rangle = \operatorname{Tr} \hat{a} \dot{\rho} = -\frac{i}{\hbar} \operatorname{Tr} \hat{a} \, [H_R, \rho] = -i\omega_r \langle \left[\hat{a}, \hat{a}^\dagger \right] \hat{a} \rangle = -i\omega_r \langle \hat{a} \rangle$

[12] We will justify this decay with a quantum master equation in the next chapter. Let us consider only losses due to the coupling of the resonator to our coupling device (the transmission line). In a single port measurement, photons will leak into the line at a rate κ, and $\langle \hat{a} \rangle$ and $\langle \hat{a}^\dagger \rangle$ will lose coherence at a rate $\kappa/2$. However, we always place our resonators and samples in a transmission line with two ports. In this two-port setup, both rates are multiplied by a factor of two.

The relative strength of ω_r and κ is encapsulated in the quality factor Q:

$$Q := \frac{\omega_r}{2\kappa}. \tag{3.25}$$

3.3 Coupling molecular spin qubits to lumped-element resonators

If molecular spin qubits were directly coupled to the transmission line, their interaction time with the photons sent through the line would be too short for them to interact coherently. In order to have longer interaction times we need to couple the spins to photons inside a cavity or resonator. In section 3.3.1 we model the interaction between a single molecular spin qubit and a lumped element resonator.

Unfortunately, we can not use this model because we are not performing experiments on single molecules yet. The coupling G_1 of each molecule to the resonator is still too weak for quantum applications, its enhancement being a subject of current research in molecular spin qubits [6]. However, it is still possible to test our molecules if we measure large ensembles of them. This gives a collective coupling G_N that enhances the single molecule coupling by a factor $\sqrt{N}$, where N is the number of spins in the ensemble.

Here, we model the ensemble. The simplest case is an ensemble of spin 1/2 molecules, like in free radicals, which we review in section 3.3.2. Finally, in section 3.3.3 we generalize the results for spin 1/2 ensembles to higher spin ensembles.

3.3.1 Molecular spin qubit-resonator coupling

A single molecular spin qubit and a resonator are coupled via the interaction of the magnetic moment of the molecule with the zero-point magnetic field $\boldsymbol{B_0}$ of the resonator, that is, the field generated by the vacuum state of the resonator [7]. Both subsystems exchange excitations at the single qubit-resonator coupling rate G_1, with $\hbar G_1$ being the matrix element of the Zeeman interaction (see equation (3.7)) generated by the field $\boldsymbol{B_0}$ at the position $\boldsymbol{r}$ of the molecule:

$$\hbar G_1 := \langle 0 | \, \mu_\mathrm{B} \boldsymbol{B_0}(\boldsymbol{r}) \cdot \boldsymbol{g} \cdot \hat{\boldsymbol{S}} \, | 1 \rangle \, . \tag{3.26}$$

Here $|0\rangle$ and $|1\rangle$ are the eigenstates of the qubit Hamiltonian of equation (3.12) and $\hat{z}$ the orientation of the static magnetic field $\boldsymbol{B}$. In the most general case, we have to be careful to write everything in equation (3.26) in the same

reference frame (see section 3.1.4). The simplest case is an isotropic spin 1/2, with qubit frequency $\omega_q = \mu_\mathrm{B} g B$ and coupling:

$$\begin{aligned}\hbar G_1 :=& \frac{\mu_\mathrm{B} g}{2} \langle 0| \left[B_{0,\,x}(\boldsymbol{r})\hat{\sigma_x} + B_{0,\,y}(\boldsymbol{r})\hat{\sigma_y} + B_{0,\,z}(\boldsymbol{r})\hat{\sigma_z}\right] |1\rangle \\ =& \frac{\mu_\mathrm{B} g}{2} \left[B_{0,\,x}(\boldsymbol{r}) - i B_{0,\,y}(\boldsymbol{r})\right],\end{aligned} \tag{3.27}$$

that is, only the components of $\boldsymbol{B_0}(\boldsymbol{r})$ perpendicular to $\boldsymbol{B}$ contribute to the complex coupling. In the case of a single qubit we have the freedom to choose $\hat{x}$ as the orientation of $\boldsymbol{B_0}(\boldsymbol{r})$ and write a real G_1:

$$\hbar G_1 := \frac{\mu_\mathrm{B} g B_{0,\,\perp}(\boldsymbol{r})}{2}, \tag{3.28}$$

where $B_{0,\,\perp}(\boldsymbol{r})$ is the proyection of $\boldsymbol{B_0}(\boldsymbol{r})$ in plane the perpendicular to $\boldsymbol{B}$.

Another common situation with a simple description is a molecule with axial symmetry, with a longitudinal g-value $g_\parallel$ and a perpendicular g-value $g_\perp$ (see section 3.1.2). Applying the magnetic field $\boldsymbol{B}$ in the direction of the symmetry axis with $g_\parallel$ we have $\omega_q = \mu_\mathrm{B} g_\parallel B$ and:

$$\hbar G_1 := \frac{\mu_\mathrm{B} g_\perp B_{0,\,\perp}(\boldsymbol{r})}{2}. \tag{3.29}$$

While qubit and resonator exchange excitations at the rate G_1, each subsystem loses coherence. The qubit coherence decays at a rate γ (the inverse of T_2 or T_m, see section 3.1.3) and the resonator field at a rate κ (see figure 3.3). In order to use the qubit-resonator system for quantum computing we need to operate the qubit coherently. That is, we need $G_1 \gg \kappa, \gamma$ so that both qubit and resonator field remain coherent for long enough time for G_1 to perform the operation. When this condition is fulfilled, the qubit-resonator system is said to be in the strong coupling regime.

The quantum Rabi model gives a Hamiltonian for the closed (lossless) qubit-resonator system [5]:

$$H_\mathrm{Rabi} = \frac{\hbar\omega_q}{2}\hat{\sigma}_z + \hbar\omega_r \hat{a}^\dagger \hat{a} + \hbar\sigma_x \left(G_1 \hat{a} + G_1^* \hat{a}^\dagger\right), \tag{3.30}$$

where we have used the Pauli matrices $\hat{\sigma}_x$ and $\hat{\sigma}_z$ from equation (3.13).

Typically, the qubit-resonator coupling rate $|G_1|$ is much lower than both ω_q and ω_r. We can then use the rotating wave approximation, in which we neglect the counter-rotating terms in equation (3.30) that do not preserve the number of excitations in the qubit-resonator system.[13] With this approximation we

[13] Writing $\hat{\sigma}_x = \hat{\sigma}_+ + \hat{\sigma}_-$, this means dropping terms with $\hat{\sigma}_+\hat{a}^\dagger$ or $\hat{\sigma}_-\hat{a}$ and keeping the terms with $\hat{\sigma}_+\hat{a}$ or $\hat{\sigma}_-\hat{a}^\dagger$.

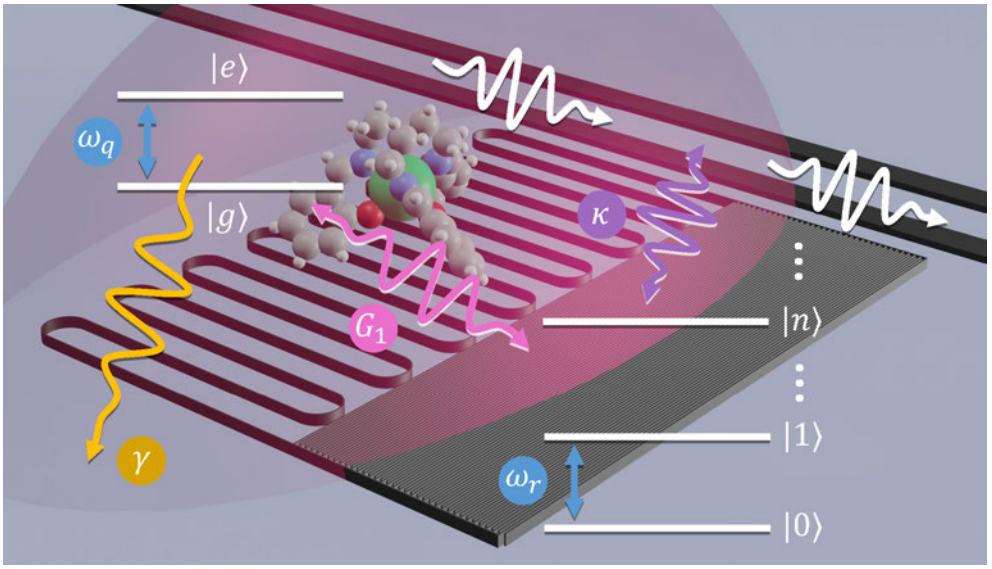

Figure 3.3: Scheme of the qubit-resonator coupling. The spin/qubit can be in any complex superposition of its two eigenstates $|g\rangle$ (ground) and $|e\rangle$ (excited). The energy difference $\hbar\omega_q$ between $|g\rangle$ and $|e\rangle$ determines the frequency of operation ω_q of the qubit. The coherence of the encoded state decays with γ (without including the interaction with the resonator). The resonator can be in any superposition of its eigenstates, labelled by the number n of photons in the cavity. The state of the resonator decays into the transmission line at a rate κ. The two subsytems, qubit and resonator, exchange excitations at a rate G_1.

obtain the so-called Jaynes-Cummings Hamiltonian [8, Ch.2]:

$$H_{\mathrm{JC}} = \frac{\hbar\omega_q}{2}\hat{\sigma}_z + \hbar\omega_r \hat{a}^\dagger\hat{a} + \hbar\left(G_1\hat{\sigma}_+\hat{a} + G_1^*\hat{\sigma}_-\hat{a}^\dagger\right). \tag{3.31}$$

Hamiltonian (3.31) is the starting point for any description of our system. The ground state of the JC model is $|\psi_{0,g}\rangle \equiv |0\rangle \otimes |g\rangle$, the tensor product of the Fock state of zero photons in the resonator ($|0\rangle$) and the ground state of the qubit ($|g\rangle$),[14] with energy $E_{0,g} = -\frac{\hbar\omega_q}{2}$. The excited states are pairs of hybridized qubit-resonator states $|\psi_{n,\pm}\rangle$, known as polaritons.[15] These states

[14] Obeying $\hat{\sigma}_z|g\rangle = -|g\rangle \;\Rightarrow\; |g\rangle = \begin{pmatrix}0\\1\end{pmatrix}$.

[15] The total number of excitations in the qubit-resonator system, given by the number operator $\mathcal{N} := \hat{a}^\dagger\hat{a} + \hat{\sigma}_+\hat{\sigma}_-$, and the parity operator, $\mathcal{P} := (-1)^{\hat{a}^\dagger\hat{a}}$, form a complete set of commuting operators for the qubit-resonator system. Besides, they commute with the Jaynes-Cummings Hamiltonian (3.31). We can use the eigenvalues of these two observables to label the polaritonic states. However, it is common to label the states with the same letter n as for the number of excitations in the resonator, instead of a new letter $\mathcal{N}$ for the total number of excitations.

are superpositions of the $|\psi_{n,\,g}\rangle \equiv |n\rangle \otimes |g\rangle$ and $|\psi_{n-1,\,e}\rangle \equiv |n-1\rangle \otimes |e\rangle$ states ($|e\rangle$ is the excited state of the qubit).[16]

The energy gap between the polaritonic states is $\hbar$ times the Rabi frequency Ω_n. Shifting the zero of energy to $E_{0,\,g}$, this gives [8, Ch.6]:

$$E_{n,\,\pm} = n\hbar\omega_r + \frac{\hbar\Delta}{2} \pm \frac{\hbar\Omega_n}{2}, \qquad \Omega_n \equiv \sqrt{\Delta^2 + 4n|G_1|^2}, \tag{3.32}$$

These energies are controlled by the frequency detuning $\Delta = \omega_q - \omega_r$ between the spin and resonator characteristic frequencies. The corresponding polaritonic states $|\psi_{n,\,\pm}\rangle$ are (see figure 3.4):

$$|\psi_{n,\,\pm}\rangle = \frac{1}{\sqrt{2}}\left(\sqrt{1 \mp \frac{\Delta}{\Omega_n}}\,|\psi_{n,\,g}\rangle \pm \sqrt{1 \pm \frac{\Delta}{\Omega_n}}\,|\psi_{n-1,\,e}\rangle\right). \tag{3.33}$$

In resonance ($\Delta = 0$), these are symmetric and antisymmetric superpositions:

$$|\psi_{n,\,\pm}\rangle = \frac{1}{\sqrt{2}}\left(|\psi_{n,\,g}\rangle \pm |\psi_{n-1,\,e}\rangle\right). \tag{3.34}$$

3.3.2 Spin 1/2 ensembles

In our setup, we need to couple the resonator to an ensemble of molecules in order to enhance the overall spin-resonator coupling. If our magnetic molecules have spin 1/2, like in free radicals, we can model them just by extending the Jaynes-Cummings model to N qubits:[17]

$$H_{\mathrm{TC}} = \sum_{i=1}^{N} \frac{\hbar\omega_{q,\,i}}{2}\hat{\sigma}_{z,\,i} + \hbar\omega_r\hat{a}^\dagger\hat{a} + \sum_{i=1}^{N}\hbar\left(G_{1,\,i}\,\hat{\sigma}_{+,\,i}\,\hat{a} + G^*_{1,\,i}\,\hat{\sigma}_{-,\,i}\,\hat{a}^\dagger\right), \tag{3.35}$$

This is the Tavis-Cummings Hamiltonian [9]. If we impose that all qubits share the same frequency of operation ω_q and qubit-resonator coupling G_1 we can write:

$$H_{\text{RWA Dicke}} = \frac{\hbar\omega_q}{2}\hat{S}_z + \hbar\omega_r\hat{a}^\dagger\hat{a} + \hbar\left(G_1\hat{S}_+\hat{a} + G_1^*\hat{S}_-\hat{a}^\dagger\right), \tag{3.36}$$

[16] Obeying $\hat{\sigma}_z\,|e\rangle = +\,|e\rangle \;\Rightarrow\; |e\rangle = \begin{pmatrix}1\\0\end{pmatrix}$.

[17] When we write any single-spin operator (like $\hat{\sigma}_{z,\,i}$) alone, we are omitting the tensor product with the identities of the subspaces of the spins with labels different than i: $\hat{\sigma}_{z,\,i} \to \hat{\sigma}_{z,\,i} \otimes (... \otimes \mathbb{I}_{j\neq i} \otimes ...)$.

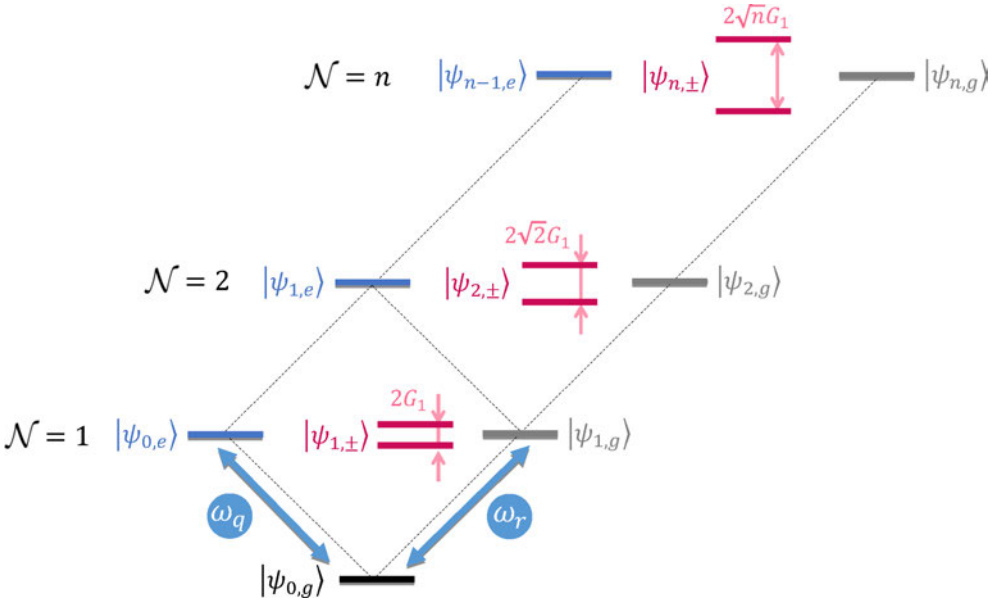

Figure 3.4: The Jaynes-Cummings 'ladder'. Ignoring the coupling, we can increase the energy of the system by either exciting the resonator with frequency ω_r (up and right in the ladder) or the qubit with frequency ω_q (up and left in the ladder). We place states with the same total number of excitations $\mathcal{N}$ at the same height in the ladder (in general, these states will have different energies if $\Delta = \omega_q - \omega_r \neq 0$). If the systems are coupled, we have a pair of polaritonic states for each $\mathcal{N}$.

with the collective spin operators $\hat{S}_z = \sum_{i=1}^{N} \hat{\sigma}_{z,i}$ and $\hat{S}_\pm = \sum_{i=1}^{N} \hat{\sigma}_{\pm,i}$. Hamiltonian (3.36) can be also seen as the result of using a rotating wave approximation in the Dicke model.

Because the collective operators fulfill the angular momentum algebra, we can apply the Holstein-Primakoff [10, Ch.6] approximation in the limit of large N and define the bosonic operators $\hat{b} := \frac{1}{\sqrt{N}}\hat{S}_-$ and $\hat{b}^\dagger := \frac{1}{\sqrt{N}}\hat{S}_+$. The resulting Hamiltonian is just that of two coupled resonators [8, Ch.2]:

$$H_{eff} = \hbar\omega_r \hat{a}^\dagger \hat{a} + \hbar\omega_q \hat{b}^\dagger \hat{b} + \hbar G_N \left(\hat{a}^\dagger \hat{b} + \hat{a}\hat{b}^\dagger\right), \tag{3.37}$$

with an enhanced coupling:

$$G_N \equiv |G_1|\sqrt{N}. \tag{3.38}$$

Note that if there are any inhomogeneities in the magnetic field felt by each spin, the decay rate Γ of the spin ensemble coherence will be the inverse of T_2^* (see section 3.1.3), which is larger than the rate γ of each individual spin. Then, for the strong coupling condition we have to compare an enhanced G_N with an also larger Γ.

The ground state of the system is $|\psi_{0,g}\rangle \equiv |0\rangle \otimes |g\rangle_1 \otimes ... \otimes |g\rangle_N$. Similarly we have the $|\psi_{n,g}\rangle$ states with n photons in the resonator. For each n we have also the excited state of the ensemble, which is a completely symmetric state in the excitation of any qubit (recall that $\hat{b}^\dagger = \frac{1}{\sqrt{N}} \sum_i \hat{\sigma}_{+,i}$):

$$|\psi_{n,e}\rangle \equiv \hat{b}^\dagger |\psi_{n,g}\rangle = |n\rangle \otimes \frac{1}{\sqrt{N}} \sum_{i=1}^{N} |e\rangle_i \otimes \left(... \otimes |g\rangle_{j\neq i} \otimes ... \right). \tag{3.39}$$

These are called Dicke states, or superradiant modes, which couple to cavity photons. As in the Jaynes-Cummings Hamiltonian (3.31), for each $n \geq 1$ we have two polaritonic states $|\psi_{n,\pm}\rangle$, superpositions of the $|\psi_{n,g}\rangle$ and $|\psi_{n-1,e}\rangle$.

Higher excitations of the spin ensemble, which are obtained with the creation operator $\hat{b}^\dagger \propto \hat{S}_+$, are completely symmetric states of more than one excited spin. The k-th excitation of the ensemble of N spins is then the completely symmetric state with $m_S = -S + k$, where $S = N/2$ is the total spin of the ensemble. The remaining degrees of freedom of the ensemble, which do not couple to the resonator, are the $2^N - (N+1)$ non-symmetric dark states, $\binom{N}{k} - 1$ for each k-th excited symmetric state. This description is valid as long as N is kept much larger than the number of photons, n [4, Ch.4].

The action of $\hat{b}^\dagger$ on the k-th excitation $|k\rangle \equiv |S, m_S = -S + k\rangle$ is similar to the action of the creation operator $a^\dagger$ of a quantum harmonic oscillator, provided that $k \ll N$ (see figure 3.5).

$$\begin{aligned}
\hat{b}^\dagger |k\rangle \equiv & \frac{1}{\sqrt{N}} \hat{S}_+ |S, m_S = -S + k\rangle \\
= & \frac{1}{\sqrt{N}} \sqrt{S(S+1) - (-S+k)(-S+k+1)}\, |S, m_S + 1 = -S + k + 1\rangle \\
\equiv & \sqrt{\frac{N-k}{N}} \sqrt{k+1}\, |k+1\rangle \quad \rightarrow \quad \sqrt{k+1}\, |k+1\rangle \quad \text{if} \quad k \ll N.
\end{aligned} \tag{3.40}$$

At low temperatures, we have $k \ll N$ when $n \ll N$ because the origin of the excitations are the photons in the resonator, and the harmonic description for the ensemble is valid. This is typically the case in the experiments that we perform with our spin ensembles.

This has a main consequence. If we rewrite Hamiltonian (3.37) in terms of normal modes $\hat{c}_+$ and $\hat{c}_-$:

$$H_{eff} = \hbar\omega_+ \hat{c}_+^\dagger \hat{c}_+ + \hbar\omega_- \hat{c}_-^\dagger \hat{c}_-, \tag{3.41}$$

with:

$$\begin{aligned} \omega_{\pm} &= \omega_r + \frac{\Delta}{2} \pm \frac{\Omega}{2}, \qquad \Omega \equiv \sqrt{\Delta^2 + 4G_N^2}, \\ \hat{c}_{\pm} &= \frac{1}{\sqrt{2}} \left(\sqrt{1 \mp \frac{\Delta}{\Omega}}\ \hat{a}\ \pm\ \sqrt{1 \pm \frac{\Delta}{\Omega}}\ \hat{b} \right). \end{aligned} \tag{3.42}$$

Thus, if the harmonic description is valid the system is characterized by two frequencies, $\omega_{\pm}$ (see figure 3.6).

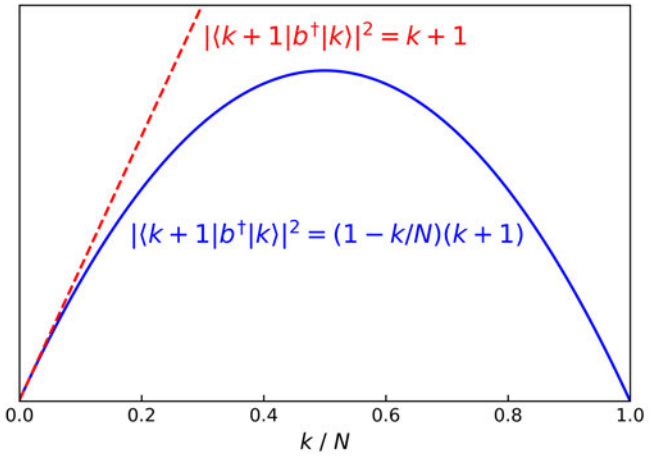

Figure 3.5: Squared matrix element of $\hat{b}^\dagger$ between the k-th and (k+1)-th excitations, as a function of k/N. The true parabolic dependence (blue solid line) is closely matched by that of the creation operator (red dashed line) only for small k/N (≤ 0.1).

Let us return again to the Tavis-Cummings Hamiltonian (3.35). It is worthy pointing out that, even with an inhomogeneous coupling, it is possible to arrive at the simple Hamiltonian (3.37) [11]. We consider again that we have at least a homogeneous qubit frequency ω_q, and define the collective operators b and $b^\dagger$ for inhomogeneous coupling as:

$$\hat{b} := \frac{1}{G_N} \sum_{i=1}^{N} G_{1,i}^{*}\, \hat{\sigma}_{-,i}, \qquad \hat{b}^\dagger := \frac{1}{G_N} \sum_{i=1}^{N} G_{1,i}\, \hat{\sigma}_{+,i}, \tag{3.43}$$

with $G_N \equiv G_{1,\mathrm{RMS}}\sqrt{N}$. $G_{1,\mathrm{RMS}}$ is the root mean square of the absolute values of the N different couplings:[18]

$$G_N \equiv G_{1,\mathrm{RMS}}\sqrt{N}, \qquad G_{1,\mathrm{RMS}} = \sqrt{\frac{1}{N} \sum_{i=1}^{N} |G_{1,i}|^2}\,. \tag{3.44}$$

[18] If the absolute values of all couplings are the same (and not necessarily their phases) in equation (3.44), we recover the definition from equation (3.38).

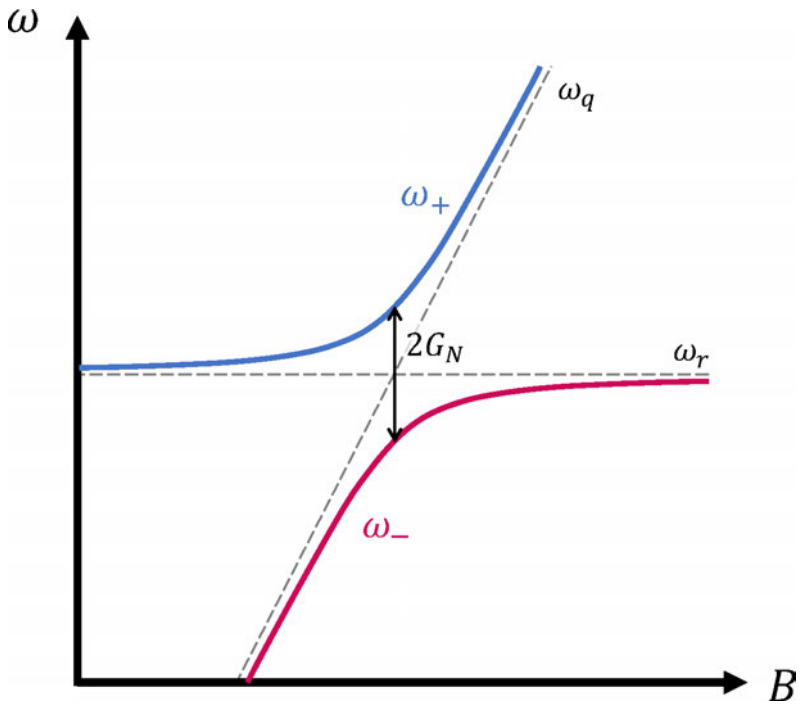

Figure 3.6: Frequency spectrum relevant to transmission experiments, plotted against applied magnetic field B. The two branches correspond to transitions with excitation energies $\hbar\omega_{\pm}$ (see equation (3.42)). When the qubit and the resonator are in resonance ($\omega_q = \omega_r$), we have $\omega_{\pm} = \omega_r \pm G_N$. The ensemble frequency ω_q is tuned by varying B.

If we work in the limit of few excited qubits, and restrict the excitations to generalized Dicke states, then b and $b^\dagger$ approximately fulfill the bosonic commutation relations and we arrive again (with these new definitions) at Hamiltonian (3.37). This time the superradiant modes are generalized Dicke states of the form:

$$|\psi_{n,e}\rangle \equiv |n\rangle \otimes \frac{1}{G}\sum_{i=1}^{N} G_{1,i}\,|e\rangle_i \otimes \left(... \otimes |g\rangle_{j\neq i} \otimes ...\right). \tag{3.45}$$

3.3.3 Generalization to a higher spin ensemble

Let us consider now a spin system with more than two states ($d > 2$), coming from either a magnetic ion with electronic spin $S > 1/2$ or to the coupling to a nuclear spin. We can still generalize the results from previous sections if we work in the eigenbasis $\{|\alpha\rangle\}$ of the spin Hamiltonian [12]. In this basis, the spin Hamiltonian takes the simple diagonal form of equation (3.15), and the Jaynes-Cummings Hamiltonian (3.31) is extended to an arbitrary spin system

as:

$$\begin{aligned} H_{\mathrm{JC}} = & \sum_{\alpha=0}^{d-1} E_\alpha \hat{X}^{\alpha\alpha} + \hbar\omega_r \hat{a}^\dagger \hat{a} \\ & + \hbar \sum_{\alpha=0}^{d-1} \sum_{\beta>\alpha} \left((G_1)_{\beta\alpha} \hat{X}^{\beta\alpha}\, \hat{a} + (G_1)_{\alpha\beta} \hat{X}^{\alpha\beta}\, \hat{a}^\dagger \right), \end{aligned} \tag{3.46}$$

where $\mathbf{G_1}$ is an Hermitian matrix encoding the coupling strengths of the different transitions, and $\hat{X}^{\alpha\beta} \equiv |\alpha\rangle\langle\beta|$ are Hubbard operators (also known as level-shift operators) [13, Ch.I.3]. These operators are a generalization of the projection operators. For instance, for $S = 1/2$ ($d = 2$) we have $\hat{X}^{1,0} = |1\rangle\langle 0| = |e\rangle\langle g| = \hat{\sigma}_+$ and $\hat{X}^{0,1} = |0\rangle\langle 1| = |g\rangle\langle e| = \hat{\sigma}_-$.[19]

Similarly, we can generalize the Tavis-Cummings Hamiltonian (3.35) for an ensemble of arbitrary spin systems as:

$$\begin{aligned} H_{\mathrm{TC}} = & \sum_{i=1}^{N} \sum_{\alpha=0}^{d-1} E_\alpha \hat{X}_i^{\alpha,\alpha} + \hbar\omega_r \hat{a}^\dagger \hat{a} \\ & + \hbar \sum_{i=1}^{N} \sum_{\alpha=0}^{d-1} \sum_{\beta>\alpha} \left((G_{1,i})_{\beta\alpha} \hat{X}_i^{\beta,\alpha} \hat{a} + (G_{1,i})_{\alpha\beta} \hat{X}_i^{\alpha,\beta} \hat{a}^\dagger \right), \end{aligned} \tag{3.47}$$

where we have assumed that all spins have the same energy spectrum $\{E_\alpha\}$, but kept the spin-index dependence in the couplings $(G_{1,i})_{\alpha\beta}$.

3.4 Dispersive regime

Now we consider the situation in which qubit and resonator have very different frequencies, hindering the exchange of excitations between them and therefore suppressing a decoherence mechanism of the qubit. This is known as the dispersive regime [14].

If we take the limit $\left|\frac{g_1}{\Delta}\right| \ll 1$ in the definition of the eigenstates of the

[19] Following the notation used in previous sections for the ground and excited states of a spin 1/2. Note that in that case we already had an Hermitian $\mathbf{G_1}$, with $(G_1)_{10} \to G_1$ and $(G_1)_{01} \to G_1^*$

Jaynes-Cummings Hamiltonian (3.33) we obtain:

$$
\begin{aligned}
|\psi_{n,+}\rangle &\simeq \begin{cases} \left|\frac{g_1\sqrt{n}}{\Delta}\right| |\psi_{n,g}\rangle + |\psi_{n-1,e}\rangle & \text{if } \Delta > 0 \\ |\psi_{n,g}\rangle + \left|\frac{g_1\sqrt{n}}{\Delta}\right| |\psi_{n-1,e}\rangle & \text{if } \Delta < 0 \end{cases} \\
|\psi_{n,-}\rangle &\simeq \begin{cases} |\psi_{n,g}\rangle - \left|\frac{g_1\sqrt{n}}{\Delta}\right| |\psi_{n-1,e}\rangle & \text{if } \Delta > 0 \\ \left|\frac{g_1\sqrt{n}}{\Delta}\right| |\psi_{n,g}\rangle - |\psi_{n-1,e}\rangle & \text{if } \Delta < 0\,. \end{cases}
\end{aligned}
\tag{3.48}
$$

In resonance ($\Delta = 0$), these states were the completely hybridized qubit-resonator states from equation (3.34), with a decay rate $\frac{\kappa+\gamma}{2}$. Now, the states of (3.48) have predominantly an excitation in either the qubit or the resonator.

Let us consider the case $\Delta > 0$. In the dispersive regime, the state $|\psi_{n,+}\rangle$ is mainly a qubit-only excitation, while the state $|\psi_{n,-}\rangle$ is in turn mainly a resonator-only excitation. Then $|\psi_{n,+}\rangle$ has a decay rate $\Gamma_{n,+} \simeq \gamma + \left(\frac{g_1\sqrt{n}}{\Delta}\right)^2 \kappa$, while $|\psi_{n,-}\rangle$ has a decay rate $\Gamma_{n,-} \simeq \kappa + \left(\frac{g_1\sqrt{n}}{\Delta}\right)^2 \gamma$, with the roles of γ and κ reversed.

$|\psi_{n,+}\rangle$ has an enhanced lifetime in the dispersive regime compared to the resonant case (Purcell effect) [15]. Besides, the qubit has a small influence on state $|\psi_{n,-}\rangle$. We will see in the following sections that it is still possible to read the state of the qubit by looking at the state of the resonator ($|\psi_{n,-}\rangle$). This is detailed in the following sections.

3.4.1 Qubit coupled to a resonator

If we use the rotating wave approximation, our starting point is the Jaynes-Cummings Hamiltonian (3.31). In the dispersive regime, the spin-resonator coupling is a perturbation $\hat{V}$ of the Hamiltonian sum of the two isolated systems, H_0:

$$
\begin{aligned}
H_{\mathrm{JC}} &\equiv H_0 + \hat{V}, \\
H_0 &= \frac{\hbar\omega_q}{2}\hat{\sigma}_z + \hbar\omega_r \hat{a}^\dagger \hat{a}, \\
\hat{V} &= \hbar\left(G_1\hat{\sigma}_+\hat{a} + G_1^*\hat{\sigma}_-\hat{a}^\dagger\right).
\end{aligned}
\tag{3.49}
$$

Now, we apply a Schrieffer-Wolff transformation $H' = e^{\hat{\theta}_{\mathrm{SW}}} H e^{-\hat{\theta}_{\mathrm{SW}}}$ to a basis where the Jaynes-Cummings Hamiltonian becomes diagonal to first order in

the perturbation $\hat{V}$. The anti-Hermitian[20] generator $\hat{\theta}_{\mathrm{SW}}$ of the transformation is chosen so as to fulfill the condition $\hat{V} + \left[\hat{\theta}_{\mathrm{SW}}, H_0\right] = 0$, and we obtain [16]:

$$H' = H_0 + \frac{1}{2}\left[\hat{\theta}_{\mathrm{SW}}, \hat{V}\right] + \frac{1}{3}\left[\hat{\theta}_{\mathrm{SW}}, \left[\hat{\theta}_{\mathrm{SW}}, \hat{V}\right]\right] + ... \tag{3.50}$$

For the Jaynes-Cummings Hamiltonian, this condition is fulfilled by (note the minus sign) [14]:

$$\hat{\theta}_{\mathrm{SW}} = \frac{1}{\Delta}\left(g_1\hat{\sigma}_+\hat{a} - G_1^*\hat{\sigma}_-\hat{a}^\dagger\right), \tag{3.51}$$

where $\Delta \equiv \omega_q - \omega_r$ is the frequency detuning between the qubit and the resonator. In the dispersive regime, this detuning is much larger than the qubit-resonator coupling ($|G_1| \ll |\Delta|$). Therefore, we can truncate the expansion of H' to the lowest order in $\hat{\theta}_{\mathrm{SW}}$ (lowest order in G_1/Δ):

$$H' \simeq H_0 + \frac{1}{2}\left[\hat{\theta}_{\mathrm{SW}}, \hat{V}\right], \tag{3.52}$$

and we obtain (plus an omitted constant term):[21]

$$H'_{\mathrm{JC}} \simeq \frac{\hbar}{2}\left(\omega_q + \chi\right)\hat{\sigma}_z + \hbar\left(\omega_r + \chi\hat{\sigma}_z\right)\hat{a}^\dagger\hat{a}, \tag{3.53}$$

with:

$$\chi := \frac{|G_1|^2}{\Delta}. \tag{3.54}$$

The term $(\omega_r + \chi\hat{\sigma}_z)\hat{a}^\dagger\hat{a}$ implies that the frequency of the resonator depends on the state of the qubits: the bare resonator frequency ω_r is shifted by either $+\chi$ or $-\chi$. Thus, the state of the qubits can be inferred from a measurement of the resonator. The frequency of operation of the qubit is also shifted by the coupling to the resonator: $\omega_q \mapsto \omega_q + \chi$. However, this shift does not depend on the state of the resonator.

Equation (3.53) is valid as long as we fulfill the condition for the rotating wave approximation ($|\Delta| \ll \omega_q + \omega_r$) that we assumed in the Jaynes-Cummings model (equation (3.31)). However, in a system with large qubit-resonator coupling we will need a large detuning to be in the dispersive regime.

We can do a similar derivation that is valid for the whole dispersive regime by including the counter-rotating terms from the Rabi Hamiltonian (3.30) in the perturbation $\hat{V}$ [17]:

$$\hat{V} = \hbar\left(G_1\hat{\sigma}_+ + G_1^*\hat{\sigma}_-\right)\left(a + a^\dagger\right), \tag{3.55}$$

[20] The generator $\hat{\theta}_{\mathrm{SW}}$ is anti-Hermitian to render $e^{\hat{\theta}_{\mathrm{SW}}}$ unitary.

[21] We used equation (3.52) combined with $[\hat{a}, \hat{a}^\dagger] = 1$, $[\hat{\sigma}_+, \hat{\sigma}_-] = \hat{\sigma}_z$, $2\hat{\sigma}_+\hat{\sigma}_- = \mathbb{I} + \hat{\sigma}_z$ and $2\hat{\sigma}_-\hat{\sigma}_+ = \mathbb{I} - \hat{\sigma}_z$.

Using the extended generator:

$$\hat{\theta}_{\mathrm{SW}} = \frac{1}{\Delta}\left(G_1\hat{\sigma}_+\hat{a} - G_1^*\hat{\sigma}_-\hat{a}^\dagger\right) + \frac{1}{\Delta + 2\omega_r}\left(G_1\hat{\sigma}_+\hat{a}^\dagger - G_1^*\hat{\sigma}_-\hat{a}\right), \tag{3.56}$$

we obtain:[22]

$$H'_{\mathrm{Rabi}} \simeq \frac{\hbar}{2}\left(\omega_q + \chi'\right)\hat{\sigma}_z + \hbar\left(\omega_r + \chi'\hat{\sigma}_z\right)\hat{a}^\dagger\hat{a} + \frac{\hbar}{2}\chi'\hat{\sigma}_z\left[a^2 + (a^\dagger)^2\right], \tag{3.57}$$

with:

$$\chi' := |G_1|^2\left(\frac{1}{\Delta} + \frac{1}{\Delta + 2\omega_r}\right) =: \frac{|G_1|^2}{\Delta'}. \tag{3.58}$$

Here we have defined a modified detuning $\Delta' = F(\Delta/\omega_r)\,\Delta$, with:

$$F(x) := \frac{1 + \frac{1}{2}x}{1 + x}\,. \tag{3.59}$$

If the cavity photons are weakly perturbed by the interaction with the spins, we can consider second-order photons processes to be negligible [12]. Then, we can drop the term with a^2 and $(a^\dagger)^2$ in Hamiltonian (3.57). This leaves the same terms we obtained with the rotating wave approximation, but with the modified detuning Δ' (and dispersive shift χ') that we just defined.

For a small detuning $\Delta \ll \omega_r$ ($x = \Delta/\omega_r \ll 1$) we have roughly the same shifts for the qubit and resonator frequencies as with the rotating wave approximation. However, when the detuning is very large ($x \gg 1$) we have $\Delta' \simeq \Delta/2$, and the approximation may overestimate $|G_1|$ by a factor $\sqrt{2}$. We can see this in figure 3.7.

3.4.2 Spin 1/2 ensembles

We want to extend the results from the previous section to ensembles of many spin 1/2 systems. If we use the rotating wave approximation, our starting point is the Tavis-Cummings Hamiltonian (3.35):

$$\begin{aligned} H_{\mathrm{TC}} &\equiv H_0 + \hat{V}, \\ H_0 &= \sum_{i=1}^{N} \frac{\hbar\omega_{q,\,i}}{2}\hat{\sigma}_{z,\,i} + \hbar\omega_r\hat{a}^\dagger\hat{a}\,, \\ \hat{V} &= \sum_{i=1}^{N} \hbar\left(G_{1,i}\hat{\sigma}_{+,\,i}\hat{a} + G_{1,i}^*\hat{\sigma}_{-,\,i}\hat{a}^\dagger\right). \end{aligned} \tag{3.60}$$

[22] Same as we did for equation (3.53). We also used that $\hat{\sigma}_+^2 = \hat{\sigma}_-^2 = 0$.

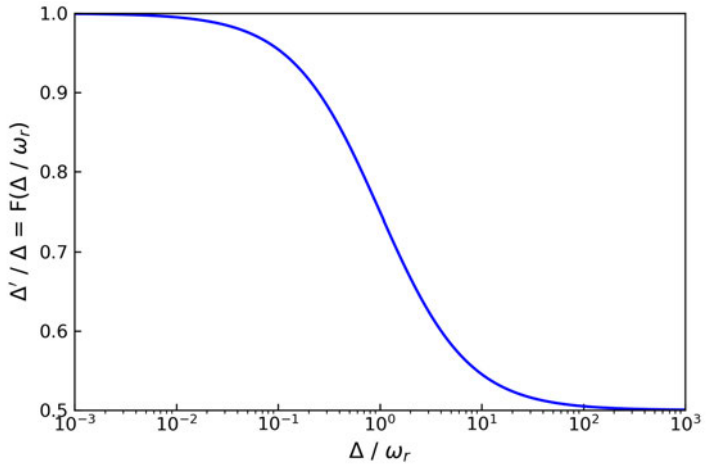

Figure 3.7: Modified detuning.

The generator of the Schrieffer-Wolff transformation for the Tavis-Cummings Hamiltonian is [17]:

$$\hat{\theta}_{\mathrm{SW}} = \sum_{i=1}^{N} \frac{1}{\Delta_i} \left(G_{1,i} \hat{\sigma}_{+,i} \hat{a} - G_{1,i}^{*} \hat{\sigma}_{-,i} \hat{a}^{\dagger} \right), \tag{3.61}$$

where $\Delta_i \equiv \omega_{q,i} - \omega_r$ is the frequency detuning between the qubit and the resonator. Using once more equation (3.52) we obtain the generalization to N qubits of the Hamiltonian (3.53):

$$\begin{aligned} H'_{\mathrm{TC}} \simeq & \frac{\hbar}{2} \sum_{i=1}^{N} \left(\omega_{q,i} + \chi_i \right) \hat{\sigma}_{z,i} + \hbar \left(\omega_r + \sum_{i=1}^{N} \chi_i \hat{\sigma}_{z,i} \right) \hat{a}^{\dagger} \hat{a} \\ & + \hbar \sum_{i=1}^{N} \sum_{j>i} \left(J_{ij} \hat{\sigma}_{+,i} \hat{\sigma}_{-,j} + J_{ij}^{*} \hat{\sigma}_{-,i} \hat{\sigma}_{+,j} \right), \end{aligned} \tag{3.62}$$

with the parameters:

$$J_{ij} := \frac{G_{1,i} G_{1,j}^{*}}{2} \left(\frac{1}{\Delta_i} + \frac{1}{\Delta_j} \right), \qquad \chi_i := J_{ii} \equiv \frac{|G_{1,i}|^2}{\Delta_i}. \tag{3.63}$$

If all qubits have roughly the same coupling $G_{1,i}$, the dispersive shift is enhanced by the number of qubits N. Also, a new term appears: a transverse exchange interaction between the qubits of strength $|J_{ij}|$ just by being coupled to the same resonator [14, 18].

As we did for single qubits, we can obtain a Hamiltonian that is valid for the whole dispersive regime including the counter-rotating terms in the

perturbation $\hat{V}$:

$$\hat{V} = \hbar \sum_{i=1}^{N} \left(g_i \hat{\sigma}_{+,i} + g_i^* \hat{\sigma}_{-,i}\right) \left(a + a^\dagger\right). \tag{3.64}$$

The generator is now:

$$\hat{\theta}_{\mathrm{SW}} = \sum_{i=1}^{N} \left[\frac{1}{\Delta_i} \left(g_i \hat{\sigma}_{+,i}\, \hat{a} - g_i^* \hat{\sigma}_{-,i}\, \hat{a}^\dagger\right) + \frac{1}{\Delta_i + 2\omega_r} \left(g_i \hat{\sigma}_{+,i}\, \hat{a}^\dagger - g_i^* \hat{\sigma}_{-,i}\, \hat{a}\right), \right] \tag{3.65}$$

and we obtain:

$$\begin{aligned} H' \simeq\ & \frac{\hbar}{2} \sum_{i=1}^{N} \left(\omega_{q,i} + \chi_i'\right) \hat{\sigma}_{z,i} + \hbar \Big(\omega_r + \sum_{i=1}^{N} \chi_i' \hat{\sigma}_{z,i}\Big) \hat{a}^\dagger \hat{a} \\ & + \frac{\hbar}{2} \sum_{i=1}^{N} \chi_i' \hat{\sigma}_{z,i} \left[a^2 + (a^\dagger)^2\right] \\ & + \hbar \sum_{i=1}^{N} \sum_{j>i} \left(2J_{ij} - J_{ij}'\right) \left(\frac{g_i}{|g_i|} \hat{\sigma}_{+,i} + \frac{g_i^*}{|g_i|} \hat{\sigma}_{-,i}\right) \left(\frac{g_j}{|g_j|} \hat{\sigma}_{+,j} + \frac{g_j^*}{|g_j|} \hat{\sigma}_{-,j}\right), \end{aligned} \tag{3.66}$$

with:

$$\begin{aligned} J_{ij} &:= \frac{|g_i||g_j|}{2} \left(\frac{1}{\Delta_i} + \frac{1}{\Delta_j}\right), \\ J_{ij}' &:= \frac{|g_i||g_j|}{2} \left(\frac{1}{\Delta_i} + \frac{1}{\Delta_j} + \frac{1}{\Delta_i + 2\omega_r} + \frac{1}{\Delta_j + 2\omega_r}\right) \\ &=: \frac{|g_i||g_j|}{2} \left(\frac{1}{\Delta_i'} + \frac{1}{\Delta_j'}\right), \\ \chi_i' &:= J_{ii}' = |g_i|^2 \left(\frac{1}{\Delta_i} + \frac{1}{\Delta_i + 2\omega_r}\right) =: \frac{|g_i|^2}{\Delta_i'}. \end{aligned} \tag{3.67}$$

Here we have a modified detuning $\Delta_i' := F(\Delta_i/\omega_r)\, \Delta_i$ for each qubit (recall the definition of $F(x)$ in equation 3.59)).

Equation (3.66) is similar to the single qubit Hamiltonian (3.57), but with an enhanced dispersive shift and a qubit-qubit interaction mediated by the resonator. As in the single qubit case, the use of the rotating wave approximation changes the dispersive shift. With many qubits and no RWA, we see that the qubit-qubit interaction strength is also modified. The type of interaction is also different [17].[23]

[23] An isotropic XY interaction in equation (3.62) if we use the rotating wave approximation. An 'Ising-like' interaction in equation (3.66) if we do not use it.

3.4.3 Generalization to higher spin systems

We will consider the case of a single spin system (with $d > 2$) to simplify the calculation (see equation (3.46)). In the previous section we have seen that the effect of having multiple particles is that the total dispersive shift increases linearly with the number of spins, N, and that these N spins are effectively coupled through the resonator.

We can have up to $d(d-1)$ different non-zero transition frequencies (positive and negative), and up to the same number of detunings from the resonator frequency ω_r. For the transition between states $|\alpha\rangle$ and $|\beta\rangle$:

$$\Delta_{\alpha\beta} = \frac{E_\alpha - E_\beta}{\hbar} - \omega_r. \tag{3.68}$$

In general, the condition for the rotating wave approximation will not hold simultaneously for all transitions. We rewrite the ensemble-resonator coupling of equation (3.46) to include the counter-rotating terms:

$$\hat{V} = \hbar \sum_{\alpha=0}^{d-1} \sum_{\beta\neq\alpha} \Lambda_{\alpha\beta} \hat{X}^{\alpha,\beta} \left(a + a^\dagger \right), \tag{3.69}$$

with $\Lambda_{\alpha\beta}$ Hermitian. The generator of the Schrieffer-Wolff transformation is now [12]:

$$\hat{\theta}_{\mathrm{SW}} = \sum_{\alpha=0}^{d-1} \sum_{\beta\neq\alpha} \Lambda_{\alpha\beta} \hat{X}^{\alpha,\beta} \left(\frac{1}{\Delta_{\alpha\beta}} \hat{a} + \frac{1}{\Delta_{\alpha\beta} + 2\omega_r} \hat{a}^\dagger \right), \tag{3.70}$$

and one obtains:

$$\begin{aligned} H' \simeq & \sum_{\alpha=0}^{d-1} E_\alpha \hat{X}^{\alpha,\alpha} + \hbar\omega_r \hat{a}^\dagger \hat{a} \\ & + \hbar \sum_{\alpha=0}^{d-1} \sum_{\beta_1\neq\alpha} \sum_{\beta_2\neq\alpha} \left(J_{\alpha\beta_1\beta_2} + J'_{\alpha\beta_1\beta_2} \hat{a}^\dagger \hat{a} \right) \hat{X}^{\beta_1,\beta_2} \\ & + \frac{\hbar}{2} \sum_{\alpha=0}^{d-1} \sum_{\beta_1\neq\alpha} \sum_{\beta_2\neq\alpha} \left(\frac{1}{\Delta_{\beta_1\alpha}} + \frac{1}{\Delta_{\beta_2\alpha} + 2\omega_r} \right) \left(\Lambda_{\beta_1\alpha} \Lambda_{\alpha\beta_2} \hat{a}^2 \hat{X}^{\beta_1,\beta_2} + \mathrm{h.c.} \right). \end{aligned} \tag{3.71}$$

We defined the parameters:

$$\begin{aligned} J_{\alpha\beta_1\beta_2} :=& \frac{\Lambda_{\beta_1\alpha}\Lambda_{\alpha\beta_2}}{2} \left(\frac{1}{\Delta_{\beta_1\alpha}} + \frac{1}{\Delta_{\beta_2\alpha}} \right), \\ J'_{\alpha\beta_1\beta_2} :=& \frac{\Lambda_{\beta_1\alpha}\Lambda_{\alpha\beta_2}}{2} \left(\frac{1}{\Delta_{\beta_1\alpha}} + \frac{1}{\Delta_{\beta_2\alpha}} + \frac{1}{\Delta_{\beta_1\alpha} + 2\omega_r} + \frac{1}{\Delta_{\beta_2\alpha} + 2\omega_r} \right) \\ =:& \frac{\Lambda_{\beta_1\alpha}\Lambda_{\alpha\beta_2}}{2} \left(\frac{1}{\Delta'_{\beta_1\alpha}} + \frac{1}{\Delta'_{\beta_2\alpha}} \right), \end{aligned} \tag{3.72}$$

with the modified detunings $\Delta'_{\beta\alpha} := F(\Delta_{\beta\alpha}/\omega_r)\,\Delta_{\beta\alpha}$.

If the ensemble is weakly perturbed by the interaction with the cavity we can keep only the dominant diagonal terms with $\hat{a}^\dagger\hat{a}$ over $\hat{a}^2$ or $(\hat{a}^\dagger)^2$, and with $\beta_1 = \beta_2$:

$$H' \simeq \sum_{\alpha=0}^{d-1} (E_\alpha + \chi_\alpha)\,\hat{X}^{\alpha,\alpha} + \hbar\left(\omega_r + \sum_{\alpha=0}^{d-1} \chi'_\alpha \hat{X}^{\alpha,\alpha}\right)\hat{a}^\dagger\hat{a}, \tag{3.73}$$

where we have defined the dispersive shifts χ_α and χ'_α in terms of $J_{\alpha\beta_1\beta_2}$ and $J'_{\alpha\beta_1\beta_2}$:

$$\begin{aligned} \chi_\alpha &:= \sum_{\beta\neq\alpha} \frac{|\Lambda_{\alpha\beta}|^2}{\Delta_{\alpha\beta}} = \sum_{\beta\neq\alpha} J_{\beta\alpha\alpha}, \\ \chi'_\alpha &:= \sum_{\beta\neq\alpha} \frac{|\Lambda_{\alpha\beta}|^2}{\Delta'_{\alpha\beta}} = \sum_{\beta\neq\alpha} J'_{\beta\alpha\alpha}. \end{aligned} \tag{3.74}$$

We can retrieve the results obtained for a qubit in section 3.4.1 by taking $d = 2$ (which implies that $\beta_1 = \beta_2$) and following our previous definitions: $\hat{X}^{1,0} = \hat{\sigma}_+$, $\Lambda_{1,0} = G_1$, $\omega_q = \frac{E_1 - E_0}{\hbar}$.

References

[1] A. Abragam and B. Bleaney, *Electron paramagnetic resonance of transition ions* (Oxford University Press, 1970).

[2] S. Stoll, *EasySpin documentation* (2023).

[3] A. Schweiger and G. Jeschke, *Principles of pulse electron paramagnetic resonance* (Oxford University Press, 2001).

[4] S. Haroche and J.-M. Raimond, *Exploring the quantum: atoms, cavities and photons* (Oxford University Press, 2006).

[5] J. García Ripoll, *Quantum information and quantum optics* (Cambridge University Press, 2022).

[6] I. Gimeno Alonso, Ph.D. thesis, Universidad de Zaragoza (2023).

[7] J. H. Wesenberg, A. Ardavan, G. A. D. Briggs, J. J. L. Morton, R. J. Schoelkopf, D. I. Schuster, and K. MÃ¸lmer4, Physical Review Letters **103**, 070502 (2009).

[8] S. M. Barnett and P. M. Radmore, *Methods in theoretical quantum optics* (Oxford Science Publications, 1997).

[9] M. Tavis and F. W. Cummings, Physical Review **170(2)**, 379 (1968).

[10] D. I. Khomskii, *Basic aspects of the theory of the quantum theory of solids: order and elementary excitations* (Cambridge University Press, 2010).

[11] T. Hümmer, G. M. Reuther, P. Hänggi, and D. Zueco, Physical Review A **85**, 052320 (2012).

[12] A. Gómez-León, F. Luis, and D. Zueco, Physical Review Applied **17**, 064030 (2022).

[13] D. Gamliel and H. Levanon, *Stochastic processes in magnetic resonance* (World Scientific, 1995).

[14] A. Blais, R.-S. Huang, A. Wallraff, S. M. Girvin, and R. J. Schoelkopf, Physical Review A **69**, 062320 (2004).

[15] E. M. Purcell, H. C. Torrey, and R. V. Pound, Physical Review **69**, 37 (1946).

[16] J. R. Schrieffer and P. A. Wolff, Physical Review **149(2)**, 491 (1966).

[17] D. Zueco, G. M. Reuther, S. Kohler, and P. Hänggi, Physical Review A **80**, 033846 (2009).

[18] J. Majer, J. M. Chow, J. M. Gambetta, J. Koch, B. R. Johnson, J. A. Schreier, L. Frunzio, D. I. Schuster, A. A. Houck, A. Wallraff, et al., Nature **449**, 443 (2007).

Chapter 4

Measurement of the quantum processor

The quantum processor we described in the previous section is not completely isolated: it interacts with its environment. In particular, we need to describe its interaction with the microwave photons that we send through the transmission line to measure the properties of the circuit. This is the focus of this chapter.

First, we give a brief description of the transmission line (section 4.1). Input-output theory (section 4.2) relates the signals that we send through the line to the evolution of some coupled quantum system. The effect of the transmission line in this evolution is modeled with a quantum master equation (section 4.3). In the remaining sections we apply this formalism to different quantum systems, from lumped-element resonators to spin ensembles.

4.1 Transmission line

Our transmission line consists of a central superconducting line with a ground plane at each side (see figure 4.1). We model this as two parallel conductors (central line and ground) with voltages and currents varying in magnitude and phase over their length. An infinitesimal piece of this conductor pair, with length Δz, can be treated as a lumped element with infinitesimal changes in voltage and current (see figure 4.2). We assign to each of these pieces a series resistance and inductance, and shunt conductance and capacitance per unit length.

In a superconducting line we consider the series resistance and shunt conductance to be small. We can describe it as a lossless line with only a series inductance l per unit length that represents the total self-inductance of the two

conductors and a shunt capacitance c per unit length between them if they are in close proximity (see figure 4.2). The impedance of this line is $Z_0 = \sqrt{l/c}$.

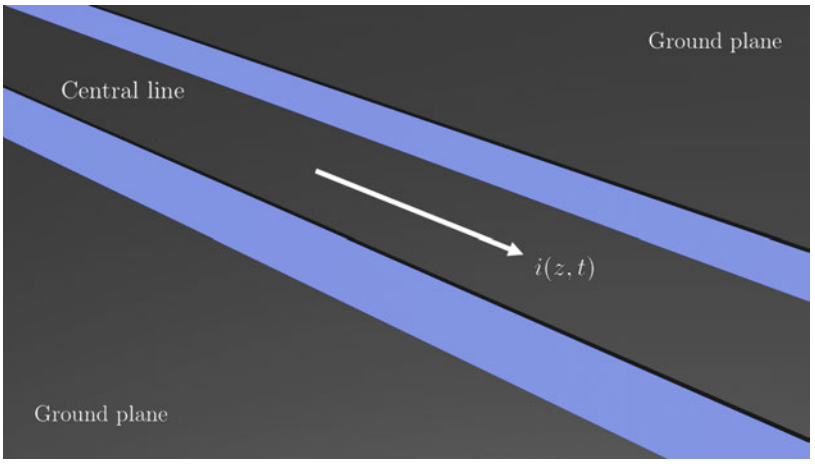

Figure 4.1: Drawing of a superconducting transmission line. The central line and the ground planes at the sides are made of a superconducting material deposited on top of an isolating substrate (blue).

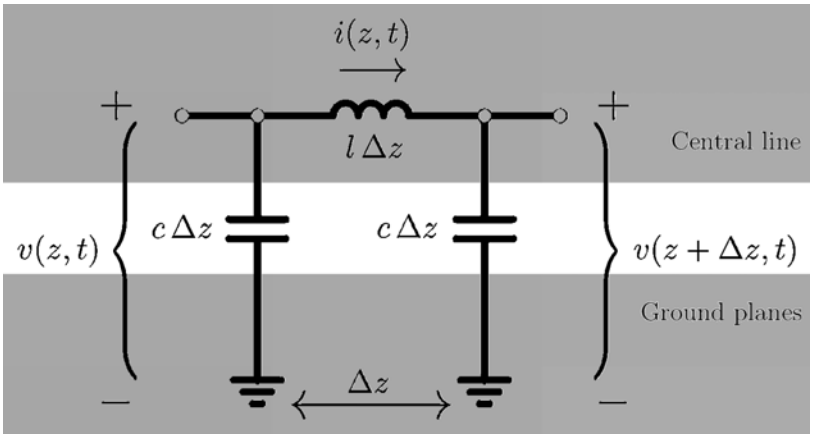

Figure 4.2: Lumped element circuit representing an infinitesimal segment of the transmission line of figure 4.1.

4.1.1 The classical transmission line

We can write Kirchhoff's voltage and current laws for each lumped element:

$$\begin{aligned} v(z,t) - l\,\Delta z\,\frac{\partial i(z,t)}{\partial t} - v(z+\Delta z,t) &= 0, \\ i(z,t) - c\,\Delta z\,\frac{\partial v(z+\Delta z,t)}{\partial t} - i(z+\Delta z,t) &= 0. \end{aligned} \tag{4.1}$$

Taking the limit $\Delta z \to 0$ we obtain a pair of differential equations — the telegrapher equations of a lossless line — for voltage and current in the line:

$$\begin{aligned} \frac{\partial v(z,t)}{\partial z} &= -l\,\frac{\partial i(z,t)}{\partial t}, \\ \frac{\partial i(z,t)}{\partial z} &= -c\,\frac{\partial v(z,t)}{\partial t}, \end{aligned} \tag{4.2}$$

which for solutions of the form $v(z,t) = V(z)e^{i\omega t}$ and $i(z,t) = I(z)e^{i\omega t}$ gives:

$$\begin{aligned} \frac{\partial^2 V(z)}{\partial z^2} &= -|k|^2\,V(z), \\ \frac{\partial^2 I(z)}{\partial z^2} &= -|k|^2\,I(z), \end{aligned} \tag{4.3}$$

where $|k| = \omega\sqrt{lc}$ is the wave vector modulus. This means that in our one-dimensional line we have for each frequency ω two solutions with $\pm|k|$ and phase velocity $v_p = \pm\omega/|k| = \pm 1/\sqrt{lc}$.

To obtain a Hamiltonian describing this system we write Kirchhoff's laws (equation 4.1) in terms of the integral variables, the flux $\phi(z,t)$ and the charge $q(z,t)$, which are related to $v(z,t) = \dot{\phi}(z,t)$ and $i(z,t) = \dot{q}(z,t)$. To do so, we integrate in time the voltage law, and combine the two equations into a single equation for $\phi(z,t)$:

$$\ddot{\phi}(z,t) = \left(\frac{v_p}{\Delta z}\right)^2 \Big\{ [\phi(z+\Delta z,t) - \phi(z,t)] + [\phi(z-\Delta z,t) - \phi(z,t)] \Big\}. \tag{4.4}$$

This is just the discrete version of a wave equation for $\phi(z,t)$ with phase velocity v_p:

$$\frac{\partial^2 \phi(z,t)}{\partial t^2} = v_p^2\,\frac{\partial^2 \phi(z,t)}{\partial z^2}\,. \tag{4.5}$$

Defining $\phi_n(t) = \phi(z,t)$ and $\phi_{n\pm1}(t) = \phi(z \pm \Delta z, t)$, we rewrite equation (4.4) as:

$$\ddot{\phi}_n(t) = \left(\frac{v_p}{\Delta z}\right)^2 \Big\{ [\phi_{n+1}(t) - \phi_n(t)] + [\phi_{n-1}(t) - \phi_n(t)] \Big\}, \tag{4.6}$$

which are the equations of motion that can be derived from the Lagrangian L_B or Hamiltonian H_B of an array of N coupled resonators with periodic boundary conditions ($\phi_{N+1} = \phi_1$):

$$\begin{aligned} L_B &= \frac{1}{2}\,c\,\Delta z \sum_{n=1}^{N} \dot{\phi}_n^2 - \frac{1}{2}\,\frac{1}{l\,\Delta z} \sum_{n=1}^{N} (\phi_{n+1} - \phi_n)^2\,, \\ H_B &= \frac{1}{2}\,\frac{1}{c\,\Delta z} \sum_{n=1}^{N} q_n^2 + \frac{1}{2}\,\frac{1}{l\,\Delta z} \sum_{n=1}^{N} (\phi_{n+1} - \phi_n)^2\,, \end{aligned} \tag{4.7}$$

where the charge $q_n := \partial\, L_B\,/\partial\dot{\phi}_n$ is the conjugate canonical variable of the flux ϕ_n.

We are interested in the limit $\Delta z \to 0$. We define the charge density $\rho(z)$ as:

$$\rho(z) := \lim_{\Delta z \to 0} \frac{q_n}{\Delta z}. \tag{4.8}$$

Then, taking the limit $\Delta z \to 0$ in equation 4.7 we obtain [1, Ch.11]:[1]

$$\begin{aligned} L_B &= \int dz\, \mathcal{L}_B(z) = \int dz \left[\frac{1}{2}\, c\, \dot{\phi}^2(z) - \frac{1}{2l}\left(\frac{\partial\phi(z)}{\partial z}\right)^2\right], \\ H_B &= \int dz\, \mathcal{H}_B(z) = \int dz \left[\frac{1}{2c}\rho^2(z) + \frac{1}{2l}\left(\frac{\partial\phi(z)}{\partial z}\right)^2\right], \end{aligned} \tag{4.9}$$

where $\mathcal{L}_B(z)$ and $\mathcal{H}_B(z)$ are the Lagrange and Hamilton densities. $\phi(z)$ and $\rho(z)$ are canonically conjugate fields related by $\rho(z) = \delta\, L_B\,/\delta\dot{\phi}(z)$.[2]

4.1.2 Quantization of the transmission line

The quantization of the LC resonator was described in section 3.2.2. We promote the pairs of conjugate canonical variables ϕ_n and q_n to pairs of non-commuting operators $\hat{\phi}_n$ and $\hat{q}_n$ with $[\hat{\phi}_m, \hat{q}_n] = i\hbar\delta_{mn}$. Similarly, in the limit $\Delta z \to 0$ we have $\hat{\phi}(z)$ and $\hat{\rho}(z)$ with $[\hat{\phi}(z), \hat{q}(z')] = i\hbar\delta(z - z')$,[3] and the Hamilton density reads:

$$\mathcal{H}_B(z) = \frac{1}{2c}\hat{\rho}^2(z) + \frac{1}{2l}\left(\frac{\partial\hat{\phi}(z)}{\partial z}\right)^2. \tag{4.10}$$

We want to write the Hamiltonian as a sum of independent oscillators. Let us define the Fourier transforms of the field operators $\hat{\phi}(z)$ and $\hat{\rho}(z)$:

$$\hat{\phi}_k := \frac{1}{\sqrt{L}}\int_0^l dz\, e^{ikz}\hat{\phi}(z), \qquad \hat{\rho}_k := \frac{1}{\sqrt{L}}\int_0^l dz\, e^{-ikz}\hat{q}(z), \tag{4.11}$$

[1] Rewrite L_B and H_B in equation 4.7 in terms of $\dot{\phi}_n$, $(\phi_{n+1} - \phi_n)/\Delta z$ and $q_n/\Delta z$. This leaves a factor Δz inside the sums in n. Then, taking the limit $\Delta z \to 0$ we have $\sum_n(\Delta z) \to \int dz$ with:

$$\dot{\phi}_n \to \dot{\phi}(z), \qquad \frac{\phi_{n+1} - \phi_n}{\Delta z} \to \frac{\partial\phi(z)}{\partial z}, \qquad \frac{q_n}{\Delta z} \to \rho(z).$$

[2] $\dfrac{\delta\, L_B}{\delta\dot{\phi}(z)}$ is a functional derivative, defined as $\lim_{\Delta z\to 0}\left(\dfrac{L_B[\dot{\phi}(z+\Delta z)] - L_B[\dot{\phi}(z)]}{\Delta z}\right)$.

[3] $[\hat{\phi}(z), \hat{\rho}(z')] = \lim_{\Delta z\to 0}\left[\hat{\phi}_m, \dfrac{\hat{q}_n}{\Delta z}\right] = \lim_{\Delta z\to 0}\left(i\hbar\dfrac{\delta_{mn}}{\Delta z}\right) = i\hbar\delta(z - z')$.

where $L = N\Delta z$ is the length of the line. Then we can write $\hat{\phi}(z)$ and $\hat{\rho}(z)$ as:

$$\hat{\phi}(z) = \frac{1}{\sqrt{L}} \sum_k e^{-ikz} \hat{\phi}_k, \qquad \hat{q}(z) = \frac{1}{\sqrt{L}} \sum_k e^{ikz} \hat{\rho}_k, \tag{4.12}$$

with $k = 2\pi m/L$, where m is an integer. Inserting the definitions of equation (4.12) in equation (4.10) we obtain a Hamiltonian that is a sum of independent oscillators with different k:

$$H_B = \sum_k \left(\frac{1}{2c} \hat{\rho}_k \hat{\rho}_{-k} + \frac{1}{2l} k^2 \hat{\phi}_k \hat{\phi}_{-k} \right). \tag{4.13}$$

As we did with the lumped-element resonator, we define the creation and annihilation operators $\hat{a}_k^\dagger$ and $\hat{a}_k$:

$$\hat{a}_k := \sqrt{\frac{k}{2\hbar Z_0}} \left(\hat{\phi}_k + i \frac{Z_0}{k} \hat{\rho}_k \right), \qquad \hat{a}_k^\dagger := \sqrt{\frac{k}{2\hbar Z_0}} \left(\hat{\phi}_k - i \frac{Z_0}{k} \hat{\rho}_k \right), \tag{4.14}$$

to obtain:

$$H_B = \sum_k \hbar\omega_k \, \hat{a}_k^\dagger \hat{a}_k + \text{constant}. \tag{4.15}$$

The sum in k includes positive and negative wave numbers. For each pair $+|k|$, $-|k|$ we have the same positive frequency ω_k. Then we can rewrite the sum in k as a sum in frequency:[4]

$$H_B = \sum_\omega \hbar\omega \, \left(\hat{r}_\omega^\dagger \hat{r}_\omega + \hat{l}_\omega^\dagger \hat{l}_\omega \right) + \text{constant}, \tag{4.16}$$

where we dropped the subscript k in ω_k. We have distinguished between right- ($\hat{a}_k \to \hat{r}_\omega$, $k > 0$) and left-moving ($\hat{a}_k \to \hat{l}_\omega$, $k < 0$) photons with different operators to highlight that they commute ($[\hat{r}_\omega, \hat{l}_\omega^\dagger] = [\hat{a}_k, \hat{a}_{-k}^\dagger] = 0$): the two types of photons have the same frequency but opposite momentum, therefore they are represented by different quantum states.

Finally, if we consider an infinite transmission line we will have all possible values for k (and ω) instead of those that fulfill the condition $k = 2\pi m/L$. We can then replace the sum of equation (4.16) by an integral over ω:[5]

$$H_B = \int \mathrm{d}\,\omega \, \hbar\omega \, \left(\hat{r}_\omega^\dagger \hat{r}_\omega + \hat{l}_\omega^\dagger \hat{l}_\omega \right) + \text{constant}. \tag{4.17}$$

[4]The constant in H_B (the zero-point energy) diverges because we have infinitely many modes. It does not matter in an experiment, as we only measure energy differences [2, Ch.4].

[5]With $\hat{r}_\omega$ and $\hat{l}_\omega$ redefined as $\lim_{\Delta\omega\to 0} \left(\frac{\hat{r}_\omega}{\Delta\omega} \right)$ and $\lim_{\Delta\omega\to 0} \left(\frac{\hat{l}_\omega}{\Delta\omega} \right)$.

4.2 Input-output theory

In our superconducting chip, the waveguide is coupled to the quantum system we want to probe (see figure 4.3). To do so, we send photons through the line. These photons are then scattered by the system. We are interested in the dynamics of the outgoing photons in the system-line setup. We can measure them recording the transmission and reflection of the waveguide.

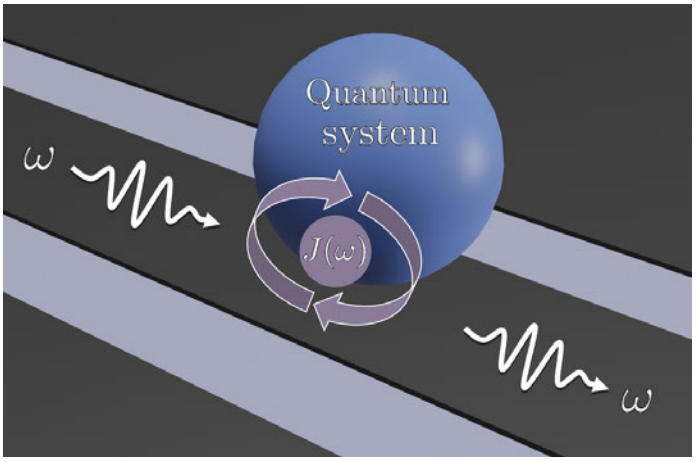

Figure 4.3: Drawing of a quantum system coupled to a transmission line with a spectral function $J(\omega)$.

The general Hamiltonian describing a quantum system and discrete collection of resonant modes in waveguide, with an interaction between the two subsystems, can be written as:

$$\begin{aligned} H &= H_S + H_B + H_1 \\ &= H_S + \sum_n \hbar\omega_n \left(\hat{r}^\dagger_{\omega_n}\hat{r}_{\omega_n} + \hat{l}^\dagger_{\omega_n}\hat{l}_{\omega_n}\right) + \hbar\hat{S}\sum_n G_1(\omega_n)\left(\hat{r}^\dagger_{\omega_n} + \hat{l}^\dagger_{\omega_n} + \hat{r}_{\omega_n} + \hat{l}_{\omega_n}\right), \end{aligned} \tag{4.18}$$

where the index n labels the modes (ω_n) of the waveguide. $\hat{S}$ is the system coupling operator, with a non-chiral (the same for both types of photons) coupling $G_1(\omega_n)$.[6] In the continuous limit, we can define the spectral function $J(\omega)$ as [3, Ch.17]:[7]

$$J(\omega) = \lim_{\Delta\omega\to 0}\left[\frac{1}{\Delta\omega}\sum_{\omega<\omega_n<\omega+\Delta\omega}|G_1(\omega_n)|^2\right] \tag{4.19}$$

[6] The subscript in $G_1(\omega_n)$ indicates that it is the coupling for a single system, similar to the single spin-resonator coupling that was derived in section 3.3 of chapter 3.

[7] In reference [3, Ch.17] the spectral function $J(\omega)$ is called the 'strength function' $g(\omega)$.

Using the definition of $J(\omega)$, the continuous limit of equation (4.18) reads:

$$\begin{aligned} H &= H_S + H_B + H_1 \\ &= H_S + \int \mathrm{d}\,\omega\ \hbar\omega \left(\hat{r}_\omega^\dagger \hat{r}_\omega + \hat{l}_\omega^\dagger \hat{l}_\omega\right) + \hbar\hat{S} \int \mathrm{d}\,\omega\ \sqrt{J(\omega)} \left(\hat{r}_\omega^\dagger + \hat{l}_\omega^\dagger + \hat{r}_\omega + \hat{l}_\omega\right), \end{aligned} \tag{4.20}$$

4.2.1 Input-output relations

Assuming decoupled initial conditions we compute the time evolution of the expectation values of $\hat{r}_\omega$ and $\hat{l}_\omega$:

$$\begin{aligned} \frac{\mathrm{d}}{\mathrm{d}\,t}\langle\hat{r}_\omega\rangle(t) &= -i\omega\langle\hat{r}_\omega\rangle(t) - i\sqrt{J(\omega)}\langle\hat{S}\rangle(t), \\ \frac{\mathrm{d}}{\mathrm{d}\,t}\langle\hat{l}_\omega\rangle(t) &= -i\omega\langle\hat{l}_\omega\rangle(t) - i\sqrt{J(\omega)}\langle\hat{S}\rangle(t). \end{aligned} \tag{4.21}$$

The solution to these equation is, rearranging terms:

$$\begin{aligned} \langle\hat{r}_\omega\rangle(t_f)e^{i\omega t_f} &= \langle\hat{r}_\omega\rangle(t_0)e^{i\omega t_0} - i\sqrt{J(\omega)}\int_{t_0}^{t_f} \mathrm{d}\,\tau\langle\hat{S}\rangle(\tau)e^{i\omega\tau}, \\ \langle\hat{l}_\omega\rangle(t_f)e^{i\omega t_f} &= \langle\hat{l}_\omega\rangle(t_0)e^{i\omega t_0} - i\sqrt{J(\omega)}\int_{t_0}^{t_f} \mathrm{d}\,\tau\langle\hat{S}\rangle(\tau)e^{i\omega\tau}, \end{aligned} \tag{4.22}$$

where t_0 marks the time in which the incident wave packet is injected in the line, and t_f is any time after the interaction between the wave packet and the scatterers has already occurred. We define the expectation values of the input and output fields as [4, Ch.3]:

$$\begin{aligned} \langle\hat{r}_{in}\rangle(t) &:= \int_0^\infty \frac{\mathrm{d}\,\omega}{\sqrt{2\pi}}\langle\hat{r}_\omega\rangle(t_0)e^{-i\omega(t-t_0)}, \\ \langle\hat{l}_{in}\rangle(t) &:= \int_0^\infty \frac{\mathrm{d}\,\omega}{\sqrt{2\pi}}\langle\hat{l}_\omega\rangle(t_0)e^{-i\omega(t-t_0)}, \\ \langle\hat{r}_{out}\rangle(t) &:= \int_0^\infty \frac{\mathrm{d}\,\omega}{\sqrt{2\pi}}\langle\hat{r}_\omega\rangle(t_f)e^{-i\omega(t-t_f)}, \\ \langle\hat{l}_{out}\rangle(t) &:= \int_0^\infty \frac{\mathrm{d}\,\omega}{\sqrt{2\pi}}\langle\hat{l}_\omega\rangle(t_f)e^{-i\omega(t-t_f)}. \end{aligned} \tag{4.23}$$

Then, taking $t_0 \to -\infty$ and $t_f \to \infty$, equation (4.22) reads:

$$\begin{aligned} \langle\hat{r}_{out}\rangle(t) &= \langle\hat{r}_{in}\rangle(t) - i\int_0^\infty \frac{\mathrm{d}\,\omega}{\sqrt{2\pi}}e^{-i\omega t}\sqrt{J(\omega)}\int_{-\infty}^\infty \mathrm{d}\,\tau e^{i\omega\tau}\langle\hat{S}\rangle(\tau), \\ \langle\hat{l}_{out}\rangle(t) &= \langle\hat{l}_{in}\rangle(t) - i\int_0^\infty \frac{\mathrm{d}\,\omega}{\sqrt{2\pi}}e^{-i\omega t}\sqrt{J(\omega)}\int_{-\infty}^\infty \mathrm{d}\,\tau e^{i\omega\tau}\langle\hat{S}\rangle(\tau). \end{aligned} \tag{4.24}$$

Equation (4.24) is a central result. They link the input and output fields through the dynamics of the operator $\hat{S}$ that describes a system that is side coupled to the transmission line. If the system interrupts the line, then we have to exchange the roles of $\langle \hat{r}_{out} \rangle$ and $\langle \hat{l}_{out} \rangle$ (see figure 4.4).

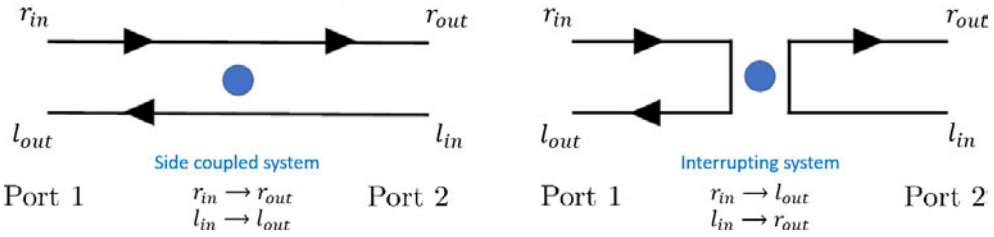

Figure 4.4: Input-output for side coupled and interrupting systems. Note that in the case of interrupting systems the roles of $\langle \hat{r}_{out} \rangle$ and $\langle \hat{l}_{out} \rangle$ are exchanged in equation 4.24. Lumped-element resonators read out via a transmission line are an example of a side coupled system.

We set port 1 in figure 4.4 as our input port. Then, we can define the scattering parameters S_{21} (transmission) and S_{11} (reflection) from equation (2.1) in chapter 2 in terms of the input and output fields as:

$$S_{21}(t) := \frac{\langle \hat{r}_{out} \rangle(t)}{\langle \hat{r}_{in} \rangle(t)}, \qquad S_{11}(t) := \frac{\langle \hat{l}_{out} \rangle(t)}{\langle \hat{r}_{in} \rangle(t)}, \tag{4.25}$$

with $\langle \hat{l}_{in} \rangle(t) = 0$ (no input in port 2). Then, from equation (4.24) it follows that $S_{21} = 1 + S_{11}$.

4.2.2 Coherent drive

A simple form of the input-output relations in equation (4.24) is obtained if the input field is a coherent drive of frequency ω_d:

$$\langle \hat{r}_{in} \rangle(t) = \alpha_{in} e^{-i\omega_d t}. \tag{4.26}$$

The coupling of $\hat{S}$ to this field is:[8]

$$H_1 = \hbar \hat{S} \left(\sqrt{2\pi J(\omega_d)} \alpha_{in} e^{-i\omega_d t} \right) \tag{4.27}$$

Once the transient state of $\hat{S}$ decays, we will have a driven state of the form:

$$\langle \hat{S} \rangle(t) \simeq \chi_{\hat{S}}(\omega_d) \sqrt{2\pi J(\omega_d)} \alpha_{in} e^{-i\omega_d t} \tag{4.28}$$

[8] Comparing with the coupling term in Hamiltonian (4.20), note the $\sqrt{2\pi}$ factor here from the definition of the input fields in equation (4.23).

where the susceptibility $\chi_{\hat{S}}(\omega_d)$ encodes the frequency dependence of the system response to the coherent driving. If we insert this expression for $\langle \hat{S} \rangle(t)$ in the input-output relations we obtain:

$$\begin{aligned} \langle \hat{r}_{out} \rangle(t) &= \langle \hat{r}_{in} \rangle(t) - 2\pi J(\omega_d) \chi_{\hat{S}}(\omega_d) \langle \hat{r}_{in} \rangle(t), \\ \langle \hat{l}_{out} \rangle(t) &= \langle \hat{l}_{in} \rangle(t) - 2\pi J(\omega_d) \chi_{\hat{S}}(\omega_d) \langle \hat{r}_{in} \rangle(t), \end{aligned} \tag{4.29}$$

We consider $J(\omega_d)$ to be a smooth function. Then, driving close to a resonant frequency Ω_S of the system we may write $J(\omega_d) \simeq J(\Omega_S)$.

In a typical experiment we input a coherent drive into the system, so we will obtain the input-output relations from equation (4.29). Then, all that we need is to compute the susceptibility $\chi_{\hat{S}}(\omega_d)$ for the each particular system that we measure. If we ignore the dissipation of the quantum system into the line (or other pathways of dissipation), the function $\chi_{\hat{S}}(\omega_d)$ diverges when ω_d is in resonance with a frequency Ω_S of the system. We know that this is not what happens in experiments: every resonance has a finite height and width due to dissipation. In the next section we describe how we model dissipation in a quantum system.

4.3 Dissipation of the quantum system through the transmission line

Hamiltonian (4.20) allows calculating the time evolution of the density matrix ρ that describes the coupled waveguide and quantum system:

$$\dot{\rho} = -\frac{i}{\hbar} [H, \rho] = -\frac{i}{\hbar} [H_S, \rho] - \frac{i}{\hbar} [H_B, \rho] - \frac{i}{\hbar} [H_1, \rho] . \tag{4.30}$$

In order to describe the evolution of the quantum system we need to derive a self-contained equation for the density matrix of our quantum system alone (ρ_S) — the quantum master equation — which will inevitably be approximate. The effect of the coupling to the transmission line will enter in this equation as a decay of the elements of ρ_S to those in thermal equilibrium at the temperature T of the transmission line.

4.3.1 Time-dependent perturbation theory in the interaction picture

We define the unperturbed Hamiltonian H_0:

$$H_0 := H_S + H_B . \tag{4.31}$$

The evolution of the density matrix is then given by:

$$\dot{\rho} = -\frac{i}{\hbar}\left[H_0, \rho\right] - \frac{i}{\hbar}\left[H_1, \rho\right]. \tag{4.32}$$

Now we change to the interaction picture, with a new density matrix defined by $\rho^{(I)}(t) \equiv e^{i\,H_0\,t/\hbar}\rho(t)e^{-i\,H_0\,t/\hbar}$ [5, Ch.5]. With this density matrix we remove the first term from equation (4.32):[9]

$$\dot{\rho}^{(I)} = \frac{i}{\hbar}\left[H_0, \rho^{(I)}\right] + e^{i\,H_0\,t/\hbar}\dot{\rho}\,e^{-i\,H_0\,t/\hbar} = -\frac{i}{\hbar}\left[H_1(t), \rho^{(I)}\right], \tag{4.33}$$

but now H_1 evolves (according to the interaction picture) with H_0:

$$H_1(t) = e^{i\,H_0\,t/\hbar}\,H_1\,e^{-i\,H_0\,t/\hbar}. \tag{4.34}$$

The formal solution to equation (4.33) is found by integration:

$$\rho^{(I)}(t) = \rho^{(I)}(t_0) - \frac{i}{\hbar}\int_{t_0}^{t} \mathrm{d}\,t'\left[H_1(t'), \rho^{(I)}(t')\right]. \tag{4.35}$$

We can obtain an approximate solution for equation (4.35) as an infinite series of powers of H_1 by iteration.[10] In our case, we consider that the interaction term is small and we truncate the series to second order in H_1:

$$\begin{aligned}
\rho^{(I)}(t) &= \rho^{(I)}(t_0) - \frac{i}{\hbar}\int_{t_0}^{t} \mathrm{d}\,t'\left[H_1(t'), \rho^{(I)}(t_0) - \frac{i}{\hbar}\int_{t_0}^{t'} \mathrm{d}\,t''\left[H_1(t''), \rho^{(I)}(t'')\right]\right] \\
&\simeq \rho^{(I)}(t_0) - \frac{i}{\hbar}\int_{t_0}^{t} \mathrm{d}\,t'\left[H_1(t'), \rho^{(I)}(t_0)\right] \\
&\quad - \frac{1}{\hbar^2}\int_{t_0}^{t} \mathrm{d}\,t'\int_{t_0}^{t'} \mathrm{d}\,t''\left[H_1(t'), \left[H_1(t''), \rho^{(I)}(t_0)\right]\right],
\end{aligned} \tag{4.36}$$

[9] We used the product rule of differentiation combined with the fact that H_0 commutes with $e^{\pm i\,H_0\,t/\hbar}$ (which are only functions of H_0 and time) but not with ρ or $\dot{\rho}$:

$$\begin{aligned}
\dot{\rho}^{(I)} &= \frac{\mathrm{d}}{\mathrm{d}\,t}\left(e^{i\,H_0\,t/\hbar}\rho(t)e^{-i\,H_0\,t/\hbar}\right) = (i\,H_0)\rho^{(I)} + e^{i\,H_0\,t/\hbar}\dot{\rho}\,e^{-i\,H_0\,t/\hbar} + \rho^{(I)}(-i\,H_0) \\
&= \frac{i}{\hbar}\left[H_0, \rho^{(I)}\right] + e^{i\,H_0\,t/\hbar}\dot{\rho}\,e^{-i\,H_0\,t/\hbar}.
\end{aligned}$$

Then, we inserted equation (4.32) in the second term. Using again that H_0 commutes with $e^{\pm i\,H_0\,t/\hbar}$ but not with $\dot{\rho}$ or H_1, we have:

$$\begin{aligned}
e^{i\,H_0\,t/\hbar}\dot{\rho}\,e^{-i\,H_0\,t/\hbar} &= -\frac{i}{\hbar}e^{i\,H_0\,t/\hbar}\left[H_0, \rho\right]e^{-i\,H_0\,t/\hbar} - \frac{i}{\hbar}e^{i\,H_0\,t/\hbar}\left[H_1, \rho\right]e^{-i\,H_0\,t/\hbar} \\
&= -\frac{i}{\hbar}\left[H_0, \rho^{(I)}\right] - \frac{i}{\hbar}\left[e^{i\,H_0\,t/\hbar}\,H_1\,e^{-i\,H_0\,t/\hbar}, \rho^{(I)}\right]
\end{aligned}$$

[10] We build a 'Dyson-like' series for $\rho^{(I)}(t)$ in the same way that we can build the Dyson series for the time-evolution operator in the interaction picture.

where we approximated $\rho^{(I)}(t'')$ by $\rho^{(I)}(t_0)$ in the last term to keep an equation of second order in H_1. The time derivative of equation (4.36) is:

$$\dot{\rho}^{(I)}(t) = -\frac{i}{\hbar}\left[H_1(t), \rho^{(I)}(t_0)\right] - \frac{1}{\hbar^2}\int_{t_0}^{t} \mathrm{d}\, t' \left[H_1(t), \left[H_1(t'), \rho^{(I)}(t_0)\right]\right], \quad (4.37)$$

where all the time-dependence is inside the evolution of H_1.

4.3.2 Tracing the line

The trace of $\dot{\rho}^{(I)}$ is the sum of all diagonal elements of $\dot{\rho}^{(I)}$ in any basis:

$$\mathrm{Tr}\, \dot{\rho}^{(I)} = \sum_n \sum_m \dot{\rho}^{(I)}_{nm}\delta_{nm} = \sum_n \dot{\rho}^{(I)}_{nn}, \quad (4.38)$$

where n (or m) is an index that labels the basis states. In order to obtain an equation for the density matrix of the system alone, we want to trace out only the degrees of freedom of the line. Let us label the basis states with the pair of indices n_S, n_B (or m_S, m_B), one for the system and the other for the line. Then, we write the trace over the line as:

$$\begin{aligned}(\dot{\rho}^{(I)}_S)_{n_S m_S} &= (\underset{B}{\mathrm{Tr}}\ \dot{\rho}^{(I)})_{n_S m_S} \\ &= \sum_{n_B}\sum_{m_B} \dot{\rho}^{(I)}_{n_S n_B m_S m_B}\delta_{n_B m_B} \\ &= \sum_{n_B} \dot{\rho}^{(I)}_{n_S n_B m_S n_B}.\end{aligned} \quad (4.39)$$

We need to write equation (4.37) in such a way that we can easily trace over the line states. We begin by considering that H_1 is of the form $H_1 := \hat{S}\otimes\hat{B}$, where $\hat{S}$ is an operator of the system and $\hat{B}$ is an operator of the line. This is true for Hamiltonian (4.20), with:

$$\hat{B} = \hbar\int \mathrm{d}\,\omega\ \sqrt{J(\omega)}\left(\hat{r}^\dagger_\omega + \hat{l}^\dagger_\omega + \hat{r}_\omega + \hat{l}_\omega\right). \quad (4.40)$$

Besides, the line is in its thermal equilibrium state, with:

$$\rho^e_B = Z^{-1} e^{-\beta\int \mathrm{d}\,\omega\ \hbar\omega\left(\hat{r}^\dagger_\omega\hat{r}_\omega + \hat{l}^\dagger_\omega\hat{l}_\omega\right)}, \quad (4.41)$$

where $\beta = 1/k_\mathrm{B}T$, and Z is a normalization factor (the partition function).

Let us assume decoupled initial conditions, that is, that at the initial time t_0 the system-line density matrix is the product $\rho_S(t_0)\otimes\rho_B(t_0)$ of the density matrix of the system times the density matrix of the line. This allows us to

have products of line operators with ρ_B^e that we can trace out. We can write the time evolution of the interaction term as $H_1(t) = \hat{S}(t) \otimes \hat{B}(t)$, with:

$$\begin{aligned} \hat{S}(t) &= e^{i\,H_S\,t/\hbar}\hat{S}e^{-i\,H_S\,t/\hbar}, \\ \hat{B}(t) &= e^{i\,H_B\,t/\hbar}\hat{B}e^{-i\,H_B\,t/\hbar}, \end{aligned} \tag{4.42}$$

where $\hat{S}$ evolves with H_S and $\hat{B}$ with H_B because each term of the unperturbed Hamiltonian acts on a different Hilbert space.

Defining $\langle\theta\rangle_e := \underset{B}{\mathrm{Tr}}\ \theta\rho_B^e$, where θ is any combination of line operators, we obtain an equation in terms of the density matrix of the system by tracing the degrees of freedom of the line from $\dot{\rho}^{(I)}(t)$:

$$\begin{aligned} \dot{\rho}_S^{(I)}(t) = \underset{B}{\mathrm{Tr}}\ \dot{\rho}^{(I)}(t) = &-\frac{i}{\hbar}\left[\hat{S}(t), \rho_S^{(I)}(t_0)\right]\langle\hat{B}(t)\rangle_e \\ &-\frac{1}{\hbar^2}\int_{t_0}^{t}\mathrm{d}\,t'\left[\hat{S}(t), \hat{S}(t')\rho_S^{(I)}(t_0)\right]\langle\hat{B}(t)\hat{B}(t')\rangle_e \\ &+\frac{1}{\hbar^2}\int_{t_0}^{t}\mathrm{d}\,t'\left[\hat{S}(t), \rho_S^{(I)}(t_0)\hat{S}(t')\right]\langle\hat{B}(t')\hat{B}(t)\rangle_e. \end{aligned} \tag{4.43}$$

For the line operator we considered in equation (4.40), $\langle\hat{B}(t)\rangle_e = 0$.[11] The remaining terms have the two-time correlators $\langle\hat{B}(t)\hat{B}(t')\rangle_e$:[12]

$$\begin{aligned} \langle\hat{B}(t)\hat{B}(t')\rangle_e = 2\hbar^2\int\mathrm{d}\,\omega J(\omega)\Big[&\bar{n}(\omega,T)e^{i\omega(t-t')} \\ &+ (\bar{n}(\omega,T)+1)e^{-i\omega(t-t')}\Big], \end{aligned} \tag{4.44}$$

Here $n(\omega, T)$ is the bosonic occupation number for thermal photons of frequency ω in the transmission line at temperature T:

$$\bar{n}(\omega,T) \equiv \langle\hat{l}_\omega^\dagger\hat{l}_\omega\rangle_e = \langle\hat{r}_\omega^\dagger\hat{r}_\omega\rangle_e = \frac{1}{e^{\beta\hbar\omega}-1}. \tag{4.45}$$

4.3.3 Secular and rotating wave approximations

For the evolution of $\hat{S}$, we can write its spectral decomposition in the frequencies Ω_S [4, Ch.3]. Then, each component $\hat{S}(\Omega_S)$ evolves with frequency Ω_S:

$$\hat{S} = \sum_{\Omega_S}\hat{S}(\Omega_S) \quad\rightarrow\quad \hat{S}(t) = \sum_{\Omega_S}\hat{S}(\Omega_S)e^{i\Omega_S t}, \tag{4.46}$$

[11] The density matrix of the line in equilibrium, ρ_B^e, is diagonal in the basis of eigenstates of H_B, while the coupling line operator $\hat{B}$ from equation (4.40) does not have any terms in the diagonal in this same basis. It follows that the trace of the product of $\hat{B}$ times ρ_B^e is zero.

[12] Actually they depend only on the time difference.

and we can write the commutators as:

$$\begin{aligned}\left[\hat{S}(t),\hat{S}(t')\rho_S^{(I)}(t_0)\right] &= \sum_{\Omega_S}\sum_{\Omega'_S}\left[\hat{S}(\Omega_S),\hat{S}(\Omega'_S)\rho_S^{(I)}(t_0)\right]e^{i\Omega_S(t-t')}e^{i(\Omega_S+\Omega'_S)t'},\\ \left[\hat{S}(t),\rho_S^{(I)}(t_0)\hat{S}(t')\right] &= \sum_{\Omega_S}\sum_{\Omega'_S}\left[\hat{S}(\Omega_S),\rho_S^{(I)}(t_0)\hat{S}(\Omega'_S)\right]e^{i\Omega_S(t-t')}e^{i(\Omega_S+\Omega'_S)t'}.\end{aligned} \tag{4.47}$$

They contain fast oscillating terms except when $\Omega'_S \simeq -\Omega_S$. In the secular approximation we only keep terms with $\Omega'_S = -\Omega_S$. If the spectral decomposition of $\hat{S}$ is non-degenerate, that is, if all frequencies Ω_S are different:

$$\begin{aligned}\left[\hat{S}(t),\hat{S}(t')\rho_S^{(I)}(t_0)\right] &\simeq \sum_{\Omega_S}\left[\hat{S}(\Omega_S),\hat{S}(-\Omega_S)\rho_S^{(I)}(t_0)\right]e^{i\Omega_S(t-t')},\\ \left[\hat{S}(t),\rho_S^{(I)}(t_0)\hat{S}(t')\right] &\simeq \sum_{\Omega_S}\left[\hat{S}(\Omega_S),\rho_S^{(I)}(t_0)\hat{S}(-\Omega_S)\right]e^{i\Omega_S(t-t')}.\end{aligned} \tag{4.48}$$

Inserting the expression for the two-time correlators (equation (4.44)) and the commutators back in equation (4.43) for $\dot{\rho}_S^{(I)}(t)$ we obtain fast oscillating terms except for $\Omega_S \simeq \omega$ where we have $e^{i(\Omega_S-\omega)(t-t')}$, and $\Omega_S \simeq -\omega$ where we have $e^{i(\Omega_S+\omega)(t-t')}$. In the rotating wave approximation we neglect these fast oscillating terms and keep only terms with $e^{\pm i(\Omega_S-\omega)(t-t')}$, where $\Omega_S, \omega > 0$.

4.3.4 Markovian regime

We define the memory function of the line as the Fourier transform of the spectral function $J(\omega)$. If $J(\omega)$ is a smooth function over a broad range of frequencies around each Ω_S, this memory function decays with a very short characteristic time τ_c [6, App.B].[13]

In the Markovian regime, we assume that the timescale of the decay of the memory function of the line is smaller than any timescale of the system (given by the different $1/\Omega_S$). That is, we consider that the line immediately loses all memory of its interaction with the system. Then, the integrand of the time integral vanishes quickly for $\tau = t' - t_0 \gg \tau_c$ and we can extend the upper

[13] We can think that the spectral function is a very wide resonance. Then its Fourier transform — the memory function — is an exponential decay with a very short characteristic time that is inversely proportional to the width of the spectral function.

limit of the integral to infinity to obtain:[14]

$$\begin{aligned}\int_{t_0}^{\infty} \mathrm{d}\, t'\, e^{\pm i(\Omega_S-\omega)t'} &= e^{\pm i(\Omega_S-\omega)t_0} \int_0^{\infty} \mathrm{d}\,\tau\, e^{\pm i(\omega-\Omega_S)\tau} \\ &= e^{\pm i(\Omega_S-\omega)t_0}\Big[\pi\delta(\Omega_S-\omega) \pm i\mathcal{PV}\Big(\frac{1}{\Omega_S-\omega}\Big)\Big],\end{aligned} \tag{4.49}$$

with $\mathcal{PV}$ the principal value [7, App.7]. The principal value generates a shift — the Lamb shift — that diverges with our approximations. In practice this shift is small, and can be embedded back into the frequencies Ω_S. This leaves only the term with $\delta(\Omega_S-\omega)$, from which we obtain the master equation for $\rho_S^{(I)}$:

$$\dot{\rho}_S^{(I)}(t) = \sum_{\Omega_S>0} \Gamma(\Omega_S)\Big[\bar{n}(\Omega_S,T)\mathcal{D}(\Omega_S) + (\bar{n}(\Omega_S,T)+1)\mathcal{D}(-\Omega_S)\Big], \tag{4.50}$$

with $\Gamma(\Omega_S) = 2\pi J(\Omega_S)$ and:

$$\mathcal{D}(\Omega_S) := 2\hat{S}(\Omega_S)\rho_S^{(I)}(t_0)\hat{S}(-\Omega_S) - \Big\{\hat{S}(-\Omega_S)\hat{S}(\Omega_S), \rho_S^{(I)}(t_0)\Big\}, \tag{4.51}$$

where $\{\hat{A},\hat{B}\} = \hat{A}\hat{B} + \hat{B}\hat{A}$ is the standard anti-commutator of $\hat{A}$ and $\hat{B}$.

4.3.5 Back to the Schrödinger picture

We have just obtained a master equation for the density matrix of the system in the interaction picture. Instead, we want a master equation in the Schrödinger picture so that all the time dependence is in the density matrix ρ_S and not in the system operators. Using that $\rho_S = e^{-i\,H_S\,t/\hbar}\rho_S^{(I)}(t)e^{i\,H_S\,t/\hbar}$, we obtain:

$$\begin{aligned}\dot{\rho}_S(t) &= -\frac{i}{\hbar}[H_S,\rho_S(t)] + e^{-i\,H_S\,t/\hbar}\dot{\rho}_S^{(I)}(t)e^{i\,H_S\,t/\hbar} \\ &= -\frac{i}{\hbar}[H_S,\rho_S(t)] + \mathcal{R}(t)\end{aligned}, \tag{4.52}$$

with the relaxation operator:

$$\mathcal{R}(t) := \sum_{\Omega_S>0} \Gamma(\Omega_S)\Big(\bar{n}(\Omega_S,T)\mathcal{D}(\Omega_S,t) + (\bar{n}(\Omega_S,T)+1)\mathcal{D}(-\Omega_S,t)\Big), \tag{4.53}$$

and the dissipators:

$$\begin{aligned}\mathcal{D}(\Omega_S,t) &:= e^{-i\,H_S\,t/\hbar}\mathcal{D}(\Omega_S)e^{i\,H_S\,t/\hbar} \\ &= 2\hat{S}(\Omega_S)\rho_S(t)\hat{S}(-\Omega_S) - \Big\{\hat{S}(-\Omega_S)\hat{S}(\Omega_S), \rho_S(t)\Big\},\end{aligned} \tag{4.54}$$

where we used that phases from $\hat{S}(\Omega_S)$ and $\hat{S}(-\Omega_S)$ in each term cancel out and that, at the time t_0 when the interaction started, $\rho_S(t_0) = \rho_S^{(I)}(t_0)$.

[14] We change the integration variable from t' to $\tau = t' - t_0$, the elapsed time since the interaction started.

4.4 Measurement of a lumped-element resonator

4.4.1 Dynamics of a resonator without driving

One of the simplest applications of the quantum master equation is a resonator coupled to a transmission line. The system coupling operator of Hamiltonian (4.20) is now $\hat{S} = \hat{a} + \hat{a}^\dagger$. From section 3.2.2 we know that the time-evolution of $\hat{S}$ without interactions is $S(t) = \hat{a}e^{-i\omega_r t} + \hat{a}^\dagger e^{i\omega_r t}$, where ω_r is the resonator frequency as defined in equation (3.16). The spectral decomposition of $\hat{S}$ is then given by $\hat{S}(\omega_r) = \hat{a}^\dagger$ and $\hat{S}(-\omega_r) = \hat{a}$. The sum in Ω_S in equation (4.53) has only one term with $\Omega_S = \omega_r$:

$$\mathcal{R}(t) = \Gamma(\omega_r)\Big[\bar{n}(\omega_r, T)\mathcal{D}(\omega_r, t) + (\bar{n}(\omega_r, T) + 1)\mathcal{D}(-\omega_r, t)\Big], \tag{4.55}$$

with:

$$\begin{aligned} \mathcal{D}(\omega_r, t) &= 2\hat{a}^\dagger\rho(t)\hat{a} - \Big\{\hat{a}\hat{a}^\dagger, \rho(t)\Big\}, \\ \mathcal{D}(-\omega_r, t) &= 2\hat{a}\rho(t)\hat{a}^\dagger - \Big\{\hat{a}^\dagger\hat{a}, \rho(t)\Big\}, \end{aligned} \tag{4.56}$$

where $\rho(t)$ is the density matrix of the resonator. The time evolution of the expectation value of the annihilation operator is then given by the Hamiltonian of the resonator, H_R (recall equation (3.22) in chapter 3), and the relaxation operator $\mathcal{R}(t)$:[15]

$$\begin{aligned} \frac{\mathrm{d}}{\mathrm{d}\,t}\langle\hat{a}\rangle(t) &= \operatorname{Tr}\hat{a}\dot{\rho}(t) \\ &= -\frac{i}{\hbar}\operatorname{Tr}\hat{a}\left[H_R, \rho(t)\right] + \operatorname{Tr}\hat{a}\mathcal{R}(t) \\ &= -i\omega_r\langle\hat{a}\rangle(t) - \kappa_c\langle\hat{a}\rangle(t), \end{aligned} \tag{4.57}$$

with $\kappa_c \equiv \Gamma(\omega_r) = 2\pi J(\omega_r)$, having the dimensions of frequency.

In practice, there are also internal losses (κ_i), so that we get a total decay rate $\kappa \equiv \kappa_i + \kappa_c$. The complete time evolution reads (recall equation (3.24) in chapter 3):

$$\frac{\mathrm{d}}{\mathrm{d}\,t}\langle\hat{a}\rangle = -i\omega_r\langle\hat{a}\rangle - \kappa\langle\hat{a}\rangle \;\;\Rightarrow\;\; \langle\hat{a}\rangle(t) = \langle\hat{a}\rangle(0)e^{-(i\omega_r+\kappa)t}. \tag{4.58}$$

Usually, instead of the decay rates κ, κ_i and κ_c we use the dimensionless quality factors Q, Q_i and Q_c, which are defined in terms of the former as:

$$Q := \frac{\omega_r}{2\kappa}, \qquad Q_i := \frac{\omega_r}{2\kappa_i}, \qquad Q_c := \frac{\omega_r}{2\kappa_c}. \tag{4.59}$$

[15] $\operatorname{Tr}\hat{a}\mathcal{D}(\omega_r, t)$ and $\operatorname{Tr}\hat{a}\mathcal{D}(-\omega_r, t)$ can be easily computed by using the commutation rule $\left[\hat{a}, \hat{a}^\dagger\right] = 1$ to transform the sums of products of $\hat{a}$ and $\hat{a}^\dagger$ into only $\hat{a}$.

We can also compute the time evolution of the expectation value of the number of photons in the cavity, $\hat{n} = \hat{a}^\dagger \hat{a}$:[16]

$$\begin{aligned} &\frac{\mathrm{d}}{\mathrm{d}\,t}\langle\hat{n}\rangle = -2\kappa\left[\langle\hat{n}\rangle - \bar{n}(\omega_r, T)\right] \;\Rightarrow \\ \Rightarrow\;\; &\langle\hat{n}\rangle(t) = \langle\hat{n}\rangle(0)e^{-2\kappa t} + \bar{n}(\omega_r, T)\left(1 - e^{-2\kappa t}\right). \end{aligned} \tag{4.60}$$

At very long times ($t \gg \kappa^{-1}$), we have $\langle\hat{n}\rangle \to \bar{n}(\omega_r, T)$ and $\langle\hat{a}\rangle \to 0$. That is, the number of photons in the resonator will be the number of thermal photons at frequency ω_r, and the coherence of the state of the resonator will be zero.

4.4.2 Driving the resonator

From the definitions in section 4.2.2 we write the coupling Hamiltonian of the resonator with a coherent drive field as:

$$H_{\text{drive}} = \hbar\sqrt{\kappa_c}\alpha_{in}(\hat{a} + \hat{a}^\dagger)e^{-i\omega_d t}. \tag{4.61}$$

Including this term in the master equation of $\langle\hat{a}\rangle$ we obtain:

$$\frac{\mathrm{d}}{\mathrm{d}\,t}\langle\hat{a}\rangle = -\left(i\omega_r + \kappa\right)\langle\hat{a}\rangle - i\sqrt{\kappa_c}\alpha_{in}e^{-i\omega_d t}, \tag{4.62}$$

with the solution:

$$\langle\hat{a}\rangle(t) = \langle\hat{a}\rangle(0)e^{-(i\omega_r+\kappa)t} - i\sqrt{\kappa_c}\frac{1 - e^{-(i(\omega_r-\omega_d)+\kappa)t}}{i(\omega_r - \omega_d) + \kappa}\alpha_{in}e^{-i\omega_d t}. \tag{4.63}$$

The first term is the transient state of the resonator. From the previous section we know that if we waited long enough ($t \gg \kappa^{-1}$) since the last time we sent a signal to resonator we will have $\langle\hat{a}\rangle(0) = 0$. The remaining term is the emerging driven state with frequency ω_d:

$$\langle\hat{a}\rangle(t) \simeq \chi_{\hat{a}}(\omega_d)\sqrt{\kappa_c}\langle\hat{r}_{in}\rangle(t) \quad , \quad \chi_{\hat{a}}(\omega_d) = \frac{-i}{i(\omega_r - \omega_d) + \kappa}, \tag{4.64}$$

where $\chi_{\hat{a}}$ is the susceptibility of $\hat{a}$.

Substituting equation 4.64 in the input-output relations (equation (4.29)):

$$\begin{aligned} \langle\hat{r}_{out}\rangle(t) &= \langle\hat{r}_{in}\rangle(t)\;\left(1 - i\kappa_c\chi_{\hat{a}}(\omega_d)\right), \\ \langle\hat{l}_{out}\rangle(t) &= \langle\hat{r}_{in}\rangle(t)\;\left(-i\kappa_c\chi_{\hat{a}}(\omega_d)\right), \end{aligned} \tag{4.65}$$

and with the definition of scattering parameters from equation (4.25) we obtain:

$$\begin{aligned} S_{21}(\omega_d) &= 1 - i\kappa_c\chi_{\hat{a}}(\omega_d) = 1 - \frac{\kappa_c}{i(\omega_r - \omega_d) + \kappa}, \\ S_{11}(\omega_d) &= -i\kappa_c\chi_{\hat{a}}(\omega_d) = -\frac{\kappa_c}{i(\omega_r - \omega_d) + \kappa}. \end{aligned} \tag{4.66}$$

[16] Again, using $\left[\hat{a}, \hat{a}^\dagger\right] = 1$.

4.5 Measurement of a spin 1/2 ensemble

Before diving into the model for the measurement of a hybrid system of a spin ensemble coupled to a resonator, let us describe the simpler case in which the ensemble is directly coupled to the transmission line.

4.5.1 Dynamics of a single spin without driving

We begin considering a single spin coupled to the transmission line. The system coupling operator of Hamiltonian (4.20) is now $\hat{S} = \hat{\sigma}_+ + \hat{\sigma}_-$. The evolution of the expectation value of $\sigma_\pm$ with the Hamiltonian of a single spin, $H_S = \frac{\hbar\omega_q}{2}\hat{\sigma}_z$, is:

$$\frac{\mathrm{d}}{\mathrm{d}\,t}\langle\hat{\sigma}_\pm\rangle = -\frac{i}{\hbar}\operatorname{Tr}\hat{\sigma}_\pm\left[H_S,\rho\right] = \pm\omega_q\langle\hat{\sigma}_\pm\rangle \;\;\rightarrow\;\; \langle\hat{\sigma}_\pm\rangle(t) = \langle\hat{\sigma}_\pm\rangle(0)e^{\pm i\omega_q t}, \quad (4.67)$$

where $\rho(t)$ is the density matrix of the spin. Then, the time-evolution of $\hat{S}$ without interactions is $S(t) = \hat{\sigma}_+ e^{i\omega_q t} + \hat{\sigma}_- e^{-i\omega_q t}$, and its spectral decomposition is given by $\hat{S}(\omega_q) = \hat{\sigma}_+$ and $\hat{S}(-\omega_q) = \hat{\sigma}_-$. The sum in Ω_S in equation (4.53) has only one term with $\Omega_S = \omega_q$:

$$\mathcal{R}(t) = \Gamma(\omega_q)\Big[\bar{n}(\omega_q,T)\mathcal{D}(\omega_q,t) + (\bar{n}(\omega_q,T)+1)\mathcal{D}(-\omega_q,t)\Big], \quad (4.68)$$

with the dissipators:

$$\begin{aligned}\mathcal{D}(\omega_q,t) &= 2\hat{\sigma}_+\rho(t)\hat{\sigma}_- - \Big\{\hat{\sigma}_-\hat{\sigma}_+,\rho(t)\Big\},\\ \mathcal{D}(-\omega_q,t) &= 2\hat{\sigma}_-\rho(t)\hat{\sigma}_+ - \Big\{\hat{\sigma}_+\hat{\sigma}_-,\rho(t)\Big\},\end{aligned} \quad (4.69)$$

The quantum master equation of the coherence $\hat{\sigma}_\pm$ reads:[17]

$$\begin{aligned}\frac{\mathrm{d}}{\mathrm{d}\,t}\langle\hat{\sigma}_\pm\rangle &= \operatorname{Tr}\hat{\sigma}_\pm\dot{\rho}(t)\\ &= -\frac{i}{\hbar}\operatorname{Tr}\hat{\sigma}_\pm\left[H_S,\rho(t)\right] + \operatorname{Tr}\hat{\sigma}_\pm\mathcal{R}(t)\\ &= \pm i\omega_q\langle\hat{\sigma}_\pm\rangle - \Gamma_\perp\langle\hat{\sigma}_\pm\rangle,\end{aligned} \quad (4.70)$$

with $\Gamma_\perp := (2\bar{n}(\omega_q,T)+1)\,G_1^{(\mathrm{line})}$, where $G_1^{(\mathrm{line})} := \Gamma(\omega_q) = 2\pi J(\omega_q)$. In practice, there are also internal losses ($\gamma_\perp = T_2^{-1}$), so that we get a total decay rate $\Gamma_\perp := \gamma_\perp + (2\bar{n}(\omega_q,T)+1)\,G_1^{(\mathrm{line})}$. Solving the differential equation, one obtains:

$$\langle\hat{\sigma}_\pm\rangle(t) = \langle\hat{\sigma}_\pm\rangle(0)e^{(\pm i\omega_q - \Gamma_\perp)t}. \quad (4.71)$$

[17] The time evolution of $\hat{\sigma}_\pm$ is encoded in the off-diagonal terms of the density matrix, that is, the spin coherence.

We will see in the next section that, unlike the case of a resonator, we do not get an equation for $\hat{\sigma}_+$ or $\hat{\sigma}_-$ alone when we excite the system with a coherent drive. The driving term will contain the expectation value of $\hat{\sigma}_z$. Let us compute it now without driving. Because $\hat{\sigma}_z$ commutes with H_S, we only have the relaxation term of the quantum master equation:

$$\frac{\mathrm{d}}{\mathrm{d}\,t}\langle\hat{\sigma}_z\rangle = \mathrm{Tr}\,\hat{\sigma}_z\mathcal{R}(t) = -\Gamma_\parallel\left(\langle\hat{\sigma}_z\rangle + (\Delta P)_e\right), \tag{4.72}$$

where we already included internal losses ($\gamma_\parallel = T_1^{-1}$) in $\Gamma_\parallel := \gamma_\parallel + 2(2\bar{n}(\omega_q, T)+1)\,G_1^{(\mathrm{line})}$. $(\Delta P)_e = (2\bar{n}(\omega_q, T)+1)^{-1} = \tanh\left(\hbar\omega_q/k_\mathrm{B}T\right)$ is the population difference between the ground and excited spin states in thermal equilibrium. At long times ($t \gg \Gamma_\perp^{-1}, \Gamma_\parallel^{-1}$) the coherences ($\hat{\sigma}_\pm$) vanish and the expectation value of $\hat{\sigma}_z$ decays to its value in thermal equilibrium, $-(\Delta P)_e$.

4.5.2 Driving a single spin

The interaction of the spin with the coherent drive of equation (4.26) is:

$$H_\mathrm{drive} = \hbar\sqrt{G_1^{(\mathrm{line})}}\alpha_{in}e^{-i\omega_d t}(\hat{\sigma}_+ + \hat{\sigma}_-). \tag{4.73}$$

Including this term in the quantum master equations of $\langle\hat{\sigma}_\pm\rangle$ and $\langle\hat{\sigma}_z\rangle$ one obtains:

$$\begin{aligned}
\frac{\mathrm{d}}{\mathrm{d}\,t}\langle\hat{\sigma}_\pm\rangle &= \pm\, i\omega_q\langle\hat{\sigma}_\pm\rangle - \Gamma_\perp\langle\hat{\sigma}_\pm\rangle \mp i\sqrt{G_1^{(\mathrm{line})}}\alpha_{in}e^{-i\omega_d t}\langle\hat{\sigma}_z\rangle,\\
\frac{\mathrm{d}}{\mathrm{d}\,t}\langle\hat{\sigma}_z\rangle &= -\,\Gamma_\parallel\left(\langle\hat{\sigma}_z\rangle + (\Delta P)_e\right)\\
&\quad - i\sqrt{G_1^{(\mathrm{line})}}\alpha_{in}e^{-i\omega_d t}\langle\hat{\sigma}_+\rangle + i\sqrt{G_1^{(\mathrm{line})}}\alpha_{in}e^{-i\omega_d t}\langle\hat{\sigma}_-\rangle.
\end{aligned} \tag{4.74}$$

Instead of solving these equations, let us consider the typical transmission experiment. By the time we start driving the spin, its free evolution has relaxed to $\hat{\sigma}_\pm = 0$ and $\hat{\sigma}_z = -(\Delta P)_e$. Also, the spin-line coupling $G_1^{(\mathrm{line})}$ is very small compared to the decay rates $\Gamma_\perp$ and $\Gamma_\parallel$. Then, we can neglect the equation from $\hat{\sigma}_z$ and approximate that $\hat{\sigma}_z(t) = -(\Delta P)_e$ at all times. With this approximation, we find equations for $\hat{\sigma}_+$ and $\hat{\sigma}_-$ alone:

$$\frac{\mathrm{d}}{\mathrm{d}\,t}\langle\hat{\sigma}_\pm\rangle = \pm i\omega_q\langle\hat{\sigma}_\pm\rangle - \Gamma_\perp\langle\hat{\sigma}_\pm\rangle \pm i\sqrt{G_1^{(\mathrm{line})}}(\Delta P)_e\alpha_{in}e^{-i\omega_d t}. \tag{4.75}$$

In particular, for positive ω_d we are interested in the expectation value of $\hat{\sigma}_-$. The solution of its equation, assuming $\hat{\sigma}_-(0) = 0$, is:

$$\langle\hat{\sigma}_-\rangle(t) = -i\sqrt{G_1^{(\mathrm{line})}}(\Delta P)_e\frac{1 - e^{-(i(\omega_q-\omega_d)+\Gamma_\perp)t}}{i(\omega_q-\omega_d)+\Gamma_\perp}\alpha_{in}e^{-i\omega_d t}, \tag{4.76}$$

and we find at long times ($t \gg \Gamma_\perp^{-1}$):

$$\langle\hat{\sigma}_-\rangle(t) \simeq \chi_{\hat{\sigma}_-}(\omega_d)\sqrt{G_1^{(\mathrm{line})}}\langle\hat{r}_{in}\rangle(t) \quad , \quad \chi_{\hat{\sigma}_-}(\omega_d) = \frac{-i(\Delta P)_e}{i(\omega_q-\omega_d)+\Gamma_\perp}, \tag{4.77}$$

where $\chi_{\hat{a}}$ is the susceptibility of $\hat{a}$.

The equations for the outputs of the coherent drive are:

$$\begin{aligned}\langle\hat{r}_{out}\rangle(t) &= \langle\hat{r}_{in}\rangle(t)\,\left(1 - iG_1^{(\mathrm{line})}\chi_{\hat{\sigma}_-}(\omega_d)\right),\\ \langle\hat{l}_{out}\rangle(t) &= \langle\hat{r}_{in}\rangle(t)\,\left(-iG_1^{(\mathrm{line})}\chi_{\hat{\sigma}_-}(\omega_d)\right).\end{aligned} \tag{4.78}$$

Following the definitions from equation (4.25), the scattering parameters S_{21} and S_{11} are given by:

$$\begin{aligned}S_{21}(\omega_d) &= 1 - iG_1^{(\mathrm{line})}\chi_{\hat{\sigma}_-}(\omega_d) = 1 - \frac{G_1^{(\mathrm{line})}(\Delta P)_e}{i(\omega_q-\omega_d)+\Gamma_\perp},\\ S_{11}(\omega_d) &= -iG_1^{(\mathrm{line})}\chi_{\hat{\sigma}_-}(\omega_d) = -\frac{G_1^{(\mathrm{line})}(\Delta P)_e}{i(\omega_q-\omega_d)+\Gamma_\perp}.\end{aligned} \tag{4.79}$$

4.5.3 Driving a spin 1/2 ensemble

We want similar expressions for the reflection and transmission of a spin 1/2 ensemble. However, this is not as simple as taking the product of the single-spin scattering parameters S_{11} or S_{21} of all spins in the ensemble. We defined these parameters with an input field coming from port 1 ($\langle\hat{r}_{in}\rangle$) and no input field from port 2. Similarly, we have S_{12} and S_{22} with only an input from port 2 ($\langle\hat{l}_{in}\rangle$). We assumed a non-chiral coupling, so $S_{12} = S_{21}$ and $S_{22} = S_{11}$. Together they form the two-port scattering matrix $\boldsymbol{S}$:

$$\boldsymbol{S} = \begin{pmatrix} S_{11} & S_{12} \\ S_{21} & S_{22}\end{pmatrix}, \tag{4.80}$$

which relates the inputs from both ports to their outputs:

$$\begin{pmatrix}\langle\hat{l}_{out}\rangle \\ \langle\hat{r}_{out}\rangle\end{pmatrix} = \boldsymbol{S}\begin{pmatrix}\langle\hat{l}_{in}\rangle \\ \langle\hat{r}_{in}\rangle\end{pmatrix}. \tag{4.81}$$

We need to change from a description with the scattering matrix $\boldsymbol{S}$ of a single spin, which relates the inputs and outputs of the system, to a description with the transfer matrix $\boldsymbol{T}$, which relates the input and output in port 1 to those of port 2 (see figure 4.4):

$$\begin{pmatrix}\langle\hat{r}_{out}\rangle \\ \langle\hat{l}_{in}\rangle\end{pmatrix} = \boldsymbol{T}\begin{pmatrix}\langle\hat{r}_{in}\rangle \\ \langle\hat{l}_{out}\rangle\end{pmatrix} = \begin{pmatrix} T_{11} & T_{12} \\ T_{21} & T_{22}\end{pmatrix}\begin{pmatrix}\langle\hat{r}_{in}\rangle \\ \langle\hat{l}_{out}\rangle\end{pmatrix}. \tag{4.82}$$

The elements of the transfer matrix are related to those of the scattering matrix. Defining $\theta := S_{11}/S_{21}$:

$$\theta(\omega_d) := \frac{S_{11}(\omega_d)}{S_{21}(\omega_d)} = \frac{-G_1^{(\mathrm{line})}(\Delta P)_e}{i\,(\omega_q - \omega_d) + \left[\Gamma_\perp - G_1^{(\mathrm{line})}(\Delta P)_e\right]}, \tag{4.83}$$

we can write $\boldsymbol{T}$ as:

$$\boldsymbol{T} = \begin{pmatrix} 1+\theta & \theta \\ -\theta & 1-\theta \end{pmatrix} = \mathbb{I} + \theta\boldsymbol{\epsilon}, \qquad \boldsymbol{\epsilon} = \begin{pmatrix} 1 & 1 \\ -1 & -1 \end{pmatrix}, \tag{4.84}$$

where we used that $S_{21} = 1 + S_{11}$.

Now we model the ensemble as an array of N spins and compute the collective transfer matrix as the product of all the single-spin transfer matrices: $\boldsymbol{T} = \prod_{j=1}^{N} \boldsymbol{T_j}$. That is, the fields in port 2 for one spin become the fields in port 1 for the next one. If we have N spins, $\boldsymbol{T}$ will be a series of powers of $\boldsymbol{\epsilon}$ up to order N. But $\boldsymbol{\epsilon}^2 = 0$, so only terms up to first order in $\boldsymbol{\epsilon}$ are non-zero and we obtain a transfer matrix similar to that of a single spin:

$$\boldsymbol{T} = \mathbb{I} + \left(\sum_{j=1}^{N} \theta_j\right) \boldsymbol{\epsilon} \equiv \mathbb{I} + \theta\boldsymbol{\epsilon}, \tag{4.85}$$

with:

$$\theta(\omega_d) = \sum_{j=1}^{N} \theta_k(\omega_d) = -\sum_{j=1}^{N} \frac{G_{1,\,j}^{(\mathrm{line})}(\Delta P)_e}{i\,(\omega_r - \omega_d) + \left[\Gamma_{\perp,\,j} - G_{1,\,j}^{(\mathrm{line})}(\Delta P)_e\right]}, \tag{4.86}$$

and we retrieve S_{11} and S_{21} using again that $S_{21} = 1 + S_{11}$ and $\theta = S_{11}/S_{21}$:

$$S_{21}(\omega_d) = \frac{1}{1 - \theta(\omega_d)}, \qquad S_{11}(\omega_d) = \frac{\theta(\omega_d)}{1 - \theta(\omega_d)}. \tag{4.87}$$

At very low temperatures ($T \ll \hbar\omega_q/k_\mathrm{B}$) the population difference between the ground and excited states is approximately one ($\Delta P \simeq 1$). Then, using that $\Gamma_{\perp,\,j} = \gamma_\perp + G_{1,\,j}^{(\mathrm{line})}$ we obtain a much simpler expression for $\theta(\omega_d)$:

$$\theta(\omega_d) \simeq -\frac{G_N^{(\mathrm{line})}\Delta P}{i\,(\omega_q - \omega_d) + \gamma_\perp}, \tag{4.88}$$

with:

$$G_N^{(\mathrm{line})} = \sum_{j=1}^{N} G_{1,\,j}^{(\mathrm{line})}. \tag{4.89}$$

In practice, if we have inhomogeneous broadening the coherence time T_2 is substituted by T_2^* in $\gamma_\perp$. Inserting $\theta(\omega_d)$ back in the expressions for the scattering parameters we obtain:

$$\begin{aligned} S_{21}(\omega_d) &= 1 - \frac{G_N^{(\text{line})}(\Delta P)_e}{i(\omega_q - \omega_d) + \gamma_\perp + G_N^{(\text{line})}(\Delta P)_e}, \\ S_{11}(\omega_d) &= -\frac{G_N^{(\text{line})}(\Delta P)_e}{i(\omega_q - \omega_d) + \gamma_\perp + G_N^{(\text{line})}(\Delta P)_e}. \end{aligned} \tag{4.90}$$

4.6 Measurement of a spin 1/2 ensemble-resonator system

We have described so far the measurement of a lumped-element resonator and the measurement of a spin 1/2 ensemble. Now we want measure the spin 1/2 ensemble through a lumped-element resonator. The quantum system we will probe is an ensemble-resonator modeled by Tavis-Cummings Hamiltonian (3.35). Let us consider first the single spin case, as we did in the previous section.

4.6.1 Spin-resonator system

The spin-resonator system is described by Jaynes-Cummings Hamiltonian (3.31). We assume that there is no direct coupling between the spin and the transmission line, only a resonator-line coupling. We compute first the quantum master equation for $\langle\hat{a}\rangle$, $\langle\hat{\sigma}_-\rangle$ and $\langle\hat{\sigma}_z\rangle$ without driving:[18]

$$\begin{aligned} \frac{\mathrm{d}}{\mathrm{d}\,t}\langle\hat{a}\rangle &= -(i\omega_r + \kappa)\langle\hat{a}\rangle - iG_1^*\langle\hat{\sigma}_-\rangle, \\ \frac{\mathrm{d}}{\mathrm{d}\,t}\langle\hat{\sigma}_-\rangle &= -(i\omega_q + \gamma_\perp)\langle\hat{\sigma}_-\rangle + iG_1\langle\hat{\sigma}_z\hat{a}\rangle, \\ \frac{\mathrm{d}}{\mathrm{d}\,t}\langle\hat{\sigma}_z\rangle &= -\gamma_\parallel\left(\langle\hat{\sigma}_z\rangle + (\Delta P)_e\right) - 2iG_1\langle\hat{\sigma}_+\hat{a}\rangle + 2iG_1^*\langle\hat{\sigma}_-\hat{a}^\dagger\rangle, \end{aligned} \tag{4.91}$$

where we wrote $\gamma_\perp$ and $\gamma_\parallel$ instead of $\Gamma_\perp$ and $\Gamma_\parallel$ because now the spin is not coupled to the transmission line. The coupling of the spin with its environment takes $\langle\hat{\sigma}_z\rangle$ to its equilibrium value $-(\Delta P)_e$ at long times ($t \gg \gamma_\parallel^{-1} = T_1$).

These equations look very similar to equation (4.74) for a spin coupled to a line with coherent driving, now with the resonator field playing the role of the

[18] The equations for $\langle\hat{a}^\dagger\rangle$ and $\langle\hat{\sigma}_+\rangle$ are just the Hermitian conjugates of those of $\langle\hat{a}\rangle$ and $\langle\hat{\sigma}_-\rangle$.

input field on the spin. However, there is an important difference: spin and resonator are entangled, so this drive is entering into the spin equations as the correlators $\langle\hat{\sigma}_z\hat{a}\rangle$, $\langle\hat{\sigma}_+\hat{a}\rangle$ and $\langle\hat{\sigma}_-\hat{a}^\dagger\rangle$. In fact, if we compute the equations for these correlators we find an infinite hierarchy of coupled equations for higher order correlators of spin and resonator operators. Thus, in order to obtain an approximate solution we have to truncate the infinite system of equations.

4.6.2 Ensemble-resonator system

Luckily, we have a justification for the truncation of the system of equations if we consider an ensemble of N spins coupled to the resonator instead of a single spin. Now we have a quantum master equation for every single spin in the ensemble [8]:

$$\begin{aligned}
\frac{\mathrm{d}}{\mathrm{d}\,t}\langle\hat{a}\rangle &= -(i\omega_r+\kappa)\langle\hat{a}\rangle - i\sum_{k=1}^{N} G^*_{1,\,k}\langle\hat{\sigma}_{-,\,k}\rangle,\\
\frac{\mathrm{d}}{\mathrm{d}\,t}\langle\hat{\sigma}_{-,\,k}\rangle &= -(i\omega_q+\gamma_\perp)\langle\hat{\sigma}_{-,\,k}\rangle + iG_{1,\,k}\langle\hat{\sigma}_{z,\,k}\hat{a}\rangle,\\
\frac{\mathrm{d}}{\mathrm{d}\,t}\langle\hat{\sigma}_{z,\,k}\rangle &= -\gamma_\parallel\left(\langle\hat{\sigma}_{z,\,k}\rangle + (\Delta P)_e\right) - 2iG_{1,\,k}\langle\hat{\sigma}_{+,\,k}\hat{a}\rangle + 2iG^*_{1,\,k}\langle\hat{\sigma}_{-,\,k}\hat{a}^\dagger\rangle,
\end{aligned} \tag{4.92}$$

where $\gamma_\perp$ is now the inverse of T_2^* if we have inhomogeneous broadening. In the semi-classical limit ($N\to\infty$) we can approximate the correlators $\langle\hat{\sigma}_{z,\,j}\hat{a}\rangle$, $\langle\hat{\sigma}_{+,\,j}\hat{a}\rangle$ and $\langle\hat{\sigma}_{-,\,j}\hat{a}^\dagger\rangle$ by the factorizations $\langle\hat{\sigma}_{z,\,j}\rangle\langle\hat{a}\rangle$, $\langle\hat{\sigma}_{+,\,j}\rangle\langle\hat{a}\rangle$ and $\langle\hat{\sigma}_{-,\,j}\rangle\langle\hat{a}^\dagger\rangle$ [9]:

$$\begin{aligned}
\frac{\mathrm{d}}{\mathrm{d}\,t}\langle\hat{a}\rangle &= -(i\omega_r+\kappa)\langle\hat{a}\rangle - i\sum_{j=1}^{N} G^*_{1,\,j}\langle\hat{\sigma}_{-,\,j}\rangle,\\
\frac{\mathrm{d}}{\mathrm{d}\,t}\langle\hat{\sigma}_{-,\,j}\rangle &= -(i\omega_q+\gamma_\perp)\langle\hat{\sigma}_{-,\,j}\rangle + iG_{1,\,j}\langle\hat{\sigma}_{z,\,j}\rangle\langle\hat{a}\rangle,\\
\frac{\mathrm{d}}{\mathrm{d}\,t}\langle\hat{\sigma}_{z,\,j}\rangle &= -\gamma_\parallel\left(\langle\hat{\sigma}_{z,\,j}\rangle + (\Delta P)_e\right)\\
&\quad - 2iG_{1,\,j}\langle\hat{\sigma}_{+,\,j}\rangle\langle\hat{a}\rangle + 2iG^*_{1,\,j}\langle\hat{\sigma}_{-,\,j}\rangle\langle\hat{a}^\dagger\rangle.
\end{aligned} \tag{4.93}$$

At long times all the coherences $\langle\hat{\sigma}_{-,\,j}\rangle$ vanish, and therefore all $\langle\hat{\sigma}_{z,\,j}\rangle$ relax to their equilibrium value $-(\Delta P)_e$.

4.6.3 Driving the ensemble-resonator system

Let us assume that we already have $\langle\hat{a}\rangle = \langle\hat{\sigma}_{-,\,j}\rangle = 0$ and $\langle\hat{\sigma}_{z,\,j}\rangle = -(\Delta P)_e$ when we start driving the system. We can consider that each $\langle\hat{\sigma}_{z,\,j}\rangle$ remains

close to its equilibrium value during all the measurement if the single spin-photon couplings $G_{1,k}$ are small enough. Then, introducing the driving only in the resonator (see equation (4.27)) we obtain:

$$\begin{aligned}\frac{\mathrm{d}}{\mathrm{d}\,t}\langle\hat{a}\rangle &= -(i\omega_r+\kappa)\langle\hat{a}\rangle - i\sum_{j=1}^{N} G_{1,j}^{*}\langle\hat{\sigma}_{-,j}\rangle - i\sqrt{\kappa_c}\alpha_{in}e^{-i\omega_d t},\\ \frac{\mathrm{d}}{\mathrm{d}\,t}\langle\hat{\sigma}_{-,j}\rangle &= -(i\omega_q+\gamma_\perp)\langle\hat{\sigma}_{-,j}\rangle - iG_{1,j}(\Delta P)_e\langle\hat{a}\rangle.\end{aligned} \tag{4.94}$$

We define now the collective ladder operator $\hat{\sigma}_-$ (recall the operator $\hat{b}$ in equation (3.43 of chapter 3):

$$\hat{\sigma}_- := \frac{1}{G_N}\sum_{j=1}^{N} G_{1,j}^{*}\,\hat{\sigma}_{-,j}\,, \tag{4.95}$$

with $G_N = G_{1,\mathrm{rms}}\sqrt{N}$. $G_{1,\mathrm{rms}}$ is the root mean square of the N different couplings as defined in equation (3.44) of chapter 3. Substituting in the equations, one finds:

$$\begin{aligned}\frac{\mathrm{d}}{\mathrm{d}\,t}\langle\hat{a}\rangle &= -(i\omega_r+\kappa)\langle\hat{a}\rangle - iG_N\langle\hat{\sigma}_-\rangle - i\sqrt{\kappa_c}\alpha_{in}e^{-i\omega_d t},\\ \frac{\mathrm{d}}{\mathrm{d}\,t}\langle\hat{\sigma}_-\rangle &= -(i\omega_q+\gamma_\perp)\langle\hat{\sigma}_-\rangle - iG_N(\Delta P)_e\langle\hat{a}\rangle,\end{aligned} \tag{4.96}$$

or, in matrix form:

$$\frac{\mathrm{d}}{\mathrm{d}\,t}\boldsymbol{x}(t) = \boldsymbol{M}\boldsymbol{x}(t) + \boldsymbol{f}(t)e^{-i\omega_d t}, \tag{4.97}$$

where we have defined:

$$\boldsymbol{x}(t) := \begin{pmatrix}\langle\hat{a}\rangle(t)\\ \langle\hat{\sigma}_-\rangle(t)\end{pmatrix}, \qquad \boldsymbol{f}(t) := \begin{pmatrix}-i\sqrt{\kappa_c}\alpha_{in}(t)\\ 0\end{pmatrix} \tag{4.98}$$

and

$$\boldsymbol{M} := -\begin{pmatrix}(i\omega_r+\kappa) & iG_N\\ iG_N(\Delta P)_e & (i\omega_q+\gamma_\perp)\end{pmatrix}. \tag{4.99}$$

The solution of equation (4.97) is given by:

$$\boldsymbol{x}(t) = e^{\boldsymbol{M}t}\boldsymbol{x}(0) + \int_0^t d\tau e^{\boldsymbol{M}(t-\tau)}e^{-i\omega_d\tau}\boldsymbol{f}(\tau)\ . \tag{4.100}$$

As in the dynamics of the bare resonator (see equation (4.63)), we have a first term that is the transient state of the system, and a second term that is the emerging driven state with frequency ω_d. The driving $\boldsymbol{f}(t)$ is time-dependent in general, with $\alpha_{in}(t)$ being the envelope of the input signal. However, for

a square pulse $\boldsymbol{f}(t)$ is constant, and the response can be easily obtained by computing the eigenvalues λ_n and eigenvectors $\boldsymbol{q}_n$ of $\boldsymbol{M}$:

$$\begin{aligned}\boldsymbol{x_{pulse}}(t) &= \sum_{n=1,2} \boldsymbol{q}_n \boldsymbol{q}_n^* \left(e^{\lambda_n t} \boldsymbol{x}(0) + \frac{e^{(\lambda_n + i\omega_d)t} - 1}{\lambda_n + i\omega_d} \boldsymbol{f} \right), \\ \boldsymbol{x_{decay}}(t) &= \sum_{n=1,2} \boldsymbol{q}_n \boldsymbol{q}_n^* e^{\lambda_n t} \boldsymbol{x_{pulse}}(T),\end{aligned} \tag{4.101}$$

For long times only the driven state remains, yielding the scattering parameters S_{11} and S_{21}:

$$\begin{aligned}S_{21}(\omega_d) &= 1 - \frac{\kappa_c}{i(\omega_r - \omega_d) + \kappa + \dfrac{G_N^2(T)}{i(\omega_q - \omega_d) + \gamma_\perp}}, \\ S_{11}(\omega_d) &= -\frac{\kappa_c}{i(\omega_r - \omega_d) + \kappa + \dfrac{G_N^2(T)}{i(\omega_q - \omega_d) + \gamma_\perp}},\end{aligned} \tag{4.102}$$

where we have defined the temperature dependent coupling $G_N(T)$:

$$G_N^2(T) := G_N^2(\Delta P)_e. \tag{4.103}$$

$G_N \equiv G_N(T = 0)$ is the limit of the coupling at zero temperature. At very low temperatures we have $(\Delta P)_e \simeq 1$, and the ensemble-resonator is equivalent to a system of two coupled resonators with a coupling rate G_N.

4.6.4 Weak and strong coupling

In section 3.3 from chapter 3 we described how the qubit-resonator (or spin-resonator, or spin ensemble-resonator) system formed pairs of polaritonic states, that is, superpositions of qubit/spin/ensemble states and resonator states. In resonance, when the frequencies of the two subsystems are the same, the energies of the states of each pair are split by twice the coupling between the subsystems.

Consider the case of the ensemble-resonator system. How does the strength of the coupling translate to the observed transmission $S_{21}(\omega_d)$. We have two distinct regimes defined as the limits of the ratio between $G_N\sqrt{(\Delta P)_e}$ and $\gamma_\perp$. In the strong coupling regime ($G_N\sqrt{(\Delta P)_e}/\gamma_\perp > 1$), the ensemble-resonator coupling is faster than the decoherence rate of the ensemble, which is typically much faster than the decoherence rate of the resonator, κ. In the weak coupling regime ($G_N\sqrt{(\Delta P)_e}/\gamma_\perp \ll 1$), the decoherence of the ensemble is the dominant process.

Let us study $S_{21}(\omega_d)$ in these two regimes. The transmission is minimum when the imaginary part of the denominator in equation (4.102) vanishes. That is, when:

$$(\omega_r - \omega_d)(\omega_q - \omega_d)^2 + (\omega_r - \omega_d)\gamma_\perp^2 + (\omega_d - \omega_q)G_N^2(\Delta P)_e = 0. \tag{4.104}$$

In the strong coupling regime (strong enough so that $G_N\sqrt{(\Delta P)_e}/\gamma_\perp \gg 1$), we neglect the second term and write:

$$(\omega_r - \omega_d)(\omega_q - \omega_d) \simeq G_N^2(\Delta P)_e, \tag{4.105}$$

which gives:

$$\omega_{d,\pm} = \frac{\omega_r + \omega_q}{2} \pm \sqrt{\left(\frac{\omega_r - \omega_q}{2}\right)^2 + G_N^2(\Delta P)_e}. \tag{4.106}$$

In resonance ($\omega_r = \omega_q$) we have $\omega_{d,\pm} = \omega_r \pm G_N\sqrt{(\Delta P)_e}$. That is, we find two minima of the transmission at the frequencies of the two normal modes of the system (see equation (3.42) and figure 3.6 in chapter 3). We can plug $\omega_{d,\pm}$ as the driving frequency in the real part of the denominator to find that the half width of each of the two peaks in resonance is approximately $\kappa + \gamma_\perp$.

In the weak coupling regime, we find a single minimum of the transmission instead of two, with resonance frequency and half width similar to those of the bare resonator. Substituting $\omega_q - \omega_d$ by $\omega_q - \omega_r$ in the transmission we find that the imaginary part of the denominator vanishes when $\omega_d = \tilde{\omega}_r$, with:

$$\tilde{\omega}_r := \omega_r + \left[\frac{G_N^2(\Delta P)_e}{(\omega_q - \omega_r)^2 + \gamma_\perp^2}\right](\omega_r - \omega_q), \tag{4.107}$$

The peak half width is given by the real part of the denominator:

$$\tilde{\kappa} := \kappa + \left[\frac{G_N^2(\Delta P)_e}{(\omega_q - \omega_r)^2 + \gamma_\perp^2}\right]\gamma_\perp. \tag{4.108}$$

Unfortunately, in many experiments we are in between these two regimes ($G_N\sqrt{(\Delta P)_e}/\gamma_\perp \sim 1$), with the coupling slightly below $\gamma_\perp$ but large enough to reach the high-cooperativity regime. In this regime, defined by a cooperativity $C := G_N^2(\Delta P)_e/\gamma_\perp\kappa$ larger than one, the coupling is strong in the sense that at resonance nearly every photon entering the cavity is coherently transferred into the qubits/spins [10]. While strong coupling ensures a double peak in the transmission, this is not necessarily the case for high-cooperativity (see figure 4.5).

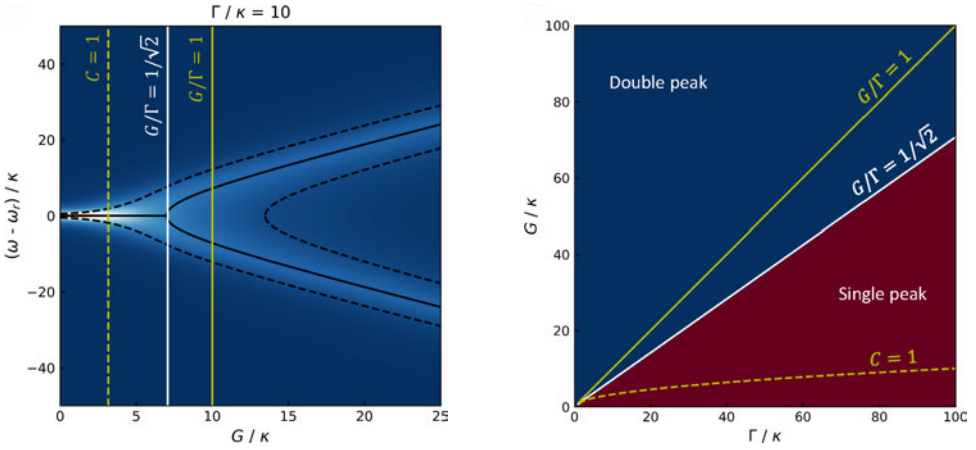

(a) (b)

Figure 4.5: (a) Transmission of the spin ensemble-resonator system as a function of the coupling G and the detuning from the frequency of the resonator, ω_r, both normalized by the resonator decoherence rate κ. The ratio of the spin decoherence rate Γ to κ is 10. The minima of the transmission at different values of G trace the solid black lines, with the points at half height of the peaks trace the dashed lines. Note the bifurcation point at $G/\Gamma = 1/\sqrt{2}$. (b) Classification of the transmission by the number of peaks for different values of G/κ and Γ/κ. The single peak and double peak regions are separated by the $G/\Gamma = 1/\sqrt{2}$ line.

4.7 Generalization to high spin systems

In this last section we generalize the results from the previous sections to higher spin ensembles. We will start the simplest case: a single spin $S > 1/2$ directly coupled to a transmission line.

4.7.1 Single spin $S > 1/2$ coupled to a transmission line

The system coupling operator of Hamiltonian (4.20) is now:

$$\hat{S} = \sum_{\alpha=0}^{2S} \sum_{\beta>\alpha} \left(\hat{X}^{\alpha\beta} + \hat{X}^{\beta\alpha} \right). \tag{4.109}$$

We compute the evolution of the expectation value of each $\hat{X}^{\alpha\beta}$ with the Hamiltonian of a single spin $S > 1/2$ (recall equation (**??**) in chapter 3):

$$\begin{aligned}\frac{\mathrm{d}}{\mathrm{d}\,t}\langle\hat{X}^{\alpha\beta}\rangle &= -\frac{i}{\hbar}\,\mathrm{Tr}\,\hat{X}^{\alpha\beta}\,[H_S,\rho] \\ &= -\frac{i}{\hbar}\,\mathrm{Tr}\,\hat{X}^{\alpha\beta}\sum_{\gamma=0}^{2S}E_\gamma\left[\hat{X}^{\gamma\gamma},\rho\right] \\ &= i\frac{E_\alpha - E_\beta}{\hbar}\langle\hat{X}^{\alpha\beta}\rangle,\end{aligned} \tag{4.110}$$

where $\rho(t)$ is the density matrix of the spin. The solution of this equation for $\langle\hat{X}^{\alpha\beta}\rangle$ is just:

$$\langle\hat{X}^{\alpha\beta}\rangle = \langle\hat{X}^{\alpha\beta}\rangle(0)e^{i\frac{E_\alpha-E_\beta}{\hbar}t}, \tag{4.111}$$

as expected from the definition of the level shift operators $\langle\hat{X}^{\alpha\beta}\rangle$.[19] The time-evolution of $\hat{S}$ without interactions is then:

$$\hat{S}(t) = \sum_{\alpha=0}^{2S}\sum_{\beta>\alpha}\left(\hat{X}^{\alpha\beta}e^{-i\omega_{\alpha\beta}t} + \hat{X}^{\beta\alpha}e^{i\omega_{\alpha\beta}t}\right), \tag{4.112}$$

where we defined the (positive) frequencies $\omega_{\alpha\beta}$:[20]

$$\omega_{\alpha\beta} = \frac{E_\beta - E_\alpha}{\hbar}. \tag{4.113}$$

Assuming a non-degenerate frequency spectrum, that is, that all $\omega_{\alpha\beta}$ are different, the spectral decomposition is given by $\hat{S}(\omega_{\alpha\beta}) = \hat{X}^{\beta\alpha}$ and $\hat{S}(-\omega_{\alpha\beta}) = \hat{X}^{\alpha\beta}$. The sum in Ω_S in equation (4.53) runs over all the different frequencies $\omega_{\alpha\beta}$:

$$\begin{aligned}\mathcal{R}(t) = \sum_{\alpha=0}^{2S}\sum_{\beta>\alpha}\Gamma(\omega_{\alpha\beta})\Big(&\bar{n}(\omega_{\alpha\beta},T)\mathcal{D}(\omega_{\alpha\beta},t) \\ &+ (\bar{n}(\omega_{\alpha\beta},T)+1)\mathcal{D}(-\omega_{\alpha\beta},t)\Big),\end{aligned} \tag{4.114}$$

with:[21]

$$\begin{aligned}\mathcal{D}(\omega_{\alpha\beta},t) &= 2\hat{X}^{\beta\alpha}\rho(t)\hat{X}^{\alpha\beta} - \left\{\hat{X}^{\alpha\alpha},\rho(t)\right\}, \\ \mathcal{D}(-\omega_{\alpha\beta},t) &= 2\hat{X}^{\alpha\beta}\rho(t)\hat{X}^{\beta\alpha} - \left\{\hat{X}^{\beta\beta},\rho(t)\right\},\end{aligned} \tag{4.115}$$

[19] If $\langle\hat{X}^{\alpha\beta}\rangle = |\alpha\rangle\langle\beta|$, where $|\alpha\rangle$ and $|\beta\rangle$ are stationary states of the Hamiltonian, then $\langle\hat{X}^{\alpha\beta}\rangle(t) = |\alpha\rangle(t)\langle\beta|(t) = |\alpha\rangle(0)\langle\beta|(0)e^{i\frac{E_\alpha-E_\beta}{\hbar}t} = \langle\hat{X}^{\alpha\beta}\rangle(0)e^{i\frac{E_\alpha-E_\beta}{\hbar}t}$.

[20] Remember that we use the labels α and β so that $E_\beta > E_\alpha$.

[21] In the last term of the dissipators $\mathcal{D}(\pm\omega_{\alpha\beta},t)$ we use that $\hat{X}^{\alpha\beta}\hat{X}^{\beta\alpha} = \hat{X}^{\alpha\alpha}$ and $\hat{X}^{\beta\alpha}\hat{X}^{\alpha\beta} = \hat{X}^{\beta\beta}$.

where $\rho(t)$ is again the density matrix of the spin. Let us consider first the time evolution of the expectation value of the coherence $\hat{X}^{\alpha\beta}$ (with $\beta > \alpha$):

$$\begin{aligned}\frac{\mathrm{d}}{\mathrm{d}\,t}\langle\hat{X}^{\alpha\beta}\rangle &= \mathrm{Tr}\,\hat{X}^{\alpha\beta}\dot{\rho}(t)\\ &= -\frac{i}{\hbar}\,\mathrm{Tr}\,\hat{X}^{\alpha\beta}\,[H_S,\rho(t)] + \mathrm{Tr}\,\hat{X}^{\alpha\beta}\mathcal{R}(t)\\ &= -i\omega_{\alpha\beta}\langle\hat{X}^{\alpha\beta}\rangle - \Gamma_{\perp,\alpha\beta}\langle\hat{X}^{\alpha\beta}\rangle,\end{aligned} \tag{4.116}$$

with $\Gamma_{\perp,\alpha\beta} := \gamma_{\perp,\alpha\beta} + \Gamma_\alpha + \Gamma_\beta$, where $\gamma_{\perp,\alpha\beta}$ is the inverse of the coherence time T_2 of the $\alpha \to \beta$ transition without coupling to the transmission line, and where we defined the decay rates:

$$\Gamma_\alpha = \sum_{\gamma<\alpha}(G_1^{(\mathrm{line})})_{\gamma\alpha}(\bar{n}(\omega_{\gamma\alpha},T)+1) + \sum_{\gamma>\alpha}(G_1^{(\mathrm{line})})_{\alpha\gamma}\bar{n}(\omega_{\alpha\gamma},T). \tag{4.117}$$

Here we identified the couplings $(G_1^{(\mathrm{line})})_{\alpha\beta}$ to the rates $\Gamma(\omega_{\alpha\beta}) = 2\pi J(\omega_{\alpha\beta})$ in $\mathcal{R}(t)$. Solving the differential equation, one obtains:

$$\langle\hat{X}^{\alpha\beta}\rangle(t) = \langle\hat{X}^{\alpha\beta}\rangle(0)e^{\left(-i\omega_{\alpha\beta}-\Gamma_{\perp,\alpha\beta}\right)t}. \tag{4.118}$$

We can do the same derivation for $\langle\hat{X}^{\beta\alpha}\rangle$, and we obtain:

$$\langle\hat{X}^{\beta\alpha}\rangle(t) = \langle\hat{X}^{\beta\alpha}\rangle(0)e^{\left(i\omega_{\alpha\beta}-\Gamma_{\perp,\alpha\beta}\right)t}, \tag{4.119}$$

with the same decay rate $\Gamma_{\perp,\alpha\beta}$.

If we compute the quantum master equation for the population $\langle\hat{X}^{\alpha\alpha}\rangle$, we obtain:

$$\begin{aligned}\frac{\mathrm{d}}{\mathrm{d}\,t}\langle\hat{X}^{\alpha\alpha}\rangle &= \mathrm{Tr}\,\hat{X}^{\alpha\alpha}\dot{\rho}(t)\\ &= [H_S,\rho(t)] + \mathrm{Tr}\,\hat{X}^{\alpha\alpha}\mathcal{R}(t)\\ &= 2\sum_{\gamma<\alpha}(G_1^{(\mathrm{line})})_{\gamma\alpha}(\bar{n}(\omega_{\gamma\alpha},T)+1)\langle\hat{X}^{\gamma\gamma}\rangle\\ &\quad + 2\sum_{\gamma>\alpha}(G_1^{(\mathrm{line})})_{\alpha\gamma}\bar{n}(\omega_{\alpha\gamma},T)\langle\hat{X}^{\gamma\gamma}\rangle\\ &\quad - 2\Gamma_\alpha\langle\hat{X}^{\alpha\alpha}\rangle.\end{aligned} \tag{4.120}$$

We have a system $2S+1$ coupled first order linear differential equations, so in general $\langle\hat{X}^{\alpha\alpha}\rangle(t)$ will not be an exponential decay but a sum of exponential decays. Still, we can easily obtain the steady state $\langle\hat{X}^{\alpha\alpha}\rangle_{ss}$, the value to which $\langle\hat{X}^{\alpha\alpha}\rangle$ decays at long times. Taking $\frac{\mathrm{d}}{\mathrm{d}t}\langle\hat{X}^{\alpha\alpha}\rangle = 0$, we find that the steady states of the populations are related by:

$$\begin{aligned}\langle\hat{X}^{\alpha\alpha}\rangle_{ss} = \frac{1}{\Gamma_\alpha}\Big(&\sum_{\gamma<\alpha}(G_1^{(\mathrm{line})})_{\gamma\alpha}(\bar{n}(\omega_{\gamma\alpha},T)+1)\langle\hat{X}^{\gamma\gamma}\rangle_{ss}\\ &+\sum_{\gamma>\alpha}(G_1^{(\mathrm{line})})_{\alpha\gamma}\bar{n}(\omega_{\alpha\gamma},T)\langle\hat{X}^{\gamma\gamma}\rangle_{ss}\Big),\end{aligned} \tag{4.121}$$

with the solution:

$$\langle \hat{X}^{\alpha\alpha} \rangle_{ss} = \frac{e^{-E_\alpha/k_\mathrm{B}T}}{Z(T)} =: \langle \hat{X}^{\alpha\alpha} \rangle_e, \tag{4.122}$$

with $Z(T) = \sum_\gamma e^{-E_\gamma/k_\mathrm{B}T}$. That is, the population $\langle \hat{X}^{\alpha\alpha} \rangle$ relaxes to its value $\langle \hat{X}^{\alpha\alpha} \rangle_e$ in thermal equilibrium, as expected.[22]

4.7.2 Driving a single spin $S > 1/2$ through the transmission line

The coherent drive interaction is given by:

$$\begin{aligned} H_\mathrm{drive} = \hbar \sum_{\alpha=0}^{2S} \sum_{\beta>\alpha} \Big(& \sqrt{(G_1^{(\mathrm{line})})_{\alpha\beta}} \langle \hat{X}^{\alpha\beta} \rangle \\ & + \sqrt{(G_1^{(\mathrm{line})})_{\beta\alpha}} \langle \hat{X}^{\beta\alpha} \rangle \Big) \alpha_{in} e^{-i\omega_d t}. \end{aligned} \tag{4.123}$$

We assume that the populations have already decayed to their values in thermal equilibrium by the time we start driving, and that the couplings $(G_1^{(\mathrm{line})})_{\alpha\beta}$ are small enough so the deviation from these values is negligible. Defining the difference of population in thermal equilibrium $(\Delta P_{\alpha\beta})_e := \langle \hat{X}^{\alpha\alpha} \rangle_e - \langle \hat{X}^{\beta\beta} \rangle_e$, one obtains for the coherences $\langle \hat{X}^{\alpha\beta} \rangle$:

$$\begin{aligned} \frac{\mathrm{d}}{\mathrm{d}\,t} \langle \hat{X}^{\alpha\beta} \rangle &= \mathrm{Tr}\, \hat{X}^{\alpha\beta} \dot{\rho}(t) \\ &= -\frac{i}{\hbar} \mathrm{Tr}\, \hat{X}^{\alpha\beta} \left[H_S, \rho(t) \right] + \mathrm{Tr}\, \hat{X}^{\alpha\beta} \mathcal{R}(t) \\ &\quad - \frac{i}{\hbar} \mathrm{Tr}\, \hat{X}^{\alpha\beta} \left[H_\mathrm{drive}, \rho(t) \right] \\ &= -(i\omega_{\alpha\beta} + \Gamma_{\perp,\alpha\beta}) \langle \hat{X}^{\alpha\beta} \rangle \\ &\quad - i \sqrt{(G_1^{(\mathrm{line})})_{\alpha\beta}} (\Delta P_{\alpha\beta})_e \alpha_{in} e^{-\omega_d t} \\ &\quad - i\alpha_{in} e^{-\omega_d t} \sum_{\gamma \neq \alpha,\beta} \sqrt{(G_1^{(\mathrm{line})})_{\beta\gamma}} \langle \hat{X}^{\alpha\gamma} \rangle \\ &\quad + i\alpha_{in} e^{-\omega_d t} \sum_{\gamma \neq \alpha,\beta} \sqrt{(G_1^{(\mathrm{line})})_{\gamma\alpha}} \langle \hat{X}^{\gamma\beta} \rangle. \end{aligned} \tag{4.124}$$

If we are measuring the transition $\alpha \to \beta$, then $\omega_d \simeq \omega_{\alpha\beta}$. Assuming that the frequency spectrum of the spin is non-degenerate, then none of the terms

[22] We do not need to solve the equations. We already expected the solution to be the population of the states in thermal equilibrium, so we only have to plug $\langle \hat{X}^{\gamma\gamma} \rangle_{ss} = e^{-E_\gamma/k_\mathrm{B}T}/Z(T)$ into the equations and check that we obtain $\langle \hat{X}^{\alpha\alpha} \rangle_{ss} = e^{-E_\alpha/k_\mathrm{B}T}/Z(T)$.

in the last row oscillate with frequencies close to ω_d or $\omega_{\alpha\beta}$. Dropping these terms, we obtain:

$$\frac{\mathrm{d}}{\mathrm{d}\,t}\langle\hat{X}^{\alpha\beta}\rangle \simeq -(i\omega_{\alpha\beta}+\Gamma_{\perp,\alpha\beta})\langle\hat{X}^{\alpha\beta}\rangle - i\sqrt{(G_1^{(\mathrm{line})})_{\alpha\beta}}(\Delta P_{\alpha\beta})_e\alpha_{in}e^{-\omega_d t}. \quad (4.125)$$

By the time we start driving, all coherences have decayed to zero. Then, at long times ($t \gg \Gamma^{-}_{\perp,\alpha\beta}1$), we obtain the following scattering parameters S_{21} and S_{11}:

$$\begin{aligned} S_{21}(\omega_d \simeq \omega_{\alpha\beta}) &= 1 - \frac{(G_1^{(\mathrm{line})})_{\alpha\beta}(\Delta P_{\alpha\beta})_e}{i(\omega_{\alpha\beta}-\omega_d)+\Gamma_{\perp,\alpha\beta}}, \\ S_{11}(\omega_d \simeq \omega_{\alpha\beta}) &= -\frac{(G_1^{(\mathrm{line})})_{\alpha\beta}(\Delta P_{\alpha\beta})_e}{i(\omega_{\alpha\beta}-\omega_d)+\Gamma_{\perp,\alpha\beta}}. \end{aligned} \quad (4.126)$$

4.7.3 Driving a spin $S > 1/2$ ensemble through the transmission line

Following the steps from section 4.5.3, we obtain for a higher spin ensemble:

$$\begin{aligned} S_{21}(\omega_d \simeq \omega_{\alpha\beta}) &= \frac{1}{1-\theta(\omega_d \simeq \omega_{\alpha\beta})}, \\ S_{11}(\omega_d \simeq \omega_{\alpha\beta}) &= \frac{\theta(\omega_d \simeq \omega_{\alpha\beta})}{1-\theta(\omega_d \simeq \omega_{\alpha\beta})}, \end{aligned} \quad (4.127)$$

with:

$$\begin{aligned} \theta(\omega_d \simeq \omega_{\alpha\beta}) &= \sum_{j=1}^{N}\theta_k(\omega_d \simeq \omega_{\alpha\beta}) \\ &= -\sum_{j=1}^{N}\frac{(G_{1,\,j}^{(\mathrm{line})})_{\alpha\beta}(\Delta P_{\alpha\beta})_e}{\left[(\Gamma_{\perp,\,j})_{\alpha\beta} - (G_{1,\,j}^{(\mathrm{line})})_{\alpha\beta}(\Delta P_{\alpha\beta})_e\right] + i\,(\omega_{\alpha\beta}-\omega_d)}. \end{aligned} \quad (4.128)$$

In general we will not have $(\Delta P_{\alpha\beta})_e \simeq 1$, and we can not simplify the sum as in the spin 1/2 case.

4.7.4 Driving a spin $S > 1/2$ ensemble-resonator system

In order to factorize the correlators between spin operators and resonator operators we need a large number of spins in the ensemble (see sections 4.6.1 and 4.6.2). This system is described by the generalized Tavis-Cummings Hamiltonian (3.47). We assume that the ensemble is not coupled to the transmission

line. Sending a coherent drive to the resonator we obtain the following quantum master equations for $\langle\hat{a}\rangle$ and each $\langle\hat{X}_j^{\alpha\beta}\rangle$:

$$\begin{aligned}\frac{\mathrm{d}}{\mathrm{d}\,t}\langle\hat{a}\rangle &= -(i\omega_r+\kappa)\langle\hat{a}\rangle - i\sum_{j=1}^{N}\sum_{\alpha=0}^{2S}\sum_{\beta>\alpha}(G_{1,j})_{\alpha\beta}\langle\hat{X}_j^{\alpha\beta}\rangle - i\sqrt{\kappa_c}\alpha_{in}e^{-i\omega_d t},\\ \frac{\mathrm{d}}{\mathrm{d}\,t}\langle\hat{X}_j^{\alpha\beta}\rangle &\simeq -(i\omega_{\alpha\beta}+\gamma_{\perp,\alpha\beta})\langle\hat{X}_j^{\alpha\beta}\rangle - i(G_{1,j})_{\beta\alpha}\Delta P_{\alpha\beta}\langle\hat{a}\rangle,\end{aligned} \tag{4.129}$$

where we already substituted the populations $\langle\hat{X}_j^{\alpha\alpha}\rangle$ by their values in thermal equilibrium.

We define a collective operator $\hat{X}^{\alpha\beta}$ (as we did in section 4.6.3 for a spin 1/2 ensemble coupled to a resonator, see equation (4.95)):

$$\hat{X}^{\alpha\beta} := \frac{1}{(G_N)_{\alpha\beta}}\sum_{j=1}^{N}(G_{1,j})_{\alpha\beta}\,\hat{X}_j^{\alpha\beta}, \tag{4.130}$$

with $(G_N)_{\alpha\beta} = (G_{1,\mathrm{rms}})_{\alpha\beta}\sqrt{N}$:

$$(G_{1,\mathrm{rms}})_{\alpha\beta} = \sqrt{\frac{1}{N}\sum_{j=1}^{N}|(G_{1,j})_{\alpha\beta}|^2}\,. \tag{4.131}$$

Substituting in equation (4.129) we obtain:

$$\begin{aligned}\frac{\mathrm{d}}{\mathrm{d}\,t}\langle\hat{a}\rangle &= -(i\omega_r+\kappa)\langle\hat{a}\rangle - i\sum_{\alpha=0}^{2S}\sum_{\beta>\alpha}(G_N)_{\alpha\beta}\langle\hat{X}^{\alpha\beta}\rangle - i\sqrt{\kappa_c}\alpha_{in}e^{-i\omega_d t},\\ \frac{\mathrm{d}}{\mathrm{d}\,t}\langle\hat{X}^{\alpha\beta}\rangle &\simeq -(i\omega_{\alpha\beta}+\gamma_{\perp,\alpha\beta})\langle\hat{X}^{\alpha\beta}\rangle - i(G_N)_{\alpha\beta}\Delta P_{\alpha\beta}\langle\hat{a}\rangle.\end{aligned} \tag{4.132}$$

At long times, these equations yield the following scattering parameters [11]:

$$\begin{aligned}S_{21}(\omega_d\simeq\omega_{\alpha\beta}) &= 1 - \frac{\kappa_c}{i(\omega_r-\omega_d)+\kappa+\dfrac{(G_N)_{\alpha\beta}^2\Delta P_{\alpha\beta}}{i(\omega_{\alpha\beta}-\omega_d)+\gamma_{\perp,\alpha\beta}}}\\ S_{11}(\omega_d\simeq\omega_{\alpha\beta}) &= -\frac{\kappa_c}{i(\omega_r-\omega_d)+\kappa+\dfrac{(G_N)_{\alpha\beta}^2\Delta P_{\alpha\beta}}{i(\omega_{\alpha\beta}-\omega_d)+\gamma_{\perp,\alpha\beta}}}.\end{aligned} \tag{4.133}$$

The discussion of equation (4.133) in the weak and strong regimes is similar at the one in section 4.6.4.

References

[1] H. Goldstein, *Classical Mechanics* (Addison-Wesley, 2006).

[2] W. Greiner and J. Reinhardt, *Field quantization* (Springer, 1996).

[3] N. G. van Kampen, *Stochastic processes in physics and chemistry (Revised and enlarged edition)* (North-Holland, 1992).

[4] I. F. Quijandría Díaz, Ph.D. thesis, Universidad de Zaragoza (2016).

[5] J. J. Sakurai and J. Napolitano, *Modern quantum mechanics (Second edition* (Cambridge University Press, 2017).

[6] J. García Ripoll, *Quantum information and quantum optics* (Cambridge University Press, 2022).

[7] S. M. Barnett and P. M. Radmore, *Methods in theoretical quantum optics* (Oxford Science Publications, 1997).

[8] S. Weichselbaumer, M. Zens, C. W. Zollitsch, M. S. Brandt, S. Rotter, R. Gross, and H. Huebl, Physical Review Letters **125**, 137701 (2020).

[9] M. Zens, D. O. Krimer, and S. Rotte, Physical Review A **100**, 013856 (2019).

[10] D. I. Schuster, A. P. Sears, E. Ginossar, L. DiCarlo, L. Frunzio, J. J. L. Morton, H. Wu, G. A. D. Briggs, B. B. Buckley, D. D. Awschalom, et al., Physical Review Letters **105**, 140501 (2010).

[11] A. Gómez-León, F. Luis, and D. Zueco, Physical Review Applied **17**, 064030 (2022).

Chapter 5

Strong coupling of organic free-radical molecules to lumped-element resonators

Chapter 2 introduced superconducting lumped-element resonators (LERs) as a suitable platform for controlling and measuring molecular spin qubits. LERs have several interesting properties as compared to coplanar resonators. Several LERs with different resonance frequencies ω_r can be coupled to the same readout transmission line, which allows measuring them independently (frequency multiplexing). Also, the impedance $Z = \sqrt{L/C}$ of the LER is independent from the transmission line impedance $Z_0 = 50\ \Omega$. This gives more freedom in the fabrication of low-inductance LERs (small L) in order to enhance the spin-photon coupling [1].

While coplanar resonators have been already used to reach the strong coupling regime with molecular spin ensembles [2, 3], with LERs this regime has been achieved only with non-molecular spin ensembles [4]. In this chapter I explore whether strong coupling can be achieved with molecular spin qubits coupled to LERs, in particular organic free radicals that realize model $S = 1/2$ systems. These experiments illustrate the basic characteristics of a hybrid spin-LER platform.

5.1 Chip design and characterization

5.1.1 Chip design

I have used two superconducting chips, labeled *Test 1* and *Test 2*, made of a 100 nm-thick niobium (Nb) film deposited on top of a silicon substrate (see section 2.1.1 in chapter 2). Niobium is superconducting below $T_c = 9.26$ K. Twelve LERs with different resonance frequencies ω_r were patterned in the surface of each chip, side-coupled to the same transmission line. I labeled them from 1 to 12 from lowest to highest ω_r. Figure 5.1) shows both chip designs.

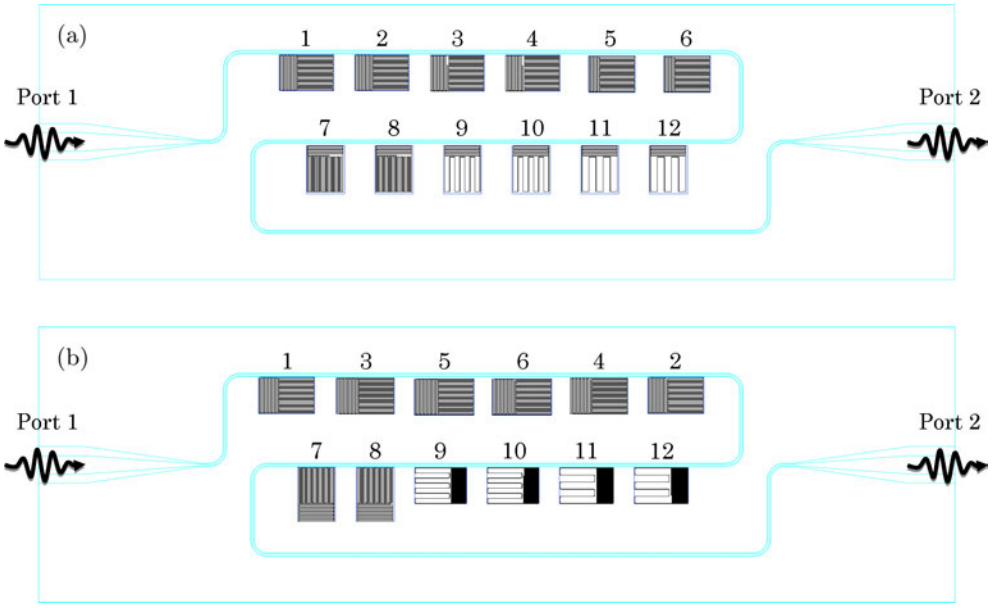

Figure 5.1: Vector file design of *Test 1* (a) and *Test 2* (b). All twelve LERs (black) in each chip are side-coupled to a single transmission line (blue), and labeled in increasing ω_r. The ordering in the top row in *Test 2* is different from the ordering in *Test 1* so that some pairs of resonators with similar frequencies (LERs 1 and 2, and LERs 3 and 4) are farther apart.

Chips *Test 1* and *Test 2* were fabricated to explore different LER designs and test how different parameters affect the spin-photon coupling and the transmission characteristics. LER designs are shown in figures 5.2) and 5.3. Most of the resonators have both inductive and capacitive coupling to the transmission line, that is, they have parts of both the meandering inductor and the inter-digitated capacitor very close to the line (figure 5.2). The rest are placed so that only the inductor or the capacitor are close to the line, which gives either an inductive or capacitive resonator-line coupling (figure 5.3).

There also LERs with different geometric inductance L_{geo} in order to see its effect on the spin-resonator coupling. Between resonators with a similar design, the frequency is tuned by increasing or decreasing the length of the last finger of the inter-digitated capacitor.

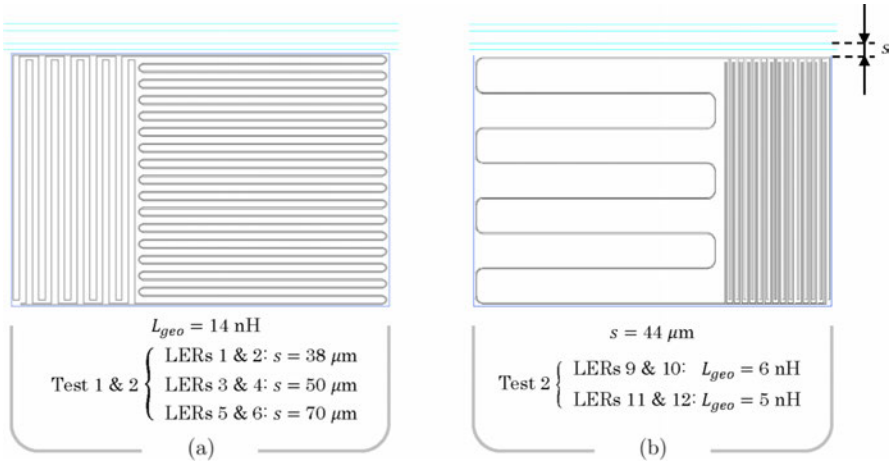

Figure 5.2: Examples of resonator designs having both inductive and capacitive coupling to the transmission line. The magnitude of this coupling is controlled by s, the shortest distance between the borders of the resonator and the central line of the transmission line. Higher line-resonator couplings are expected for shorter s. There are LERs with high (a) and low (b) geometric inductance L_{geo}.

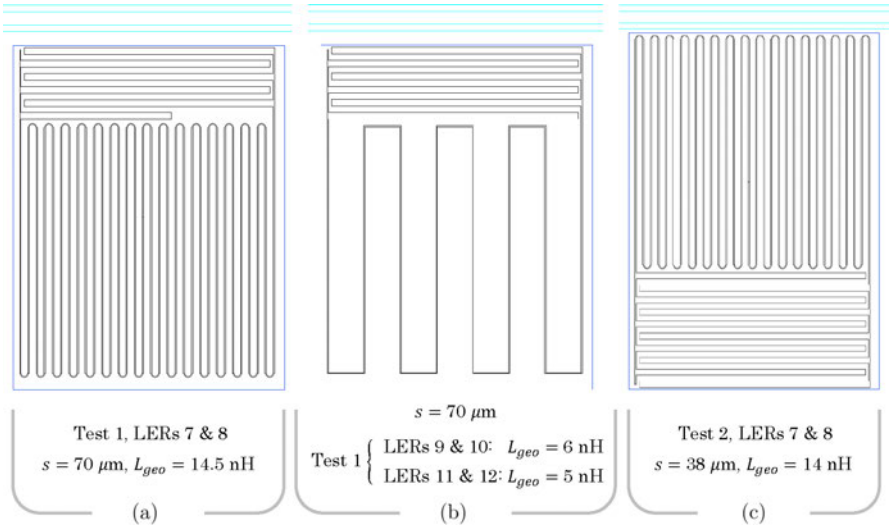

Figure 5.3: Examples of resonator designs with only capacitive coupling (a, b) or with only inductive coupling (c) to the transmission line. Designs (a) and (c) have a higher geometric inductance L_{geo} than design (b).

The ensemble-resonator coupling depends on the microwave magnetic field generated by the resonator, which in resonance is concentrated around the inductor. I used the 3D-MLSI software [5], which solves London equations for thin superconducting films with a finite element method, to compute the current distribution in the inductor in resonance. The magnetic field distribution on top of the inductor is then computed from this current distribution. This field is mainly contained within the plane perpendicular to the longer induction lines of the LER (see figure 5.4a). In a sample of free-radicals molecules with spin 1/2 only the microwave magnetic field perpendicular to the static magnetic $\boldsymbol{B_{dc}}$ contributes to the coupling (see section 3.3.1, and in particular equation (3.28)). Then, the best configuration in the experiment is to apply $\boldsymbol{B_{dc}}$ parallel to the longer inductor lines, as shown in figure 5.4a.

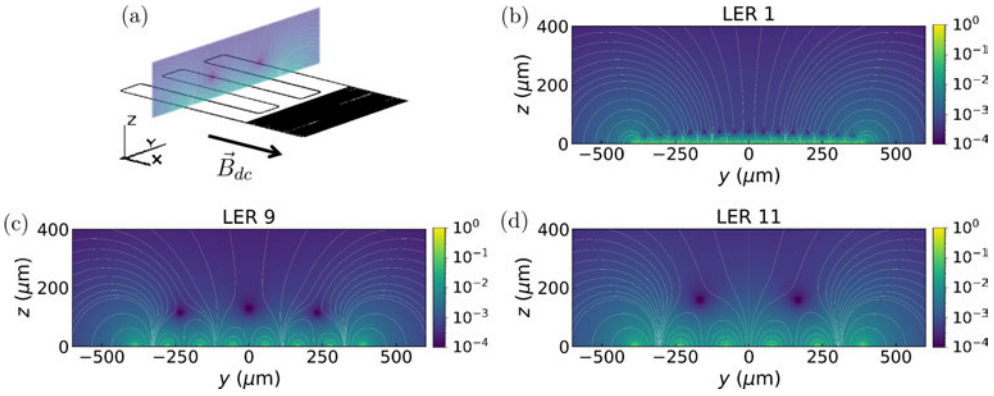

Figure 5.4: (a) Orientation of the plane containing the microwave magnetic field generated by the longer inductor lines with respect to the resonator design. The coupling is maximum if the static field $\boldsymbol{B_{dc}}$ is applied perpendicular to this plane (parallel to the inductor lines). (b, c, d) Maps showing the amplitude of the magnetic field within this plane generated by vacuum fluctuations in the resonator at the resonance frequency ω_r. The field distributions of three resonators in *Test 2* with different geometric inductance L_{geo} are shown: LERs 1 (b), 9 (c) and 11 (d). Maps are normalized by the maximum field within the plane in each case: 3.05 nT for LER 1, 4.22 nT for LER 9 and 3.08 nT for LER 11. White solid lines show the field lines.

Figures 5.4b, 5.4c and 5.4d show the distribution of the magnetic field above the inductor in this plane for LERs 1, 9 and 11 of *Test 2*. These resonators have different geometric inductance L_{geo}: 14 nH for LER 1, 6 nH for LER 9 and 5 nH for LER 11. The magnetic field generated by LER 1 is localized within a few microns above the inductor lines. This small mode volume is better suited for samples place very close to the chip surface. Conversely, LERs 9 and 11, with lower L_{geo}, generate a magnetic field distribution that spreads further from the surface (large mode volume), which is better for larger samples.

5.1.2 Characterization of *Test 1*

Prior to the experiments with spin samples, LERs in *Test 1* were characterized with transmission experiments at 17 mK and zero magnetic field. Each resonator has a resonance, that is, a dip in transmission (S_{21}) centered around the resonance frequency ω_r. Figure 5.5) shows the resonances in this chip (except for LER 10). The results were fitted with he model for S_{21} around ω_r given by equation (4.66) in chapter 4, which is reproduced here for clarity:

$$S_{21}(\omega_d) = 1 - \frac{\kappa_c}{i(\omega_r - \omega_d) + \kappa}, \tag{5.1}$$

where ω_d is the input (driving) frequency and κ comprises the total losses of the photon mode, including internal losses (κ_i) and the line-resonator coupling (κ_c). Figures showing experimental results are shown in terms of the regular input frequency $f = \omega_d/2\pi$.

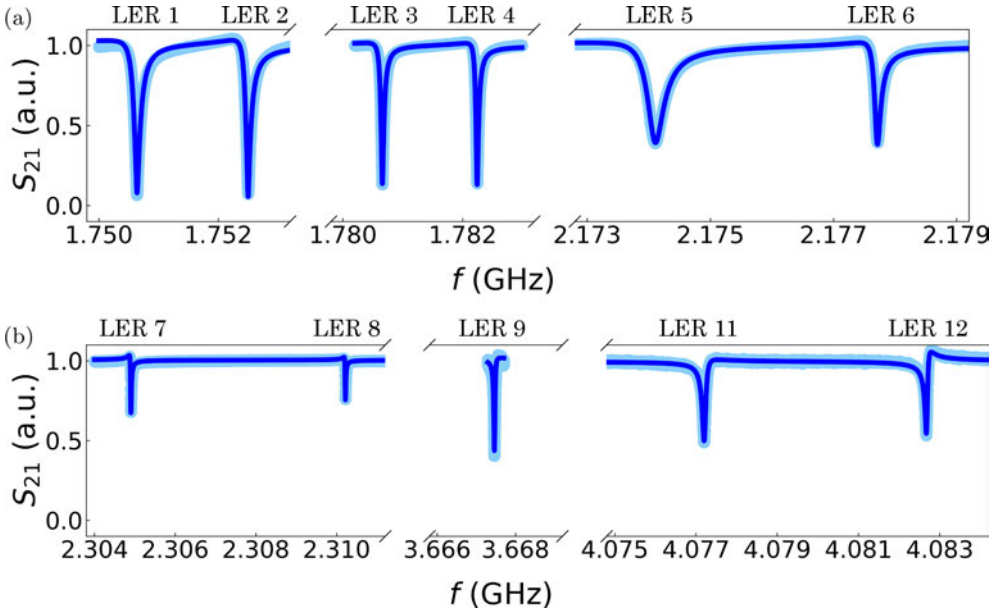

Figure 5.5: Module of the microwave transmission S_{21} (light blue dots) of *Test 1*, measured at 17 mK and zero magnetic field near the resonance frequency ω_r of each LER (except LER 10). Solid blue line shows the fit of the resonances of each pair of LERs, ordered in increasing resonance frequency: LERs 1 to 6 (a), LERs 7 to 12 (b).

The asymmetry of the resonances arises from the coupling of the mode of the resonator to modes in the transmission line (Fano resonance). These modes appear due to reflections in a slightly mismatched transmission line. Instead of doing a complete description of the modes in the line, a simple model was used: the Diameter Correction Method (DCM), which describes

the asymmetry in S_{21} with only one additional parameter [6]. In the DCM model the line-resonator coupling rate κ_c is a complex quantity with module $|\kappa_c|$ and argument ϕ_c. κ depends only on the real part of κ_c:

$$\kappa := \mathrm{Re}(\kappa_\mathrm{c}) + \kappa_\mathrm{i} = |\kappa_\mathrm{c}| \cos\phi_\mathrm{c} + \kappa_\mathrm{i}, \tag{5.2}$$

while the imaginary component of κ_c accounts for the transmission asymmetry. The visibility of the resonance is defined as the ratio:

$$\eta := \mathrm{Re}(\kappa_\mathrm{c})/\kappa = 1 - \kappa_\mathrm{i}/\kappa. \tag{5.3}$$

The results of the fit with equation (5.1) yields the parameters listed in table 5.1. The resonance frequencies are shifted to lower frequencies (between 70 and 120 MHz) compared to the results from simulations with Sonnet (see table A.1 in Appendix A). This shift is associated with contributions to the resonator inductance and capacitance that these simulations do not take into account. The inductance of the resonator is increased by the kinetic inductance L_k due to the inertia of superconducting electrons at high frequencies. The capacitance is also increased due to parasitic capacitances with other elements in the chip (the ground planes or the transmission line). All resonators are also broadened (higher κ_i) in the experimental setup compared to the simulations.

LER	$\omega_r/2\pi$ (GHz)	$\kappa/2\pi$ (kHz)	$\lvert\kappa_c\rvert/2\pi$ (kHz)	ϕ_c (°)
1	$1.7506246 \pm 2 \cdot 10^{-7}$	89.3 ± 0.2	84.7 ± 0.3	-8.5 ± 0.1
2	$1.7524814 \pm 2 \cdot 10^{-7}$	70.7 ± 0.2	68.7 ± 0.3	-18.5 ± 0.1
3	$1.78065512 \pm 7 \cdot 10^{-8}$	42.7 ± 0.1	37.6 ± 0.1	-8.6 ± 0.1
4	$1.78223735 \pm 6 \cdot 10^{-8}$	38.2 ± 0.1	33.8 ± 0.1	-13.7 ± 0.1
5	$2.1740753 \pm 4 \cdot 10^{-7}$	199.6 ± 0.4	124.6 ± 0.3	-13.3 ± 0.1
6	$2.1776990 \pm 2 \cdot 10^{-7}$	74.5 ± 0.2	47.3 ± 0.2	-21.9 ± 0.1
7	$2.30489941 \pm 7 \cdot 10^{-8}$	12.7 ± 0.1	4.57 ± 0.03	-30.1 ± 0.2
8	$2.31021363 \pm 8 \cdot 10^{-8}$	10.0 ± 0.1	2.67 ± 0.03	-28.5 ± 0.3
9	$3.66747128 \pm 6 \cdot 10^{-8}$	22.1 ± 0.1	12.70 ± 0.04	11.0 ± 0.1
10	–	–	–	–
11	$4.0772129 \pm 2 \cdot 10^{-7}$	61.6 ± 0.2	31.4 ± 0.1	15.9 ± 0.1
12	$4.0826920 \pm 2 \cdot 10^{-7}$	42.3 ± 0.2	21.6 ± 0.1	33.8 ± 0.2

Table 5.1: Fitting parameters of the experimental results of figure 5.5 with equation (5.1). ω_r is the resonance frequency of the LER. κ is the decay rate of the photon mode and comprises the total losses of the resonator. These include internal losses (κ_i) and the line-resonator coupling (κ_c). Using DCM, κ_c is complex-valued with module $|\kappa_c|$ and argument ϕ_c.

Figure 5.6 shows the module of the line-resonator coupling, $|\kappa_c|$ for each resonator. LERs with inductive coupling (LERs 1 to 6) display higher line-resonator coupling rates than those with only capacitive coupling (LERs 7 to 12). The magnetic field generated by the inductor extends farther than the electric field, which is typically confined close to the superconducting surface of the capacitor fingers, enhancing the line-resonator coupling. In fact, LERs 1 to 6 are over-coupled, with a visibility larger than 0.5 ($\eta > 0.5$), while those with only capacitive coupling are either critically coupled ($\eta = 0.5$), or under-coupled ($\eta < 0.5$). In particular, LERs 7 and 8 have by far the lowest line-resonator coupling rates and are clearly under-coupled.

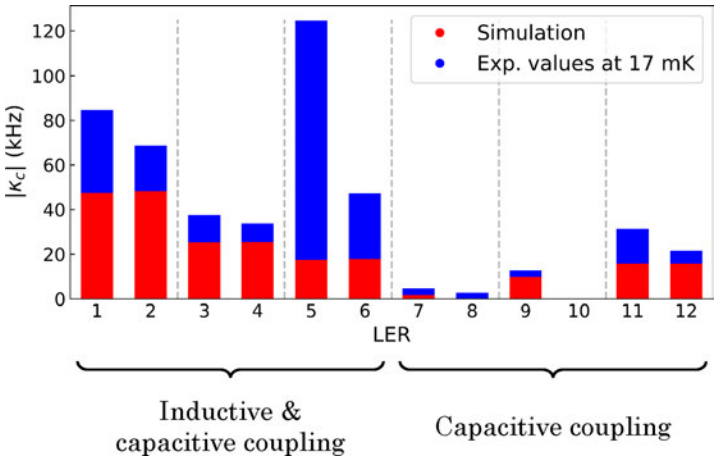

Figure 5.6: Absolute value of the complex line-coupling κ_c for LERs in *Test 1*.

Resonators LERs 1 and 2, which are closer to the transmission line than LERs 3 and 4, show higher line-resonator coupling rates than the latter. However, there is no clear dependence on the resonator-line distance s if LERs 5 and 6 are included, which have also the same design. This broadening of LER 5 (or LER 6, depending on the design) has been repeatedly observed in our experiments with chip designs like *Test 1* or *Test 2*.

5.1.3 Characterization of *Test 2*

The resonances in *Test 2* span a much narrower frequency range than those in *Test 1*. As with *Test 1*, these resonances were characterized with transmission experiments at 17 mK and zero magnetic field and fitted with 5.1. This chip was also characterized at 4.2 K in order to see the effect of temperature on the resonances. Figures 5.7 and 5.8 show the resonances at 17 mK at 4.2 K respectively, with the fitting parameters listed in tables 5.2 and 5.3.

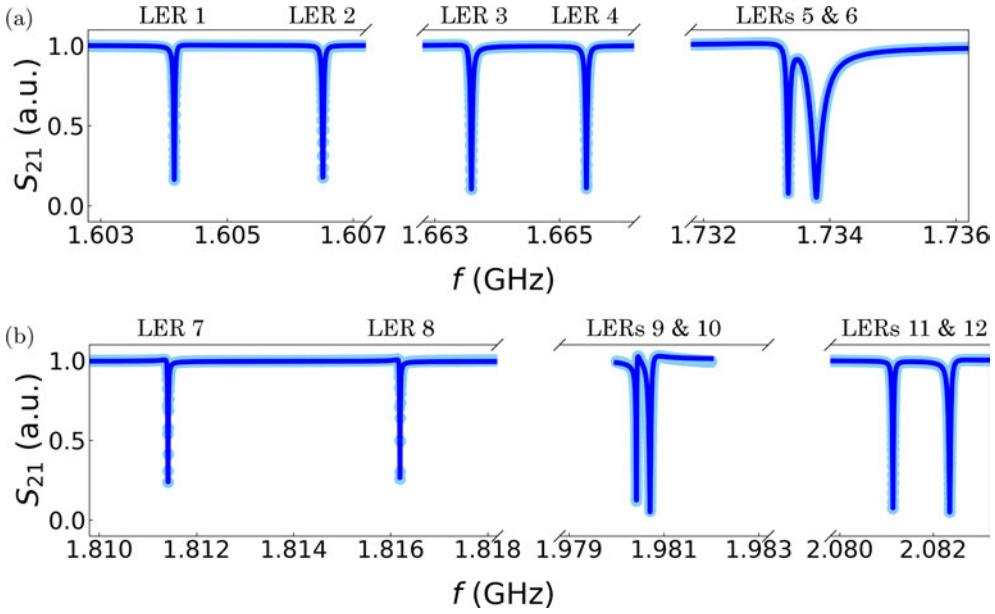

Figure 5.7: Microwave transmission (light blue dots) of *Test 2* measured at 17 mK near the resonance frequencies of all LERs. Solid blue line shows the fit of the resonances of each pair of LERS, ordered in increasing resonance frequency: LERs 1 to 6 (a), LERs 7 to 12 (b).

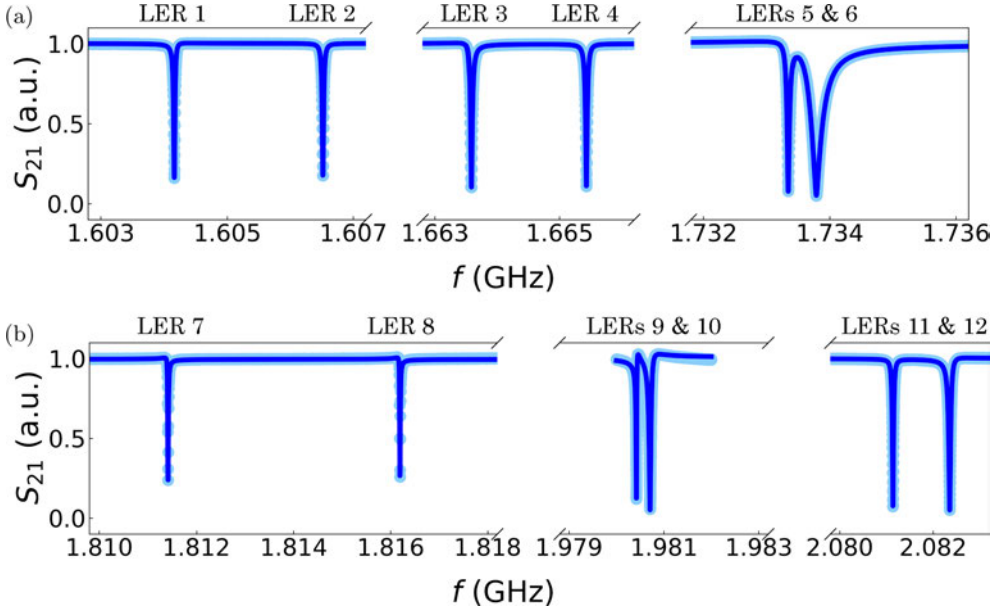

Figure 5.8: Microwave transmission (light blue dots) of *Test 2* measured at 4.2 K near the resonance frequencies of all LERs. The solid blue line shows the fit of the resonances of each pair of LERs, ordered in increasing resonance frequency: LERs 1 to 6 (a), LERs 7 to 12 (b).

LER	$\omega_r/2\pi$ (GHz)	$\kappa/2\pi$ (kHz)	$\lvert\kappa_c\rvert/2\pi$ (kHz)	ϕ_c (°)
1	$1.60416155 \pm 1 \cdot 10^{-8}$	16.51 ± 0.01	13.87 ± 0.01	4.92 ± 0.03
2	$1.60651821 \pm 1 \cdot 10^{-8}$	18.17 ± 0.01	15.08 ± 0.02	-0.45 ± 0.03
3	$1.66357945 \pm 1 \cdot 10^{-8}$	24.10 ± 0.01	21.86 ± 0.02	-5.54 ± 0.02
4	$1.66543185 \pm 1 \cdot 10^{-8}$	23.72 ± 0.01	21.07 ± 0.02	0.25 ± 0.02
5	$1.73334419 \pm 5 \cdot 10^{-8}$	33.4 ± 0.1	31.5 ± 0.1	15.0 ± 0.1
6	$1.7337608 \pm 1 \cdot 10^{-7}$	152.4 ± 0.1	149.0 ± 0.2	-14.14 ± 0.03
7	$1.81141912 \pm 3 \cdot 10^{-8}$	9.75 ± 0.03	7.62 ± 0.03	-9.5 ± 0.1
8	$1.81619219 \pm 2 \cdot 10^{-8}$	8.82 ± 0.02	6.88 ± 0.03	-10.3 ± 0.1
9	$1.98042651 \pm 3 \cdot 10^{-8}$	11.68 ± 0.03	10.56 ± 0.04	27.1 ± 0.1
10	$1.98071604 \pm 4 \cdot 10^{-8}$	34.94 ± 0.04	34.2 ± 0.1	7.94 ± 0.05
11	$2.08114007 \pm 1 \cdot 10^{-8}$	21.65 ± 0.01	20.04 ± 0.02	1.72 ± 0.02
12	$2.08235739 \pm 1 \cdot 10^{-8}$	36.75 ± 0.02	35.10 ± 0.03	4.80 ± 0.01

Table 5.2: Parameters from the fit of the experimental results in figure 5.7 with equation (5.1).

LER	$\omega_r/2\pi$ (GHz)	$\kappa/2\pi$ (kHz)	$\lvert\kappa_c\rvert/2\pi$ (kHz)	ϕ_c (°)
1	$1.59847075 \pm 6 \cdot 10^{-8}$	99.7 ± 0.1	14.91 ± 0.01	7.11 ± 0.03
2	$1.60081773 \pm 6 \cdot 10^{-8}$	102.3 ± 0.1	15.62 ± 0.01	4.29 ± 0.03
3	$1.65759532 \pm 9 \cdot 10^{-8}$	112.4 ± 0.1	19.74 ± 0.02	-7.89 ± 0.03
4	$1.65944270 \pm 8 \cdot 10^{-8}$	113.6 ± 0.1	20.85 ± 0.02	-4.24 ± 0.03
5	$1.7270242 \pm 3 \cdot 10^{-7}$	132.7 ± 0.2	33.9 ± 0.1	16.5 ± 0.1
6	$1.7274524 \pm 2 \cdot 10^{-7}$	238.7 ± 0.2	132.3 ± 0.1	-10.98 ± 0.04
7	$1.8045798 \pm 1 \cdot 10^{-7}$	121.7 ± 0.1	7.00 ± 0.01	-2.02 ± 0.05
8	$1.8093356 \pm 2 \cdot 10^{-7}$	119.1 ± 0.2	5.83 ± 0.01	-2.7 ± 0.1
9	$1.9744671 \pm 6 \cdot 10^{-7}$	144.3 ± 0.6	16.7 ± 0.1	26.2 ± 0.3
10	$1.9747926 \pm 3 \cdot 10^{-7}$	137.7 ± 0.3	33.2 ± 0.1	4.2 ± 0.1
11	$2.0753418 \pm 1 \cdot 10^{-7}$	127.6 ± 0.1	18.36 ± 0.03	1.81 ± 0.05
12	$2.0765439 \pm 1 \cdot 10^{-7}$	142.8 ± 0.1	32.49 ± 0.03	3.83 ± 0.03

Table 5.3: Parameters from the fit of the experimental results in figure 5.8 with equation (5.1).

The changes in transmission with temperature are those expected for superconducting lumped-element resonators [7]. Although the DC-resistance of a superconductor is zero below T_c (~ 9.2 K for Nb), its AC-impedance can be non-zero. In particular, this impedance increases with frequency and temperature (still below T_c), and makes for the increase of around one order of magnitude in the internal losses of the resonator (κ_i) between 17 mK and 4.2 K (from 10–35 kHz to 100-145 kHz). This increase in κ_i accounts for the wider lineshapes (higher κ) with lower visibility, while κ_c is temperature-independent.

There is also a decrease in ω_r of about 6 MHz for all resonators as temperature is increased. The penetration depth of the superconducting material increases with temperature, which in turn increases the resonator inductance L. The magnitude of the shift in the resonance frequency $\omega_r = 1/\sqrt{LC}$ depends on the contribution of this effect to the total L.

5.2 DPPH samples

5.2.1 The DPPH radical

2,2-diphenyl-1-picrylhydrazyl (DPPH) is an organic free radical molecule with spin 1/2 that is widely used as an standard in Electron Paramagnetic Resonance (EPR) [8]. Each DPPH molecule consists of a hydracyl radical bridging a picryl group and two phenyl groups (see figure 5.9). The spin 1/2 of the unpaired electron of the radical behaves nearly as the spin of a free electron. It is described by a spin Hamiltonian that is just an isotropic electronic Zeeman term:

$$H = \mu_B g_S B \hat{S}_z = \frac{\mu_B g_S B}{2} \hat{\sigma}_z, \tag{5.4}$$

with a g-factor $g_S = 2.004$ just above the value for a free electron [9].

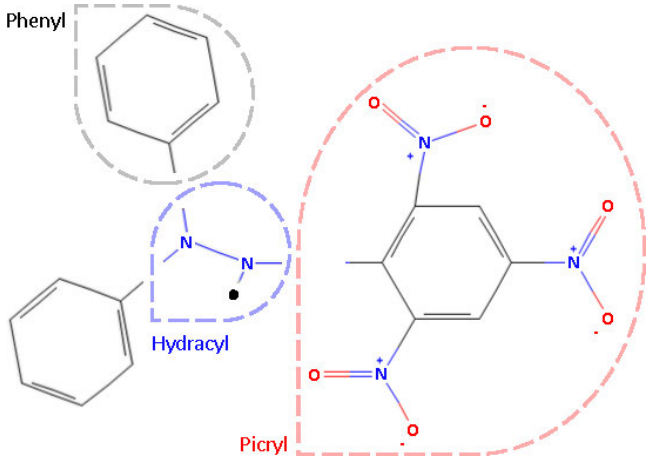

Figure 5.9: Chemical structure of DPPH, adapted from [10]. The unpaired electron (pictured as a black dot) that gives the effective spin 1/2 of the molecule is localized in the nitrogen atom of the hydracyl group closest to the picryl group.

The spin 1/2 is biased by a static field $\boldsymbol{B_{dc}}$ of magnitude B, which tunes its transition frequency $\omega_q = \mu_B g_S B/\hbar$. As stated in section 5.1.1, a spin 1/2 couples only to oscillating fields perpendicular to $\boldsymbol{B_{dc}}$. The coupling is the modulation of the isotropic electronic Zeeman term by these components.

5.2.2 Sample characterization

All experiments in this chapter used DPPH in powder form, as purchased from Sigma Aldrich (reference D9132), pressed onto a 1 mm wide, 0.2 mm thick pellets. Solvent-free DPPH is known to have at least two different crystal structures usually labeled DPPH-I and DPPH-III. Information on their crystal lattice parameters was reported in 1965 [11, 12], but a full structural determination was not performed until 2010 [9]. The results of X-ray diffraction experiments on these samples, shown in figure 5.10a, suggest that they exhibit the DPPH-III structure (figure 5.10b).

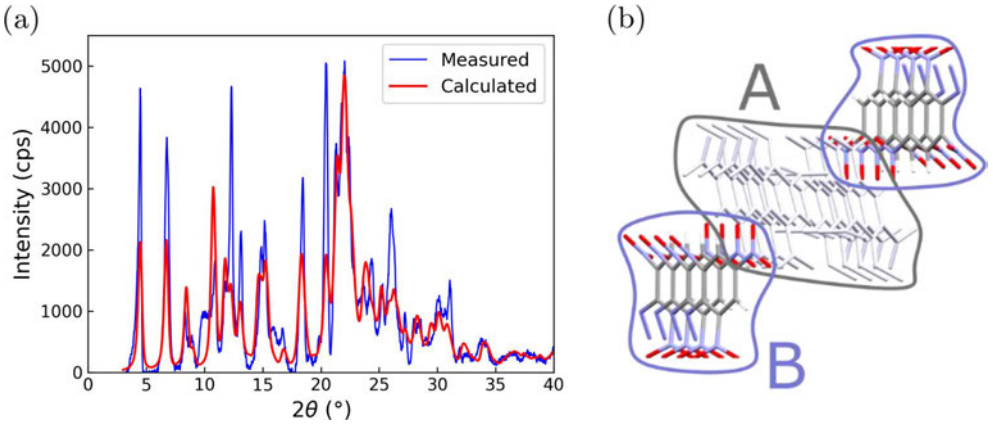

Figure 5.10: (a) X-ray diffraction experiment on our powder samples (blue solid line) and calculated spectrum for DPPH-III (red solid line). (b) Picture of the two subspecies (labeled A and B) present in the structure of the sample (DPPH-III). They are distinguished by the formation of dimers (A) or spin chains (B) at low temperatures.

Information on the magnetic response of DPPH was obtained by a combination of magnetic, heat capacity and magnetic resonance experiments. In all these, the DPPH pellets were then glued to the sample holder with apiezon N grease in order to improve its thermalization.

Magnetic measurements were performed, between 1.7 K and 300 K, using a commercial SQUID magnetometer. The dc susceptibility χ was measured with a magnetic field $B = 0.1$ T. Magnetization isotherms were also measured at fixed temperatures by varying B from 0 to 5 T. Measurements for temperatures lower than 1.7 K were performed with a home-made micro-Hall magnetometer, based on a high-mobility $2D$ electron gas created at the interface between GaAs and GaInAs semiconducting layers, coupled to a ^{3}He cryostat. A few microns wide DPPH sample was placed close to one of the three Hall crosses patterned onto the device. The net Hall voltage, proportional to the sample

magnetic moment, was recorded between 0.35 K and 5 K with a $B = 0.1$ T magnetic field applied along the plane of the sensor. The bare device signal was measured independently and then subtracted from the experimental data, with the results showing no thermal hysteresis.

The dc-magnetic susceptibility χ and heat capacity c_P of powdered DPPH samples are shown in figures 5.11a and 5.11b. From room temperature down to about 35 K, χ follows a Curie-Weiss law $\chi = C/(T - \theta)$, with C the Curie constant and θ the Weiss temperature, see the inset of figure 5.11a. The constant $C = 0.320 \pm 0.001$ emu K/mol Oe measured in this region is smaller, by a factor $x \equiv C/C_{S=1/2} \cong 0.85$, than $C_{S=1/2} = N_A g_s^2/4k_B = 0.375$ emu K/mol Oe that would be expected for isolated $S = 1/2$ with $g = 2.004$. This suggests that a fraction of DPPH molecules are in their oxidized form, which is diamagnetic ($S = 0$).

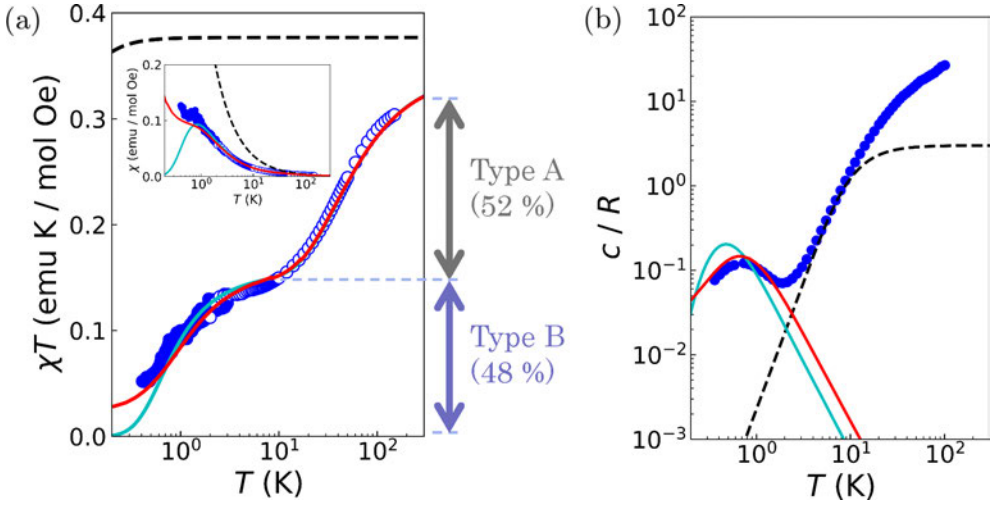

Figure 5.11: (a) Dependence of the χT product (where χ is magnetic susceptibility) of a DPPH powder sample with temperature, measured at $\mu_0 H = 0.1$ T. Hollow blue dots are SQUID measurements, while solid blue dots are Hall voltage measurements. Solid lines consist of the contribution from a model of AF dimers from type A molecules and the contribution from type B molecules. For the latter, the cyan solid line is a model of AF dimers, while the red solid line is a model of AF chains. As a reference, the dashed black line shows the expected χT for a fully paramagnetic DPPH sample. Inset: χ vs. temperature. (b) Temperature dependence of the heat capacity at $\mu_0 H = 0$ T of a powder sample of DPPH (blue dots). The contribution from type B molecules appears at low temperatures. A model of infinite AF chains (red solid line) follows the experimental data much better than the model of AF dimer (cyan solid line). Black dashed line is the Debye model for the lattice heat capacity, with $\theta_D = 47$ K.

The finite negative $\theta = -21$ K reflects the existence of relatively strong antiferromagnetic (AF) interactions. These interactions lead to the drop in the χT product, proportional to the effective magnetic moment squared, which is observed experimentally (figure 5.11a). A quite similar behaviour has been observed in diverse DPPH derivatives [9, 13, 14]. It is associated with the coupling between nearest neighbour molecules, which tend to form AF dimers with an $S = 0$ ground state. In the DPPH-III structure, such spin dimers are formed by DPPH molecules belonging to the A crystal sublattice [9].

This picture agrees also with the results of magnetic resonance experiments. Continuous wave EPR measurements (cw-EPR) were performed with a Bruker Biospin ELEXSYS E-580 spectrometer operating in the X-band (9–10 GHz). A DPPH pellet was glued with vacuum grease onto a diamagnetic holder and introduced in the EPR cavity. The single narrow line measured, shown in figure 5.12a, agrees with a spin $S = 1/2$ and $g = 2.004$. The line intensity I shows a paramagnetic behaviour, with IT behaving very much as χT (see figure 5.12b). The spin resonance line is homogeneously broadened as temperature is decreased from room temperature to 4 K. It is known that, in the paramagnetic phase of DPPH, exchange interactions tend to suppress the inhomogenous broadening associated with dipole-dipole interactions [15] via the exchange narrowing mechanism [16].

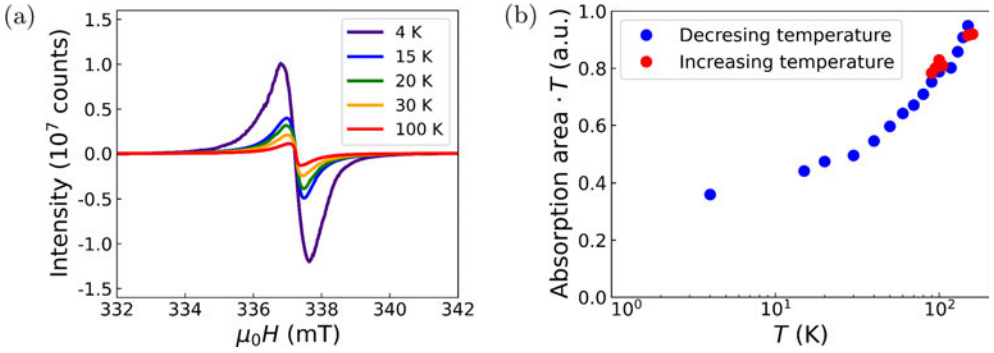

Figure 5.12: (a) cw-EPR of a powder sample of DPPH at 4, 15, 20, 30, 100 K. The complete set of measurements span from 4 K to room temperature. (b) Product of absorption area and temperature. The cw-EPR spectra were initially measured going from room temperature down to 4 K (blue dots), then a few measurements were carried out at high temperatures going back to room temperature (red dots). No hysteresis is observed.

Time-domain EPR measurements of the Free Induction Decay (FID) were carried out at 7.7 K (figure 5.13a) and at room temperature (figure 5.13b). This signal is the decay of the magnetization of the sample after a single excitation pulse, without refocusing. When homogeneous broadening is dominant, there

is no echo signal, and T_m is obtained as the characteristic time constant of the decay of the FID. The fit of the two signals is compatible with a homogeneous broadening $\gamma_\perp/2\pi = 1/2\pi T_\mathrm{m} \cong 4.8$ MHz at 7.7 K and 4.3 MHz at room temperature, which correspond to decoherence times $T_\mathrm{m} = 33.5$ ns and 37 ns respectively.

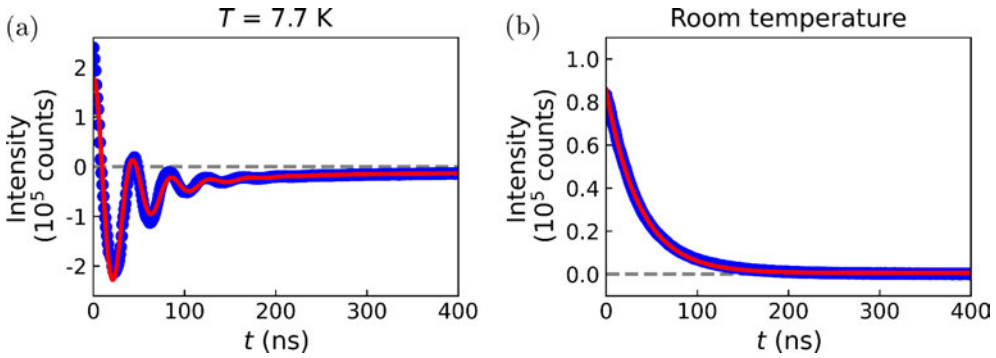

Figure 5.13: FID signal of a DPPH powder sample measured at 7.7 K (a) and at room temperature (b). Experimental data (blue dots) is fitted with an oscillating decay with two decay rates (bi-exponential). I assign the faster rate with T_m, yielding $T_\mathrm{m} = 33.5$ ns at 7.7 K and 37 ns at room temperature.

Below 10 K, χT shows a second drop, as seen in figure 5.11a. In this temperature region, χ follows also a Curie-Weiss law, but with a smaller C and a much smaller $\theta = -0.65$ K. This behaviour probably reflects the weaker interactions between spins in sublattice B of DPPH-III. The response remains paramagnetic down to very low-T, with no clear indication of a phase transition. It is consistent with the formation of either AF dimers or low dimensional (1D) antiferromagnetic chains.

In order to decide between these two alternatives, the specific heat of the samples was measured with a commercial physical properties measurement platform that uses the relaxation method [17]. The temperature was varied between 0.35 K and 200 K and magnetic fields between 0 and 2 T were applied parallel to the sample plane. Above 2 K, specific heat data measured at zero field (figure 5.11b) are dominated by a large contribution arising from lattice and molecular vibrations. At lower temperatures, an additional contribution shows up, which depends on magnetic field as shown in figure 5.14. Therefore, it reflects spin excitations. The broad shape of this anomaly confirms that no phase transition to long-range magnetic order takes place in this temperature region. The data agree well with predictions for the specific heat of infinite AF chains at zero magnetic field [18] and seem to rule out the formation of dimers within the B sublattice of DPPH.

Figure 5.14 shows the temperature dependence of the heat capacity at increasing magnetic fields. Without an extension of the model of infinite AF chains to include an applied magnetic field, the measured heat capacity was tentatively described with a model of finite AF chains. At low fields, this model fits the measured heat capacity, while the paramagnetic theory fails. Conversely, for $\mu_0 H > 1$ T the paramagnetic theory is a good description of the system: magnetic order is broken by the application of a strong enough magnetic field. At intermediate fields ($\mu_0 H = 1$ T), a model of finite AF chains is not enough to describe the measured heat capacity.

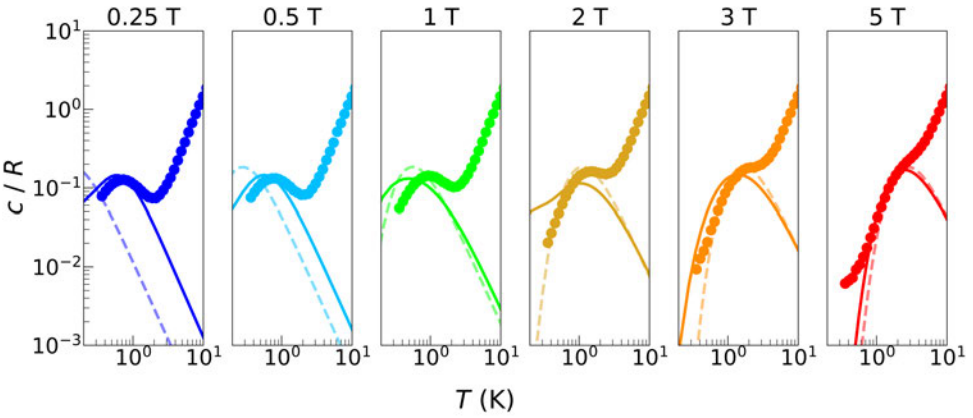

Figure 5.14: Molar specific heat of a powder DPPH sample measured at 0.25, 0.5, 1, 2, 3 and 5 T. The experimental results (dots) are compared with a theory of AF chains (solid lines) and the paramagnetic theory for spin 1/2 (dashed lines).

The above interpretation is also compatible with the magnetic susceptibility data. The dc susceptibility of finite chains of N $S = 1/2$ spins coupled by a Heisenberg AF coupling was calculated. Figure 5.11a shows how the experimental χT can be described by the combination of two contributions: one arising from AF dimers of A-type DPPH molecules and another one resulting from AF chains formed within the B sub-lattice. The reason why the low-T χ can be accounted for with a model that considers small-N chains is that the contribution per spin to the total susceptibility tends to vanish as $N \to \infty$. The uncompensated spins in odd-N chains are responsible for the incomplete cancellation of χT as $T \to 0$. The origin of finite size chains can be associated with the presence of about 15 % of diamagnetic DPPH molecules, which are randomly distributed over the crystal lattice.

Finally, for completeness, figure 5.15a shows the magnetization isotherms that were measured in the same experiment as the dc-magnetic susceptibility from figure 5.11a. The magnetization of each spin 1/2 is expected to saturate to μ_B at high fields. However, as discussed in the measurement of χT, $\sim 15\%$

of the sample is already diamagnetic at high temperatures, and at 10 K the A-type DPPH molecules have already formed diamagnetic dimers. Normalizing by the total number of molecules in the sample, a lower saturation value for the magnetization is obtained. The remaining contribution from B-type DPPH molecules is fitted with a scaled paramagnetic theory for spins 1/2. At the lower measured temperatures (0.5, 1 and 2 K) and low fields, this theory fails due to the onset of antiferromagnetic interactions in lattice B, which oppose the onset of magnetization due to the applied magnetic field see (5.15b).

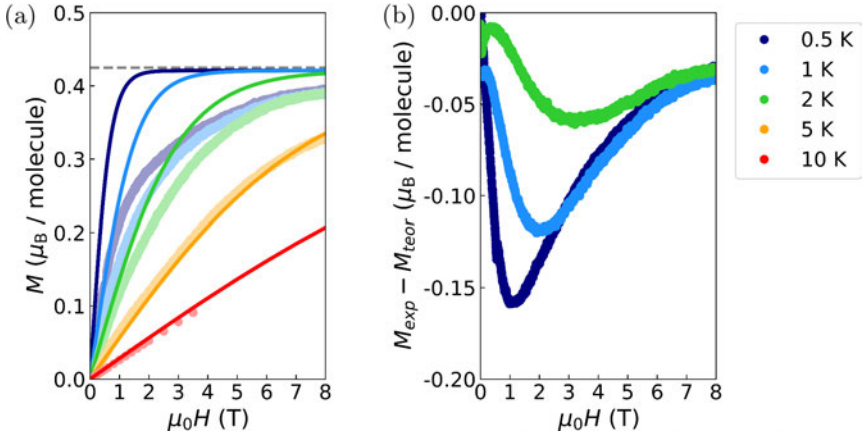

Figure 5.15: (a) Field-dependent magnetization isotherms of a DPPH powder sample measured at 0.5, 1, 2, 5 and 10 K (dots), in units of Bohr magnetons (μ_B) per molecule. The dashed line is the saturation value of the magnetization per molecule taking into account that a 15% of the sample is diamagnetic. Solid lines are the paramagnetic theory of a spin 1/2. (b) Difference between measured magnetization and the predicted magnetization with the paramagnetic theory of a spin 1/2 at 0.5, 1 and 2 K.

5.3 Coupling of DPPH to LERs in *Test 1*

5.3.1 Effect of the resonator geometry and orientation on its visibility

The transmission experiments to study the coupling of DPPH samples to LERs were carried out at 4.2 K. At this temperature, A-type DPPH molecules have formed AF dimers, but B-type DPPH molecules still remain paramagnetic. However, LERs in *Test 1* were only characterized at 17 mK right after fabrication. Figure 5.16 shows the transmission of these resonators at 4.2 K. Only the resonances of LERs 1 to 6 were detected at zero magnetic field, which were fitted with equation (5.1). The fitting parameters are listed in table 5.4.

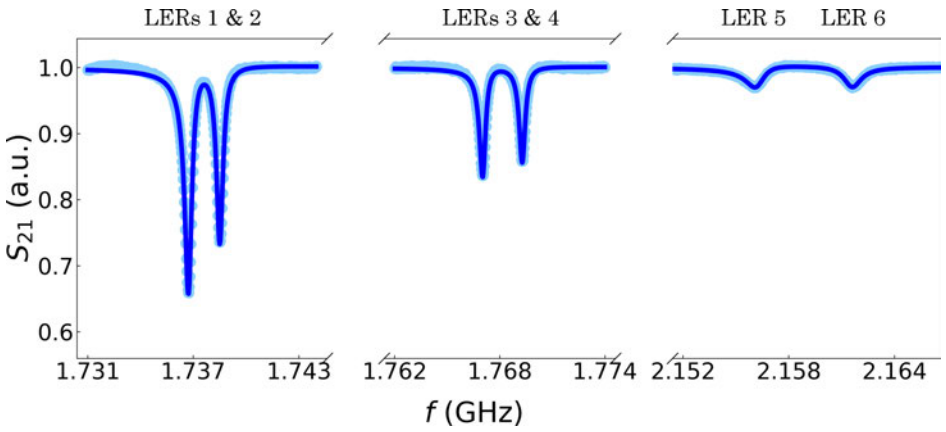

Figure 5.16: Transmission (light blue dots) of the lumped-element resonators in chip *Test 1* at 4.2 K and zero magnetic field. The solid blue line shows the fit of the resonances of LERs 1 to 6, ordered in increasing resonance frequency.

LER	$\omega_r/2\pi$ (GHz)	$\kappa/2\pi$ (kHz)	$\lvert\kappa_c\rvert/2\pi$ (kHz)	ϕ_c (°)
1	$1.736763 \pm 2 \cdot 10^{-6}$	273.2 ± 1.9	93.7 ± 0.8	9.6 ± 0.3
2	$1.738524 \pm 2 \cdot 10^{-6}$	243.0 ± 2.2	65.3 ± 0.7	1.1 ± 0.4
3	$1.767044 \pm 2 \cdot 10^{-6}$	219.15 ± 1.98	36.3 ± 0.4	9.4 ± 0.4
4	$1.769291 \pm 2 \cdot 10^{-6}$	214.7 ± 2.2	31.2 ± 0.4	2.6 ± 0.4
5	$2.156230 \pm 6 \cdot 10^{-6}$	636.8 ± 5.5	20.3 ± 0.2	26.4 ± 0.4
6	$2.161580 \pm 6 \cdot 10^{-6}$	608.7 ± 5.6	18.9 ± 0.2	-6.6 ± 0.4

Table 5.4: Parameters from the fit of the transmission of the lumped-element resonators in chip *Test 1* at 4.2 K and zero magnetic field.

The resonances are shifted to lower frequencies by $\sim$ 14 MHz as the temperature increases from 17 mK to 4.2 K. They are also broadened, with κ increasing by one order of magnitude with respect to to its value at 17 mK in every resonator. These are the same features observed in the temperature dependence of the resonances in *Test 2* (see section 5.1.3). It is not surprising then that the resonances of LERs 7 to 12 in *Test 1* at 4.2 K may be too weak to be detected: their visibility at 17 mK was already much smaller than that of their counterparts in *Test 2*, and now they are further broadened by temperature.

Note that LERs 7 to 12 are rotated 90° with respect to LERs 1 to 6 in *Test 1* (see figure 5.1), with only capacitive line-resonator coupling. This suggests that this kind of coupling alone is not enough to measure the resonators far from the millikelvin regime (4.2 K, in this case). For that reason, *Test 2* was designed with only two rotated LERs (7 and 8), both of them with inductive resonator-line coupling.

5.3.2 Strong coupling of a DPPH ensemble to a LER

LERs 1 to 6 can be grouped in three pairs with similar frequencies: LERs 1 and 2, LERs 3 and 4, and LERs 5 and 6. They all share a similar design (type (a) resonators in figure 5.2). In this section I present the transmission of one LER of each pair coupled to the same DPPH sample, which was moved from one resonator to the next between experiments (see figure 5.17).

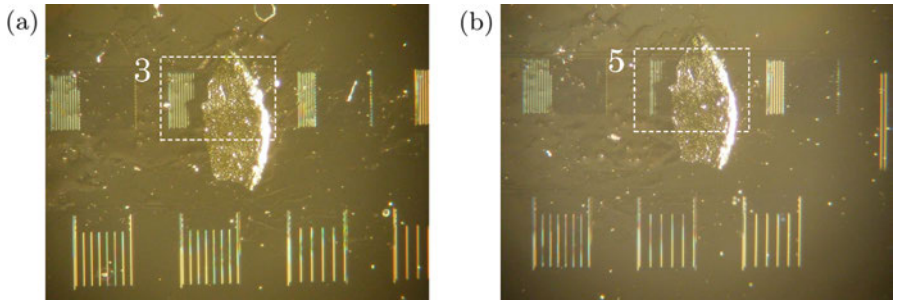

Figure 5.17: Photo of the same sample of DPPH powder (a) on top of the inductor LER 3 and then (b) placed on top of the inductor of LER 5.

The sample is a DPPH powder pellet with a thickness of ∼100 μm and an area (∼ 1 mm^2) slightly larger than the size of the resonators, covering the whole inductor. This large sample can be easily handled and moved between LERs. With a molecular density of $\sim 2 \times 10^{27}$ molecules/m^3 for DPPH-III [19], there are or the order of $N \sim 10^{17}$ spins in this sample. The sample was initially placed on top of LER 1 with Paratone oil.

Figure 5.18a shows the hybrid spins-LER system resonance around the resonator frequency ω_r of LER 1 for different magnetic fields. The coupling between the sample spins and the resonator mode becomes apparent when the field-dependent transition frequency of a spin 1/2, $\omega_q = \mu_B g_S B/\hbar$, is close to ω_r. The spin-photon resonance field B_{res} is defined by the condition $\omega_r = \omega_q = \mu_B g_S B_{res}/\hbar$. The experiment is modeled as the transmission (S_{21}) of a resonator coupled to an ensemble of non-interacting spins. This is described in equation (4.102) from chapter 4, which is reproduced here for clarity:

$$S_{21}(\omega_d) = 1 - \frac{\kappa_c}{i(\omega_r - \omega_d) + \kappa + \dfrac{G_N^2 \Delta P}{i(\omega_q - \omega_d) + \gamma_\perp}}. \tag{5.5}$$

Apart from the previously characterized LER parameters (ω_r, κ, and κ_c), equation (5.18) depends on the spin transition frequency, ω_q, the decoherence rate of the spin ensemble, $\gamma_\perp$, and the temperature dependent collective spin-photon $G_N(T) \propto \sqrt{\Delta P}$, where ΔP is the population difference between the

spin down and spin up states at temperature T. In the experiment, S_{21} is measured for different regular input frequencies $f = \omega_d/2\pi$ and magnetic fields B (tuning ω_q). LER parameters resulting from the least-squares fit are listed in table A.2 in Appendix A. The g-factor g_S and the coupling G_N for $\gamma_\perp = 6.5 \pm 0.5$ MHz are reported in table 5.5. This value of $\gamma_\perp$ is consistent with previous reported values for DPPH pellets coupled to superconducting resonators [20, Ch.7].

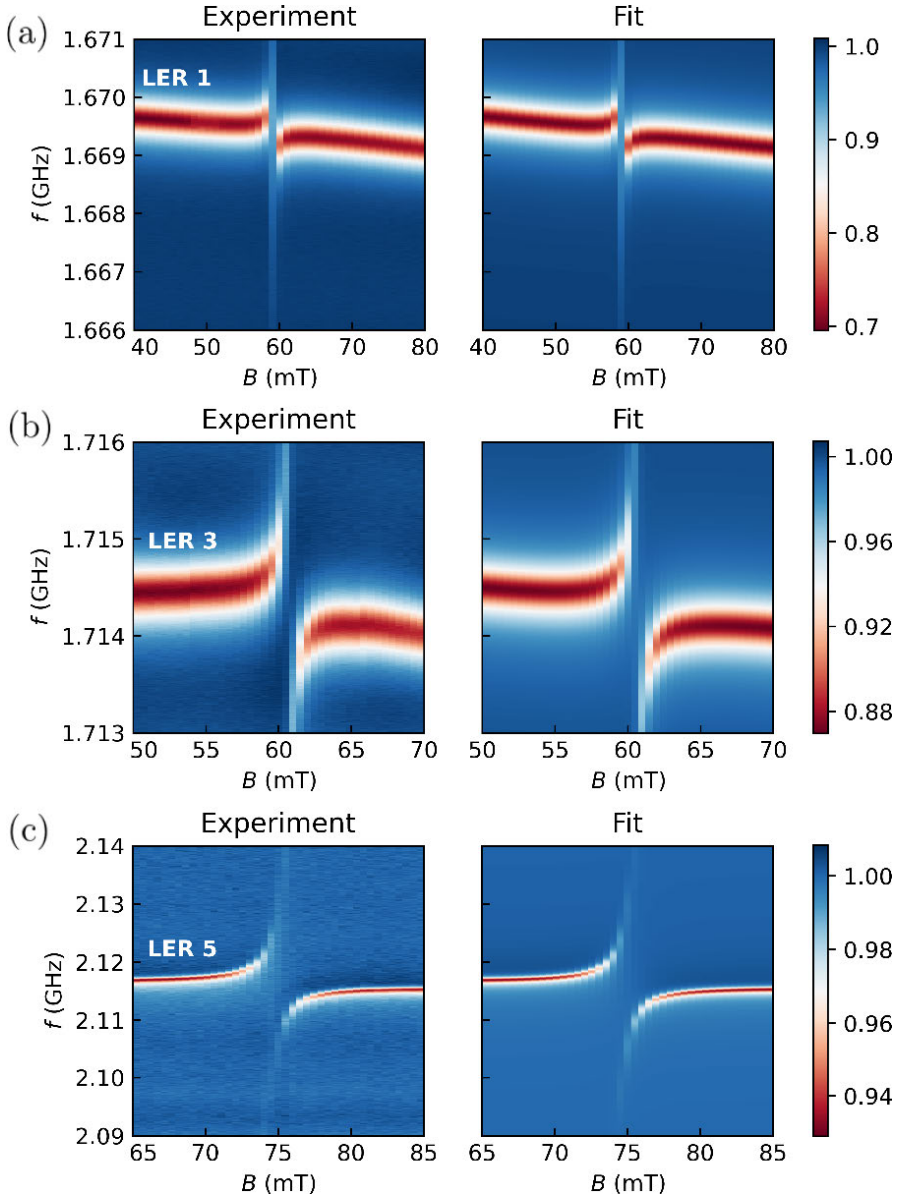

Figure 5.18: Transmission of *Test 1* LERs 1 (a), 3 (b) 5 (c) coupled to the same DPPH powder sample (see figure 5.17).

LER	g_S	G_N (MHz)	$G_N/\gamma_\perp$	C
1	$2.02058 \pm 5 \cdot 10^{-5}$	2.586 ± 0.003	0.40 ± 0.03	4.0 ± 0.3
3	$2.01953 \pm 5 \cdot 10^{-5}$	3.758 ± 0.003	0.58 ± 0.04	10.6 ± 0.8
5	$2.01928 \pm 4 \cdot 10^{-5}$	12.491 ± 0.004	1.9 ± 0.1	57.9 ± 4.5

Table 5.5: Parameters from the fit of the magnetic field dependent resonances of LERs 1, 3 and 5 in chip *Test 1* at $T = 4.2$ K shown in Fig. 5.18. The same DPPH was coupled to each of the three resonators. G_N is the collective spin-photon coupling defined by equation (4.103), measured at 4.2 K. The cooperativity is defined as $C = G_N^2/\gamma_\perp\kappa$ (see section 4.6.4).

The same sample was moved to LERs 3 and 5 (see figure 5.17), and transmission experiments were carried out the same way around their corresponding ω_r and B_{res} (figures 5.18b and 5.18c). These experiments were fitted with equation (5.5), see table A.2 in Appendix A and table 5.5. All measurements were fitted with the same decoherence rate $\gamma_\perp$, which is intrinsic to the sample.

The collective spin-photon coupling of LER 5 reaches both strong coupling and high cooperativity regimes, defined by $G_N/\gamma_\perp > 1$ and $C = G_N^2/\gamma_\perp\kappa > 1$ respectively. The strong spin-resonator coupling of LER 5, together with the high coupling of the resonator to the readout line, enables the detection of two transmission dips in resonance ($B = B_{\text{res}}$). Figure 5.19 shows these two dips at the measured field closest to the resonance field.

In LERs 1 and 3 the collective spin-photon coupling is nearly high enough to achieve the strong collective coupling regime, with $G_N/\gamma_\perp$ close to one. It is high enough to achieve the high cooperativity regime. High cooperativity is achieved, with $C = G_N^2/\gamma_\perp\kappa = 4$ and 10.6 respectively. A single broadened dip in transmission is observed, as $G_N/\gamma_\perp < 1/\sqrt{2}$ (see figure 4.5 in chapter 4). Both LERs have an inductor design similar to that LER 5,[1] so one could expect for them similar collective spin-photon couplings G_N. Instead, the G_N of LER 5 is significantly higher.

A possible explanation for the different G_N value observed for LERs 1, 3 and 5 could be associated to the magnitude of the microwave field, rather than with the its distribution (which depends only the inductor design). This field which scales with the square root of the resonance frequency ω_r [4, App.]. However, this effect alone cannot explain the change in G_N. Let us take the resonators with highest (LER 5) and lowest (LER 1) spin-resonator coupling. The effect of their different resonance frequencies accounts for an increase by a factor 1.13 in G_N from LER 1 to LER 5. Instead, what an increase by a

[1] Figure 5.4 shows the field distribution for LER 1 in chip *Test 2*. The design of this resonator is similar to the design of the resonators that are being discussed here (LERs 1 to 6 in chip *Test 1*).

factor 4.83 is measured. Therefore, other effects may be more relevant to G_N than its dependency on ω_r.

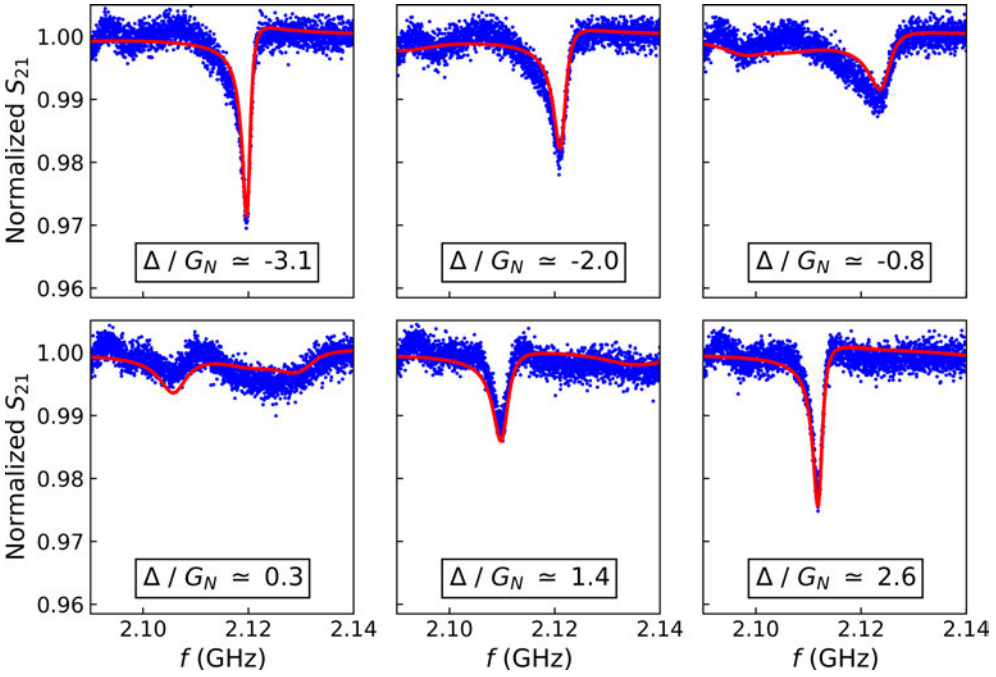

Figure 5.19: Transmission of *Test 1* LER 5 coupled to a DPPH sample for three different detunings $\Delta = \omega_q - \omega_r$ (blue dots). Δ is given in units of the collective coupling G_N. The theoretical transmission with the fit parameters from table A.2 in Appendix A and table 5.5 is also shown (red solid lines). The ensemble-resonator coupling of LER 5 is high enough to be in the strong coupling regime. Two peaks can be seen in the transmission for $|\Delta/G_N| < 1$. These two peaks look slightly different because $\Delta \neq 0$.

In this experimental setup, the position of the sample has a large effect on the coupling: it determines which volume of the inhomogeneous magnetic field generated by the resonator is actually filled with spins. The reason for this is that the intensity of the microwave field decays very rapidly as the sample moves away from the surface (see figure 5.4) [3]. Any irregularities in the sample, as well as the layer of oil that is needed to stick the samples to the surface of the chip, create a gap of the order of a few micrometres at the sample-chip interface [21]. In these measurements, the rapid increase in the coupling suggests that the gap was closing as the sample was moved from the first resonator (LER 1) to the last one (LER 5), see figure 5.20. This can explained as the sample leaving part of the oil layer between sample and surface as it is moved from one resonator to the next. Still, there is a non-negligible gap in LER 5 that might be due to irregularities in the sample surface.

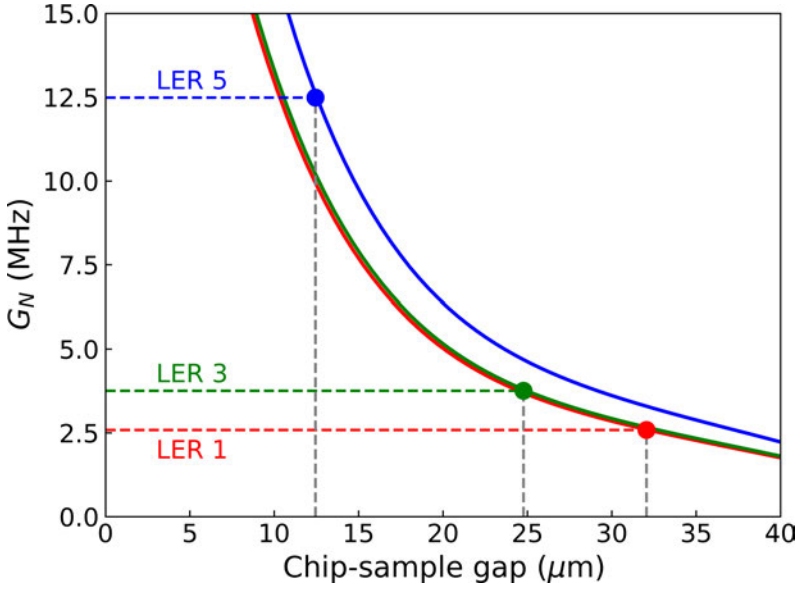

Figure 5.20: Simulation of the coupling of the magnetic field generated by the inductor of resonators 1, 3 and 5 to a sample of DPPH as a function of the sample-resonator gap (solid lines). A comparison with the experimental G_N (horizontal dashed lines) gives an estimation of the gap in each LER (vertical dashed lines). The gap decrease as the sample was moved from LER 1 to 3 and then to 5 as part of the oil layer between sample and chip surface remains attached to the chip surface.

5.3.3 Effect of the magnetic field orientation

Three different DPPH samples were deposited on LERs 7, 8 and 9. Only one of the six missing resonators (7 to 12) was identified, most probably LER 7 (labeled LER 7 from here onwards), through its coupling to the DPPH sample (see figure 5.21, largest sample is on top of LER 7). The resonator had a very small coupling κ_c to the transmission line compared to its total losses κ, which explains why its visibility was so low at $T \sim 4.2$ K.

The design of LER 7 is rotated 90° with respect to the design of LERs 1 to 6. The microwave magnetic field generated by its indcutor has then some components parallel to the readout transmission line (the chip axis). Therefore, the geometry that was used to measure the spin-photon coupling in the case of LERs 1, 3 and 5, with the magnetic field applied along the chip axis, might not be ideal. For this reason, the resonance of LER 7 was measured with magnetic fields applied at various angles θ from the chip axis The results are shown in figures 5.22 and 5.23. The parameters obtained from the fit of these measurements with equation (5.5) are given in table 5.6).

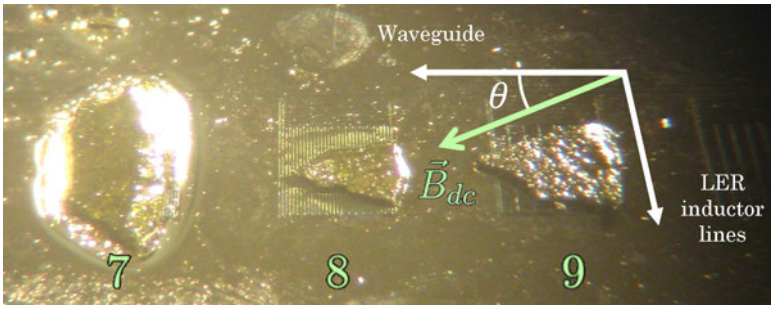

Figure 5.21: Photo of three DPPH powder samples on top of LERs 7 (hidden behind the largest sample), 8 and 9. Only one resonance was measured (attributed to LER 7 or 8, based on their expected resonance frequency). From the large ensemble coupling it can be assumed that it belongs to LER 7, which hosts the largest sample. The other two resonances are difficult to measure due to the combination of low resonator-line coupling (like LER 7) and low ensemble-resonator coupling (smaller samples). The direct spin ensemble to transmission line coupling observed for low θ values comes from the large sample located on LER 7, which covers part of the transmission line.

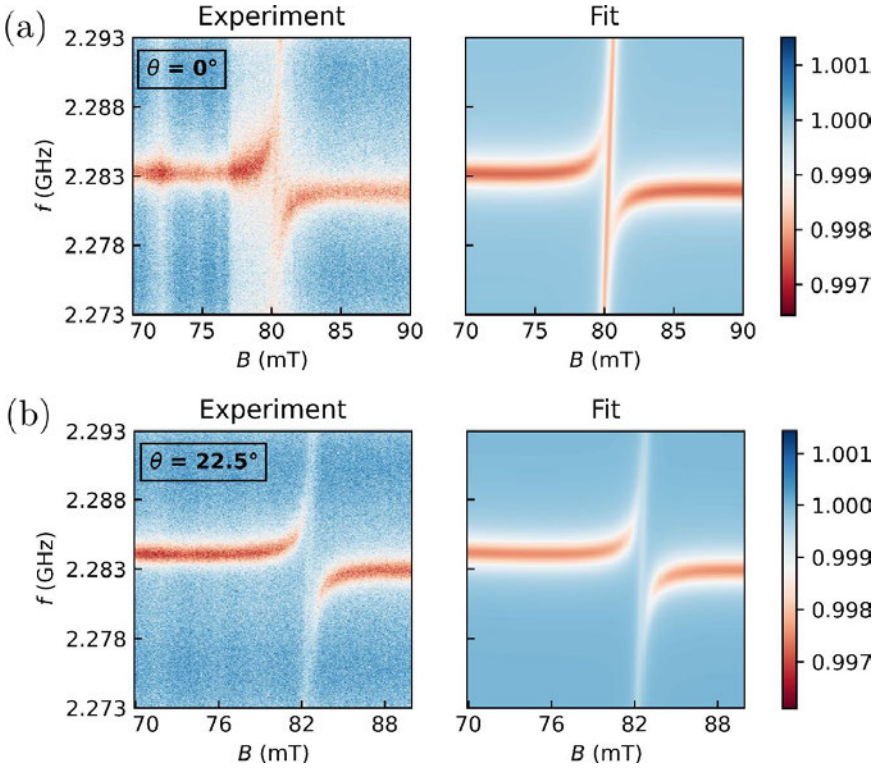

Figure 5.22: Transmission of LER 7 of chip *Test 1* coupled to a DPPH sample when the magnetic field is applied (a) parallel to the transmission line of the chip or (b) at an angle of 22.5° from the transmission line. See table 5.6 for the fit parameters.

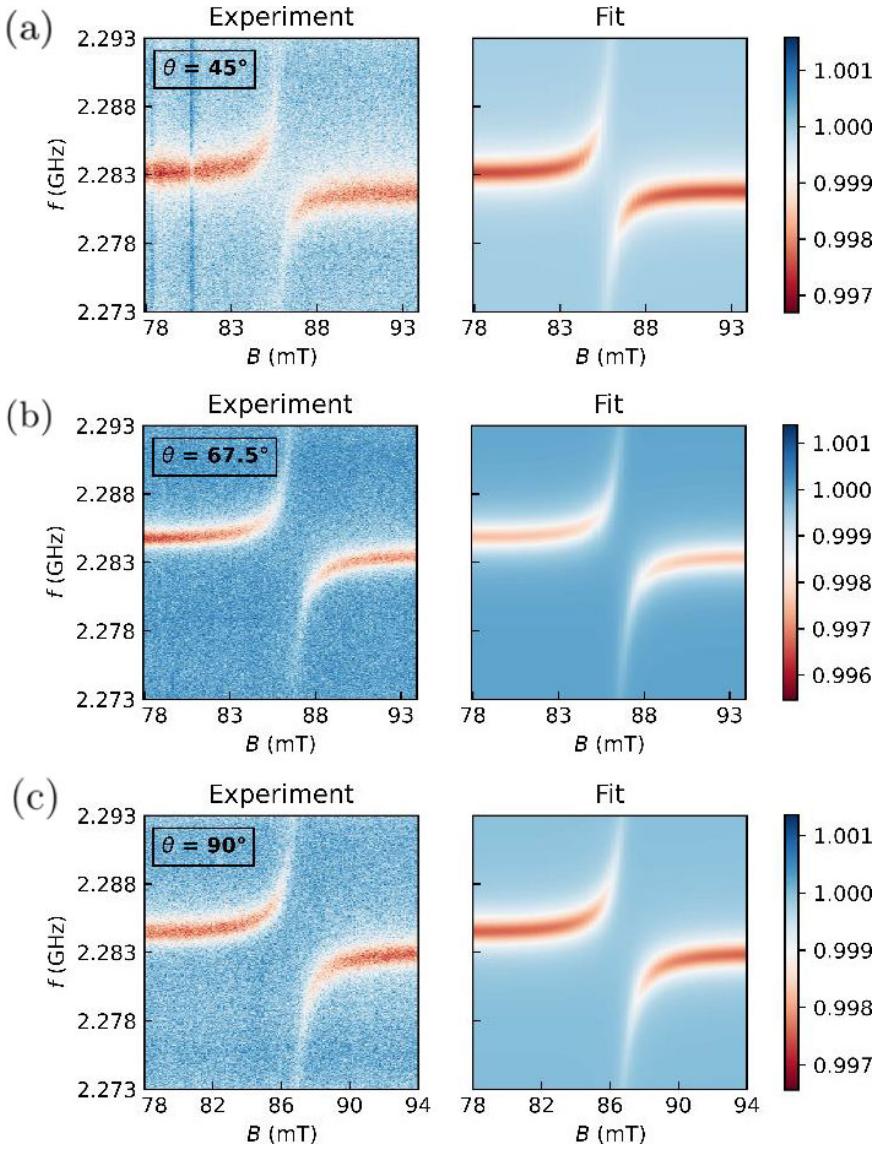

Figure 5.23: Transmission of LER 7 of chip *Test 1* coupled to a DPPH sample when the magnetic field is applied at an angle of (a) 45°, (b) 67.5° or (c) 90.0° from the transmission line. See table 5.6 for the fit parameters.

The ensemble-resonator coupling is in the strong regime ($G_N > \gamma_\perp$). G_N increases as the magnetic field is rotated from $\theta = 0°$, when it is parallel to the transmission line, to $\theta = 90°$, when it is parallel to the resonator inductor lines. The microwave magnetic field generated by the inductor lines lies mainly in the plane perpendicular to them (see figure 5.4), and only the components of this oscillating field perpendicular to the static field contribute to the coupling. The maximum coupling is obtained then for $\theta = 90°$. At $\theta = 0°$, when part of the

microwave magnetic field is parallel to the static magnetic field, the ensemble-resonator coupling line is lower. It is still non-zero thanks to the microwave field component perpendicular to the surface of the chip. A sufficiently large sample covers enough of the resonator field volume so that the in-plane and out-plane components of the microwave field contribute equally to the coupling. From the definition of the ensemble-resonator coupling (equation (3.44) in chapter 3), losing half of the contributions when the in-plane componenents are parallel to static magnetic field should give rise to decrease of G_N to $1/\sqrt{2}$ (∼70%) of its maximum. This agrees very well with our observations (see figure 5.24). This effect was also observed with DPPH pellets on coplanar resonators [20, Ch.7].

θ (°)	g-factor	G_N (MHz)	$G_N/\gamma_\perp$	C
0.0	$2.03001 \pm 2 \cdot 10^{-5}$	7.53 ± 0.01	1.032 ± 0.004	8.87 ± 0.04
22.5	$1.97559 \pm 7 \cdot 10^{-5}$	7.43 ± 0.01	1.017 ± 0.004	8.62 ± 0.04
45.0	$1.90015 \pm 7 \cdot 10^{-5}$	8.47 ± 0.01	1.160 ± 0.004	11.21 ± 0.05
67.5	$1.88166 \pm 6 \cdot 10^{-5}$	9.19 ± 0.01	1.259 ± 0.005	13.2 ± 0.1
90.0	$1.87924 \pm 6 \cdot 10^{-5}$	10.15 ± 0.01	1.39 ± 0.01	16.1 ± 0.1

Table 5.6: Parameters from the fit of the transmission of LER 7 in chip *Test 1* at different orientations of the magnetic field. All experiments were fitted with the same ensemble decoherence rate $\gamma_\perp = 7.30 \pm 0.03$ MHz, and the same resonator parameters except the resonance frequency ω_r: $\kappa/2\pi = 876.22 \pm 0.96$ kHz, $|\kappa_c|/2\pi = 2.175 \pm 0.003$ kHz and $\phi_c = (-4.05 \pm 0.05)°$. The average fitted resonance frequency is $\omega_r/2\pi = 2.2838 \pm 7 \cdot 10^{-4}$ GHz.

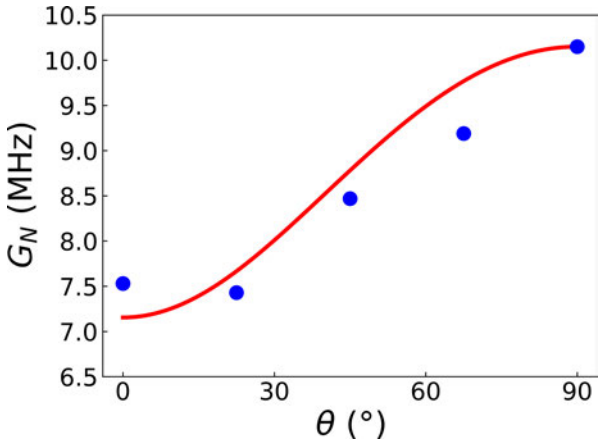

Figure 5.24: Collective spin-photon coupling between LER 7 and the DPPH sample as a function of the angle θ that the static magnetic field $\boldsymbol{B_{dc}}$ makes with the transmission line (see figure 5.21). Blue dots mark the values obtained from the fit of the experiments. Red solid lines are the estimated coupling from the simulation of the microwave magnetic field generated by the resonator.

At $\theta = 0°$ and $\theta = 22.5°$, the contribution from spins in the ensemble that are directly coupled transmission line can be also seen clearly. Figure ?? shows how subtracting the fit of the ensemble-resonator coupling from the experimental data leaves the absorption signal of DPPH coupled the transmission line. The ensemble-line coupling is maximum for $\theta = 0°$, as the transmission line is perpendicular to the inductor lines of LER 7. From the simulation of the field generated by the waveguide, the same dependence with θ as in the case of the resonator was expected, only switching the roles of the orientations defined by $\theta = 0°$ and $\theta = 90°$. Instead, the line-resonator coupling vanished quickly for $\theta > 0°$ (see figure 5.26).

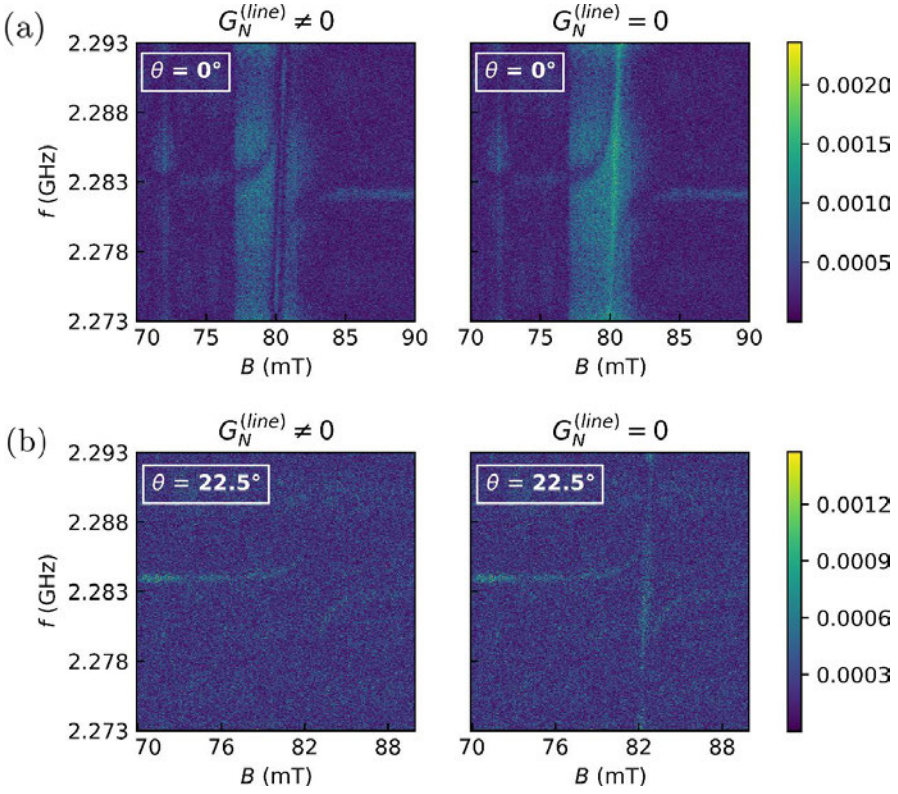

Figure 5.25: Absolute value of the difference between experimental transmission and its fit with the model, for $G_N^{(line)} \neq 0$ and $G_N^{(line)} = 0$. The two angles θ with higher $G_N^{(line)}$ are compared: (a) $\theta = 0°$ and (b) $\theta = 22.5°$. Subtracting the transmission of the fitted model with $G_N^{(line)} = 0$ removes only the transmission of the coupled resonator and leaves the transmission of the line coupled to the ensemble.

A tentative explanation to this unexpectedly drastic angular dependence of the ensemble-line coupling is the competition between the coupling rates of spins to the resonator field and the line field. Where the line field is higher, the direct coupling of the spins to the input signal through the line is observed.

However, if the resonator field is higher, then the hybrid spin-resonator system is measured (as an ensemble-resonator system). The line field is in general much weaker than the resonator field, and it is only stronger in the part of the sample that sits just on top of the central line of the waveguide. In this region, there is only an in-plane oscillating magnetic field perpendicular to the line. The out-of-plane component does not contribute to the coupling, which explains the vanishing of the coupling when the static field is aligned with the in-plane component.

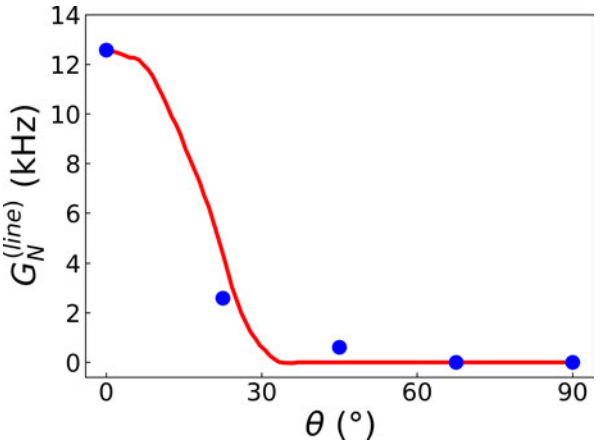

Figure 5.26: Collective spin-photon coupling of the DPPH sample to the transmission line as a function of the angle θ that the static magnetic field $\boldsymbol{B_{dc}}$ makes with the transmission line (see figure 5.21). Blue dots mark the values obtained from the fit of the experiments. Red solid lines are the estimated coupling from the simulation of the microwave magnetic field generated by the transmission line. A lower bound was imposed to the microwave magnetic field of the line that contributes to the coupling. This is a simple model for the suppression of the ensemble-line coupling where the resonator field is higher than the line field.

There is another effect that the orientation of the static magnetic field has on the transmission: at each θ, the resonance field B_{res} is different. The drift in B_{res} is shown in figure 5.27 by plotting the effective g-value at each angle θ. The change in the resonator characteristic frequency between different angles is not more than 0.1%, thus not enough to account for the dispersion of 7% in the effective g-factor. This is unexpected, as the effect of anisotropy in the g-tensor of free-radical electrons is usually very small, and I am using a powder sample. The comparison of the experimental effective g-values with those expected if magnetic anisotropy is introduced (neglecting that the sample is a powder) rules out that the change in the g-values is due to g-tensor anisotropy.

Another possible source of the error is the vector magnet. In particular, I suspect it is a problem of the magnet axis that is used to rotate the static field in

the plane of the chip surface (x-axis in the magnet frame of reference). It is not a current to field conversion error, which would appear as a g-tensor anisotropy. The results from figure 5.27 can be explained with a zero-point error of around 7 mT in the magnet x-axis due to an error in the magnet calibration. This problem has been previously reported in previous experiments with the x-axis of the magnet [20, Ch.7]. These experiments have therefore allowed us to detect it and correct it.

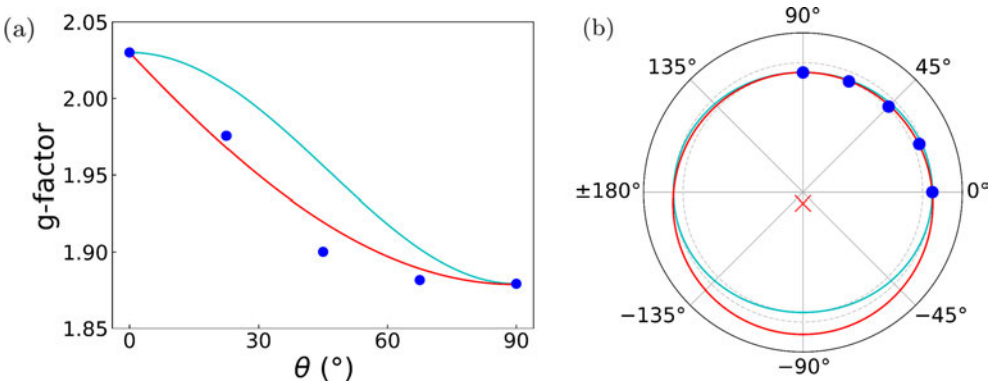

Figure 5.27: (a) g-factor (blue dots) for different angles θ between the static magnetic field $\boldsymbol{B_{dc}}$ and the orientation of the transmission line. Solid lines are the g-factor that would be measured if there was g-tensor anisotropy or if there was a scale error in one of the components of the field generated by the vector magnet (light blue) or a zero-point error in this same field component (red). (b) The same plot in polar coordinates, with the zero-point error as red crosses.

5.4 Coupling of DPPH to LERs in *Test 2*

5.4.1 Testing the bare resonator response with magnetic field

The resonators of chip *Test 2* were measured at 4 K before depositing the DPPH samples. Note that in this chip LERs 7 and 8 are in the same orientation in which their resonances could not be initially detected in *Test 1* (see figure 5.1), but now with the inductor placed closer to the transmission line. This geometry provides a higher coupling of the resonator to the transmission line, improving the visibility of the resonator response. Still, the resonator-line coupling in this configuration is much smaller than that obtained with the longer parts of the inductor lines placed parallel to the transmission lines.

The bare resonator responses were measured for magnetic fields up to 100 mT (see figure 5.28), which are enough to perform the coupling experiments shown below. The effect of high static magnetic fields parallel to the chip surface in the resonances is akin to an increase in temperature (see section

5.1.3) [22]. As the magnetic field increases, the resonances shift towards lower frequencies. Also, the resonances of LERs 7 and 8 broaden with magnetic field, but the line-resonator coupling rate κ_c remains nearly constant. Therefore, the increase in κ is associated with an increase in the internal decay rate κ_i.

5.4.2 Frequency shift by sample deposition

In the first run of experiments with the *Test 2* chip, a DPPH powder sample was placed on top of six of the twelve resonators: LERs 1, 4, 5, 8, 10 and 12, as shown in figure 5.29. The resonance frequencies measured at zero field for all twelve resonators are listed in table A.4 in Appendix, with the relative shift from the resonance frequencies of the bare resonators plotted in figure 5.30. LERs hosting a DPPH sample show larger frequency shifts, enough to swap the order in frequency in each pair of LERs.[2] LERs 4, 8, 10 and 12 show the largest shifts. Figure 5.29 shows that these resonators were deposited with more oil. We therefore assign the shift to the increase in the resonator capacitance as the space between capacitor fingers is filled with the oil (with a relative permittivity $\epsilon_r > 1$).

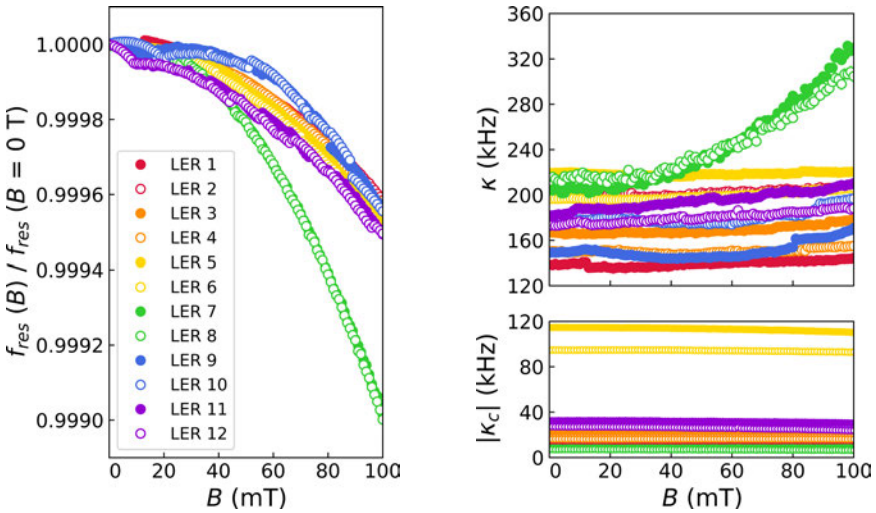

Figure 5.28: (a) Drift with magnetic field of the resonance frequencies of *Test2* LERs. (b) Change with magnetic field of the total decay rate κ and the module of the line-resonator coupling rate κ_c for the same set of resonators.

[2] I know that there is a swap in some pairs because only one resonator of each pair is coupled to an ensemble in the transmission measurements around the resonance field B_{res}.

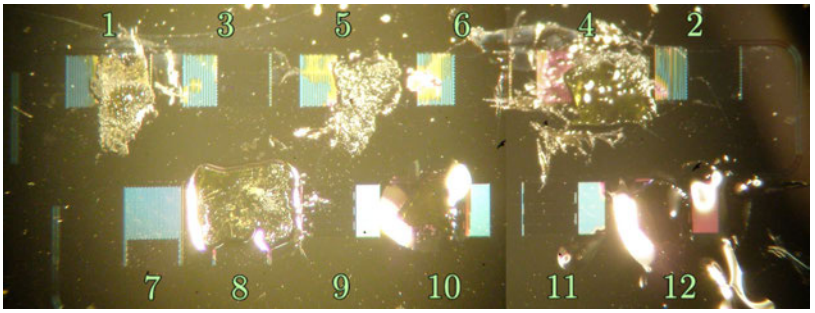

Figure 5.29: Locations of DPPH samples in the first run of experiments with chip *Test 2*. Samples where placed on LERs 1, 4, 5, 8, 10 and 12.

A frequency shift is observed too in the empty resonators, although smaller than in the resonator of each pair that is coupled to a magnetic sample. Part of the resonator capacitance comes from the parasitic capacitance between the whole lumped-element circuit and the ground plane, which can be partially filled by oil from the samples in neighbouring resonators. The shifts of LERs 9 and 11, which sit next to the two resonators with the largest shifts (LERs 10 and 12), are an example of this effect.

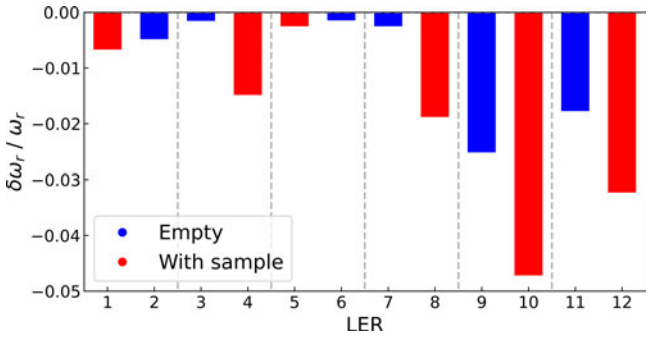

Figure 5.30: Relative shift of the resonance frequency of each LER in chip *Test 2* after the deposition of DPPH samples on LERs 1, 4, 5, 8, 10 and 12 (in red). Shift for the six empty resonators (LERs 2, 3, 6, 7, 9 and 11) in blue.

5.4.3 Spin-photon coupling in chip *Test 2*: coupling to remote resonators and dependence on ω_r

The transmission of *Test 2* was measured near the resonances of LERs 1, 4, 5, 8, 10 and 12 that are coupled to DPPH samples, and also near the resonances of two of the other six resonators that are 'empty' (LERs 2 and 3) for magnetic fields around their respective resonance fields B_{res}. The experimental results and their fits are shown in figures 5.31, 5.32 and 5.33. The fitting parameters are listed in table A.5 in Appendix A and table 5.7.

Chip *Test 2* has pairs of resonators with very close frequencies (a few MHz between their resonance frequencies): LERs 1 and 2, LERs 3 and 4, and so on. The samples were deposited only in one resonator of each pair. This was done as an attempt to detect a coupling of the spin ensemble to the 'empty' resonator through its coupling to the other resonator of the pair. This remote coupling would be mediated by the transmission line. However, this effect could not be detected (no coupling in LERs 2 and 3). This means that the line-mediated coupling between resonators in this setup is too small. Current research on this topic in our research group is focused on improving resonator-resonator coupling by closing in the distance between the capacitors of a pair of resonators.

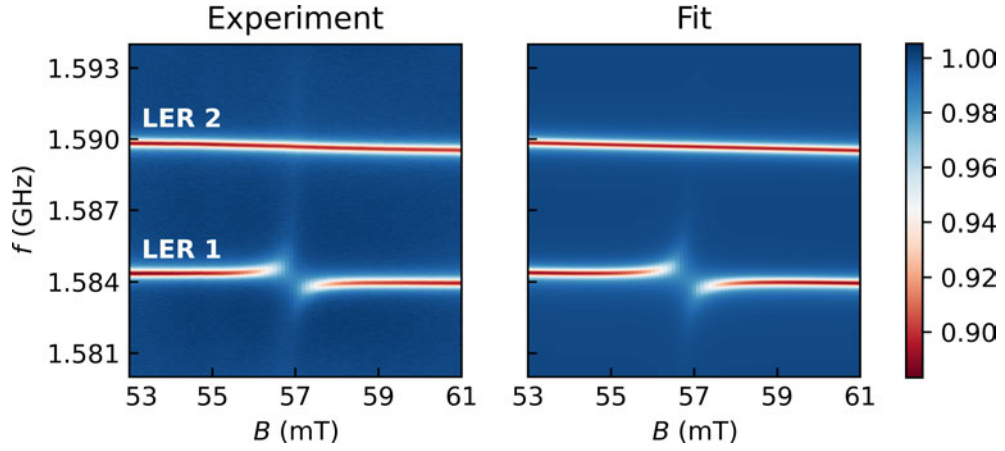

(a)

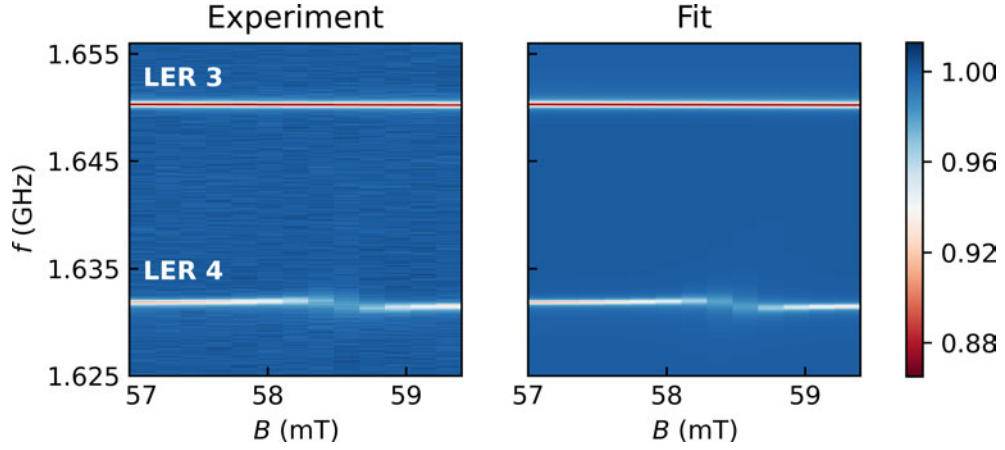

(b)

Figure 5.31: (a) Transmission (absolute value, here and in the figures to follow) of LERs 1 and 2 of chip *Test 2* with a DPPH sample coupled to LER 1. (b) Transmission of LERs 3 and 4 of chip *Test 2* with a DPPH sample coupled to LER 4. See table A.5 in Appendix A and table 5.7 for the fit parameters.

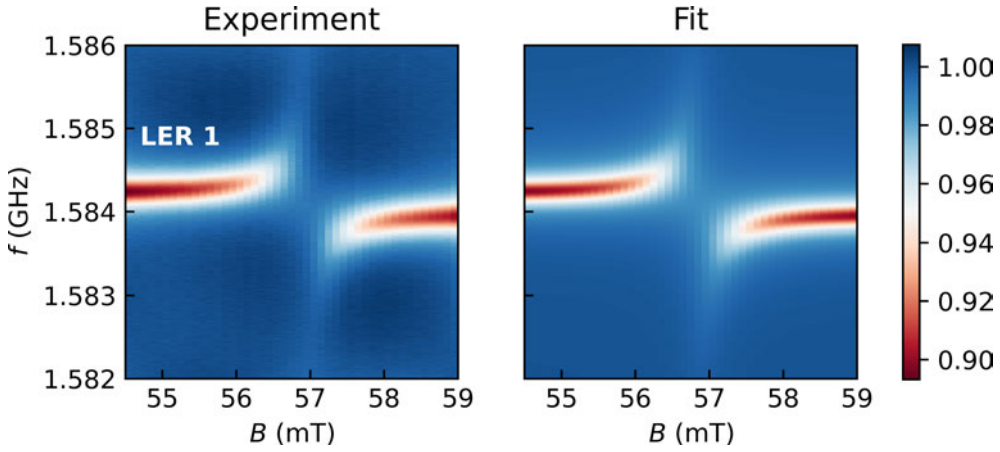

(a)

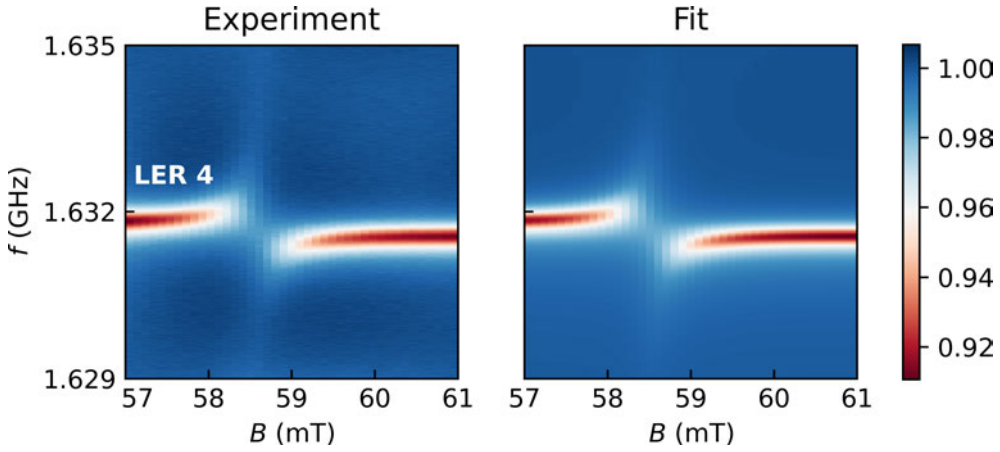

(b)

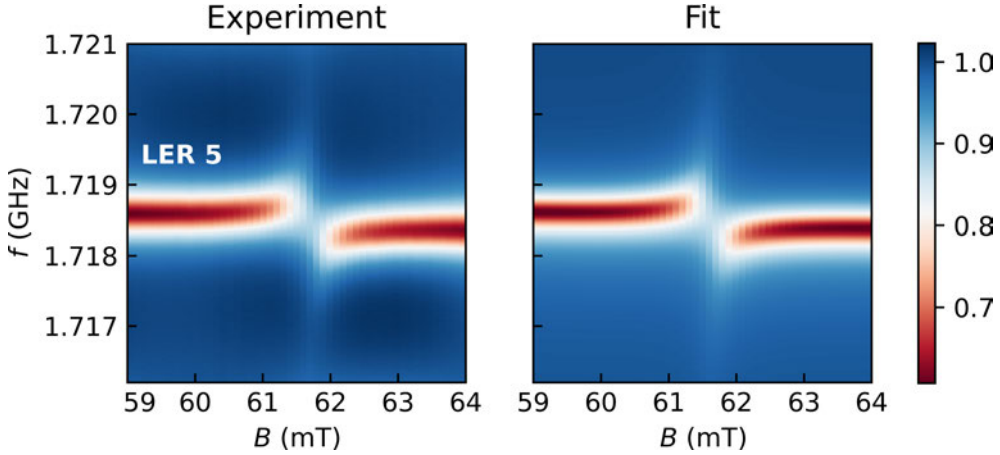

(c)

Figure 5.32: (a) Transmission of LER 1 of chip *Test 2* coupled to a DPPH sample. Below, transmission of (b) LER 4 and (c) LER 5 of the same chip, each coupled to a DPPH sample. See table A.5 in Appendix A and table 5.7 for the fit parameters.

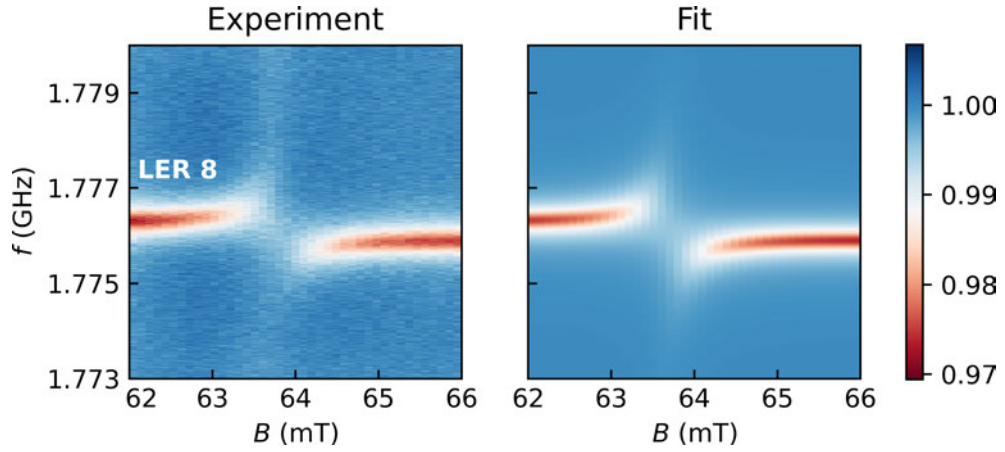

(a)

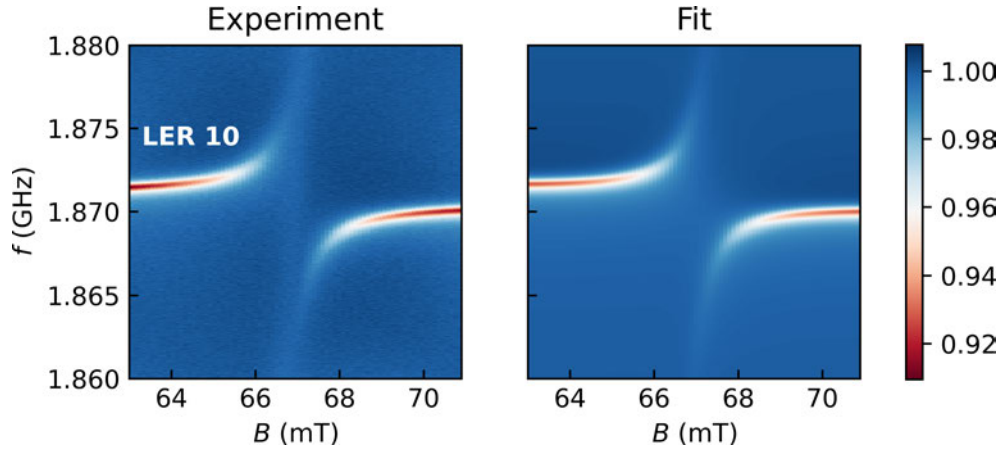

(b)

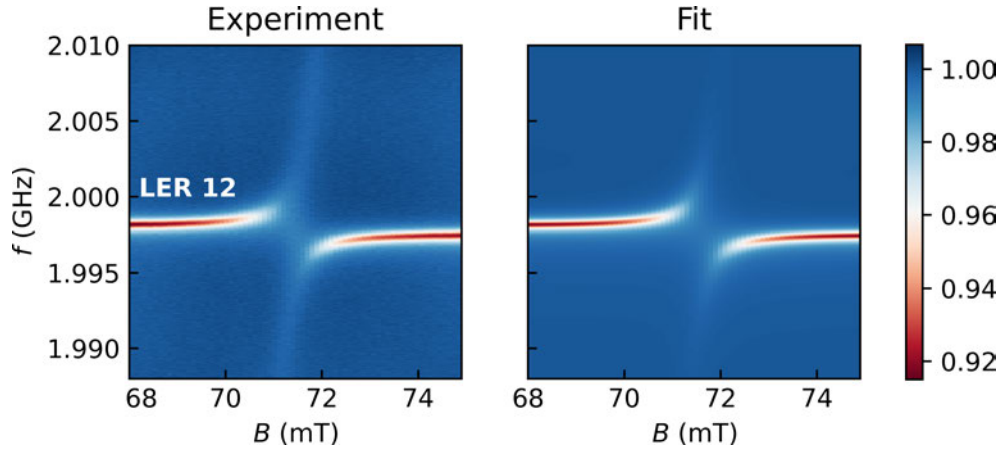

(c)

Figure 5.33: Transmission of (a) LER 8, (b) LER 10 and (c) LER 12 of chip *Test 2*, each coupled to a DPPH sample. See table A.5 in Appendix A and table 5.7 for the fit parameters.

LER	g-factor	G_N (MHz)	$G_N/\gamma_\perp$	C
1	$1.98818 \pm 3 \cdot 10^{-5}$	2.530 ± 0.002	0.35 ± 0.02	6.2 ± 0.3
4	$1.9928 \pm 1 \cdot 10^{-4}$	2.10 ± 0.01	0.29 ± 0.01	4.5 ± 0.2
5	$1.98965 \pm 3 \cdot 10^{-5}$	1.819 ± 0.002	0.25 ± 0.01	2.0 ± 0.1
8	$1.98878 \pm 4 \cdot 10^{-5}$	2.555 ± 0.004	0.35 ± 0.02	4.8 ± 0.2
10	$1.99324 \pm 2 \cdot 10^{-5}$	7.395 ± 0.002	1.0 ± 0.1	29.9 ± 1.5
12	$1.99829 \pm 2 \cdot 10^{-5}$	4.670 ± 0.002	0.64 ± 0.03	13.7 ± 0.7

Table 5.7: Parameters from the fit of the transmission of the lumped-element resonators in chip *Test 2* at 4 K.

All experiments were fitted with the same ensemble decoherence rate $\gamma_\perp = 7.30 \pm 0.03$ MHz. The collective spin-photon coupling is largest for LERs 12 and 10, which lies just in the limit of strong coupling ($G_N = \gamma_\perp$). For these resonators, the spin-photon coupling is enhanced by their larger resonance frequency (see section 5.3.2) and lower inductance. This can be seen with a simple description of the conversion of the energy in the resonator in resonance into the amplitude of its oscillating magnetic field. The energy of the vacuum fluctations of the resonator is $E_0 = \hbar\omega_r/2$, with half of this energy is stored in the inductor in resonance. Then the RMS (root mean square) current in the inductor is $I_{\mathrm{RMS}} = \sqrt{\hbar\omega_r/2L}$. The oscillating field (and therefore the spin-photon coupling) is proportional to this current, so it increases with increasing ω_r and decreases with increasing L.

The ensemble-line coupling was not included in the fit of these experiments, although in some of the resonators with larger ensemble-resonators coupling (LERs 10 and 12, see figure 5.33) it seems that it could be present. The coupling should be present in all measurements, but a consistent value of $G_N^{(line)}$ for all of them was not found.

5.4.4 Effect of the magnetic field inhomogeneity: coupling to small spin ensembles

For the the second run of experiments with chip *Test 2*, the DPPH samples were moved to the previously empty resonators (more details in figure 5.34): LERs 2, 3, 6, 7, 9 and 11. Only the transmission of the pairs of LERs 1 and 2, 7 and 8, and 11 and 12, was measured. Results are shown in figure 5.35). The fit parameters are listed in table A.6 in Appendix A and table 5.8. Both resonators in each pair are coupled to an ensemble, one of them with higher coupling (presumably the one with the DPPH sample on top).

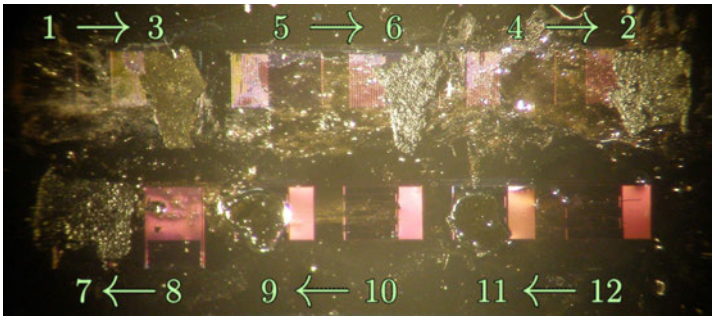

Figure 5.34: Deposition of DPPH samples in the second run of experiments with chip *Test 2*. Samples on LERs 2, 3, 6, 7, 9 and 11. Each sample was moved from its position in figure 5.29 to the closest empty resonator. Small pieces of DPPH powder remain in the resonators where the samples were previously placed, most noticeably in LER 8. However, samples that were originally deposited withe more oil could be moved more easily and left almost no powder behind (see LERs 10 and 12).

LER	g-factor	G_N (MHz)	$G_N/\gamma_\perp$	C
1	$2.04501 \pm 4 \cdot 10^{-5}$	1.166 ± 0.001	0.16 ± 0.01	1.9 ± 0.1
2	$2.04407 \pm 3 \cdot 10^{-5}$	3.343 ± 0.002	0.46 ± 0.02	10.8 ± 0.5
7	$2.04529 \pm 6 \cdot 10^{-5}$	5.437 ± 0.004	0.75 ± 0.04	20.06 ± 0.99
8	$2.04209 \pm 8 \cdot 10^{-5}$	2.020 ± 0.004	0.28 ± 0.01	3.7 ± 0.2
11	$2.03565 \pm 2 \cdot 10^{-5}$	4.812 ± 0.001	0.66 ± 0.03	19.0 ± 0.9
12	$2.0336 \pm 1 \cdot 10^{-4}$	0.515 ± 0.003	0.071 ± 0.004	0.24 ± 0.01

Table 5.8: Parameters from the fit of the transmission of the lumped-element resonators in chip *Test 2* at 4 K. All experiments were fitted with the same ensemble decoherence rate $\gamma_\perp = 7.30 \pm 0.03$ MHz.

Let us focus first in the ensemble-resonator coupling of resonators hosting a large DPPH sample. These are LERs 2, 7 and 11. The coupling observed for samples on LERs 2 and 7 is higher than in the previous run for the same samples on LERs 4 and 8. This increase in the coupling is due to the smaller gap between the chip and sample surface as some oil is lost during sample transfer, the same effect already discussed in section 5.3.2. In the case of the sample on LER 11, the coupling remains similar to the one measured for LER 12 in the previous section. This sample was deposited with more oil, so the relative change in the gap as the sample is moved is smaller. Also, the increase in the coupling is probably compensated by the slight shift in the sample location with respect to the inductor, which leaves half a turn of the inductor without sample on top (check the upper part of LER 11 in figure 5.34). This highlights the importance of the filling factor.

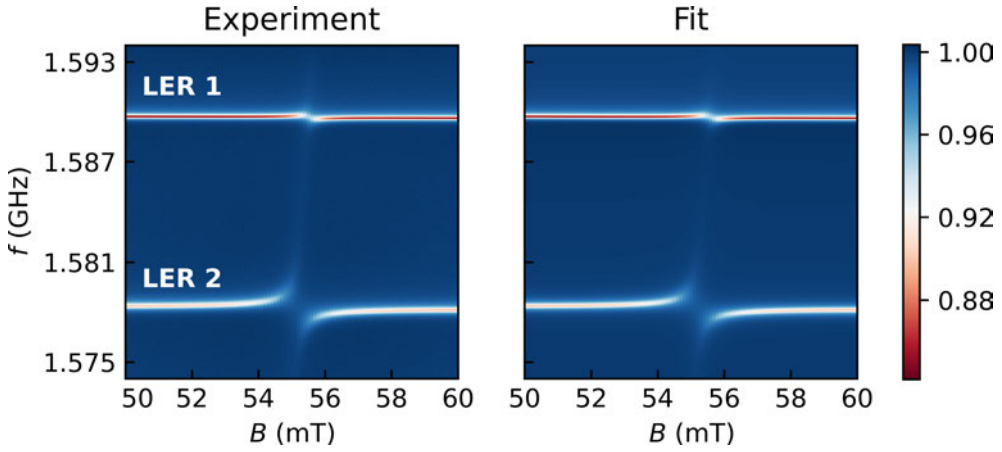

(a)

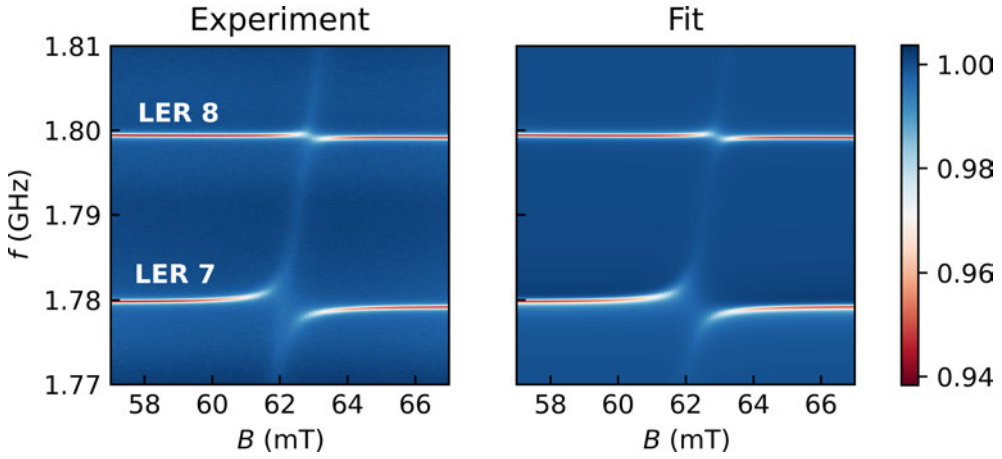

(b)

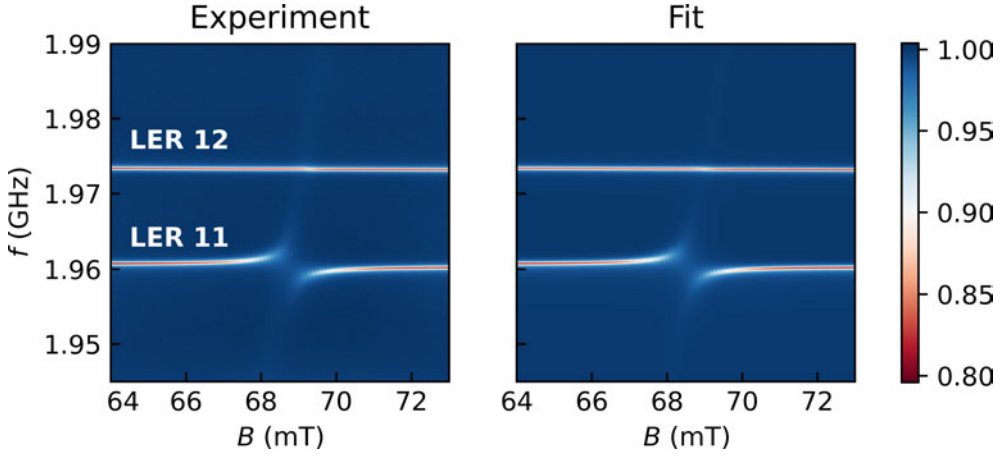

(c)

Figure 5.35: Transmission of (a) LERs 1 and 2, (b) LERs 7 and 8, and (c) LERs 11 and 12 of chip *Test 2*, with DPPH samples on top of LERs 2, 7 and 11. See table A.6 in Appendix A and table 5.8 for the fit parameters.

For the coupling of the empty resonators (LERs 1, 8 and 12), the effect of the ensemble on the empty resonator through a resonator-resonator coupling (which is possible) can be ruled out, as this effect was not present in the previous section. The resonator-resonator coupling in this chip is too low. If it is smaller than the resonator bandwidth, then its hardly detectable. In a closer inspection of figure 5.34 we can see that small pieces of DPPH powder have remained stuck on the oil layer when the samples were moved, which make for the coupling that is observed in the otherwise empty resonators (see figure 5.36a).

The coupling of the pieces is smaller than for whole samples, yet of the same order of magnitude. This suggests that, due to the inhomogeneity of the resonator field, a small sample volume close to resonator surface contributes more to the collective coupling than large volumes farther from it. Let us focus on LER 8, where there are clearly DPPH pieces on top of the resonator after sample transfer (see figure 5.34). Figure 5.36b shows the result of the simulation of the collective spin-photon coupling in LERs 7 and 8 for a bulk sample of DPPH, together with the simulation for small pieces of DPPH embedded in the oil layer on top of LER 7, covering a 5% of the gap volume. The results are consistent with a gap of 26 μm in LER 8 that closes to 16 μm in LER 7 after sample transfer.

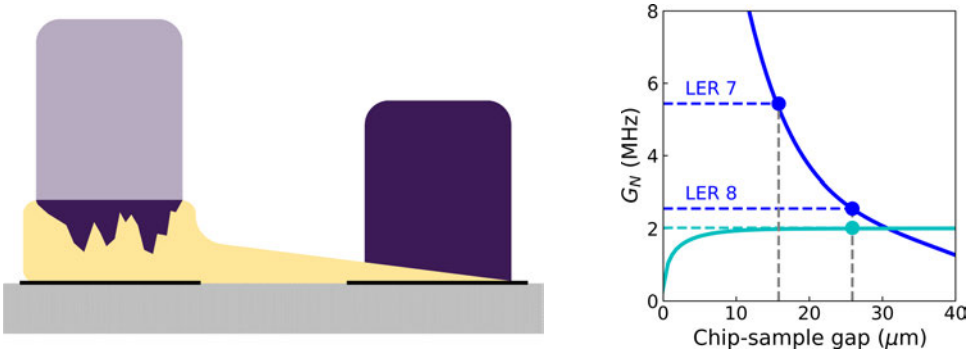

(a) (b)

Figure 5.36: (a) Scheme of the DPPH sample transfer (not to scale). A layer of oil remains in the first resonator with small pieces of DPPH embedded in it. The bulk of the sample is transferred to the second resonator, taking with it part of the oil layer. (b) Collective spin-resonator coupling computed from the simulation of the distribution of fields generated by the inductor of LERs 7 and 8 of chip *Test 2* (blue solid lines) as a function of the gap (the height of the oil layer) between the chip surface and the surface of the bulk of the DPPH sample. Cyan solid line is the simulation of the coupling for small sample pieces covering a 5% of the gap volume in LER 7. The gap in each resonator can be estimated from the measured couplings (dashed lines).

5.5 Conclusions

The coupling of spin 1/2 ensembles (DPPH samples) to superconducting lumped-element resonators was characterized. Before depositing the samples, the resonators were tested with different temperatures and magnetic fields. It was found, as expected for these superconducting circuits, that at higher temperatures and magnetic fields both the resonance frequency ω_r and the internal quality factor $Q = \omega_r/2\kappa_i$ of the resonators decrease. Different orientations of the resonators with respect to the transmission line were tested. The dominant mechanism of the line-resonator coupling is inductive coupling. Upon the deposition of the DPPH samples, the capacitance of the resonators increases due to the presence of an oil layer used to stick the samples to the chip surface. This further decreases the resonance frequency of the LERs.

Measuring the transmission of the resonators around the resonance field B_{res}, the ensemble-resonator coupling rate G_N was found to be at least of the same order of the ensemble decoherence rate $\gamma_\perp$ for all resonators, with LERs 5 and 7 in chip *Test 1* reaching the strong coupling regime $G_N > \gamma_\perp$. In the rest of resonators were coupled to samples the high cooperativity regime was attained, defined by $C = G_N^2/\kappa\gamma_\perp > 1$.

We also tested how changing the experimental setup or the properties of the resonator affects the coupling. Changing the orientation of the static magnetic field affects the coupling, as different components of the oscillating field generated by the resonator contribute to the coupling. Also, the coupling can be enhanced by using resonators with higher resonance frequency and lower geometric inductance. However, the dominant effect on the coupling is the magnitude of the gap between the chip surface and the sample. This gap is defined by the height of the oil layer that we use to stick the samples to the chip surface and by any irregularities in the sample surface. The strength inhomogeneous magnetic field generated by the resonator decays very fast as we move away from the chip surface, and a gap of ~ 9 μm means losing several MHz of collective coupling. Conversely, increasing the sample height beyond a few tens of μm does not increase the coupling much.

The next step forward, at least for free radicals, is depositing the molecules in solution on top of the resonators, minimizing the chip-sample gap. Unfortunately, we can not do that for more complex molecules with magnetic anisotropy, as we want our molecules to be identical (that is, with their anisotropy axes aligned in the laboratory frame o reference). The easiest way to do this is to synthesize a molecular crystal, but it will have a gap with the chip surface. Current research lines focused on closing the gap while preserving some order in the deposition of the sample explore magnetic molecules that deposit

in preferential positions forming self-assembling mono-layers [23] or that can bind to previously deposited mono-layers of non-magnetic molecules (linkers) [24].

References

[1] I. Gimeno Alonso, Ph.D. thesis, Universidad de Zaragoza (2023).

[2] A. Ghirri, C. Bonizzoni, F. Troiani, N. Buccheri, L. Beverina, A. Cassinese, and M. Affronte, Physical Review A **96**, 063855 (2016).

[3] M. Mergenthaler, J. Liu, J. J. L. Roy, N. Ares, A. L. Thompson, L. Bogani, F. Luis, S. J. Blundell, T. Lancaster, A. Ardavan, et al., Physical Review Letters **119**, 147701 (2017).

[4] S. Weichselbaumer, M. Zens, C. W. Zollitsch, M. S. Brandt, S. Rotter, R. Gross, and H. Huebl, Physical Review Letters **125**, 137701 (2020).

[5] M. M. Khapaev, M. Y. Kupriyanov, E. Goldobin, and M. Siegel, Superconductor Science and Technology **16**, 24 (2003).

[6] M. S. Khalil, M. J. A. Stoutimore, F. C. Wellstood, and K. D. Osborn, Journal of Applied Physics **111**, 054510 (2012).

[7] S. Doyle, Ph.D. thesis, Cardiff University (2008).

[8] N. D. Yordanov, Applied Magnetic Resonance **10**, 339 (1996).

[9] D. Z. Žilić, D. Pajić, M. Jurić, K. Molčanov, B. Rakvin, P. Planinić, and K. Zadro, Journal of Magnetic Resonance **207**, 34 (2010).

[10] *PubChem Compound Summary for CID 74358, 1,1-Diphenyl-2-picrylhydrazine.*, https://pubchem.ncbi.nlm.nih.gov/compound/1_1-Diphenyl-2-picrylhydrazine. Accessed Aug. 31, 2023.

[11] D. E. Williams, Journal of the American Chemical Society **88(23)**, 5665 (1966).

[12] D. E. Williams, Journal of the American Chemical Society **89(17)**, 4280 (1967).

[13] H. Ohya-Nishiguchi, Bulletin of the Chemical Society of Japan **52(12)**, 3480 (1979).

[14] B. M. Flanagan, P. V. Bernhardt, E. R. Krausz, S. R. Lüthi, and M. J. Riley, Bulletin of the Chemical Society of Japan **54(10)**, 3110 (1981).

[15] J. H. Van Vleck, Physical Review **74(9)**, 1168 (1948).

[16] P. W. Anderson and P. R. Weiss, Reviews of Modern Physics **25(1)**, 269 (1953).

[17] R. Bachmann, J. DiSalvo, F. J., T. H. Geballe, R. L. Greene, R. E. Howard, C. N. King, H. C. Kirsch, K. N. Lee, R. E. Schwall, H. Thomas, et al., Review of Scientific Instruments **43(2)**, 205 (1972).

[18] H. W. J. Blöte, Physica B+C **79(5)**, 427 (1975).

[19] C. T. Kiers, J. L. de Boer, R. Olthof, and A. L. Spek, Acta Crystallographica **B32**, 2297 (1976).

[20] M. D. Jenkins Sánchez, Ph.D. thesis, Universidad de Zaragoza (2015).

[21] V. Rollano, M. C. de Ory, C. D. Buch, M. Rubín-Osanz, D. Zueco, C. Sánchez-Azqueta, A. Chiesa, D. Granados, S. Carretta, A. Gomez, et al., Communications Physics **5**, 246 (2022).

[22] N. Ebensperger, M. Thiemann, M. Dressel, and M. Scheffler, Superconductor Science and Technology **29**, 115004 (2016).

[23] A. Urtizberea, a. E. Natividad, P. J. Alonso, L. Pérez-Martínez, a. M. A. Andrés, a. I. Gascón, a. I. Gimeno, F. Luis, and O. Roubeau, Material Horizons **7**, 885 (2020).

[24] L. Tesi, F. Stemmler, M. Winkler, S. S. Y. Liu, S. Das, X. Sun, M. Zharnikov, S. Ludwigs, and J. van Slageren, Advanced Materials **35**, 2208998 (2023).

Chapter 6

Dispersive qubit readout: pump-probe experiments on PTM organic free radicals

The experimental results from the previous chapter demonstrate that the high cooperativity and strong coupling regimes can be attained with molecular spin qubits coupled to lumped-element resonators (LERs). The experiments described in it measure the response of the hybrid spin-LER system to low microwave power excitations and for long times. These conditions keep the system in equilibrium or stationary conditions. The goal in a quantum processor like that shown in chapter 1 is however very different from this: the qubits are firstly set out of equilibrium (or away from the initialized ground state $|0\rangle$ in a single qubit) with microwave pulses that represent the quantum gates, then their final state is measured.

This chapter is dedicated to the first experiments towards qubit manipulation with microwave pulses combined with quantum non-demolition (QND) measurements performed by coupling the molecular spin qubits to LERs. For this, the hybrid spin-LER system must be set in the dispersive regime (see section 3.4 in chapter 3 for a proper definition), where the spin transition frequency ω_q (the qubit frequency) and the resonator frequency ω_r are sufficiently detuned so that no real exchange of excitations occurs between both systems. This condition is met for a qubit-resonator detuning $\Delta = \omega_q - \omega_r$ much larger than the collective spin-photon coupling G_N (in absolute value, that is, $|\Delta| \gg G_N$). The interest of the dispersive regime lies in that, even if the resonator and spin states are effectively decoupled, their frequencies ω_q and ω_r are still modulated ('dressed') by the coupling. In particular, ω_r is shifted to lower of higher frequencies depending on the state of the spins. That is, the

spin state can be inferred from the response the resonator.

6.1 Experimental setup for pulse experiments

6.1.1 Chip design

Two superconducting chips were designed for pulse experiments, labeled *Test 3* and *Test 4*. *Test 3* hosts 10 superconducting LERs coupled to a single transmission line, with resonance frequencies between 1.7 and 2.9 GHz. *Test 4* is an evolution of *Test 3* with an additional transmission line, and hosts 10 lumped-element resonators with resonance frequencies between 1.4 and 2.8 GHz. In both chips, LERs are labeled from highest resonance frequency to lowest (that is, in increasing order of resonator area). The designs of both chips are shown in figure 6.1.

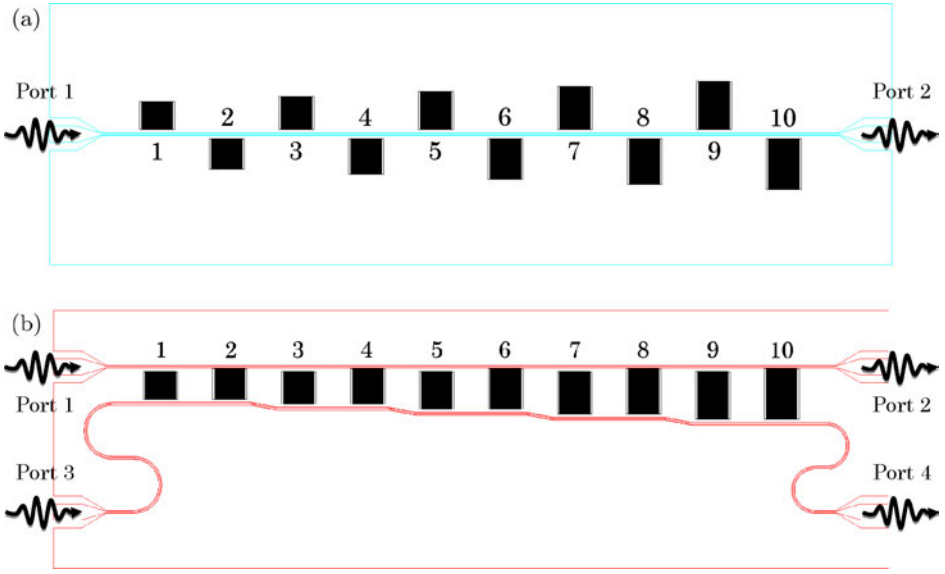

Figure 6.1: Vector file design of *Test 3* (a) and *Test 4* (b). LERs (black) are side-coupled to either a single transmission line (*Test 3*, blue) or two transmission lines (*Test 4*, red), and labeled in order of decreasing resonance frequency ω_r.

The first tests of the microwave setup for pulse experiments were performed with *Test 3*. This chip was originally intended for achieving the highest possible single spin-photon coupling strength [1, Ch.5], which calls for the highest possible current at the inductor in resonance, thus the smallest possible inductance L. This implies that the design of the resonators is radically different from those shown in the previous chapter: most of the LER area is now taken by

the inter-digital capacitor, with the inductor being just a short superconducting strip connecting the two ends of the capacitor (see figure 6.2). In addition, a nano-constriction was fabricated in the inductor by FIB lithography in order to locally increase the microwave magnetic field, thus further enhancing the spin-photon coupling for molecules sitting just above the constriction.

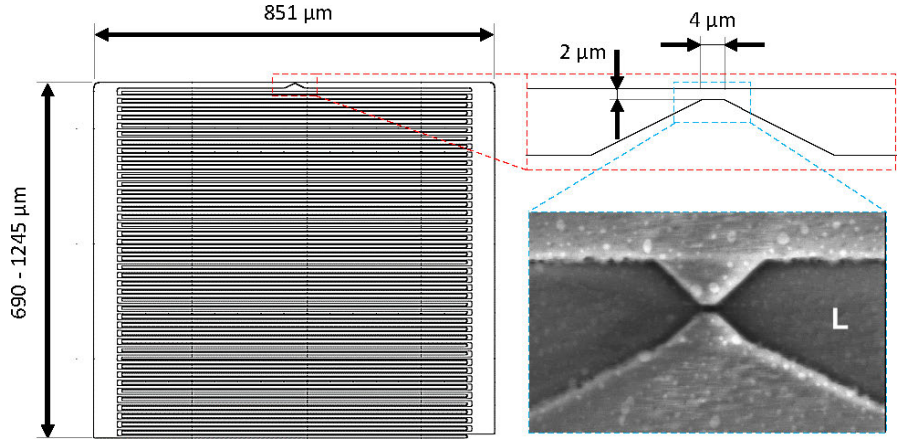

Figure 6.2: Design of a low inductance (low-L) LER with a nano-constriction, adapted from [1, Ch.5]. The inductor is the strip at the top of the figure. The frequency of the resonator is tuned by changing the size of the capacitor, thus the different lengths in the dimension perpendicular to the inductor (ranging from 690 to 1245 μm). The inductor has a 2 μ-wide constriction that is further narrowed to tens of nm by FIB lithography.

Test 4 introduces an additional transmission line, which allows sending excitation and readout signals separately via different lines. LERs are coupled to both lines. The excitation line goes from port 1 to port 2 in figure 6.1b. This line is coupled to the inductor of the LERs that mainly host the sample. The readout line connects ports 3 and 4 in figure 6.1b, and it is capacitively coupled to the opposite side of the resonators. The weak capacitive coupling between this line and the resonator does not pose a limitation to the visibility of the resonances if the measurements are carried out in the millikelvin regime. None of the resonators in this chip has a nano-constriction in the inductor.

6.1.2 Molecular spin samples

Free radicals provide the simplest systems to test the pump-probe microwave setup. Hosting a spin 1/2, each radical molecule has a single spin transition that is easily tunable with magnetic field ($\omega_q \propto B$). For clarity, the Hamilto-

nian of a free radical is reproduced here:

$$H = \mu_{\mathrm{B}} g_S B \hat{S}_z = \frac{\mu_{\mathrm{B}} g_S B}{2} \hat{\sigma}_z, \tag{6.1}$$

which contains just the Zeeman term of the interaction of the $S = 1/2$ spin with the magnetic field. The spin transition frequency is $\omega_q = \mu_{\mathrm{B}} g_S B/\hbar$.

If g_S is isotropic and the radicals can be considered as non-interacting spin systems, all of them are identical from a magnetic point of view. This makes DPPH an unsuitable candidate for pulse experiments, as it exhibits antiferromagnetic interactions at very low temperatures. This will discussed further in chapter 8.

A different free radical molecule, the PTM radical or $\mathrm{PTM_r}$, was chosen as the molecular spin qubit for the first tests with pulsed experiments. $\mathrm{PTM_r}$ is composed of three fully chlorinated phenyl groups bridged by a central carbon atom with an unpaired electron (see figure 6.3) [2, 3]. The spin 1/2 of this electron is the spin of the molecule.

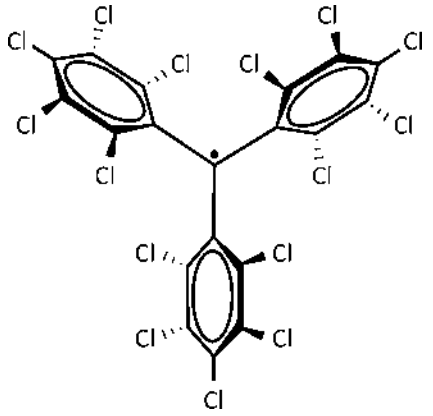

Figure 6.3: Chemical structure of the PTM radical, adapted from [3]. The unpaired electron (pictured as a black dot) that gives the effective spin 1/2 of the molecule is localized in the carbon atom that bridges the three fully chlorinated phenyl groups.

A sample of $\mathrm{PTM_r}$ and polystyrene (PS) in chlorobenzene (CB), with a mass ratio of 0.1% between $\mathrm{PTM_r}$ and PS was measured with conventional EPR by the group of Joris van Slageren (University of Stuttgart). The spectrum showed a broadening of its resonance at low temperatures [1, Ch.5]. Their tentative explanation is that this spectrum is a convolution of unresolved hyperfine splittings due to the interaction of this spin 1/2 with the nuclear spin $I = 3/2$ of the chlorine atoms. Despite these interactions, they measured a memory time $T_{\mathrm{m}} = 4$ μs at 15 K. The relaxation time T_1, which limits the repetition time of the experiments, is quite long (tens of milliseconds at 15

K). These times are expected to become even longer in the millikelvin regime. More recent measurements by the van Slageren group yielded spin coherence values as high as $T_m = 123$ μs for PTM_r in CS_2 at 7 K [4].

The samples for the experiments in these chapter were drops of PTM_r/PS in 0.1 μl of CB, with different PTM_r/PS mass ratios. PTM radical molecules were synthesized by Imma Ratera, Nuria Crivillers and Nerea González from the Nanomol-Bio group at ICMAB-CSIC (Barcelona). Drops were deposited on top of the surface of the lumped-element resonators by Anabel Gracia Lostao and Mari Carmen Pallarés from INMA (Instituto de Nanociencia y Materiales de Aragón) and LMA (Laboratorio de Microscopía Avanzada), Zaragoza. After chlorobenzene evaporates, a solid ∼7 μm thick film of PTM_r/PS remains, covering an area similar to that of a resonator (∼ 1 mm^2).

Figure 6.4 shows an example of a deposition on *Test 3*. This deposition process ensures that PTM_r molecules are homogeneously distributed and placed very close to the chip surface, thus avoiding the effect of the sample-resonator gap observed in chapter 5 (see the SEM image in figure 6.2).

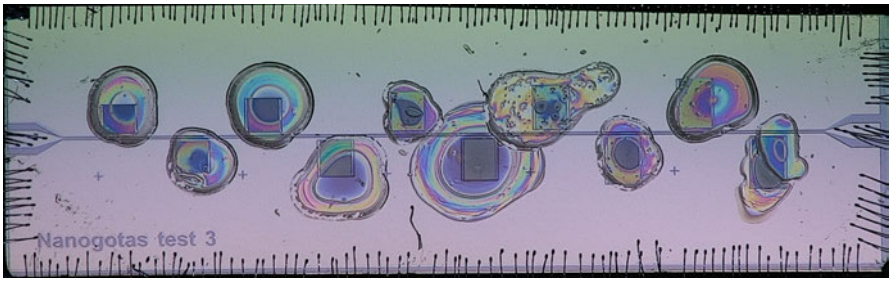

Figure 6.4: Optical close-up of the PTM_r/PS films deposited on top of *Test 3* LERs.

6.1.3 Microwave setup for pulse experiments

The microwave setup for pulse experiments can be divided into three main stages: the generation stage, the cryogenic stage, and the detection stage (see figure 6.5). The cryogenic stage includes the superconducting chip (*Test 3* or *Test 4*) with the PTM_r deposits on the LERs, which has been already discussed. The chip is placed in the center of a superconducting magnet inside a cryostat (see section 2.2 in chapter 2 for more details), which generates the magnetic field that tunes the qubit frequency ω_q. The input lines of the cryostat incorporate either 0 dB or 10 dB attenuators at each constant temperature plate (see figure 6.5). Therefore, different net attenuations can be chosen for the excitation and readout lines. (the same in the case of *Test 3*, different for *Test 4*). The output readout line is amplified at $T = 4$ K with a Low Noise Factory (LNF) cryogenic amplifier with a gain of ∼30 dB.

The generation and detection stages depend on each specific experiment. The output of the generation stage is a sequence of excitation pulses with frequencies close to ω_q that goes to the excitation line of *Test 4* or the single line of *Test 3*. An optional reference signal can be set to the readout stage for synchronisation. This stage is composed of a Keysight M9180A single-channel Arbitrary Waveform Generator (AWG), see section 2.3.2, plus all the necessary microwave elements (attenuators, amplifiers, switches, splitters/combiners) to have the desired power for each of the pulses. For *Test 4*, each signal (excitation/readout) generated by the AWG must be routed to its corresponding line in the chip.

The detection stage is either a Keysight MSOS404A oscilloscope or a ZVB14 VNA from R&S (see sections 2.3.1 and 2.3.3). The oscilloscope reads the in-phase (I) and quadrature components (Q) of the transmission of the resonator generated by an IQ mixer with a reference LO (local oscillator) signal from the generation stage. Alternatively, the VNA can be used to detect the output signal in those cases in which it also generates the readout pulses. For *Test 3*, excitation and readout signals must be separated with microwave switches in order to protect the readout stage from too high power inputs.

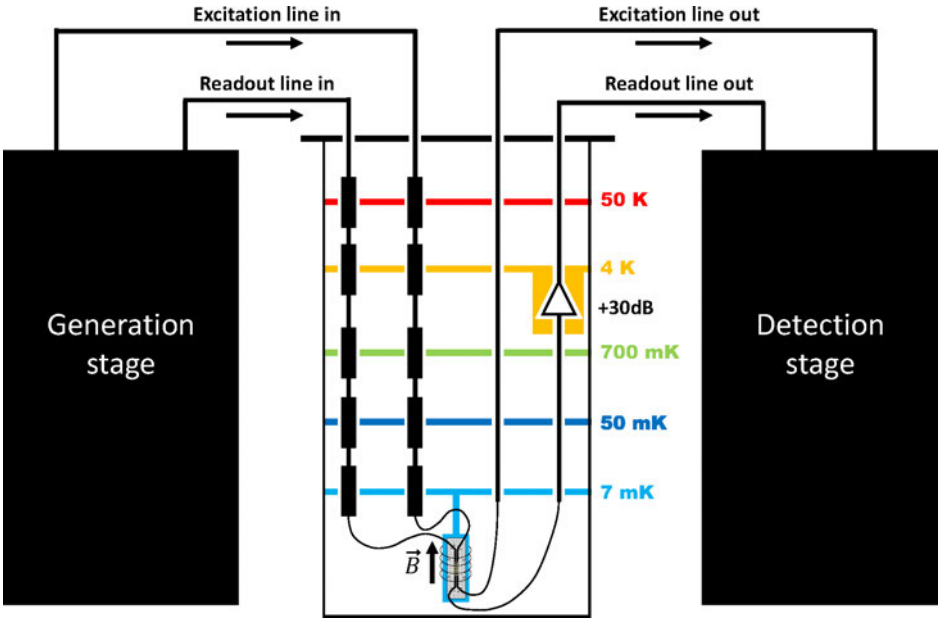

Figure 6.5: Schematic microwave setup for pulse experiments. Input excitation and readout lines have 10 dB attenuators in each plate of the cryostat, for a total of 50 dB of attenuation. The power of the excitation pulses that reach the superconducting chip can be increased by replacing some attenuators from the excitation line with 0 dB DC blocks. The readout line is amplified 30 dB at 4 K. The schemes of the generation and detection stages will be detailed below for each particular experiment.

6.2 Characterization of the collective spin-resonator coupling

This section explores the effect of using different PTM_r/PS samples on the collective spin-photon coupling G_N. The effect of changing the PTM_r/PS ratio between 0.01% ($N = 10^{11}$ spins) and 0.5% ($N = 5 \cdot 10^{12}$ spins) has been already determined. The results, reported in [1, Ch.5], show that G_N scales with $\sqrt{N_{\text{eff}}}$, where $N_{\text{eff}} \sim N/100$ is the effective number of spins that actually couple significantly to the microwave magnetic field generated by the resonator inductor (with or without constriction).

Here, I take the sample with the highest PTM_r/PS ratio (0.5%) and explore the effect of increasing the spin concentration even further by reducing the amount of PS in the solution in CB. The idea is to have more PTM radical molecules closer to the inductor by removing part of the PS matrix. The details of the samples are listed in table 6.1. Figures 6.6 and 6.7 show the resonances of the 10 *Test 3* LERs measured with these deposits at 10 mK and as a function of magnetic field. S_{21} is measured for different regular input frequencies $f = \omega_d/2\pi$ and magnetic fields B (tuning the qubit frequency ω_q $\omega_q = \mu_B g_S B/\hbar$). The input power was chosen in order to feed less than -70 dBm into the chip. For higher input powers, the collective spin-photon coupling was observed to decrease in some of the resonators.

LERs	1 and 2	3 and 4	5 and 6	7 and 8	9 and 10
PS concentration (g/l)	0	6.3	6.3	12.6	12.6
PTM/PS mass ratio (%)	–	1	0.5	1	0.5
N (10^{12} spins)	5	5	2.5	10	5

Table 6.1: Properties of the 0.1 μl PS/PTM solutions in CB that were deposited on each of the 10 *Test 3* LERs. I list the PS concentration in the 0.1 μl solution before the evaporation of CB, as well as the PTM/PS mass ratio and the estimated number N of spins in the sample.

The characterization of the resonances follows a similar procedure to that described in the previous chapter for the case of DPPH samples. The transmission of each resonator is measured around its resonance frequency ω_r for different fields around the resonance condition $\omega_r = \omega_q$ and fitted with equation (4.102) from chapter 4, which is reproduced here again for clarity:

$$S_{21}(\omega_d) = 1 - \frac{\kappa_c}{i(\omega_r - \omega_d) + \kappa + \dfrac{G_N^2 \Delta P}{i(\omega_q - \omega_d) + \gamma_\perp}} . \tag{6.2}$$

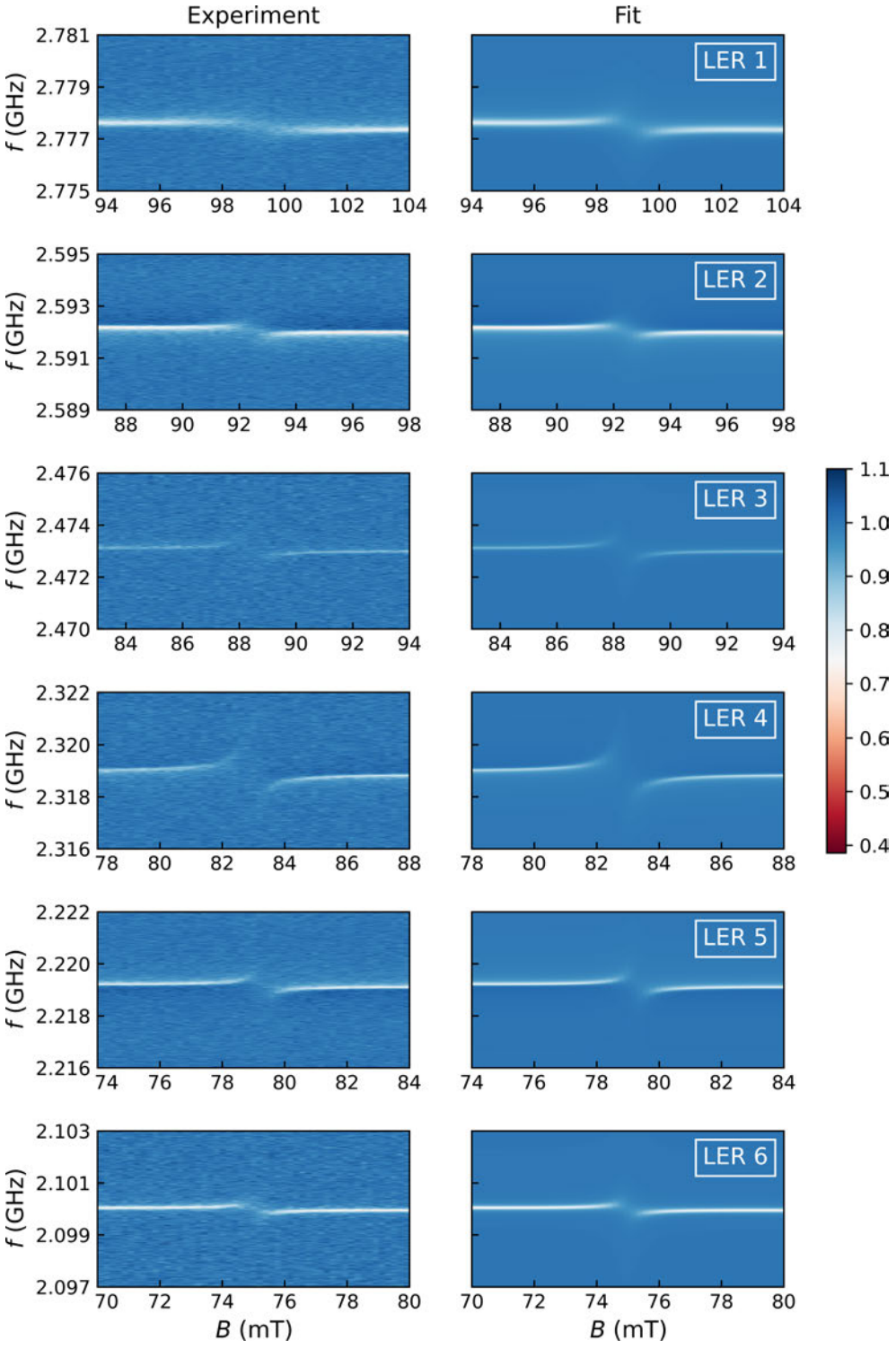

Figure 6.6: Transmission of LERs 1 to 6 of chip *Test 3* coupled to PTM samples. *Left:* Experimental results. *Right:* Theoretical simulations based on equation (6.2) with the parameters given in tables 6.2 and 6.3.

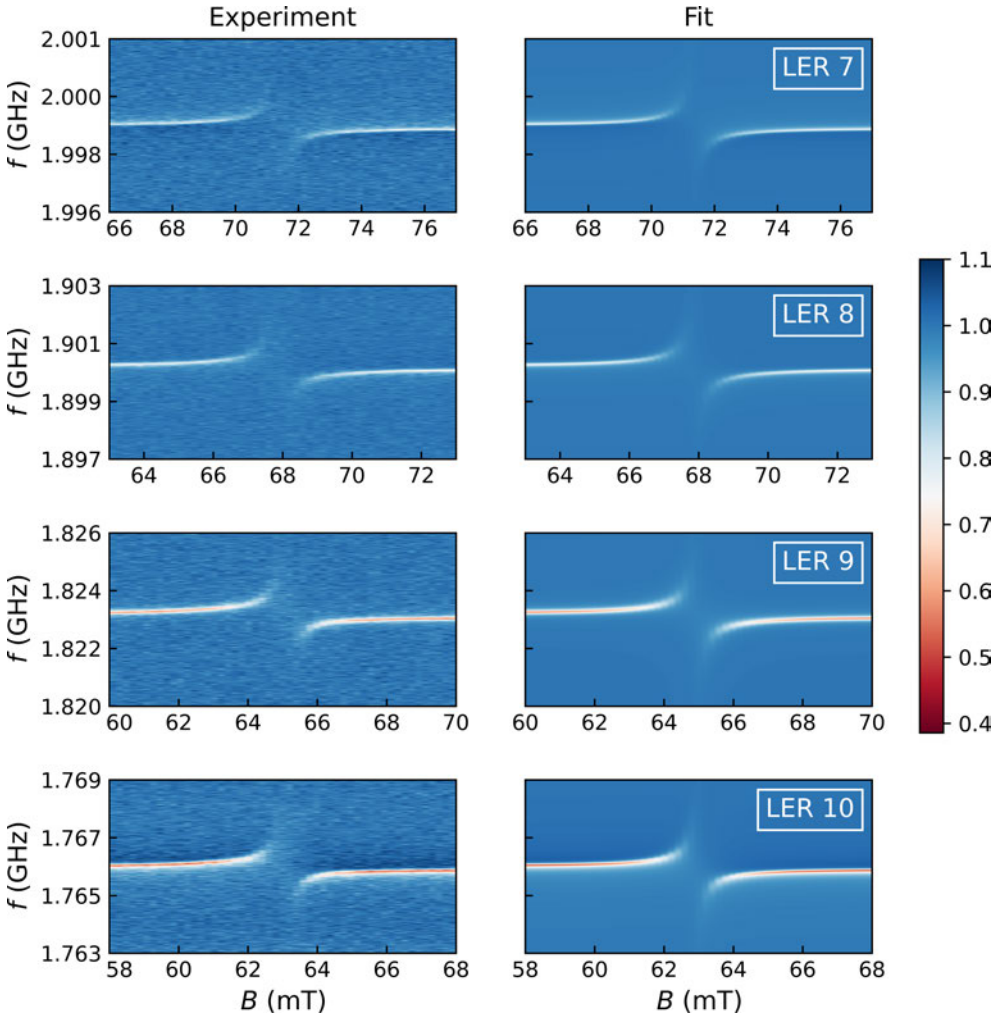

Figure 6.7: Transmission of LERs 7 to 10 of chip *Test 3* coupled to PTM_r samples. *Left:* Experimental results. *Right:* Theoretical simulations based on equation (6.2) with the parameters given in tables 6.2 and 6.3.

The resonance frequency ω_r, the photon mode decay rate κ, and line-coupling rate κ_c of each LER are listed in table 6.2. The resonators show remarkably high quality factors $Q = \omega_r/2\kappa \leqq 10^5$, i.e. small widths, which makes them well suited to perform dispersive readout experiments. Table 6.3 reports the parameters related to the sample: the g-factor g_S, the decoherence rate of the spin ensemble, $\gamma_\perp$, and the temperature dependent collective spin-photon $G_N(T) \propto \sqrt{\Delta P}$. ΔP is the population difference between the spin down and spin up states at temperature T, which at 10 mK and $\omega_q \simeq \omega_r \sim$ 1–3 GHz can be safely assumed to be nearly 1.

Collective spin-photon couplings up to 3.42 MHz are reached, almost as high as in the previous chapter with DPPH, but with the number N of spins being 5 orders of magnitude smaller. The fact that such a large G_N can be attained with much smaller spin ensembles is due to the low-inductance design of these LERs and to the reduction of the sample-chip gap. That is, there are less spins, but they are closer to an inductor that generates a much stronger magnetic field (which scales with $L^{-1/2}$). G_N is also enhanced as temperature is decreased from 4 K in the last chapter to 10 mK in these measurements. However, this would only account for an increase in by a factor $\sqrt{(\Delta P)_{T=10\,\mathrm{mK}}/(\Delta P)_{T=4\,\mathrm{K}}} < 3$. In comparison, reducing the number of spins from $N_{\mathrm{DPHH}} \sim 10^{17}$ to $N_{\mathrm{PTM}} \sim 10^{12}$ in the same experimental conditions decreases G_N by a factor $\sqrt{N_{\mathrm{DPHH}}/N_{\mathrm{PTM}}} > 300$.

LER	$\omega_r/2\pi$ (GHz)	$\kappa/2\pi$ (kHz)	$\lvert\kappa_c\rvert/2\pi$ (kHz)	ϕ_c (°)
1	$2.777535 \pm 2 \cdot 10^{-6}$	85.8 ± 1.6	23.4 ± 0.9	-10.1 ± 0.3
2	$2.5921684 \pm 9 \cdot 10^{-7}$	56.9 ± 0.5	20.1 ± 0.3	27.4 ± 0.3
3	$2.473073 \pm 3 \cdot 10^{-6}$	48.4 ± 1.8	5.1 ± 0.3	-9.5 ± 1.2
4	$2.318961 \pm 2 \cdot 10^{-6}$	50.3 ± 1.1	9.7 ± 0.4	28.3 ± 0.7
5	$2.2191717 \pm 9 \cdot 10^{-7}$	46.9 ± 0.6	12.2 ± 0.3	-29.4 ± 0.4
6	$2.100022 \pm 1 \cdot 10^{-6}$	53.7 ± 0.8	15.0 ± 0.4	-2.5 ± 0.5
7	$1.998962 \pm 1 \cdot 10^{-6}$	39.8 ± 0.8	10.7 ± 0.4	-29.8 ± 0.6
8	$1.900192 \pm 1 \cdot 10^{-6}$	46.1 ± 0.7	12.8 ± 0.3	14.8 ± 0.4
9	$1.823173 \pm 1 \cdot 10^{-6}$	58.5 ± 0.6	26.6 ± 0.5	-1.2 ± 0.3
10	$1.7659920 \pm 9 \cdot 10^{-7}$	55.5 ± 0.6	30.2 ± 0.6	24.9 ± 0.3

Table 6.2: Parameters that characterizing the resonances of the 10 *Test 3* LERs obtained by fitting the transmission through the device at 10 mK.

LER	g-factor	G_N / 2π (MHz)	$\gamma_\perp$ / 2π (MHz)
1	$2.0030 \pm 4 \cdot 10^{-4}$	3.16 ± 0.04	34.4 ± 1.0
2	$2.0029 \pm 3 \cdot 10^{-4}$	2.21 ± 0.01	15.7 ± 0.4
3	$1.999 \pm 1 \cdot 10^{-3}$	2.37 ± 0.03	8.3 ± 0.9
4	$1.9994 \pm 3 \cdot 10^{-4}$	3.31 ± 0.02	7.1 ± 0.4
5	$1.9996 \pm 2 \cdot 10^{-4}$	2.08 ± 0.01	7.1 ± 0.3
6	$1.9998 \pm 4 \cdot 10^{-4}$	1.72 ± 0.01	8.9 ± 0.5
7	$2.0010 \pm 3 \cdot 10^{-4}$	3.27 ± 0.01	5.9 ± 0.3
8	$1.9997 \pm 2 \cdot 10^{-4}$	3.42 ± 0.01	6.1 ± 0.2
9	$2.0052 \pm 2 \cdot 10^{-4}$	3.36 ± 0.01	6.6 ± 0.2
10	$2.0046 \pm 2 \cdot 10^{-4}$	3.08 ± 0.01	5.8 ± 0.2

Table 6.3: Parameters from the fit of the magnetic field dependent resonances of LERs 1, 3 and 5 in chip *Test 3* at $T = 10$ mK shown in figures 6.6 and 6.7.

The collective spin-LER coupling G_N scales with the square root of the number N of spins (see figure 6.8a). This coupling does not seem to get enhanced by reducing the PS concentration. In fact, the main consequence of removing the PS matrix is a broadening of the spin spectrum, as shown in figure 6.8b. First, there is an increase from $\gamma_\perp = 5.8$–6.6 MHz (LERs 7 to 10) to $\gamma_\perp = 7.1$–8.9 MHz (LERs 3 to 6) as the original PS concentration of 12.6 g/l is halved. Then, a sharp increase to $\gamma_\perp = 34.4$ and 15.7 MHz is observed in LERs 1 and 2, where PTM_r molecules were deposited without PS. The broadening can be attributed to the onset of spin-spin interactions that were previously suppressed by the dilution of PTM_r in the diamagnetic PS matrix. From this results I decided to keep the parameters of the deposition on LERs 9 and 10 for the pulsed experiments, as the broadening overcomes any gain achieved in G_N by removing part of the PS matrix.

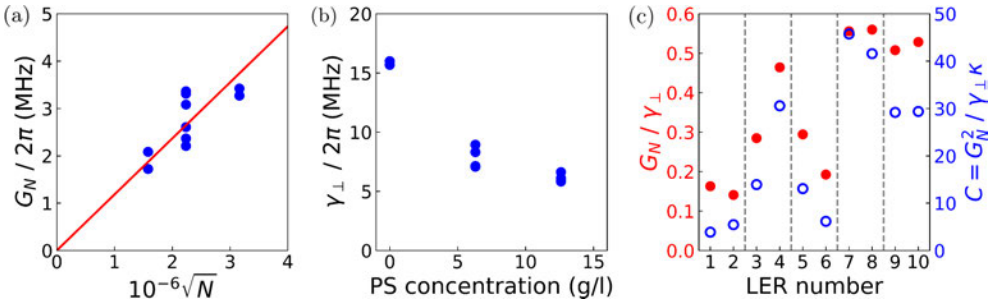

Figure 6.8: (a) Collective spin-photon coupling G_N as a function of the square root of the number of spins in the sample. (b) $\Gamma_\perp$ as a function of the PS concentration in the PTM_r/PS solution in CB. (c) The ratios $G_N/\gamma_\perp$ (red closed dots) and $C = G_N^2/\gamma_\perp\kappa$ (blue open dots) for each resonator. These quantities define the strong coupling ($G_N/\gamma_\perp > 1$) and the high cooperativity ($C > 1$) regimes. Only the latter is attained with this experimental setup.

Figure 6.8c shows the $G_N/\gamma_\perp$ ratio and the cooperativity $C = G_N^2/\gamma_\perp\kappa$ for each LER. None of the hybrid spins-LER systems is in the strong coupling regime ($G_N/\gamma_\perp > 1$), but the high cooperativity regime ($C > 1$) is achieved for all of them.

6.3 Testing pulse generation and the resonator dynamics

The pulse generation system was tested by measuring the response of a LER to 20 μs pulses with driving frequencies ω_d close to its resonance frequency ω_r. Figure 6.9a shows the output signal transmitted by the bare resonator.

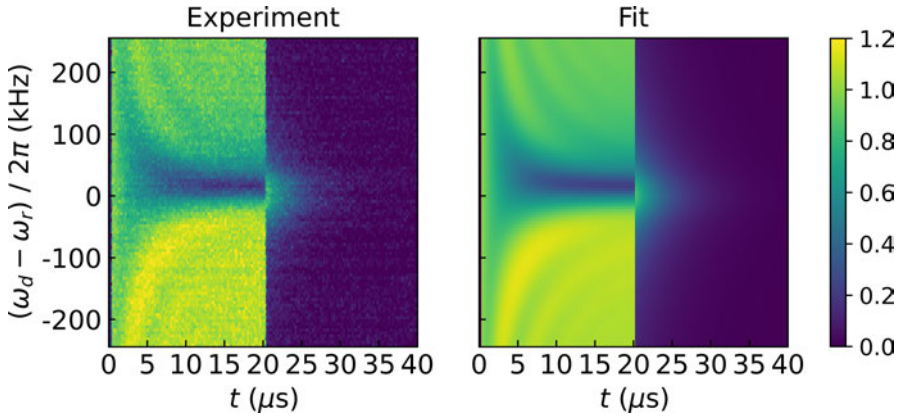

Figure 6.9: Comparison between the maps of the experimental and theoretical amplitude of the transmission of 20 μs long pulses microwave pulses with driving frequencies ω_d close to the resonance frequency ω_r of a LER, measured at zero field. At this field, the resonator is completely decoupled from the spins. Both maps show the absolute value of the output signal normalized by the amplitude of the input pulse, α_{in}.

The transmitted signal was fitted with the theory that describes the dynamics of a LER, the details of which can be seen in section 4.4.2 from chapter 4. The resonator evolution under a coherent drive $b_{in}(t) = \alpha_{in} e^{-i\omega_d t}$ is given by equation (4.63), reproduced here for clarity:

$$\langle \hat{a} \rangle(t) = \langle \hat{a} \rangle(0) e^{-(i\omega_r + \kappa)t} - i\sqrt{\kappa_c} \frac{1 - e^{-(i(\omega_r - \omega_d) + \kappa)t}}{i(\omega_r - \omega_d) + \kappa} \alpha_{in} e^{-i\omega_d t}. \tag{6.3}$$

From input-output theory, the transmitted signal is:

$$b_{out}(t) = b_{in}(t) - i\sqrt{\kappa_c} \langle \hat{a} \rangle(t) \tag{6.4}$$

Now, the response can be analyzed in two stages. The first comprises the duration of the pulse, described by the equations above with α_{in} and $\langle \hat{a} \rangle(0) = 0$. That is, the resonator is assumed to be initially discharged. It then follows that:

$$\langle \hat{a} \rangle(t) = -i\sqrt{\kappa_c} \frac{1 - e^{-(i(\omega_r - \omega_d) + \kappa)t}}{i(\omega_r - \omega_d) + \kappa} \alpha_{in} e^{-i\omega_d t} \quad \text{for } t < t_{pulse}\,, \tag{6.5}$$

which yields:

$$b_{out}(t) = \left(1 - \kappa_c \frac{1 - e^{-(i(\omega_r - \omega_d) + \kappa)t}}{i(\omega_r - \omega_d) + \kappa} \right) \alpha_{in} e^{-i\omega_d t} \quad \text{for } t < t_{pulse}\,, \tag{6.6}$$

where $t_{pulse} = 20$ μs.

After the pulse, the driving amplitude α_{in} becomes zero, and the time reference is shifted to $T = 20$ μs: $t \to t' = t - t_{pulse}$. For this second part, $\langle\hat{a}\rangle(t' = 0)$ equals the $\langle\hat{a}\rangle(t = t_{pulse})$ computed with equation (6.5). Then:

$$b_{out}(t) = -i\sqrt{\kappa_c}\langle\hat{a}\rangle(t = t_{pulse})e^{-(i\omega_r+\kappa)(t-t_{pulse})} \quad \text{for } t > t_{pulse}\,, \tag{6.7}$$

The experiment was repeated with the qubit frequency ω_q tuned with the magnetic field to lie at $\Delta/2\pi = (\omega_q - \omega_r)/2\pi = 30$ MHz from ω_q and ω_r. With this detuning, the ensemble-LER system is in the dispersive regime ($\Delta \sim 10G_N \gg G_N$). Figure 6.10b shows the transmission of 20 μs pulses with driving frequencies ω_d close to ω_r in this new experimental conditions.

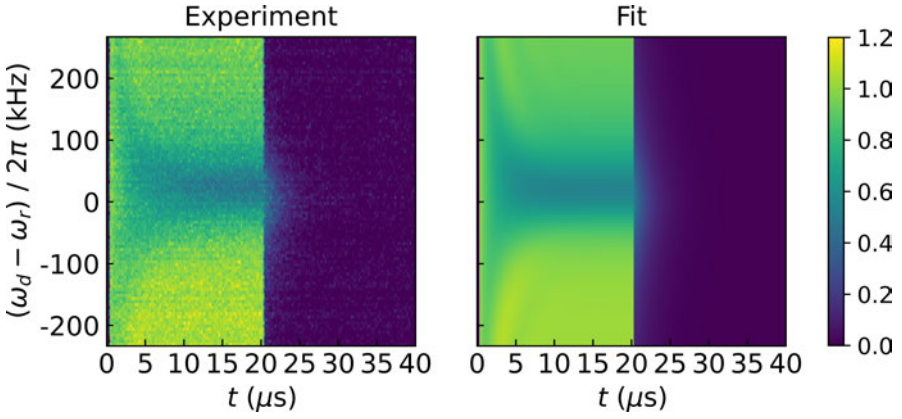

Figure 6.10: Comparison between the maps of the experimental and theoretical amplitude of the transmission of 20 μs long pulses microwave pulses sent with drive frequencies ω_d close to the LER resonance frequency $\tilde{\omega}_r$. The qubit frequency ω_q was tuned with the static magnetic field to set a detuning $(\omega_q - \omega_r)/2\pi = 30$ MHz between ω_q and the resonator frequency ω_r. $\tilde{\omega}_r$ is the resonance frequency for this detuning (see equation (6.8) in chapter 4). Both maps show the absolute value of the output signal normalized by the amplitude of the input pulse, α_{in}.

In this case, the output signal should be computed using the input-output theory for the dynamics of the hybrid spin ensemble-resonator system, which is described in section 4.6.3 from chapter 4. However, the characterization of the collective spin-LER coupling in the previous sections sets the hybrid system in the weak coupling. In this regime, the coupled resonator can be described as a bare resonator with effective resonance frequency $\tilde{\omega_r}$ and effective decay rate $\tilde{\kappa}$ modified by the spin-photon coupling (see section 4.6.4).

The expressions for $\tilde{\omega_r}$ and $\tilde{\kappa}$ are reproduced here:

$$\begin{aligned} \tilde{\omega}_r &:= \omega_r + \left[\frac{G_N^2(\Delta P)_e}{(\omega_q - \omega_r)^2 + \gamma_\perp^2}\right](\omega_r - \omega_q), \\ \tilde{\kappa} &:= \kappa + \left[\frac{G_N^2(\Delta P)_e}{(\omega_q - \omega_r)^2 + \gamma_\perp^2}\right]\gamma_\perp, \end{aligned} \tag{6.8}$$

which depend on the (uncoupled) LER resonance frequency ω_r, its photon decay rate κ, the magnetic field dependent qubit frequency ω_q, the spin decoherence rate $\gamma_\perp$, the collective spin-photon coupling G_N and the spin population difference in equilibrium $(\Delta P)_e$.

Tables 6.4 and 6.5 list the fit parameters of the resonance for the bare and coupled resonators respectively. The coupling of the LER photons to the PTM_r/PS sample broadens the resonance, with κ increasing from 35.4 to 67.6 MHz. That is, the photon lifetime $(1/\kappa)$ in the resonator is reduced, even in the dispersive regime, as can be seen by comparing figures 6.9 and 6.10. The line-resonator coupling, κ_c, does not depend on the presence of the sample and its absolute value remains in the 30–33 MHz range. Assuming $(\Delta P)_e \simeq 1$ and $\gamma_\perp \sim 6$ MHz, a collective spin-photon coupling $G_N \sim 2$ MHz can be estimated from the expression of $\tilde{\kappa}$ (see equation (6.8)).[1]

$\omega_r/2\pi$ (GHz)	$\kappa/2\pi$ (kHz)	$\lvert\kappa_c\rvert/2\pi$ (kHz)	ϕ_c (°)
$2.2515944 \pm 2 \cdot 10^{-7}$	35.4 ± 0.2	30.6 ± 0.2	-29.0 ± 0.2

Table 6.4: Fit parameters of the dynamics of the bare resonator with 20 μs long pulses.

$\tilde{\omega}_r/2\pi$ (GHz)	$\tilde{\kappa}/2\pi$ (kHz)	$\lvert\kappa_c\rvert/2\pi$ (kHz)	ϕ_c (°)
$2.2510931 \pm 5 \cdot 10^{-7}$	67.6 ± 0.5	33.3 ± 0.4	-23.0 ± 0.3

Table 6.5: Fit parameters from the fit of the dynamics of the resonator coupled to a PTM/PS sample with 20 μs long pulses and a detuning $(\omega_q - \omega_r)/2\pi = 30$ MHz between the qubit frequency ω_q and uncoupled LER resonance frequency ω_r.

Figure 6.11 highlights the fit of the dynamics of the resonator for a selection of detunings between the driving frequency of the input pulse, ω_d, and the LER resonance frequency (ω_r or $\tilde{\omega}_r$). It is remarkable that the model defined by equations (6.6) and (6.7) provides a good account of the dynamical response of the uncoupled or coupled LER for all detunings $\omega_d - \omega_r$ (or $\omega_d - \tilde{\omega}_r$) with

[1] See the reported $\gamma_\perp$ for LERs 9 and 10 in table 6.3. The PTM_r/PS sample in this experiment is the same 0.5% PTM_r/PS deposit.

a common set of parameters. Note that the asymmetry of the resonance lineshape, encoded in the argument of the complex-valued resonator-line coupling κ_c (ϕ_c), leads also to an asymmetry in the dynamics.

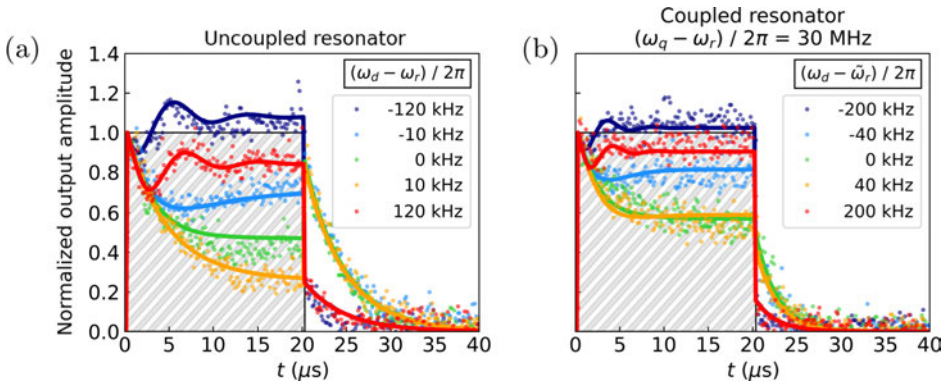

Figure 6.11: Comparison between the experimental (dots) and theoretical (solid lines) amplitudes of the chip output signal resulting from the application of 20 μs long microwave pulses with driving frequencies ω_d close to the LER resonance frequency ω_r. Two cases are illustrated: the uncoupled resonator at 0 mT (a) and the resonator coupled to a PTM_r/PS sample in the dispersive regime (b). The absolute value of the output signal is shown, normalized by the amplitude of the input pulse, α_{in}.

These results show clearly the strong effect of collective spin-photon coupling in reducing the photon lifetimes that was mentioned before. The lifetime reduction is parametrized by the increase in $\tilde{\kappa}$ predicted by equation (6.8). The coupled resonator in the dispersive regime is already in its steady-state at the end of the pulse, while the uncoupled resonator is still charging. That is, there is a dead time before the steady-state can be probed that is reduced by decreasing the detuning between ω_q and ω_r (in absolute value). This shortening of the dead time will be relevant for the readout of the resonator state that is described in the following sections.

6.4 First pump-probe experiments on PTM radicals: measurement of the spin ensemble absorption spectrum and relaxation time T_1

The first pump-probe experiments on PTM radicals were performed with the *Test 3* chip, having just one transmission line is coupled to the LERs. The PTM_r/PS samples were the 0.5% PTM_r/PS (in mass) deposits on LERs 9 and 10 (section 6.2). Therefore, a collective spin-photon coupling $G_N/2\pi \sim 3.2$ MHz is expected, with an ensemble decoherence rate $\gamma_\perp/2\pi \sim 6$ MHz. There

are $N \sim 5 \cdot 10^{12}$ spins on each PTM_r/PS sample. This gives a root mean square (RMS) single spin-photon coupling $G_{1,\,\mathrm{RMS}}/2\pi = G_N/2\pi\sqrt{N} \sim 1.4$ Hz. However, a better estimate considers only the effective number of coupled spins, $N_{\mathrm{eff}} \sim N/100$ (see section 6.2). Then, I find $G_{1,\,\mathrm{RMS}}/2\pi \sim 10.4$ Hz.

6.4.1 Basics of dispersive readout with pump-probe experiments

The theory of the dispersive regime of an ensemble of spins 1/2 coupled to a resonator is described in section 3.4.2 from chapter 3. The resonance frequency ω_r of the uncoupled LER is shifted to higher or lower frequencies depending on the state of the spins in the ensemble:

$$\omega_r \quad \rightarrow \quad \omega_r + \sum_{i=1}^{N} \chi_i \langle \hat{\sigma}_{z,\,i} \rangle, \tag{6.9}$$

which depends on the expectation value $\langle \hat{\sigma}_{z,\,i} \rangle$ for each spin. Each weight χ_i in the sum is the single spin *dispersive shift*, defined as:

$$\chi_i := \frac{|G_{1,i}|^2}{\Delta_i} = \frac{|G_{1,i}|^2}{\omega_{q,\,i} - \omega_r}. \tag{6.10}$$

Here I do not use the modified detunings Δ_i' discussed in section 3.4.2. They can be replaced by $\Delta_i = \omega_{q,\,i} - \omega_r$ in these experiments, as they are two order of magnitude smaller than ω_r. Having different qubit frequencies $\omega_{q,\,i}$ accounts for any inhomogeneous broadening of the spin resonance.

At 10 mK all molecular spin qubits are considered to be initialized in the ground state ($|0\rangle$), with $\langle \hat{\sigma}_{z,\,i} \rangle \simeq -1$ for every spin. Then, the resonance frequency that is measured without exciting the spins is not ω_r, but the *reference frequency* ω_{ref}:

$$\omega_{\mathrm{ref}} := \omega_r - \sum_{i=1}^{N} \chi_i = \omega_r - \chi, \tag{6.11}$$

where χ is the ensemble dispersive shift. After this initialization by temperature, a control sequence of *pump* pulses is sent to excite the spin system, with carrier frequencies ω_d close to the qubit frequency ω_q. These pulses induce changes in the expectation values $\langle \hat{\sigma}_{z,\,i} \rangle$. The resulting new resonance frequency $\omega_{\mathrm{shifted}}$ is measured by sending *probe* pulses with frequencies close to ω_r. $\omega_{\mathrm{shifted}}$ is then compared to the reference frequency ω_{ref}:

$$\delta\omega_r := \omega_{\mathrm{shifted}} - \omega_{\mathrm{ref}} = \sum_{i=1}^{N} \chi_i \left(1 + \langle \hat{\sigma}_{z,\,i} \rangle\right). \tag{6.12}$$

The shift $\delta\omega_r$ contains the information of the changes in the expected values $\langle\hat{\sigma}_{z,i}\rangle$ of the spins generated by the excitation pulses. It also gives insight into the distribution in couplings ($G_{1\,i}$) and in qubit frequencies ($\omega_{q,i}$) through the dispersive shifts χ_i. Figure 6.12 summarizes the basic ingredients of the dispersive readout.

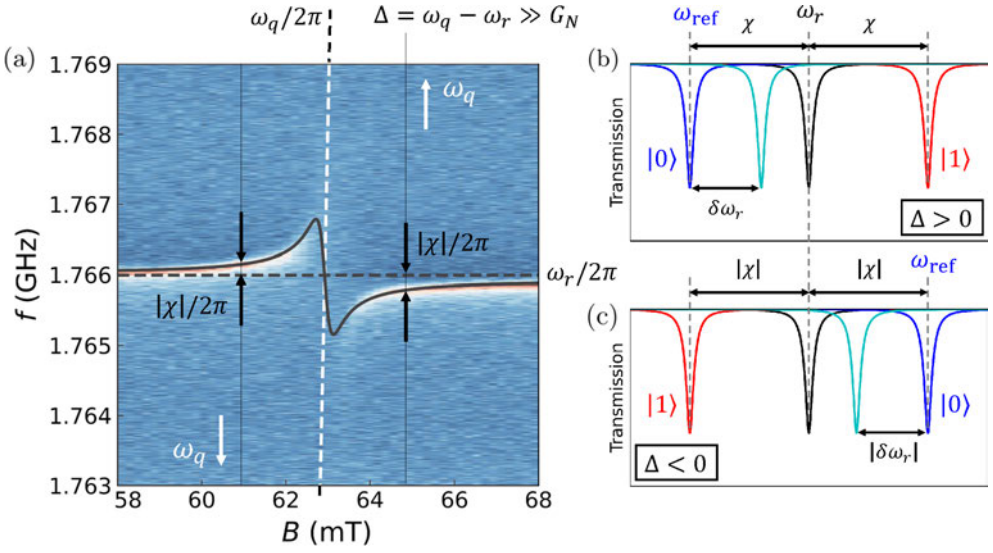

Figure 6.12: (a) Transmission of LER 10 of chip *Test 3* coupled to a PTM_r samples. The coupled LER resonance frequency $\tilde{\omega}_r$ (solid black line) is compared to the uncoupled LER resonance frequency ω_r (dashed black line). At 10 mK, with the spins initialized in the ground state, the solid black line also marks the position of the reference frequency ω_{ref} for magnetic fields in which the dispersive regime condition $|\Delta| = |\omega_q - \omega_r| \gg G_N$ is fulfilled. For $\Delta > 0$ (right hand side), the ensemble dispersive shift is positive ($\chi > 0$), and $\omega_{\text{ref}} = \omega - \chi$ is below ω_r. Conversely, for $\Delta < 0$ (left hand side), $\chi < 0$ and ω_{ref} is above ω_r. (b) Dispersive shift of ω_r for Δ, $\chi > 0$. The reference frequency ω_{ref} (blue resonance) associated with the ground state of the spins is lower than ω_r (black resonance). If all spins are excited, ω_r would be shifted by the same amount to higher frequencies (red resonance). Changes in the spin state are tracked by measuring the positive shift $\delta\omega_r$ between the LER resonance (cyan resonance) and comparing it to ω_{ref}. (c) Dispersive shift of ω_r for Δ, $\chi < 0$. ω_{ref} is now above ω_r, and any excitation of the spins is measured as a negative shift $\delta\omega_r$ from ω_{ref}.

6.4.2 Microwave generation and detection setups

Two sets of signals are required to measure the shift $\delta\omega_r$. First, a sequence of high power pulses with frequencies ω_{pump} close to ω_q are sent to control the spin state. These pulses change the expectation value $\langle\hat{\sigma}_{z,i}\rangle$ of each spin in the ensemble. Then, low power pulses with frequencies ω_{probe} close to ω_r are sent to

measure the resonance shift $\delta\omega_r$. The generation of this two different sequences of pulses, the *pump* sequence and the *probe* sequence, their interaction with the spins and the resonator, and the readout of the transmission probe signal constitute together what is called here the *pump-probe* experiment sketched in figure 6.13.

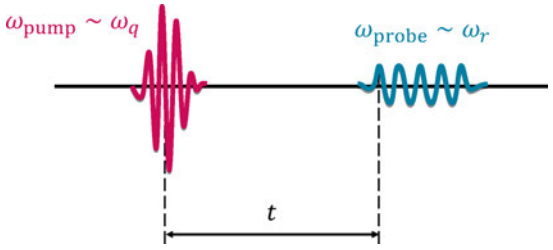

Figure 6.13: Scheme of a pump-probe experiment with a single high power pump pulse (magenta) with carrier frequency ω_{pump} close to ω_q followed after a time lapse t by a single low power probe pulse (cyan) with carrier frequency ω_{probe} close to ω_r.

The generation and detection stages for pump-probe experiments are shown in figures 6.14 and 6.15 respectively. The pump (magenta) and probe (cyan) signals are generated at a 0 dBm power level by the AWG through a single output line. A reference TTL signal (REF) generated also by the AWG triggers a switch that sends the pump signal to the excitation circuit and the probe signal to the readout circuit. In the former, the pump signal is amplified by 10 dB. The probe signal in the readout circuit is split into a local oscillator reference for the readout stage (LO) and the signal that goes through the cryogenic stage. The latter is attenuated by 20 dB. The pump and probe signals are combined again into a single line (IN) and led through the same port of the cryostat because *Test 3* has only one transmission line.

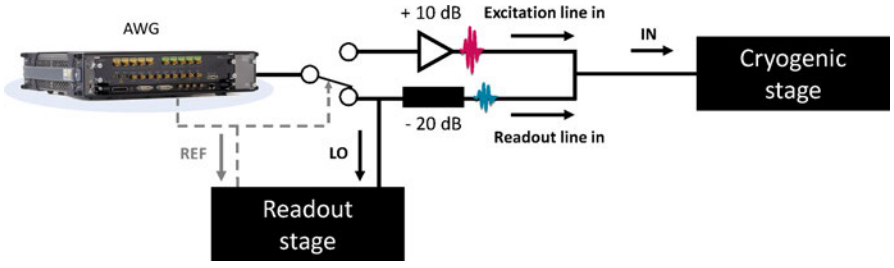

Figure 6.14: Generation stage for chip *Test 3* using an Arbitrary Waveform Generator (AWG), and its relation with the cryogenic and readout stages.

The output of the cryogenic stage (OUT) is the transmission of the pump and probe signals through *Test 3*. A second switch triggered by REF at the start of the detection stage sends the transmitted pump signal to the excitation

line and the transmitted probe signal to the readout line. The transmitted pump signal is sent to a channel of the oscilloscope.[2] The transmitted probe signal (RF) is amplified by 40 dB. After this amplification, the power of RF is roughly 0 dBm. An IQ mixer fed with the LO and RF signals demodulates the probe signal, extracting the in-phase (I, green) and quadrature (Q, yellow) components of RF. The detection stage ends with the acquisition of I and Q with the oscilloscope. The digitized I and Q signals are then sent to the computer for post-processing.

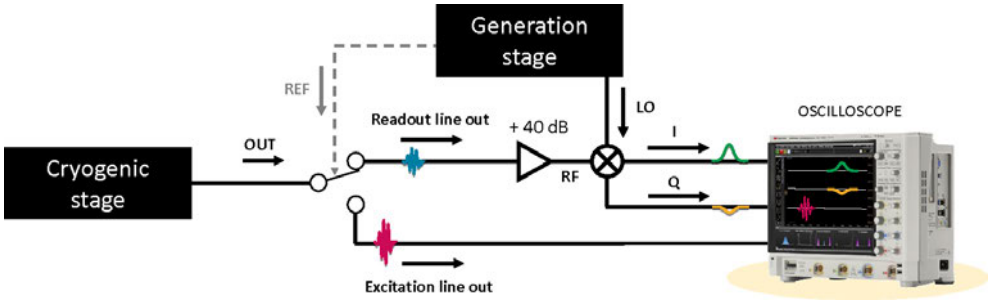

Figure 6.15: Detection stage for chip *Test 3* using an oscilloscope, and its relation with the cryogenic and generation stages.

6.4.3 Spin ensemble absorption spectrum and T_1 measurements

The qubit frequency was tuned to $\omega_q = 1.83$ GHz with the magnetic field B of 65 mT. At this field, there is a detuning $\Delta \,/\, 2\pi = (\omega_q - \omega_r) \,/\, 2\pi \sim 44$ MHz between ω_q and the resonance frequency $\omega_r \,/\, 2\pi = 1.7865$ GHz of *Test 3* LER 10. This detuning fulfills the dispersive regime condition $\Delta \gg G_N$. At 10 mK, the reference frequency is $\omega_{\text{ref}} = \omega_r - \chi$, which is below ω_r (positive dispersive shift χ). Any change in the spins from their ground state will induce a positive shift $\delta\omega_r$ from ω_{ref} (see figure 6.12b).

The pump sequence used here was a 50 μs pulse with a carrier frequency ω_{pump} close to ω_q. After the pulse, the induced shift $\delta\omega$ with respect to ω_{ref} immediately starts to decay to zero with a relaxation time T_1. In fact, there may be different times $T_{1,i}$ associated with the $\langle\hat{\sigma}_{z,i}\rangle$ of each spin. If some $T_{1,i}$ are very short, this imposes a limitation on the probe time for measuring $\delta\omega$. A simple solution is to calibrate the full resonance of the LER beforehand, then obtaining $\delta\omega_r$ from just a single pulse at a fixed frequency close to ω_r just after the excitation pulses. The calibration curve translates the IQ data of the transmission of the probe pulse into a frequency ω_{cal}. This frequency, compared to the known input probe frequency ω_{probe}, gives $\delta\omega_r$. The procedure

[2]The pump pulse is not measured, it is only sent to the oscilloscope to check it.

is illustrated in figure 6.16a. In fact, the difference $\omega_{\text{cal}} - \omega_{\text{probe}}$ has the opposite sign to $\delta\omega_r$:

$$\delta\omega_r := -\left(\omega_{\text{cal}} - \omega_{\text{probe}}\right). \tag{6.13}$$

The minus sign comes from the fact that it is not the input frequency that shifts to ω_{cal}, but the whole resonance in the opposite direction.

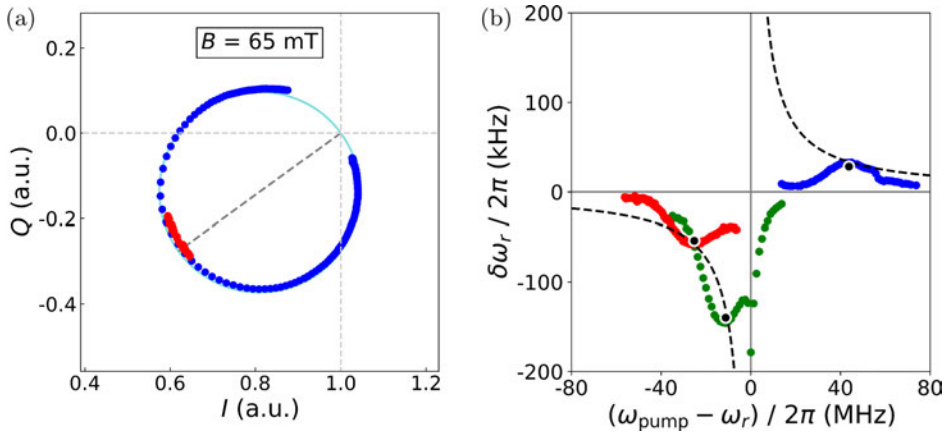

Figure 6.16: (a) Dispersive shift (red dots) of the point in the IQ plane (in-phase & quadrature) corresponding to a fixed readout frequency close to the resonance frequency ω_r of *Test 3* LER 10 as the drive frequency is swept around the qubit frequency ω_q, measured at 65 mT. In the absence of the pump pulse, the point would remain still in the plane. Blue dots are the calibration of the full resonance of LER 10 at 65 mT, which traces a circle in the IQ plane. The frequency associated to the shifted points (red dots) is then extracted by inverting this parametrized calibration curve ($I(\omega)$, $Q(\omega)$). (b) Measured shift $\delta\omega_r$ for pump frequencies ω_{pump} around the qubit frequency ω_q, measured at three fields: 62.3 mT (red dots), 63 mT (green dots) and 65 mT (blue dots). The maximum shift, in absolute value, measured at each field B is obtained for $\omega_{\text{pump}} = \omega_q = \mu_B g_S B/\hbar$. These maximum values (black dots) follow closely the predicted dependence with $1/\Delta$ (black dashed lines).

With this technique, the ensemble spin spectrum and the relaxation time T_1 of the PTM_r/PS samples were measured at 65, 63 and 62.3 mT. The latter two fields correspond to detunings $\Delta\ /\ 2\pi \sim$ -12.3 and -27.3 MHz, respectively. That is, at these two fields the qubit frequency ω_q is smaller than the bare resonator ω_r. This implies a negative dispersive shift χ, with the reference frequency ω_{ref} above ω_r and a negative shift $\delta\omega_r$ from it if the spins are excited, in agreement with the experimental results. It was necessary to use relatively long pulses (50 μs) and remove two 10 dBm attenuators from the cryostat lines in order to see a significant shift $\delta\omega_r$. This is pulse length is much longer than the expected ensemble decoherence time $T_2^* = 1/\gamma_\perp \sim 26.5$ ns, which means

that the microwave field generated by the line in this setup is too low to do coherent operations on the spins.

At each field, the ensemble spin spectrum was obtained by scanning over the pump frequency ω_{pump} and detecting the ensuing $\delta\omega_r$. The lineshape of PTM_r is inhomogeneously broadened, with a distribution of qubit frequencies $\omega_{q,\,i}$. Each pulse excites only the part of the distribution within its bandwidth, that is, in a frequency window $\Delta\omega_{\text{pump}} \sim 1/(50\,\mu\text{s}) = 20$ kHz centered at ω_{pump}. The sweep in ω_{pump} reconstructs the distribution of spins with different $\omega_{q,\,i}$.

The spectra measured at 62.3 mT, 63 mT and 65 mT (detunings $\Delta \simeq$ -27.3, -12.3 and 44 MHz) are shown in figures 6.17a-c, respectively. Also, figure 6.16b shows how the peaks of the spectra, i.e. the maximum shifts, in absolute value, measured at each field, follow closely the $1/\Delta$ dependence of the dispersive shift χ (and $\delta\omega_r$) predicted by equation (6.10).

The width of the spin resonance, in particular in relation to Δ, puts some spins with frequencies $\omega_{q,\,i}$ too close to ω_r, thus beyond the dispersive regime condition. This can be seen in the high-frequency end of the 62.3 mT spectrum not going back to $\delta\omega_r = 0$ and, most notably, in the 63 mT spectrum with $\delta\omega_r$ decreasing sharply as it crosses the LER frequency ω_r.

The spectra are fitted to Gaussian profiles with $\sigma = 10.01 \pm 0.24$ MHz. The half-width at half maximum (HWHM) of this distribution is $\sqrt{2\ln(2)}\sigma = 11.79 \pm 0.28$ MHz. This is consistent with the decoherence rate $\Gamma = 5.8 \pm 0.2$ estimated for the spin ensemble on LER 10 in section 6.3, where a Lorentzian profile $|1/i(\Gamma + (\omega_q - \omega_d)|$ with HWHM $= \sqrt{3}\Gamma = 10.0 \pm 0.3$ MHz is assumed.

Figure 6.17 also shows the measurement of the relaxation time T_1 for the same three fields. The pump frequency ω_{pump} was fixed to the value that gives the maximum of the spectrum shift at each magnetic field, $\omega_{\text{pump}} = \omega_q$. The time t between the pump and the probe pulses was varied between a few milliseconds and several seconds. The shift $\delta\omega_r$ decays back to ω_{ref} as the $\langle\hat{\sigma}_{z,\,i}\rangle$ expectation values relax to -1 with characteristic times $T_{1,\,i}$. The distribution of exponential decays can be fitted with a stretched exponential:

$$\delta\omega_r(t) := \delta\omega_r(0)e^{-(t/T_1)^x}, \tag{6.14}$$

where x is the stretch parameter, which takes here values around ~ 0.5. T_1 stands as an average relaxation time of the sample, with values of a few seconds for the three measured fields: 4.9 ± 0.2 s at 62.3 mT, 6.9 ± 0.2 at 63 mT and 8.5 ± 0.4 at 65 mT.

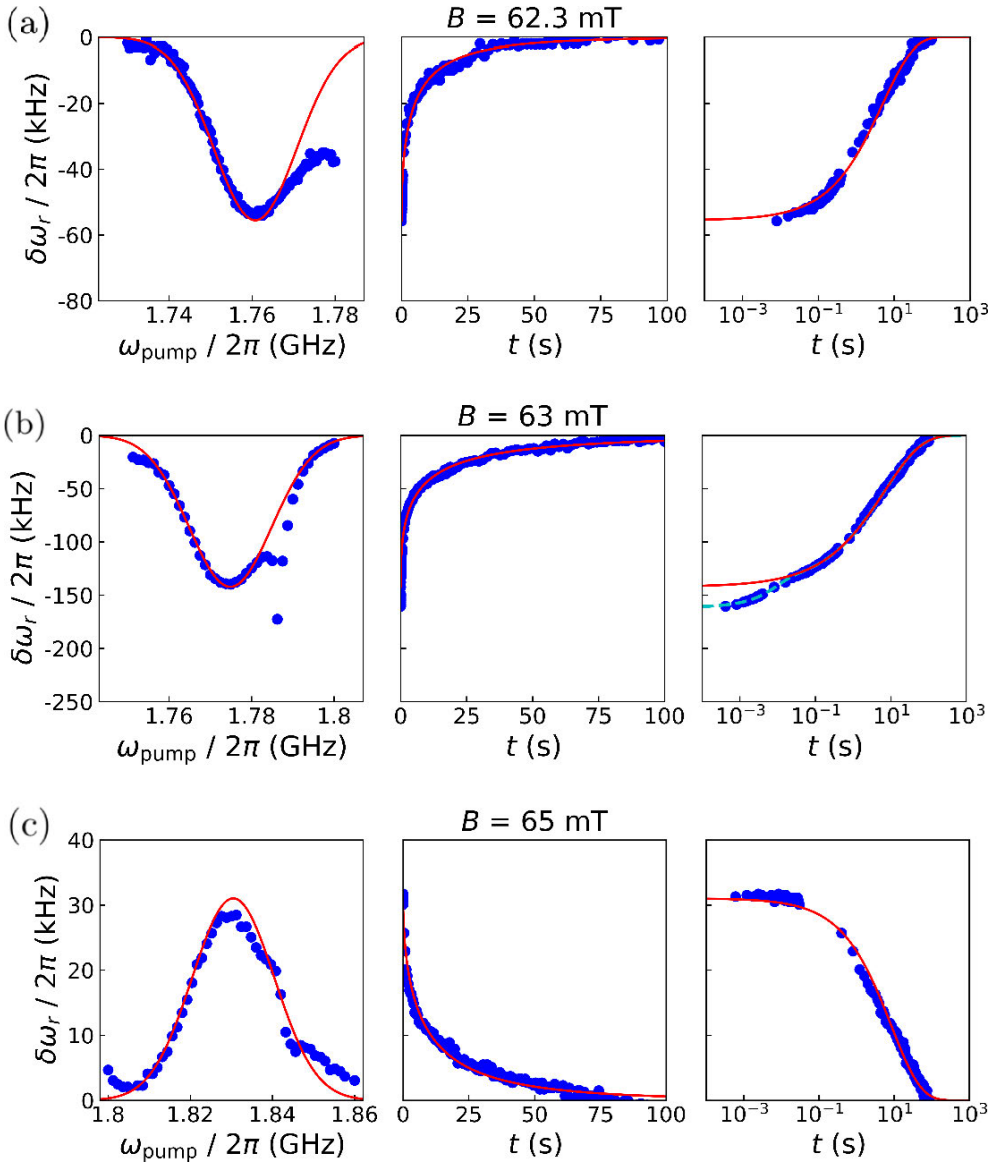

Figure 6.17: The shift ω_r in the LER resonance frequency with respect to the reference frequency ω_{ref}, measured for different drive frequencies ω_{pump} of the pump pulse and different times t between the pump and probe pulses (blue dots). The sweep in t is shown in linear and logarithmic time scales. These measurements were performed at three magnetic fields: 62.3 mT (a), 63 mT (b) and 65 mT (c). The sweep in ω_{pump} gives the inhomogeneously broadened ensemble spin spectrum of PTM_r, which is fit to a Gaussian profile (red solid line). The sweep in t gives the decay of $\delta\omega_r$ as the spins relax to their ground state. This decay has been fitted to a stretched exponential (red solid line, see equation (6.14)) that is the result of having a distribution of exponential decays with different characteristic times $T_{1,\,i}$ in the order of seconds. At 63 mT, where ω_q is closer to ω_r, an additional decay with a fast $T_1 \sim 8.6$ ms is observed at very short times.

A simple model of the distribution of spin-photon couplings accounts for the observed distribution in relaxation times. An ensemble of uncoupled spins would decay to their ground state with a single relaxation time T_1. However, spins coupled to a resonator in the dispersive regime have a small hybridization (of the order of $|G_1/\Delta| \ll 1$) with the wavefunction of a photon in the resonator (see section 3.4). The relaxation rate of the coupled spins is then:

$$\Gamma_{\parallel} := \frac{1}{T_1} + \left(\frac{G_1}{\Delta}\right)^2 \frac{1}{T_\kappa}, \tag{6.15}$$

where $T_\kappa = 1/(2\kappa) \sim 1.4$ μs is the photon lifetime in LER 10. The hybridization with the resonator imparts the distribution of spin-photon couplings $G_{1,i}$ to the decay times.

If a single wire is considered, these couplings, which are proportional to the magnetic field generate by the wire, can be assumed to scale with $1/r$, where r is the distance of the spin to wire. Integrating in a cylinder or radius R around the wire, one obtains the following expression for $\delta\omega_r(t)$:

$$\delta\omega_r(t) \propto e^{-(t/T_1)} \int_{r=w}^{R} \frac{\mathrm{d}\, r}{r} e^{-t/T_G(r)} \propto e^{-(t/T_1)} \int_{T_G(w)}^{T_G(R)} \frac{\mathrm{d}\, T_G}{T_G} e^{-t/T_G}, \tag{6.16}$$

where $T_G(r)$ is the time that characterizes the spin relaxation time induced by its coupling to photons. It is defined as:

$$T_G(r) := \left(\frac{r}{w}\right)^2 T_G(w) = \left(\frac{r}{w}\right)^2 \left(\frac{\Delta}{G_1(w)}\right)^2 T_\kappa. \tag{6.17}$$

Figure 6.18 compares the decay of $\delta\omega_r$ measured at 65 mT with the results of equation (6.16) for $T_1 \sim 60$ s, $T_G(w) = 0.2$ s and $T_G(R) = 250$ s. From these values, the single spin-photon couplings $G_1(w) \sim 116$ kHz and $G_1(R) \sim 3$ kHz are estimated. These values are of the same order of magnitude of single spin-photon couplings found in [1] for spins coupled to the inductor constriction. At 63 mT, where ω_q is closer to ω_r, the dispersive regime theory starts to fail and the effect of the coupling to the resonator is more prominent, generating an additional fast decay with a relaxation time of 8.6 ms (see figure 6.17b). This relaxation corresponds to a spin-photon coupling as high as ∼160 kHz.

Having very long spin relaxation times, even taking into account that they are shortened by the coupling to the resonator, places a limitation to the repetition time of the experiment. Before starting the next pump-probe experiment, the spins have to relax to their ground state. This means waiting $\sim 5T_1$, which in this case amounts to several minutes. However, a long T_1 also opens the possibility of measuring $\delta\omega_r$ by probing the whole LER resonance after the pump pulse. This is explored in the next sections.

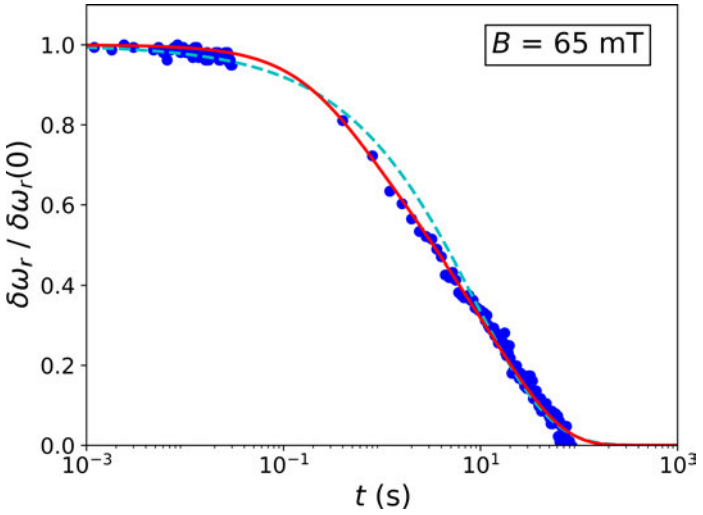

Figure 6.18: Decay of the shift ω_r in the LER resonance frequency with respect to the reference frequency ω_{ref} with the time t between the pump and probe pulses (blue dots), measured at 65 mT. The red solid line is the comparison with the model for the distribution of relaxation time from equation 6.16. The cyan dashed line is the fit with a stretched exponential decay.

6.4.4 Modulating T_1 with the magnetic field

An alternative, simple setup that allows measuring the LER resonance within a few milliseconds after the excitation of the spins is shown in figure 6.19. The probe sequence is now a train of pulses generated by a vector network analyzer (VNA). These pulses have carrier frequencies ω_{probe} spanning the whole resonance. The same VNA receives the transmitted signal and compares it to the sent pulses.

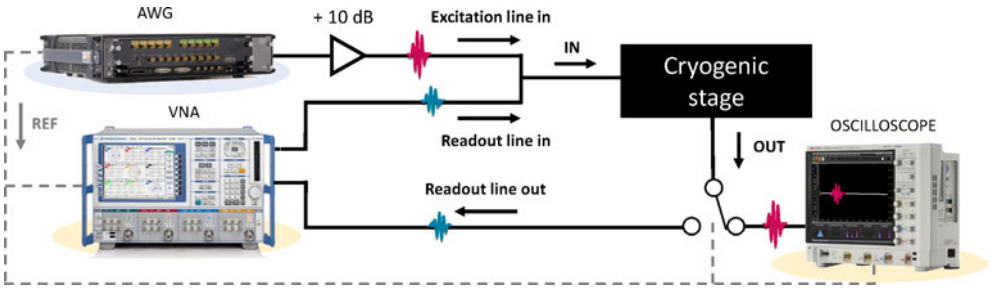

Figure 6.19: Generation and detection stages for chip *Test 3* using a vector network analyzer (VNA).

The shift $\delta\omega_r$ is obtained by comparing the resonance measured after a pump sequence (ω_{shifted}) with a reference measurement without exciting the

spins (ω_{ref}). Figure 6.20 compares the transmission of *Test 3* around the resonance frequency ω_r of LER 10 in these two situations, with the shift $\delta\omega_r$ clearly visible in the close-up of the measurement of the phase of the transmission parameter S_{21}.

Even if this shift is small compared to the width of the resonance, it can be faithfully recovered by fitting both resonances with the theory for the transmission through the transmission line for frequencies close to the resonance frequency of a LER, given by equation (4.66). The formula for the transmission parameter S_{21} is reproduced below:

$$S_{21}(\omega_d) = 1 - \frac{\kappa_c}{i(\omega_r - \omega_d) + \kappa}, \tag{6.18}$$

where $\omega_d \equiv \omega_{\text{probe}}$ is here the carrier frequency of each of the pulses of the probe sequence. The two resonances are fitted with the same resonator decay rate κ and line-resonator coupling κ_c, leaving ω_r as the only free parameter for each resonance.

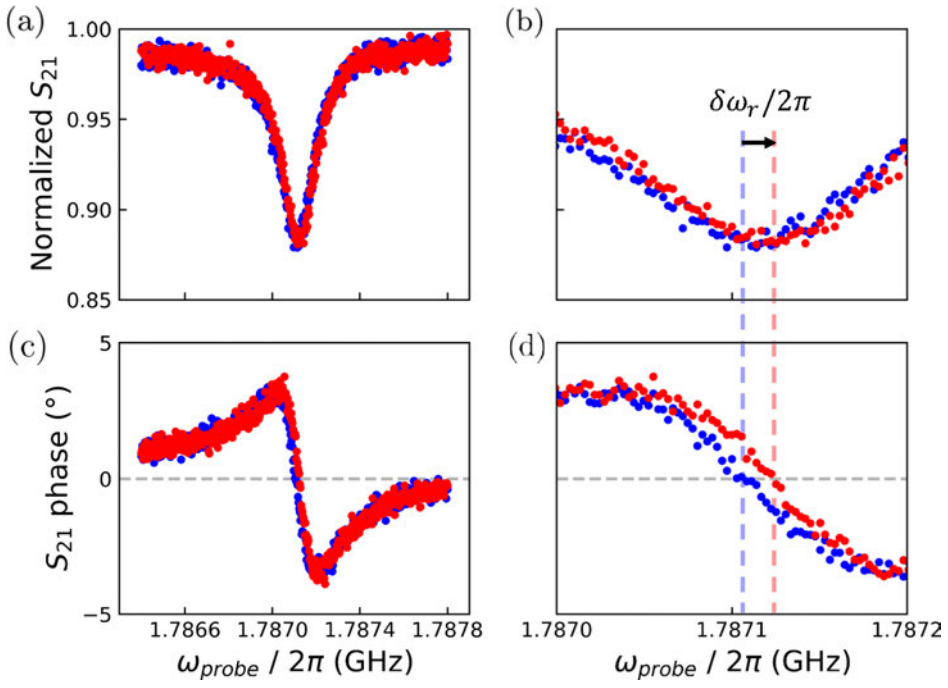

Figure 6.20: (a) Normalized module of the complex-valued transmission S_{21} of *Test 3* for probe frequencies close to the LER 10 resonance frequency ω_r, measured at $B =$ 65 mT. Two situations are compared: blue dots show the resonance without exciting the spins, red dots show the same resonance after a pump pulse at the qubit frequency $\omega_q = \mu_{\text{B}} g_S B/\hbar$ has been applied. (b) Close-up centered at ω_r, showing the shift $\delta\omega_r$ of the center frequency of the resonance. Figures (c, d) illustrate more clearly this shift with the measurement of the phase of S_{21}.

The spectrum of the PTM ensembles was measured with this technique at two fields with detuning $\Delta/2\pi = (\omega_q - \omega_r)/2\pi \simeq \pm$ 40 MHz. Figure 6.21 shows the change in $\delta\omega_r$ as the pump frequency is swept in the vicinity of the spin resonance frequency ω_q for each field. As in the previous section, the sign of the shift $\delta\omega_r$ follows the sign of Δ, which confirms that the effect is due to the coupling of the LER to the spin ensemble. Both spectra fit to a Gaussian lineshape with $\sigma = 10.01$ MHz. This confirms that the results of measuring the whole resonance are compatible with those obtained from measurements with a single probe pulse.

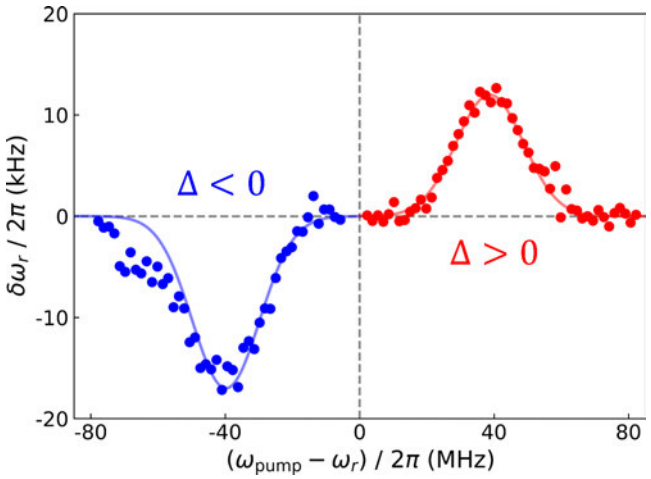

Figure 6.21: Shift $\delta\omega_r$ of *Test 3* LER 10 resonance frequency for pump frequencies ω_{pump} around the qubit frequency ω_q, measured at two magnetic fields with detunings $\Delta/2\pi = (\omega_q - \omega_r)/2\pi \simeq \pm$ 40 MHz (blue dots for negative Δ, red dots for positive Δ). The sign of the shift $\delta\omega_r$ follows the sign of Δ. In both cases, the dependence of $\delta\omega_r$ with ω_{pump} traces the absorption spectrum of the spin ensemble, centered at $\omega_q = \mu_B g_S B/\hbar$, which is fit to a Gaussian lineshape with $\sigma = 10.01$ MHz (solid lines).

Similarly, the decay of the shift $\delta\omega_r$ with the delay time between the pump pulse and probe sequence was measured again, now for a wider range of magnetic fields. Figure 6.22 shows the results of these measurements, in which $\delta\omega_r$ decays faster as the field is brought closer to the spin-LER resonance field $B_{\text{res}} = \hbar\omega_r/\mu_B g_S$. This is the well known *Purcell effect*, the enhancement of the effective decay rate of the spins due to their coupling to a cavity (in this case, the resonator). $\delta\omega_r$ is normalized at each field by $|\delta\omega_r|$, which is the shift measured by triggering the VNA right after the pump pulse. The assignation of a precise delay time is not possible for measurements with $t < 0.1$ s. This is due to the relatively slow VNA measurement, compared to the arbitrarily short pulses generated by the AWG, as well as any additional delay introduced by the triggering of the VNA.

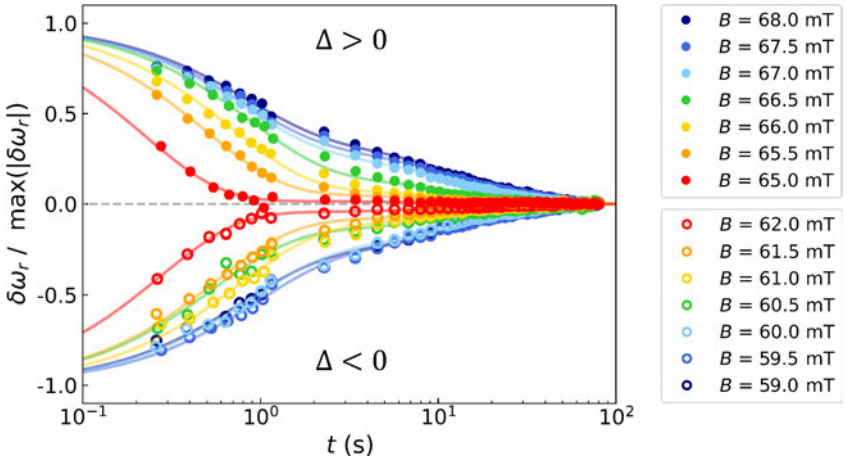

Figure 6.22: Shift $\delta\omega_r$ of *Test 3* LER 10 resonance frequency for different delay times t between the pump pulse and the probe sequence, measured at several magnetic field between 59 and 68 mT. This magnetic field includes both positive and negative detunings $\Delta/2\pi = (\omega_q - \omega_r)/2\pi$. The decay of $\delta\omega_r$ is faster for fields associated to smaller Δ (in absolute value). Solid ($\Delta > 0$) and open ($\Delta < 0$) are experimental data, solid line show their fit to a sum of two exponential decays with different characteristic times (see equation (6.19)).

Lacking the time range below $t \sim 0.1$ s, instead of explaining these results with the model of equation (6.16) is better to use a simpler model that captures the two timescales that are observed the experiment:

$$\delta\omega_r(t) = \delta\omega_r(0)\left[C_G e^{-t/T_{1,\,\mathrm{fast}}} + (1 - C_G)e^{-t/T_{1,\,\mathrm{slow}}}\right], \tag{6.19}$$

where C_G is the ratio of the contributions to $\delta\omega_r$ of spins with the shorter decay time $T_{1,\,\mathrm{fast}}$ (faster relaxation induced by resonator) and spins with the longer decay time $T_{1,\,\mathrm{slow}}$. This ratio can be related to the collective spin-photon coupling of each set of spins:

$$C_G := \frac{(\delta\omega_r)_{\mathrm{fast}}}{(\delta\omega_r)_{\mathrm{slow}}} \simeq \frac{\chi_{\mathrm{fast}}}{\chi_{\mathrm{slow}}} \simeq \left(\frac{(G_N)_{\mathrm{fast}}}{(G_N)_{\mathrm{slow}}}\right)^2. \tag{6.20}$$

Here it has been assumed that the distribution in $\langle\sigma_{z,i}\rangle$ generated by the inhomogeneity of the microwave magnetic field generated by the line is not correlated to the distribution of single spin-photon couplings to the resonator, which depends on the inhomogeneity of the microwave field generated by the resonator inductor. The same detuning Δ has been assumed as well.

The C_G ratio and the shorter decay time $T_{1,\,\mathrm{fast}}$ that result form the fit to equation (6.19) of the decay of $\delta\omega_r$ for each magnetic field are shown in figure 6.23. All fields were fitted with a longer decay time $T_{1,\,\mathrm{fast}} \sim 15$ s associated to spins in the ensemble that are more weakly coupled to the resonator.

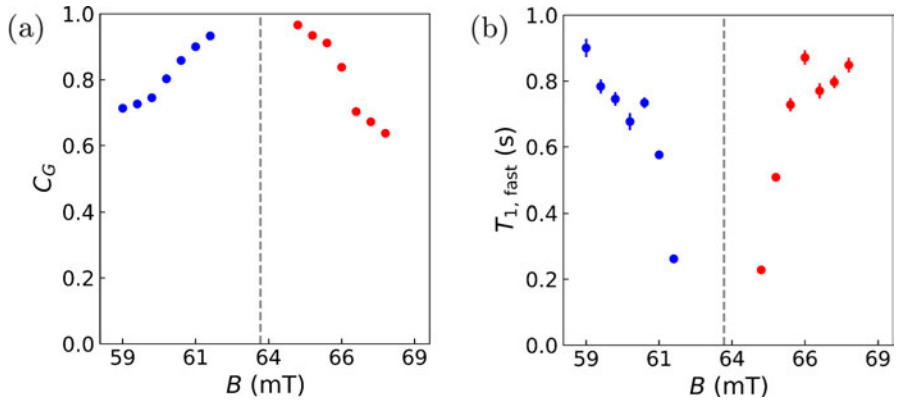

Figure 6.23: Magnetic field dependence of the C_G ratio (a) and the shorter decay time $T_{1,\,\mathrm{fast}}$ (b) that result form the fit of the decay of $\delta\omega_r$ with equation (6.19). All fields were fitted with a longer decay rate $T_{1,\,\mathrm{fast}} \sim 15$ s. Blue dots used for magnetic fields with negative Δ, red dots for fields with positive Δ. The grey dashed line marks the spin-LER resonance field $B_{\mathrm{res}} = \hbar\omega_r/\mu_{\mathrm{B}} g_S$.

As the magnetic field is set closer to the spin-LER resonance field $B_{\mathrm{res}} = \hbar\omega_r/\mu_{\mathrm{B}} g_S$, the decay time $T_{1,\,\mathrm{fast}}$ decreases sharply due to the influence of the resonator. Also, the increase of C_G towards 1 means that the resonator-induced decay of the fast decaying spins provides the dominant contribution to $\delta\omega_r$, over that of the weakly-coupled and slow decaying spins. That is, the relaxation rate of the isolated spins is so long that any hybridization with the resonator becomes the faster pathway for relaxation, unless Δ is made large enough and the spins become effectively decoupled from the photons. However, increasing the detuning has the drawback of having a lower shift $\delta\omega_r$, which scales with $1/\Delta$. In the end, there is a trade-off between the optimization of magnitude of the shift by decreasing Δ and having a sufficiently long effective decay time by increasing Δ.

6.5 Towards a coherent manipulation of molecular spin qubits

6.5.1 Testing the setup for shorter pump pulses

The pump-probe experiments described in section 6.4 were carried out with 50 μs long pump pulses in order to see a change in $\delta\omega_r$. These pulses are way too long to coherently manipulate the spins, as they should be shorter than the decoherence time $T_2^* = 1/\gamma_\perp \sim 26.5$ ns (see table 6.3). The duration of the pump pulse can be reduced by increasing the microwave power.

Test 4 was designed to overcome the power limitation of using a single transmission line for both pump and probe pulses. With its two lines (see figure 6.1b), the pump and probe pulses can be sent through two distinct coaxial lines in the cryostat. The input readout line keeps the 50 dB attenuation of the scheme shown in figure 6.5, while all the attenuators are removed removed from the input excitation line. The amplifier at 4 K is then mounted only at the output of the readout line. The main problem that can arise is a leaking from the excitation line into the readout line through the resonator, damaging the cryogenic amplifier and the detection instruments. However, by working in the dispersive regime ($|\Delta| \gg G_N \sim 3$ MHz) and high quality factor resonators ($Q \sim 16000$, $\kappa = 55.5$ kHz for LER 10), the high power pump signal is filtered by the resonator bandwidth because $\Delta \gg \kappa$. The same PTM/PS samples used in *Test 3* were deposited on top of each LER in *Test 4* (see figure 6.24a). The interfacing of the chip with the excitation and readout lines in the cryostat is shown in figures 6.24b-d.

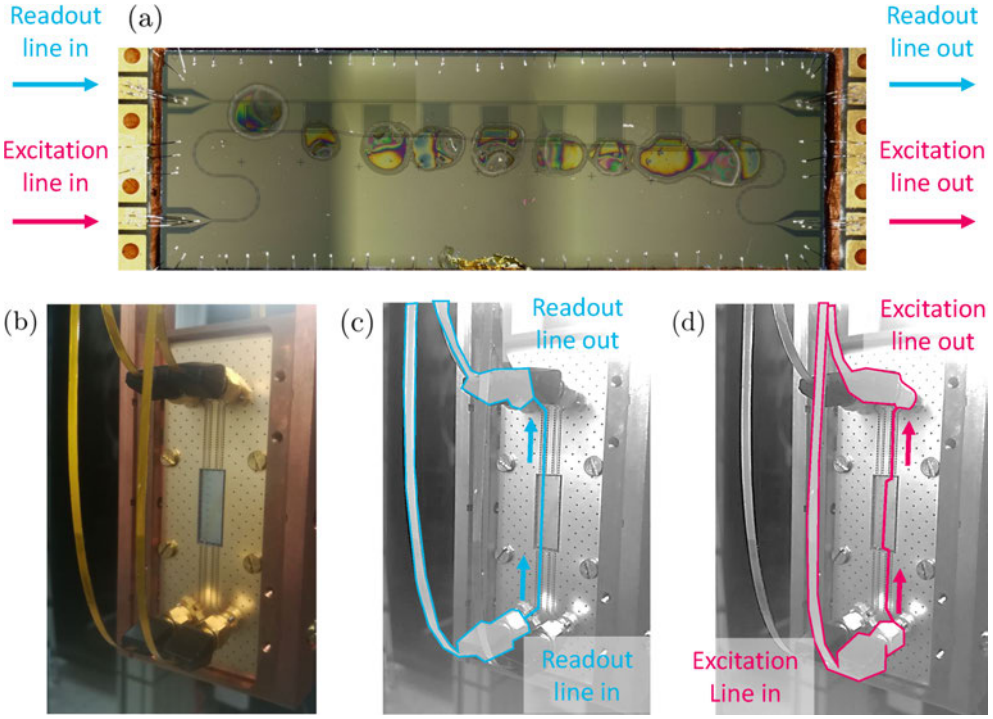

Figure 6.24: (a) PTM/PS deposits in *Test 4*. (b) Interfacing of *Test 4* with the excitation and readout lines in the cryostat (flexible cables). Readout and excitation lines are highlighted in figures (c, d).

The detection method of $\delta\omega_r$ in these new experiments with shorter pulses is a compromise between the techniques used in sections 6.4.3 and 6.4.4. The former required a previous fine calibration of the resonance to indirectly obtain

$\delta\omega_r$ with a single probe pulse, but the pulse could be easily triggered right after the pump pulse, thus minimizing the decay of $|\delta\omega_r|$. Conversely, the latter recovers the full shifted resonance, giving a nice visualization of $\delta\omega_r$ (see figure 6.20), but the slow VNA measurement tends to reduce $|\delta\omega_r|$. Here, the AWG was programmed to generate a train of probe pulses, each of a different frequency spanning the resonance, in the style of a VNA measurement. This way, $|\delta\omega_r|$ can be optimized by measuring the resonance much faster with shorter probe pulses, their length limited only by the time it takes for the resonator to reach its steady state ($t \gg 1/\tilde{\kappa}$). In addition, the AWG generates both the pump and probe pulses, which allows sending with precision the probe sequence right after the excitation of the spins.

Figure 6.25 summarizes the changes in the microwave setup for the pump-probe experiments in this section. A microwave switch triggered by the reference signal of the AWG is needed in the generation stage to send the pump and probe signals to their corresponding lines (the excitation and the readout lines). From then on, the design of *Test 4* with two transmission lines allows managing each signal independently.

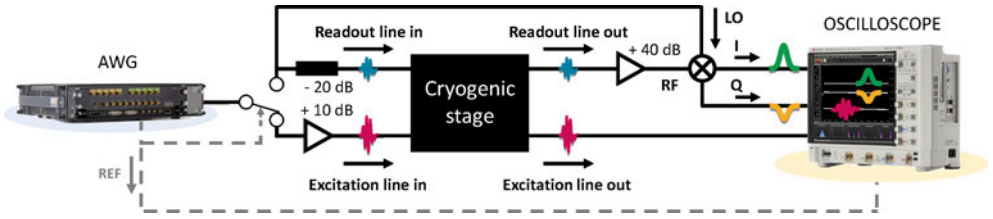

Figure 6.25: Generation and detection stages for chip *Test 4* using an Arbitrary Waveform Generator (AWG) and an oscilloscope. The setup is similar to that in figures 6.14 and 6.15, with some small changes. A microwave switch triggered by the reference signal of the AWG is needed in the generation stage to send the pump and probe signals to their corresponding lines (the excitation and the readout lines). From then on, the design of *Test 4* with two transmission lines allows managing each signal independently. The pump signal is amplified before the cryogenic stage to optimize the microwave power in the excitation line, and therefore the microwave magnetic field that drives the spins. At the output of the cryogenic stage, only the probe signal in the readout line is amplified.

The oscilloscope receives the in-phase (I) and quadrature (Q) components of the transmission of the probe pulses, acquiring the whole train of pulses in a single shot with a low sampling rate (see figure 6.26). The acquired data are processed by discarding the first $5/\tilde{\kappa} \sim 12$ μs of each pulse, when the resonator is charging, then averaging the I and Q levels in the steady state. The results are analysed as detailed in section 6.4.4: the LER resonance is fitted with (ω_{shifted}) and without (ω_{ref}) exciting the spins, obtaining the shift

of the resonance as $\delta\omega_r = \omega_{\text{shifted}} - \omega_{\text{ref}}$. Figure 6.27 shows an example of the resonance shift obtained in one of these experiments.

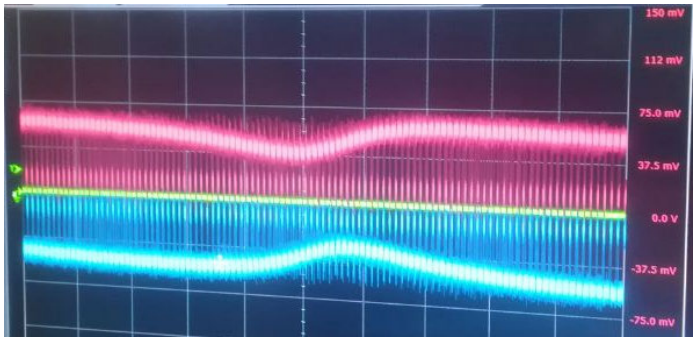

Figure 6.26: Photo of the oscilloscope screen acquiring I (magenta) and $-Q$ (cyan) signals for a train of probe pulses with carrier frequencies spanning the whole LER resonance.

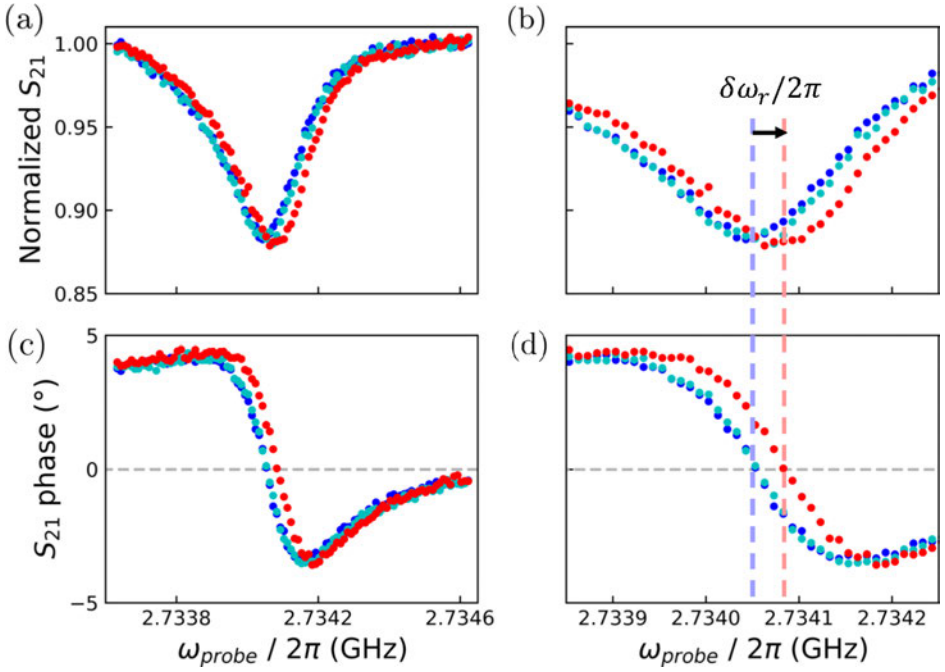

Figure 6.27: (a) Normalized module of the complex-valued transmission S_{21} of *Test 4* for probe frequencies close to the LER 1 resonance frequency ω_r, measured at $B = 99.08$ mT. Three situations are compared: blue dots show the resonance without exciting the spins, red dots show the same resonance measured after a pump pulse at the qubit frequency $\omega_q = \mu_B g_S B/\hbar$, and cyan dots are those measured after a pump pulse at the 'mirror' frequency $\omega_r - \Delta$. (b) Close-up picture of the resonance, centered at ω_r, showing its shift $\delta\omega_r$. Figures (c, d) illustrate more clearly this shift with the measurement of the phase of S_{21}.

Setting the magnetic field at 99.08 mT, the resonance of *Test 4* LER 1 was measured without the pump pulse (blue dots). The detuning at this field is $\Delta/2\pi = (\omega_q - \omega_r)/2\pi \simeq 40$ MHz. The same resonance was measured again after sending a 50 μs long pump pulse with carrier frequency $\omega_q/2\pi = \mu_B g_S B/h = 2.77424$ GHz, observing a shift $\delta\omega_r$ to higher frequencies (red dots). As a comparison, the resonance was also measured after pumping at a frequency $\omega_r - \Delta = 2.69424$ GHz (cyan dots). This 'mirror' frequency is as close to ω_r as ω_q, but no shift $\delta\omega_r$ is observed. This rules out that the shift be associated to some non-linear effect of the resonator due to the microwave power of the pump pulse leaking into the resonator.

6.5.2 Parallel pathways to generate the dispersive shift

I consider first experiments in which the excitation of the spins is induced with a square pulse. This method introduces two excitation paths that generate different dispersive shifts. The results provide an interesting insight of the nature of the states of the hybrid spin-resonator system. The magnetic field was set at $B = 98.36$ mT, with ω_q above the resonance frequency ω_r of *Test 4*. This choice sets the qubit-resonator detuning at $\Delta/2\pi = (\omega_q - \omega_r)/2\pi \simeq 20$ MHz.

The shift $\delta\omega_r$ of the resonance of LER 1 was measured for excitation pulses with carrier frequency $\omega_{\text{pump}} = \omega_q$ and pulse lengths between 10 and 500 ns. The results of this experiment are shown as red dots in figure 6.28a. As a comparison, blue dots show the result of a measurement performed with the same frequency but at zero field, where the spins and the resonator are completely decoupled and the pump pulse has no effect on the resonator frequency.

An oscillation is observed in the data measured at $B = 98.36$ mT pumping at $\omega_{\text{pump}} = \omega_q$, with a period T = 50 ns. However, the same experiment pumping at the 'mirror' frequency $\omega_{\text{pump}} = \omega_r - \Delta$ yield oscillations with similar amplitude and period, but at over a lower $\delta\omega_r$ base level (cyan dots in figure 6.28b). This means that these oscillations are not Rabi oscillations. An additional experiment was carried out pumping at $\omega_{\text{pump}} = (\omega_r + \omega_q)/2 = \omega_r + \Delta/2$. This time, the period doubles to T = 100 ns.

These results suggest that the period of the oscillation is related to the detuning between the pump frequency ω_{pump} and the resonator frequency ω_r. In figure 6.28a, the period matches $2\pi/|\omega_{\text{pump}} - \omega_r| = 2\pi/\Delta$. Similarly, in figure 6.28b the period equals $2\pi/|\omega_{\text{pump}} - \omega_r| = 4\pi/\Delta$. I argue next that the relation between pump pulse duration and $\omega_{\text{pump}} - \omega_r$ is a consequence of using square pulses.

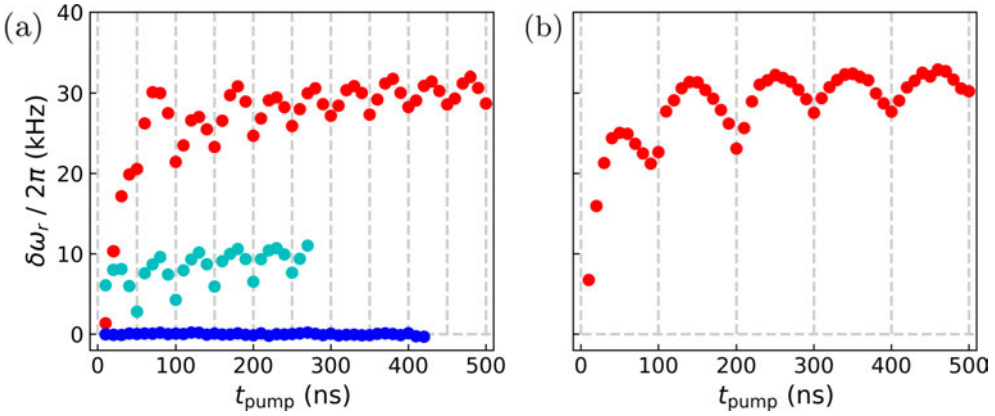

Figure 6.28: (a) Dependence of $\delta\omega_r$ on the length of the pump pulse, t_{pump}. Three experiments are shown. Red dots are the result of pumping at the qubit frequency ω_q at a magnetic field $B = 98.36$ mT, where the qubit-resonator detuning is $\Delta/2\pi \simeq 20$ MHz. Blue dots show the same experiment carried out at zero field, when spins and resonator are decoupled. Finally, cyan dots show the result of pumping at the 'mirror' frequency $\omega_r - \Delta$, again with a magnetic field $B = 98.36$ mT. (b) Dependence of $\delta\omega_r$ on the length of the pump pulse, t_{pump}. The pump frequency is in the middle between ω_r and ω_q: $\omega_{\text{pump}} = (\omega_r + \omega_q)/2 = \omega_r + \Delta/2$. The magnetic field was again at $B = 98.36$ mT.

The Fourier transform of a square pulse of length t_{pump} is the cardinal sine function function $\text{sinc}(x) = \sin(x)/x$, with $x = (\omega_{\text{pump}} - \omega_r)t_{\text{pump}}/2$. The zeros of this function are located at $x = n\pi$, that is, $(\omega_{\text{pump}} - \omega_r)t_{\text{pump}}/2\pi = n$, where $n \neq 0$ an integer (see figure 6.29). This is precisely the condition that is met by the values of t_{pump} at which the oscillation minima are observed in $\delta\omega_r$ (see vertical dashed lines in figure 6.28). The underlying physical origin of these oscillations is then that a small part of the microwave power of the pulse directly drives the resonator except when this condition is met. The fact that the excitation of the resonator by the sideband frequencies of the pump pulse leads to changes in $\delta\omega_r$ shows that those excitation carry some spin changes with them. As a proof, the measurement performed at zero field shows no change in $\delta\omega_r$ (see figure 6.28a).

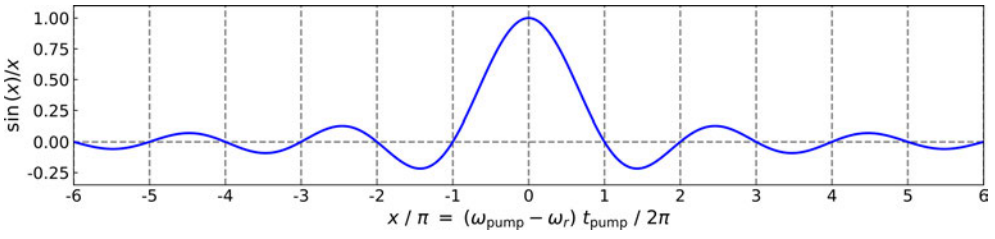

Figure 6.29: The cardinal sine function $\text{sinc}(x) = \sin(x)/x$, with $x = (\omega_{\text{pump}} - \omega_r)t_{\text{pump}}/2$. The zeros of this function are located at $x = \pi$.

The mechanism through which an excitation of the resonator changes $\delta\omega_r$ can be understood by recalling what do exciting the qubit or the resonator actually mean in the context of the dispersive regime. Assuming positive detuning ($\Delta > 0$), the hybrid qubit-resonator excited states can be approximated by (see section 3.4):

$$\begin{aligned} |\psi_{n,+}\rangle &\simeq \frac{g_1\sqrt{n}}{\Delta}\Big| \, |\psi_{n,g}\rangle + |\psi_{n-1,e}\rangle \\ |\psi_{n,-}\rangle &\simeq |\psi_{n,g}\rangle - \left|\frac{g_1\sqrt{n}}{\Delta}\right| |\psi_{n-1,e}\rangle \, . \end{aligned} \tag{6.21}$$

Figure 6.30 shows the energy levels of the spin-resonator system in the dispersive regime up to $n = 2$. From the ground state $|\psi_{0,g}\rangle$, the only transition with a frequency close to ω_r is the $|\psi_{0,g}\rangle \leftrightarrow |\psi_{1,-}\rangle$ transition, with frequency $\omega_{\text{ref}} = \omega_r - \chi$. This is the resonance that is observed in the absence of a pump pulse. The pump pulse, with carrier frequency ω_q, generates the qubit excitation $|\psi_{0,e}\rangle$, which is not a stationary state of the system. Using equation (6.21), this state can be written as the superposition $|\psi_{0,e}\rangle \simeq |\psi_{1,+}\rangle - (g_1/\Delta)\,|\psi_{1,-}\rangle$. From $|\psi_{1,+}\rangle$, the only transition with a frequency close to ω_r is the $|\psi_{1,+}\rangle \leftrightarrow |\psi_{2,+}\rangle$ transition, with frequency $\omega_r + \chi = \omega_{\text{ref}} + 2\chi$. This is the standard procedure to measure the dispersive shift of ω_r.

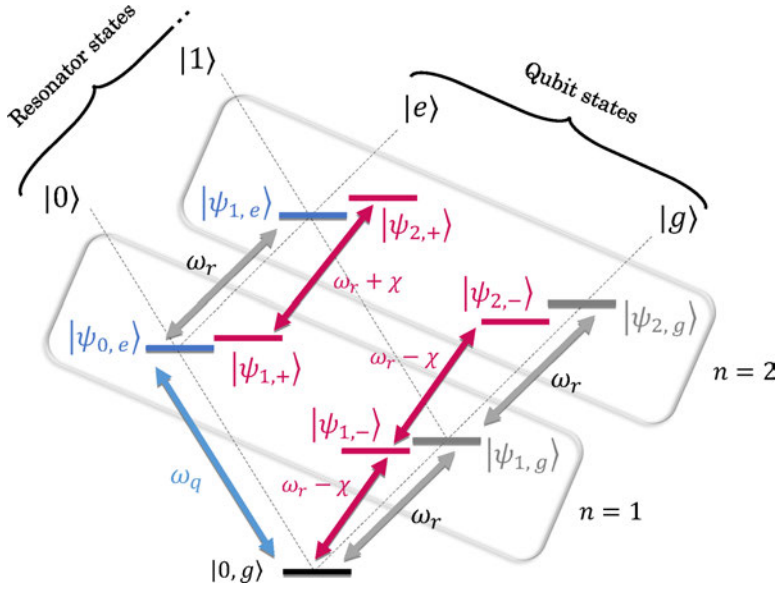

Figure 6.30: Energy levels of the spin-resonator system in the dispersive regime up to $n = 2$. Stationary states of the hybrid system are shown in magenta, with the independent excitations of the spin and the resonator in blue and grey for reference. Transitions between $|\psi_{n,-}\rangle$ states resonate at $\omega_{\text{ref}} = \omega_r - \chi$, while transitions between $|\psi_{n,+}\rangle$ states resonate at $\omega_r + \chi = \omega_{\text{ref}} + 2\chi$.

There is, however, another way of generating the state $|\psi_{1,+}\rangle$. Pumping at a frequency ω_r produces the resonator excitation $|\psi_{1,g}\rangle$. This is not a pure stationary state of the hybrid system. Inverting the relations in equation (6.21), this state can be written as the superpositio $|\psi_{1,g}\rangle \simeq |\psi_{1,-}\rangle + (g_1/\Delta)\,|\psi_{1,+}\rangle$. That is, $|\psi_{1,+}\rangle$ can be generated by the driving at the resonator frequency ω_r, although not efficiently ($|\psi_{1,+}\rangle$ is only a small part, of the order of $g_1/\Delta \ll 1$, of the resonator excitation). The resulting contribution to the dispersive shift is usually negligible, as the pump pulse is sent at ω_q, and the probe pulse at ω_r has a very low microwave power. However, the leaking of the square pump pulse with carrier frequency ω_q into the resonator whenever $(\omega_{\rm pump}-\omega_r)t_{\rm pump}/2\pi \neq 1$ has enough power to excite $|\psi_{1,+}\rangle$ significantly. The experiments provide a direct detection of the degree of 'mixture' between the spin and photon excitations at the given magnetic field (and Δ).

6.5.3 Detection of damped oscillations

The results shown in figure 6.28a are the combination of truly pumping the spins at a frequency close to ω_q (the main peak of the sinc function) and the excitation of the resonator with the frequency sidebands of the pulse. The latter can be removed by subtracting the measurement of $\delta\omega_r$ at the 'mirror' frequency $\omega_r-\Delta$, which displays the same fast oscillations due to the resonator excitation but involves no direct spin excitations. Figure 6.31 shows the hint of a damped Rabi oscillation that is recovered with this subtraction.

The fit of $\delta\omega_r$ to a damped oscillation gives a decay time $\tau = 43 \pm 4$ ns and a period $\mathrm{T} = 94 \pm 6$ ns. The time it takes for the pump pulse to invert the population is half the period, when $\delta\omega_r$ is maximum (without the damping). This time is the optimal length of the π-pulse, $t_\pi = \mathrm{T}/2 = 47 \pm 3$ ns. Both t_π and τ are similar in the experiment. τ is of the same order of the ensemble decoherence time $T_2^* = 1/\gamma_\perp \simeq 26.5$ ns. The damping of the oscillation arises from the comparison between the bandwidth of the pulse and the width of the spin spectrum. As the length of the pulse increases beyond T_2^*, the bandwidth of the pulse becomes thinner than the width of the spectrum, thus not exciting part of the spin ensemble.

A more practical removal of the effect of the leakage of the pump pulse into the resonator is the use of Gaussian pulses. The Fourier transform of a Gaussian pulse is a Gaussian distribution of frequencies, without the sidebands of the sinc function that cause the leakage. Figure 6.31b shows the result of repeating the measurement of $\delta\omega_r$ using Gaussian pulses. The pulse length is defined in this case as $t_{\rm pump} = 2\sigma$. The oscillation with $1/\Delta$ that was present for square pulses is gone, leaving only the damped Rabi oscillations. The fit of

$\delta\omega_r$ to a damped oscillation yields a decay time $\tau = 37.8 \pm 0.8$ ns and π-pulse length $t_\pi = 28.2 \pm 0.2$ ns.

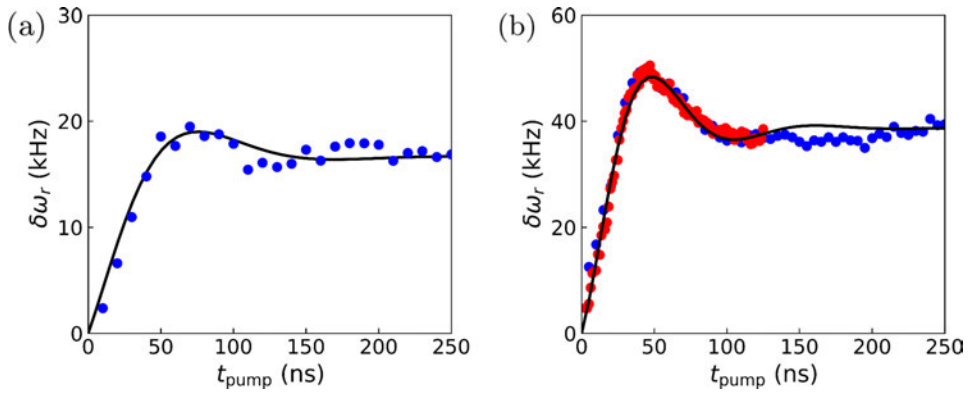

Figure 6.31: (a) Difference between the measurement of $\delta\omega_r$ sending a square pulse at the qubit frequency $\omega_q = \omega_r + \Delta$ (red dots in figure 6.28a) and at the 'mirror' frequency $\omega_r - \Delta$ (cyan dots in that same figure). The black solid line is the fit to a damped oscillation with with decay time $\tau = 43 \pm 4$ ns and a period T $= 94 \pm 6$ ns. The time it takes for the pump pulse to invert the population (π-pulse, maximum $\delta\omega_r$) is $t_\pi = \mathrm{T}/2 = 47 \pm 3$ ns. (b) Dependence of $\delta\omega_r$ on the length of the pump pulse, $t_{\mathrm{pump}} \equiv 2\sigma$, pumping at the qubit frequency ω_q with a Gaussian pulse. Two data sets are show. First, the $\delta\omega_r$ was measured with increasing t_{pump} up to 250 ns (blue dots). Then, the time range around the maximum of the oscillation was measured with a shorter step in the t_{pump} sweep (red dots). The black solid line is the fit to a damped oscillation with with decay time $\tau = 37.8 \pm 0.8$ ns and π-pulse length $t_\pi = 28.2 \pm 0.2$ ns.

6.6 Conclusions

The dispersive readout of molecular spin qubits coupled to lumped-element resonators has been demonstrated in this chapter. The absorption spectrum and the relaxation time T_1 of the spin ensemble can be obtained from the shift $\delta\omega_r$ of the LER resonance in pump-probe experiments. In addition, these measurements give some insight on the role of the resonator on the spin relaxation. An estimation of the highest single spin-photon couplings (as high as $\sim$160 kHz) and their distribution can be obtained as well.

With short pulses (10–500 ns), the first signs of coherent manipulation of the spin ensemble have been detected in a specific superconducting chip designed for that purpose (*Test 4*). π-pulse lengths t_π similar to the ensemble decoherence rate T_2^* are obtained.

A limitation of these experiments is the distribution of microwave magnetic fields in the sample. Each spin is driven by a different field b_{mw}, which reduces

the precision of the experiment compared to the ideal case of all the spins being driven together. This can be improved in future experiments by designing an excitation line that generates a more homogeneous microwave field in the sample. A promising proposal consists on two-sided superconducting chips, one side with the LERs coupled to the readout line and the other with the excitation line. This would give freedom to design a excitation line with a loop at the position of the LER inductor with the sample (on the opposite side). Another possible improvement is the use composite pulses like the BB1 sequence, which can mitigate the error generated by a small microwave field inhomogeneity [5].

References

[1] I. Gimeno Alonso, Ph.D. thesis, Universidad de Zaragoza (2023).

[2] O. Armet, J. Veciana, C. Rovira, J. Riera, J. Castañer, E. Molins, J. Rius, C. Miravitlles, S. Olivella, and J. Brichfeus, Journal of Physical Chemistry **91**, 5608 (1987).

[3] J. Guasch, X. Fontrodona, I. Ratera, C. Rovira, and J. Veciana, Acta Crystallographica **C69**, 225 (2013).

[4] D. Schüfter, J. Wischnat, L. Tesi, J. A. D. Sousa, E. Little, J. McGuire, M. Mas-Torrent, C. Rovira, J. Veciana, F. Tuna, et al., Advanced Materials **35(38)**, 2302114 (2023).

[5] J. J. L. Morton, A. M. Tyryshkin, A. Ardavan, K. Porfyrakis, S. A. Lyon, and G. A. D. Briggs, Physical Review Letters **95**, 200501 (2005).

Chapter 7

Circuit QED with electro-nuclear spin qudits

The previous chapter describes pulse experiments performed on ensembles of simple free radical molecules. With their spin 1/2, these molecules are model realizations of spin qubits. The next logical step is to extend these experiments to more complex systems, able to implement richer quantum functionalities. A promising alternative is to exploit multiple spin states within a magnetic molecule hosting multiple magnetic centers. However, synthesizing magnetically diluted crystals made of these molecules, which is necessary to combine a good protection from the decoherence induced by intermolecular interactions with the ability to resonantly address each spin transition, has proven quite challenging [1, 2].

Nuclear spins are interesting candidates to encode qubits or d-dimensional qudits due to their isolation from magnetic noise and potentially long coherence times. However, their weak coupling to external stimuli makes them hard to integrate into superconducting circuits. Coupling to electronic spins is easier, but with the drawback of having shorter coherence times. A promising architecture is based in ions with electronic spin 1/2 and non-zero nuclear spin. Here, the qubit/qudit is encoded in the nuclear spin, but the readout is performed in the electronic spin: the state of the nuclear spin is inferred from its coupling to the electronic spin.

This chapter showcases the electronic spin - nuclear spin architecture in the [Yb(trensal)] complex [3], a molecule with a Yb^{3+} ion with effective electronic spin 1/2. Two stable isotopes of Yb have non-zero nuclear spin, ^{171}Yb with $I = 1/2$ and ^{173}Yb with $I = 5/2$. The large hyperfine coupling in [Yb(trensal)] with ^{173}Yb (~ 900 MHz) ensures a non-negligible electro-nuclear mixing even with fields up to 100 mT. The hyperfine-enhanced coupling of

^{173}Yb nuclear transitions to LERs has been measured with transmission experiments and pulsed experiments [4]. Additionally, I describe the first results of dispersive readout experiments performed on a isotopically enriched crystal of [Yb(trensal)].

7.1 Experimental setup

7.1.1 [Yb(trensal)] samples

[Yb(trensal)] is a coordination complex with an effective electronic spin 1/2 localized in its Yb^{3+} ion. Here (trensal) is shorthand for the trianionic[1] form of the heptadentate[2] ligand H_3trensal [5–8]. Figure 7.1a shows the molecular structure of the complex. It has C_3 symmetry, with the symmetry axis (the C_3 axis) defined by the coordination bond between the Yb^{3+} ion and the tertiary amine of triethylamine.

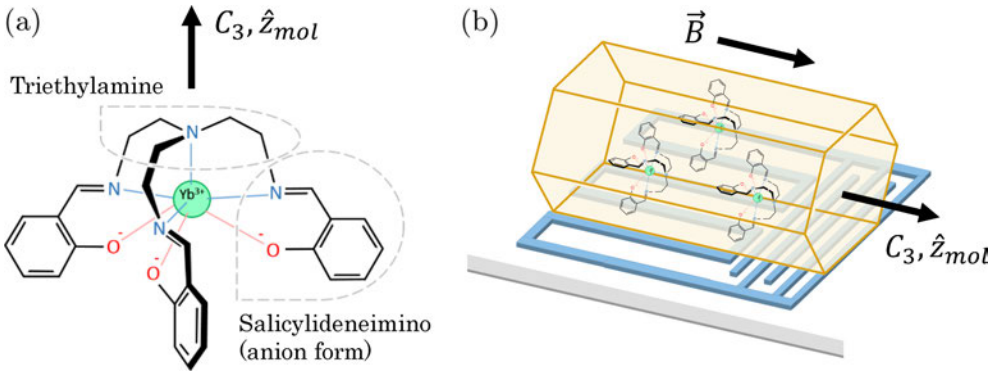

Figure 7.1: (a) Molecular structure of the Yb(trensal) complex, adapted from [6, 7]. The (trensal) trianionic ligand consists of a triethylamine bridging three salicylideneimino groups in anion form. The complex has axial symmetry, with the molecular z axis being the same as the C_3 symmetry axis defined by the coordination bond between the Yb^{3+} ion and the tertiary amine of triethylamine. (b) Scheme of a [Yb(trensal)] crystal, which is a hexagonal prism with the C_3 symmetry axis of all molecules perpendicular to the hexagonal faces, on a lumped-element resonator. The magnetic field is along the C_3 axis, parallel to the transmission line and the longer resonator inductor lines.

[1] With charge 3−, trensal forms neutral complexes with Ln^{3+} ions of the lanthanide series. The neutral H_3trensal has a hydrogen atom bonded to each oxygen atom of trensal.

[2] A heptadentate ligand has seven donor groups that can bind the magnetic ion. In this case, these donor groups are the tertiary amine in triethylamine, the three imine groups, and the three oxygen atoms.

[Yb(trensal)] samples are molecular crystals in the form of hexagonal prisms (see figure 7.1b). The C_3 symmetry axis of all [Yb(trensal)] molecules are normal to the hexagonal faces of the crystal. In order to suppress spin-spin interaction between molecules, [Yb(trensal)] is doped into a matrix of the isostructural diamagnetic host [Lu(trensal)]. In this way, the orientation of all [Yb(trensal)] molecules with respect to the applied magnetic field $\boldsymbol{B}$ and the chip remains the same.

Yb^{3+} is a Kramers ion with a two-fold degeneracy of the ground energy state at zero magnetic field (see 3.1.2 in chapter 3). Magnetic anisotropy lifts the energy of other excited states so that at low temperatures this ground doublet can be considered as an effective two-state system, that is, an effective spin 1/2 system. The electronic Zeeman term of this spin 1/2 is affected by magnetic anisotropy: the g-tensor is diagonal but non-isotropic, with $g_x = g_y \equiv g_\perp = 2.935$ and $g_z \equiv g_\parallel = 4.225$ (axial symmetry). Here the molecular z axis is the C_3 symmetry axis. The resulting spin Hamiltonian is:

$$H = H_{el,Z} = \mu_\mathrm{B} \left[g_\perp \left(B_x \hat{S}_x + B_y \hat{S}_y \right) + g_\parallel B_z \hat{S}_z \right]. \tag{7.1}$$

The hyperfine splitting of [Yb(trensal)] with a non-zero nuclear spin Yb isotope is well described by a diagonal, non-isotropic hyperfine tensor in the molecular axes defined by the anisotropy Zeeman interaction. In these experiments, I am interested in ^{173}Yb, with $I = 5/2$ and a natural abundance of 16%. The nuclear spin adds a hyperfine interaction with axial symmetry, a nuclear Zeeman interaction with $g_I = -0.02592$, and a quadrupolar term with $P_\parallel = 66$ MHz to the effective spin Hamiltonian:

$$\begin{aligned} H = H_{el,Z} &+ A_\perp \left(\hat{S}_x \otimes \hat{I}_x + \hat{S}_y \otimes \hat{I}_y \right) + A_\parallel \hat{S}_z \otimes \hat{I}_z \\ &- \mu_N g_I \boldsymbol{B} \cdot \hat{\boldsymbol{I}} + P_\parallel \left(\hat{I}_z^2 - \tfrac{1}{3} I(I+1) \right). \end{aligned} \tag{7.2}$$

The hyperfine interaction is the dominant energy scale for the ^{173}Yb nuclear spin in [Yb(trensal)], [^{173}Yb(trensal)] in what follows, with $A_\perp/h = -615$ MHz and $A_\parallel/h = -897$ MHz. The magnetic field dependence of the energy spectrum derived from (7.2) with these parameters is shown in figure 7.2a. Here, the magnetic field is along the C_3 symmetry axis, that is, parallel to the molecular z axis.

At high magnetic fields, the twelve spin states in the spectrum are divided into two subsets: six low-energy states with $m_S = -1/2$ and six high-energy states with $m_S = +1/2$. In each subset, there are five nuclear spin transitions with frequencies in the range of hundreds of MHz between states with $|\Delta m_I| = 1$. In practice, only nuclear spin transitions between states in the low-energy subset are detected (see figure 7.2b), as the population difference between

states in the high-energy subset is negligible even at very low temperatures. There are also six electronic spin transitions ($|\Delta m_S| = 1$) between the two subsets, one for each value of m_I from $-5/2$ to $+5/2$. All six transitions, with frequencies in the range of a few GHz, can be easily detected at low temperatures (see figure 7.2c).

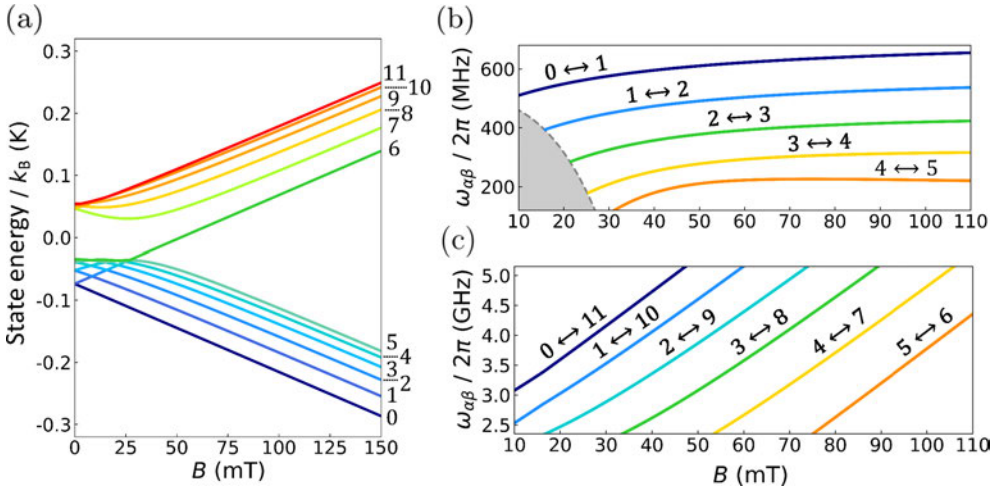

Figure 7.2: (a) Energy spectrum of [^{173}Yb(trensal)] ($I = 5/2$), with twelve states split by magnetic field into a low-energy subset with $m_S = -1/2$ and a high-energy subset with $m_S = +1/2$. The magnetic field is along the C_3 symmetry axis of the molecules. (b) Magnetic field dependence of the resonance frequencies of the transitions between the six low-energy states of [^{173}Yb(trensal)]. From highest to lowest frequency, these transitions correspond approximately (save for the mixing introduced by the hyperfine interaction) to the nuclear transitions $m_I = -5/2 \leftrightarrow -3/2$ ($0 \leftrightarrow 1$), $m_I = -3/2 \leftrightarrow -1/2$ ($1 \leftrightarrow 2$), $m_I = -1/2 \leftrightarrow +1/2$ ($2 \leftrightarrow 3$), $m_I = +1/2 \leftrightarrow +3/2$ ($3 \leftrightarrow 4$) and $m_I = +3/2 \leftrightarrow +5/2$ ($4 \leftrightarrow 5$) with $m_S = -1/2$. At low fields (shaded region) these transitions start to mix due to the hyperfine interaction. (c) Magnetic field dependence of the six transitions between the two subsets. Left to right, these transitions correspond approximately to different nuclear spin states: $m_I = -5/2$ ($0 \leftrightarrow 11$), $m_I = -3/2$ ($1 \leftrightarrow 10$), $m_I = -1/2$ ($2 \leftrightarrow 9$), $m_I = +1/2$ ($3 \leftrightarrow 8$), $m_I = +3/2$ ($4 \leftrightarrow 7$), and $m_I = +5/2$ ($5 \leftrightarrow 6$).

The strong hyperfine interaction and the presence of a sizeable quadrupolar splitting in [^{173}Yb(trensal)] gives rise to the level of anharmonicity necessary for addressing its $(2S + 1) \times (2I + 1) = 12$ spin states and, therefore, to properly encode a $d = 12$ electronuclear spin qudit. Alternatively, this system can seen as a $d = 6$ nuclear spin qudit coupled to an electronic spin ancilla. This kind of architecture has been proposed to embed quantum error correction within a single molecule [9].

Nuclear spins were one of the first platforms for quantum technologies that

were studied experimentally [10, 11]. These experiments focused on nuclear spins in organic molecules, which show long coherence times. However, nuclear spins are also difficult to address due to the weak interaction of nuclear magnetic moments with electromagnetic radiation fields. The hyperfine coupling of the nuclear and electronic spins in [^{173}Yb(trensal)] could in principle enhance the coupling of photons to nuclear spin transitions through the mixing of the electronic spin and nuclear spin wavefunctions.

7.1.2 Chip design

In order to obtain the best nuclear spin-photon coupling possible, it is interesting to study the nuclear spin qudits encoded in [Yb(trensal)] in the context of circuit quantum electrodynamics (c-QED), one of the most reliable platforms for solid-state quantum technologies [12]. Two superconducting chips were designed for coupling lumped-element resonators (LERs) to electronic spin and nuclear spin transitions in [Yb(trensal)], labeled *Yb-cw* and *Yb-pulsed*. Figure 7.3 shows both designs.

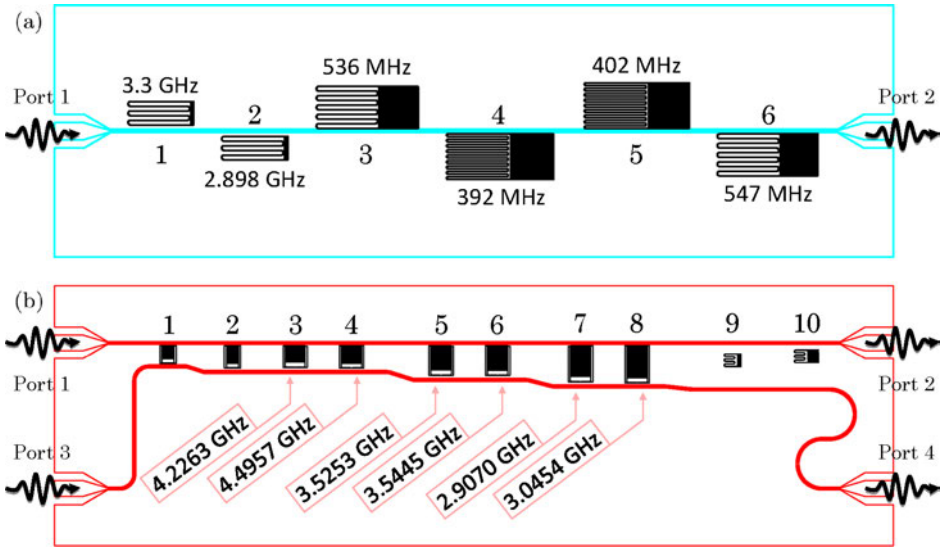

Figure 7.3: (a) Chip *Yb-cw*, with a single transmission line, designed to measure the collective spin-photon coupling of LERs to electronic spin and nuclear spin transitions in [Yb(trensal)]. LERs 1 and 2, with frequencies $\sim$ 3 GHz, are designed to couple to electronic spin transitions. LERs 3 to 6, with frequencies in the range between 400 and 550 MHz, are designed to couple to nuclear spin transitions. (b) Chip *Yb-pulsed*, with two transmission lines, designed for pulse experiments. LERs 3 and 4 (4.2–4.5 GHz) are tuned to the $0 \leftrightarrow 11$ transition ($m_I = -5/2$) with a magnetic field $B =$ 30 mT. At the same magnetic field, LERs 5 and 6 ($\sim$ 3.5 GHz) are tuned to the $1 \leftrightarrow 10$ transition ($m_I = -3/2$), and LERs 7 and 8 ($\sim$ 3 GHz) are tuned to the $2 \leftrightarrow 9$ transition ($m_I = -1/2$).

The design of *Yb-cw* follows from the designs of *Test 1* and *Test 2* for free-radicals, with 6 LERs consisting of an inter-digital capacitor and a meandering inductor. All six resonators are side-coupled to the same transmission line with both inductive and capacitive couplings. The resonance frequencies of *Yb-cw* LERs, shown in figure 7.3a, were tailored to match different electronic spin and nuclear spin transitions. LERs 1 and 2, with a smaller size, have frequencies in the range of ~ 3 GHz. These two LERs couple to the electronic spin transitions in [Yb(trensal)], see figure 7.2c. Conversely, larger resonators (LERs 3 to 6) couple to nuclear spin transitions, with frequencies in the range between 400 and 550 MHz (see 7.2b).

Yb-pulsed hosts ten LERs, of which only LERs 3 to 8 (see figure 7.3b) were designed for pulsed experiments with [Yb(trensal)]. Therefore, I will focus only on these six resonators. They share a similar design with the low-inductance resonators used in the previous chapter for dispersive readout experiments with PTM. Most of the LER area is taken by a large inter-digital capacitor, with its ends connected by a single strip, the inductor, close to the transmission line. Each pair of LERs with similar frequencies is tuned to be close to the frequency of a specific electronic spin transition of [^{173}Yb(trensal)] when a magnetic field of 30 mT is applied. LERs 3 and 4 are tuned to the $0 \leftrightarrow 11$ transition ($m_I = -5/2$), LERs 5 and 6 are tuned to the $1 \leftrightarrow 10$ transition ($m_I = -3/2$) and LERs 7 and 8 are tuned to the $2 \leftrightarrow 9$ transition ($m_I = -1/2$).

7.2 High cooperativity coupling to nuclear spin transitions

A complete characterization of the collective spin-photon coupling of electronic spin and nuclear spin transitions of [Yb(trensal)] to the photon modes of LERs in *Yb-cw* was performed with single crystals of [Yb(trensal)] having natural abundances of all Yb isotopes. Each crystal had a different concentration of [Yb(trensal)] in the diamagnetic [Lu(trensal)] matrix (see figure 7.4). With the sample sizes shown in figure 7.4, 10^{15}–10^{16} [Yb(trensal)] molecules with ^{173}Yb are estimated per crystal.

Crystals were placed on top of the meandering inductor of each LER, with the C_3 symmetry axis of the molecules aligned with both the transmission line and the inductor lines. The deposition process is detailed in figure 7.4. The magnetic field was also oriented parallel to C_3. A characterization based on the coupling to the transmission line provides broadband access to the different spin transitions. The results can be found in [4].

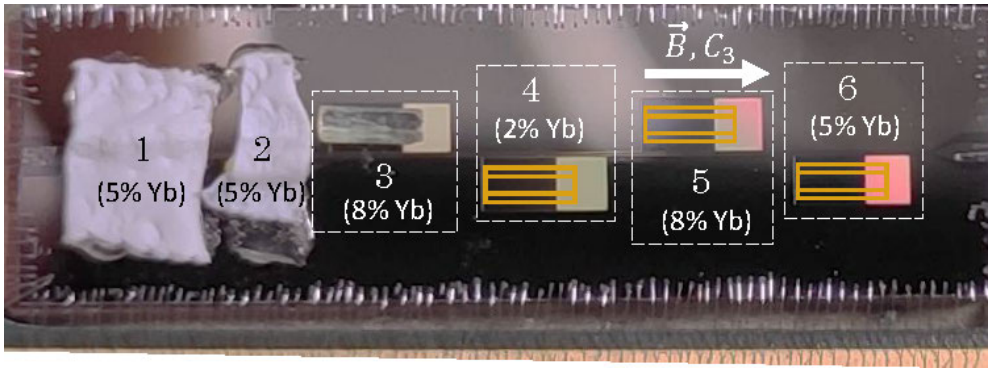

Figure 7.4: Superconducting chip with 6 LERs coupled to [Yb(trensal)] crystals. In the picture, only LERs 1, 2 and 3 have a crystal. Crystals were deposited later in the remaining resonators (represented here with pictures of the crystals). After placing the crystals on top of the resonator inductor (see LER 3), they were covered with a Teflon strips stuck to the chip surface with vacuum grease (see LERs 1 and 2). Each crystal had a different concentration of [Yb(trensal)] in a diamagnetic [Lu(trensal)] matrix. The % of [Yb(trensal)] in each crystal is shown.

7.2.1 Electronic spin transitions

First, the electronic spin transitions of [Yb(trensal)] were addressed. Electronic spin transitions are in principle easier to measure than nuclear spin transitions, as the coupling of an isolated electronic spin to microwave magnetic fields is higher than that of isolated nuclear spins (the electronic Zeeman interaction is three orders of magnitude stronger than the nuclear Zeeman interaction). Moreover, the resonance frequency of an electronic spin transition can be easily tuned with the magnetic field in order to match the resonance frequency of LERs 1 and 2 (see figure 7.2c).

Figure 7.5 shows the transmission of *Yb-cw* for input frequencies $f \equiv \omega_d/2\pi$ spanning the resonance of LER 2, measured in a range of magnetic fields in which the electronic spin transition $1 \leftrightarrow 10$ is close to this LER. This transition corresponds to the $m_S = -1/2 \leftrightarrow m_S = +1/2$ transition with $m_I = -3/2$. The transmission data are fitted the theory for a resonator coupled the transition between states α and β of a qudit (see equation (4.133), with frequency $\omega_{\alpha\beta}$:

$$S_{21}(\omega_d \simeq \omega_{\alpha\beta}) = 1 - \frac{\kappa_c}{i(\omega_r - \omega_d) + \kappa + \dfrac{(G_N)^2_{\alpha\beta}\Delta P_{\alpha\beta}}{i(\omega_{\alpha\beta} - \omega_d) + \gamma_{\perp,\alpha\beta}}}. \tag{7.3}$$

The LER parameters are its the resonance frequency ω_r and decay rate κ, and the line-resonator coupling κ_c. The $\alpha \leftrightarrow \beta$ transition has a decoherence rate

$\gamma_{\perp,\alpha\beta}$ and population difference $\Delta P_{\alpha\beta}$, and couples to the resonator with a rate $(G_N)_{\alpha\beta}$. In what follows, $\Delta P_{\alpha\beta}$ in included in the definition of the coupling: $(G_N)_{\alpha\beta} \propto \sqrt{\Delta P_{\alpha\beta}}$. The data of figure 7.5 corresponds to $\alpha = 1$ and $\beta = 10$. Table 7.1 shows the fit parameters of the resonance of LER 2 with equation (7.3).

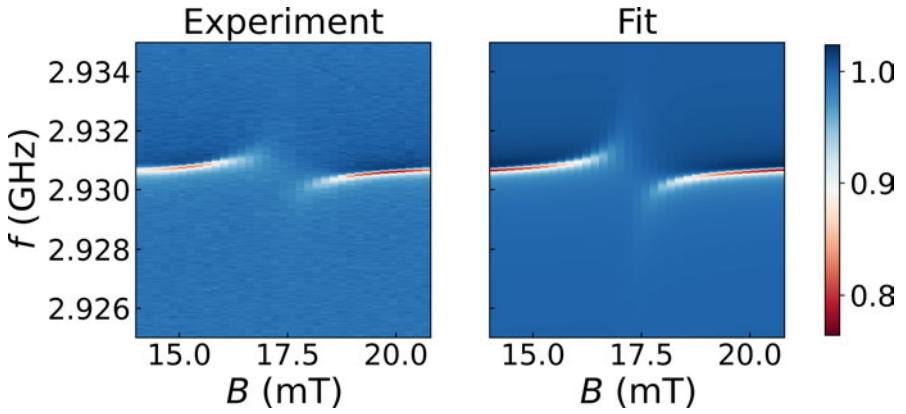

Figure 7.5: Transmission of *Yb-cw* for frequencies $f \equiv \omega_d/2\pi$ spanning the resonance of LER 2, measured for magnetic fields between 14 mT and 21 mT at $T = 10$ mK. In this field range, LER 2 couples to the $1 \leftrightarrow 10$ transition of [^{173}Yb(trensal)].

LER 2, 5% [Yb(trensal)]	
ω_r / 2π (GHz)	$2.9306714 \pm 4 \cdot 10^{-7}$
κ / 2π (kHz)	45.8 ± 0.3
$\lvert\kappa_c\rvert$ / 2π (kHz)	14.8 ± 0.2
ϕ_c (°)	33.1 ± 0.1
$(G_N)_{1\,10}$ / 2π (MHz)	4.67 ± 0.06
$\gamma_{\perp,1\,10}$ / 2π (MHz)	14.7 ± 0.1

Table 7.1: Fit parameters of the transmission of LER 2 coupled to the $1 \leftrightarrow 10$ transition of [^{173}Yb(trensal)] at 10 mK.

Since $(G_N)_{1\,10}/\gamma_{\perp,1\,10} \simeq 0.32 < 1$, the hybrid electronic spin-photon system is in the weak coupling regime. However, the high cooperativity regime is achieved, with $C_{1\,10} = (G_N)^2_{1\,10}/\gamma_{\perp,1\,10}\kappa \simeq 32.5 \gg 1$, thanks to the LER high quality factor $Q \simeq 3 \cdot 10^4$ ($\kappa = \omega_r/2Q = 45.8$ kHz). Note that only 5% of the molecules in the crystal on top of LER 2 are [Yb(trensal)], and of these only a 16% contain the ^{173}Yb isotope, that is, less than 1 out of 100 of all the molecules in the crystal have the $1 \leftrightarrow 10$ transition measured in figure 7.5. Still, a remarkably high coupling is attained. The full set of electronic transitions (6 transitions, one for each value of m_I) was studied with [^{173}Yb(trensal)] isotopically purified samples. The results are described in section 7.4 below.

7.2.2 Nuclear spin transitions

The hyperfine interaction in [^{173}Yb(trensal)] dominates over the nuclear Zeeman interactions, making the frequencies of the nuclear spin transitions almost magnetic field independent for a wide range of fields (see figure 7.2b). This calls for a careful design of the LER frequencies in order to match the nuclear spin transition frequencies. *Yb-cw* LERs 4 and 5, with respective $\omega_r = 392$ MHz and $\omega_r = 402$ MHz, were designed to match the the $1 \leftrightarrow 2$ transition at low fields ($B < 20$ mT) and the $2 \leftrightarrow 3$ transition at higher fields ($B > 60$ mT). These transitions correspond approximately to the $m_I = -3/2 \leftrightarrow -1/2$ and $m_I = -1/2 \leftrightarrow +1/2$ nuclear spin transitions with $m_S = -1/2$, respectively (see figure 7.6).

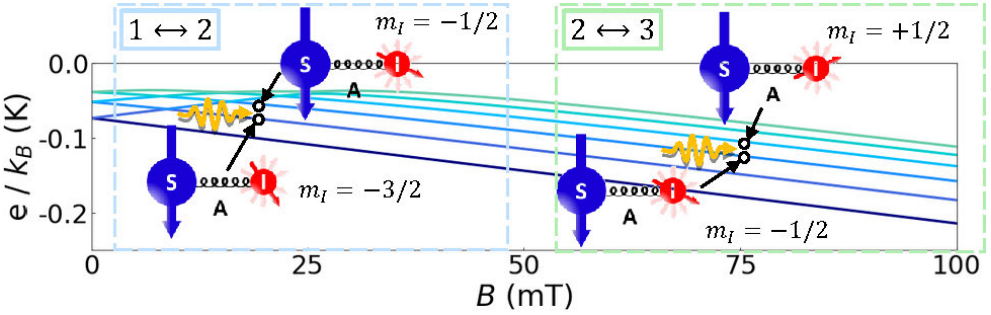

Figure 7.6: Picture of the transitions $1 \leftrightarrow 2$ and $2 \leftrightarrow 3$ in the energy scheme of figure 7.2a. These transitions correspond approximately to the $m_I = -3/2 \leftrightarrow -1/2$ and $m_I = -1/2 \leftrightarrow +1/2$ nuclear spin transitions with $m_S = -1/2$.

Figures 7.7a-b show the intersection of the transition frequencies ω_{12} and ω_{23} with the LER frequencies as the magnetic field is swept between 0 and 75 mT, in the case of LER 4, and between 0 and 100 mT for LER 5. The LER resonances were measured in these magnetic field ranges and at 10 mK (see figures 7.7c-d). In addition to the couplings associated to the $1 \leftrightarrow 2$ and $2 \leftrightarrow 3$ transitions, the couplings to transitions corresponding to other Yb isotopes are also observed.

Close-up plots of the transmission measured near the spin-photon resonant conditions for both LERs are shown in figures 7.8 (LER 4) and 7.9 (LER 5). The response of LERs 4 and 5 in the magnetic field ranges around the crossings of ω_{12} and ω_{23} with their resonance frequencies were fitted with the model of an effective, broadened resonator, that is valid in the weak spin-photon coupling regime (see section 4.6.4).

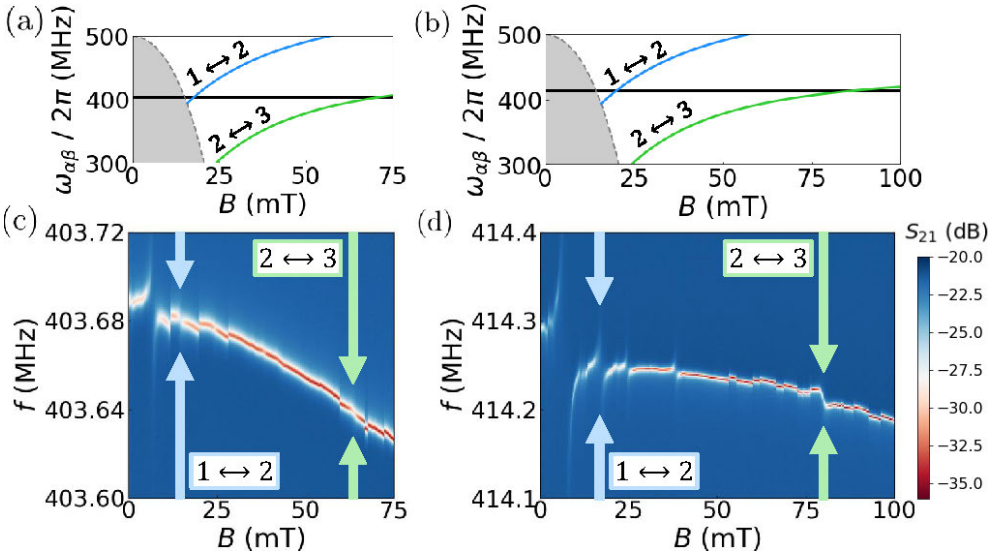

Figure 7.7: (a, b) Resonance frequencies of the nuclear spin transitions $1 \leftrightarrow 2$ and $2 \leftrightarrow 3$. Black horizontal lines are the resonance frequencies of LERs 4 (a) and 5 (b). (c, d) Transmission through the chip, measured for input frequencies $f = \omega_d/2\pi$ close to the resonance frequencies of LERs 4 (c) and 5 (d) and at $T = 10$ mK. Couplings to several transitions of [Yb(trensal)] with different Yb isotopes are observed. Here I focus on two nuclear transitions of [^{173}Yb(trensal)]: $1 \leftrightarrow 2$ and $2 \leftrightarrow 3$.

From weak coupling theory, the magnetic field dependence of $\tilde{\omega}_r$ and $\tilde{\kappa}$ is described by:

$$\begin{aligned} \tilde{\omega}_r &:= \omega_r + \left[\frac{(G_N)^2_{\alpha\beta}(\Delta P)_{e,\,\alpha\beta}}{(\omega_{\alpha\beta}-\omega_r)^2+\gamma^2_{\perp,\alpha\beta}}\right](\omega_r-\omega_{\alpha\beta}), \\ \tilde{\kappa} &:= \kappa + \left[\frac{(G_N)^2_{\alpha\beta}(\Delta P)_{e,\,\alpha\beta}}{(\omega_{\alpha\beta}-\omega_r)^2+\gamma^2_{\perp,\alpha\beta}}\right]\gamma_{\perp,\alpha\beta}, \end{aligned} \tag{7.4}$$

where $\omega_{\alpha\beta}$ is either ω_{21} (for transition $1 \leftrightarrow 2$) or ω_{32} (for $2 \leftrightarrow 3$). Each transition has a collective spin-photon coupling $(G_N)_{\alpha\beta}$ and a spin decoherence rate $\gamma_{\perp,\alpha\beta}$. $(\Delta P)_{e,\,\alpha\beta}$ is the difference of population between states α and β in equilibrium. The fit of $\tilde{\omega}_r$ and $\tilde{\kappa}$ to equation (7.4) yields the collective $(G_N)_{\alpha\beta}$ and $\gamma_{\perp,\alpha\beta}$ for spin transition, which are reported in table 7.2. The comparison between $\tilde{\omega}_r$, $\tilde{\kappa}$ and the fit is shown later in section 7.3.2. A consistent simultaneous fit of $\tilde{\omega}_r$ and $\tilde{\kappa}$ with equation (7.4) for LER 5 coupled to the $2 \leftrightarrow 3$ transition at 10 mK turned out to be impossible. For that reason, the experiment was repeated at 50 mK (see figure 7.9c).

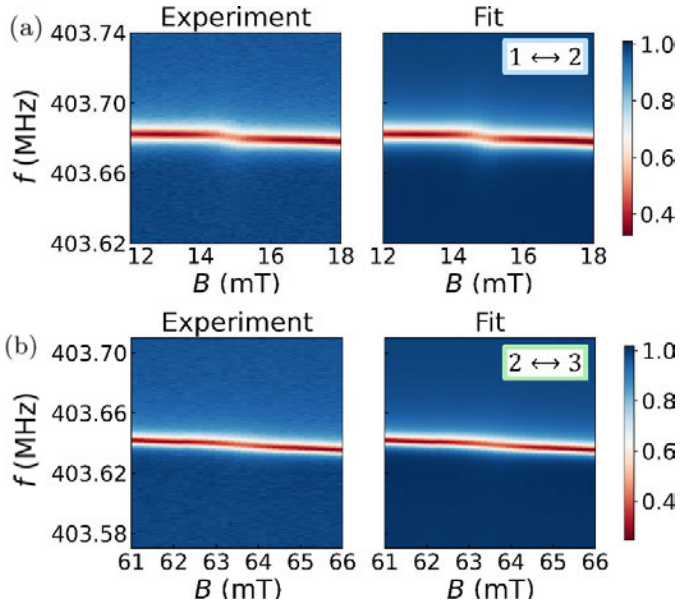

Figure 7.8: Transmission of *Yb-cw* for input frequencies close to the resonance frequency of LER 4, measured at 10 mK and for magnetic fields in which LER 4 is coupled to the $1 \leftrightarrow 2$ (a) and $2 \leftrightarrow 3$ (b) nuclear spin transitions of [^{173}Yb(trensal)]. The experimental data are compared to simulations for an effective resonance at each magnetic field, shifted in frequency and broadened by the interaction with the nuclear spins, which valid in the weak spin-photon coupling regime.

LER 4, 2% [Yb(trensal)]

Transition (temperature)	$1 \leftrightarrow 2$ (10 mK)	$2 \leftrightarrow 3$ (10 mK)
$(G_N)_{\alpha\beta}$ / 2π (kHz)	68 ± 3	29 ± 2
$\gamma_{\perp,\alpha\beta}$ / 2π (MHz)	2.6 ± 0.2	0.80 ± 0.10
$(G_N)_{\alpha\beta}$ / $\gamma_{\perp,\alpha\beta}$	0.026 ± 0.002	0.036 ± 0.005
$C_{\alpha\beta}$	0.51 ± 0.06	0.31 ± 0.06

LER 5, 8% [Yb(trensal)]

Transition (temperature)	$1 \leftrightarrow 2$ (10 mK)	$2 \leftrightarrow 3$ (50 mK)
$(G_N)_{\alpha\beta}$ / 2π (kHz)	262 ± 4	71 ± 5
$\gamma_{\perp,\alpha\beta}$ / 2π (MHz)	2.20 ± 0.06	0.39 ± 0.04
$(G_N)_{\alpha\beta}$ / $\gamma_{\perp,\alpha\beta}$	0.12 ± 0.04	0.18 ± 0.02
$C_{\alpha\beta}$	7.8 ± 0.6	3.6 ± 0.8

Table 7.2: Collective spin-photon coupling $(G_N)_{\alpha\beta}$ of LERs 4 and 5 to transitions $1 \leftrightarrow 2$ ($\alpha = 1$, $\beta = 2$) and $2 \leftrightarrow 3$ ($\alpha = 2$, $\beta = 3$), with spin decoherence rates $\gamma_{\perp,\alpha\beta}$. The difference in population in equilibrium, $(\Delta P)_{e,\,\alpha\beta}$, is included here in $(G_N)_{\alpha\beta}$: $(G_N)_{\alpha\beta} \propto \sqrt{(\Delta P)_{e,\,\alpha\beta}}$. The ratios $(G_N)_{\alpha\beta}$ / $\gamma_{\perp,\alpha\beta}$ and the cooperativities $C_{\alpha\beta} = (G_N)^2_{\alpha\beta}$ / $\kappa\gamma_{\perp,\alpha\beta}$ are also listed.

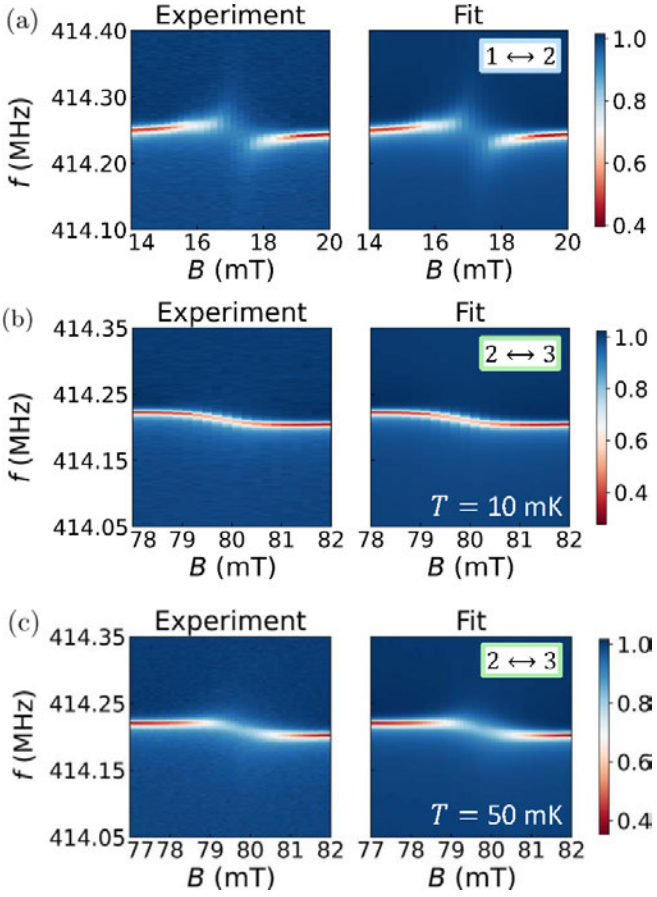

Figure 7.9: Transmission of *Yb-cw* for input frequencies close to the resonance frequency of LER 5, measured at 10 mK and for magnetic fields in which LER 5 is coupled to the $1 \leftrightarrow 2$ (a) and $2 \leftrightarrow 3$ (b) nuclear spin transitions of [^{173}Yb(trensal)]. The experimental data are compared to simulations for an effective resonance at each magnetic field, shifted in frequency and broadened by the interaction with the nuclear spins, which valid in the weak spin-photon coupling regime. The coupling of LER 5 to the $2 \leftrightarrow 3$ transition was also measured at 50 mK (c).

Couplings observed for LER 5 are clearly higher than in LER 4. This is just a consequence of the increase in the concentration of [Yb(trensal)] from the sample in LER 4 (2%) to the one in LER 5 (8%). The cooperativity is also enhanced. *High-cooperativity to nuclear spin transitions is achieved* for LER 5 with 8% of [Yb(trensal)] i.e. $C_{21}, C_{32} \gg 1$. Both the couplings ($(G_N)_{21}$, $(G_N)_{32}$), and cooperativities (C_{21}, C_{32}) reported here are about ten times smaller than what is achieved for the electronic spin transitions in the same molecular system (compare them to the values reported in section 7.2.1). They are nevertheless remarkably high. If the nuclear and electronic spins were uncoupled, the spin-photon coupling mediated by the nuclear Zeeman interac-

tion would lead to a ratio of about 10^{-4} (of the order of μ_B/μ_N) between the coupling rates of nuclear and electronic transitions. The fact that much higher couplings are observed for nuclear spin transitions means that the presence of an electronic spin ancilla acts as an effective mediator between the nuclear spin qudit and the resonator photons.

In each resonator, the coupling to the $1 \leftrightarrow 2$ transition is higher than the coupling to the $2 \leftrightarrow 3$ transition. The dominant parameter here is temperature. For LER 4, the difference in population $(\Delta P)_{e,\alpha\beta}$ in transition $1 \leftrightarrow 2$ at $\sim$15 mT is 15 times higher than in $2 \leftrightarrow 3$ at $\sim$63 mT. Similarly, for LER 5 $(\Delta P)_{e,\alpha\beta}$ is 20 times higher in $1 \leftrightarrow 2$ at $\sim$17 mT than in $2 \leftrightarrow 3$ at $\sim$80 mT. A lower decoherence rate is observed for the $2 \leftrightarrow 3$ transition. I argue that this is due to the flatness of the nuclear spin transitions at higher fields shown in figures 7.7a-b, which makes them more insensitive to magnetic field fluctuations. Conversely, the $1 \leftrightarrow 2$ transition couples to LERs 4 and 5 at lower fields, where the slope of transition frequency ω_{12} with magnetic field is still high in comparison.

7.3 Pulse experiments on [Yb(trensal)] molecular spin qudits

The coupling of *Yb-cw* LERs to electronic spin and nuclear spin transitions was also characterized by measuring the transmission of pulses with driving frequencies ω_d close to the resonance frequency ω_r of each resonator at different fields, following experimental protocols already described for LERs coupled to PTM samples (see section 6.3). Measuring the transmission of the pulses adds a new dimension, *time*, to each point of the maps in figures 7.5, 7.8 and 7.9, and allows tracking the dynamics of the system before reaching the steady state.

7.3.1 Electronic spin transitions

The transmission of 100-μs pulses with driving frequencies $\omega_d = 2\pi f$ spanning the resonance of LER 2 was measured at 10 mK for magnetic fields in the range of figure 7.5. Figure 7.10 shows the results for two fields, one at which the resonator is uncoupled from the transition (a) and one at which it is coupled (b). The results show that, as observed in stationary state measurements, the spin-photon coupling leads to a shift and broadening of the LER resonance. Besides, it has a consequence on the photon dynamics. The change and discharge of the resonator become significantly faster when the photons are close to resonance with an electronic spin transition.

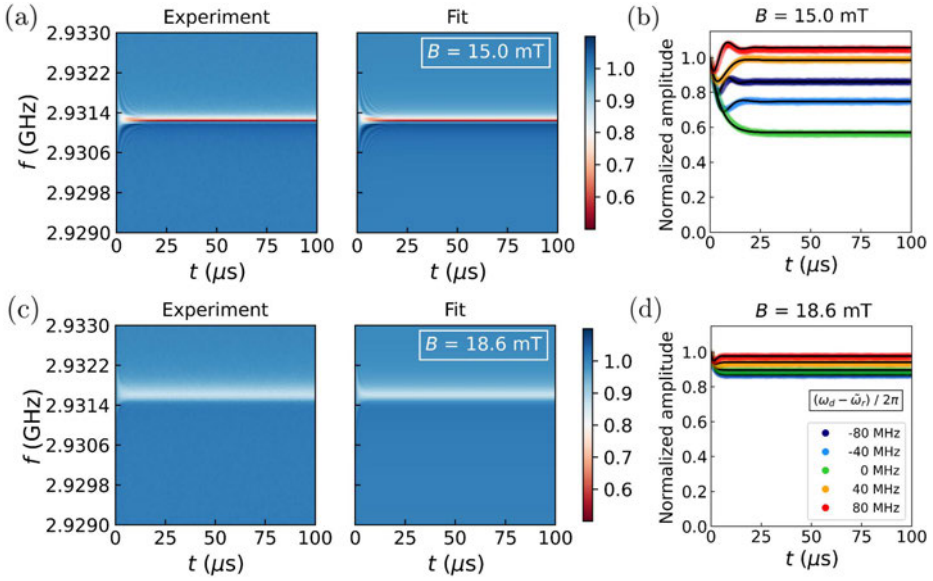

Figure 7.10: (a, c) Dynamics of LER 2 for two magnetic fields: 15 mT (a), showing the bare resonator, and 18.6 mT (b), where it is coupled to the $1 \leftrightarrow 10$ transition. (b, d) show cuts of figures (a, c) at various detunings between the driving frequency ω_d and the effective resonance frequency $\tilde{\omega}_r$.

The coupling between LER 2 and this electronic transition is in the weak coupling regime, thus the pulse transmission experiments can be fitted with the dynamical model of a broadened resonator described in section 6.3. The expression for the dynamics of the broadened resonator during the pulse is reproduced here for clarity:

$$b_{out}(t) = \left(1 - \kappa_c \frac{1 - e^{-(i(\omega_r - \omega_d) + \kappa)t}}{i(\omega_r - \omega_d) + \kappa}\right) \alpha_{in} e^{-i\omega_d t} \quad \text{for } t < t_{pulse}\,, \tag{7.5}$$

with ω_r and κ replaced by the effective effective resonance frequency $\tilde{\omega}_r$ and decay rate $\tilde{\kappa}$. Figure 7.11 shows $\tilde{\omega}_r$ and $\tilde{\kappa}$ obtained from the fit with equation (7.5) of the pulse transmission measurements on LER 2 at difference magnetic fields. These results are compared with values predicted by the weak coupling formulas in equation (7.4) using the parameters from continuous wave experiments (see table 7.1). They show a reasonable good agreement between the two experimental methods. The effective parameters derived from pulse transmission experiments can be fitted with equation (7.4) in order to obtain the collective spin-photon coupling $(G_N)_{1\,10}$ and decoherence rate $\gamma_{\perp,1\,10}$ associated to transition $1 \leftrightarrow 10$ coupled to LER 2. They are listed in table 7.3. The underestimated $\tilde{\omega}_r$ and $\tilde{\kappa}$ in pulse transmission measurements can be due to the fact that the precision of the model of an effective, broadened resonator works better for $(G_N)_{1\,10} \,/\, \gamma_{\perp,1\,10} \ll 1$ (here I find $0.1 < (G_N)_{1\,10} \,/\, \gamma_{\perp,1\,10} < 1$).

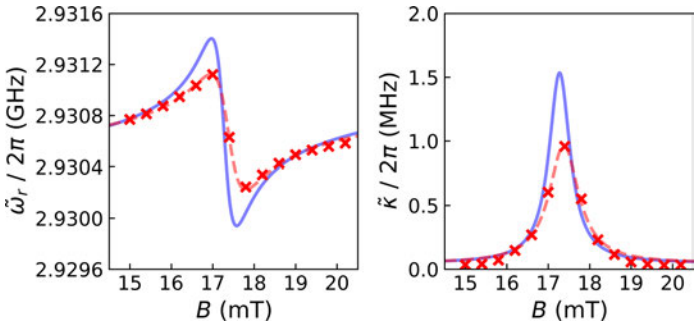

Figure 7.11: Effective resonance frequency $\tilde{\omega}_r$ and effective decay rate $\tilde{\kappa}$ of LER 2 coupled to the electronic spin transition $1 \leftrightarrow 10$, extracted from the pulse transmission experiments at 10 mK (red crosses). The red dashed lines are the fit of these effective parameters with equation (7.4). As a comparison, the blue solid line uses the parameters from the continuous wave experiment with this same equation.

LER 2, 5% [Yb(trensal)], pulse transmission	
ω_r / 2π (GHz)	$2.930673 \pm 8 \cdot 10^{-6}$
κ / 2π (kHz)	44 ± 12
$\lvert\kappa_c\rvert$ / 2π (kHz)	17 ± 3
ϕ_c (°)	35 ± 7
$(G_N)_{1\,10}$ / 2π (MHz)	4.3 ± 0.1
$\gamma_{\perp,1\,10}$ / 2π (MHz)	20.7 ± 1.0
$(G_N)_{1\,10}$ / $\gamma_{\perp,1\,10}$	0.211 ± 0.011
$C_{1\,10}$ (MHz)	21 ± 6

Table 7.3: Parameters of the fit of the effective resonance frequency $\tilde{\omega}_r$ and decay rate $\tilde{\kappa}$ of LER 2 coupled to the $1 \leftrightarrow 10$ transition with equation (7.4), obtained from pulse transmission experiments. The ratio $(G_N)_{1\,10}$ / $\gamma_{\perp,1\,10}$ and the cooperativity $C_{1\,10} = (G_N)^2_{1\,10}$ / $\kappa\gamma_{\perp,1\,10}$ are also shown.

7.3.2 Nuclear spin transitions

The transmission of 400-μs long pulses with driving frequencies $\omega_d = 2\pi f$ spanning the resonances of LERs 4 and 5 were measured at 10 mK for magnetic fields in the range of figures 7.8 and 7.9. Figure 7.12 shows the results for LER 4 coupled to the nuclear transition $1 \leftrightarrow 2$ at two magnetic fields, one at which the resonator is uncoupled from the transition (a) and one at which it is coupled (b). Similar pulse transmission experiments were carried out for LER 4 coupled to the $2 \leftrightarrow 3$ transition (figure 7.13), LER 5 coupled to the $1 \leftrightarrow 2$ transition (figure 7.14), and LER 5 coupled to the $2 \leftrightarrow 3$ transition (figure 7.15). As with the electronic transitions, the nuclear spin-photon coupling influences both the frequency and width of the resonance and the decay times of the resonators.

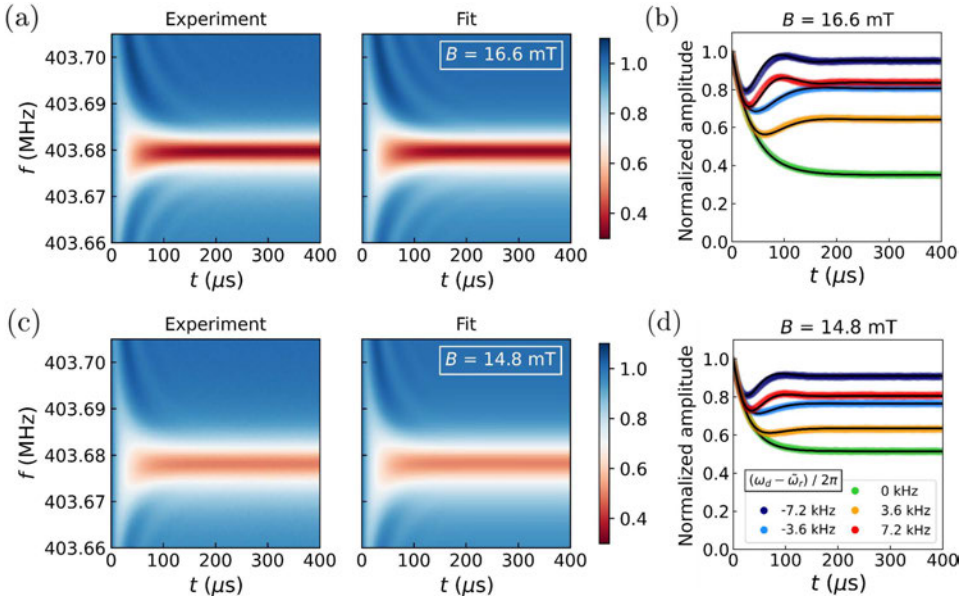

Figure 7.12: (a, c) Dynamics of LER 4 for two magnetic fields: 16.6 mT (a), showing the bare resonator, and 14.8 mT (b), where it is coupled to the $1 \leftrightarrow 2$ transition. (b, d) show cuts of figures (a, c) at various detunings between the driving frequency ω_d and the effective resonance frequency $\tilde{\omega}_r$.

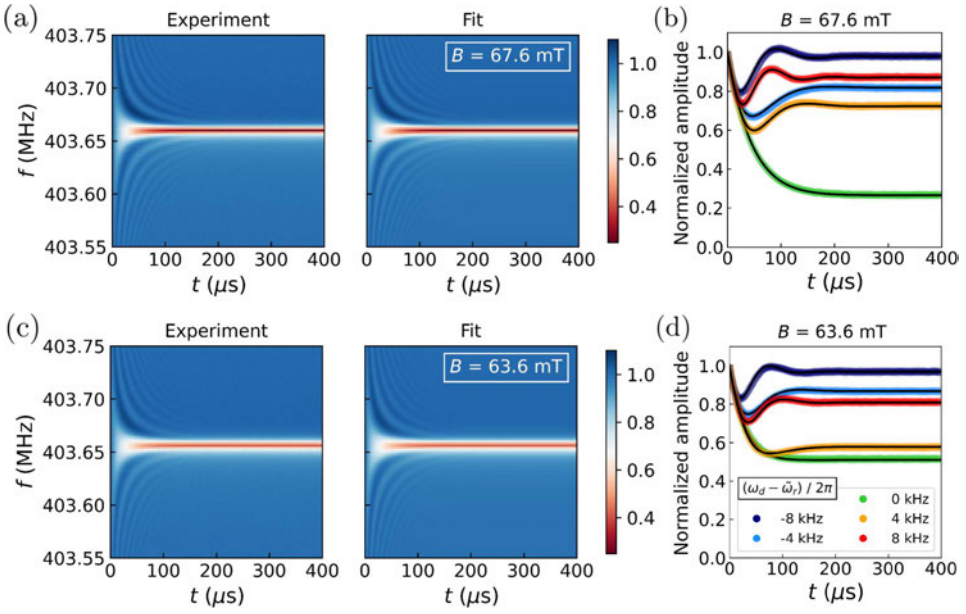

Figure 7.13: (a, c) Dynamics of LER 4 for two magnetic fields: 67.6 mT (a), showing the bare resonator, and 63.6 mT (b), where it is coupled to the $2 \leftrightarrow 3$ transition. (b, d) show cuts of figures (a, c) at various detunings between the driving frequency ω_d and the effective resonance frequency $\tilde{\omega}_r$.

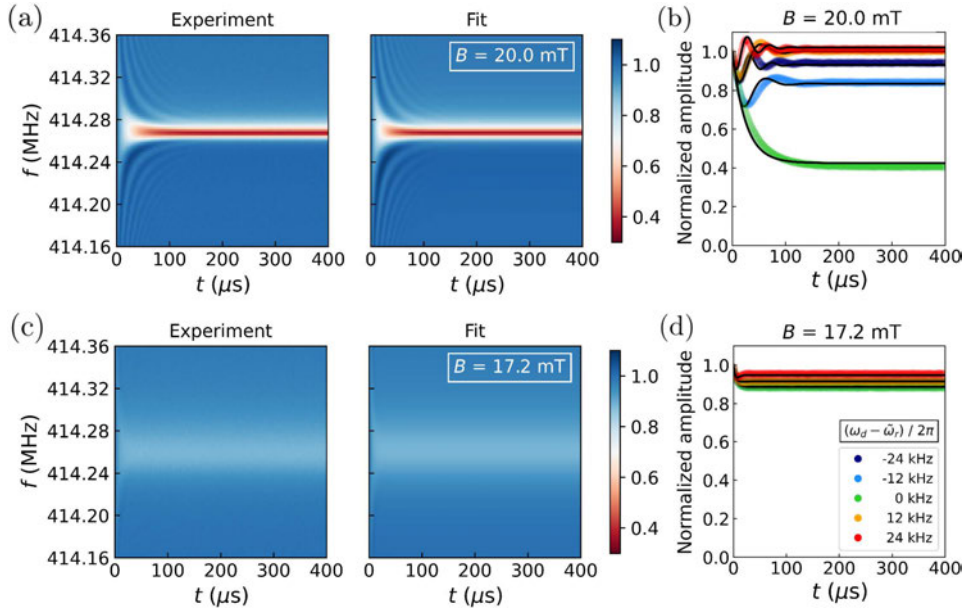

Figure 7.14: (a, c) Dynamics of LER 5 for two magnetic fields: 20.0 mT (a), showing the bare resonator, and 17.2 mT (b), where it is coupled to the $1 \leftrightarrow 2$ transition. (b, d) show cuts of figures (a, c) at various detunings between the driving frequency ω_d and the effective resonance frequency $\tilde{\omega}_r$.

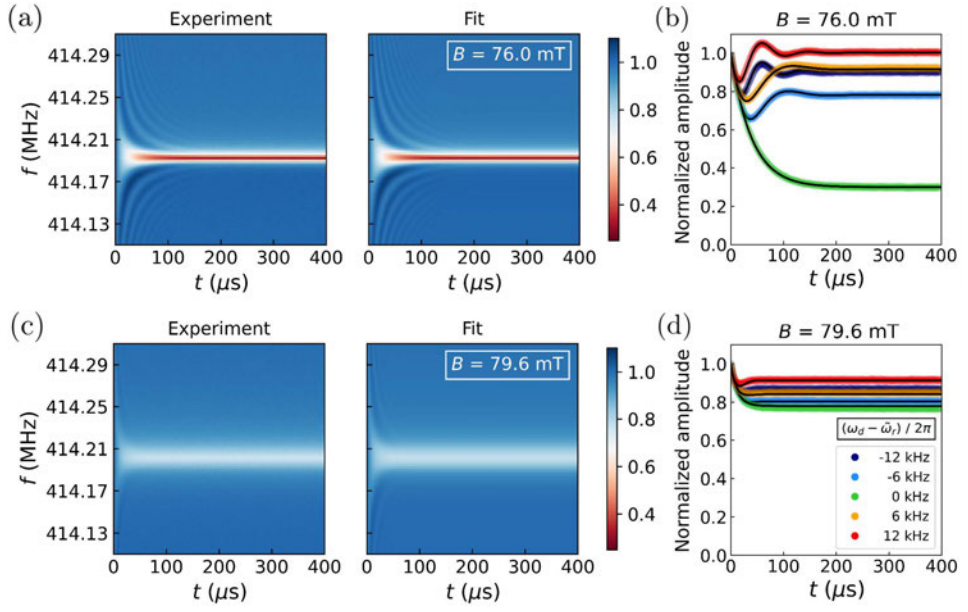

Figure 7.15: (a, c) Dynamics of LER 5 for two magnetic fields: 76.0 mT (a), showing the bare resonator, and 79.6 mT (b), where it is coupled to the $2 \leftrightarrow 3$ transition. (b, d) show cuts of figures (a, c) at various detunings between the driving frequency ω_d and the effective resonance frequency $\tilde{\omega}_r$.

As the nuclear spin-photon couplings here are also in the weak regime, the experiments can be fitted with the model of a broadened resonator shown above in equation (7.5). The resulting $\tilde{\omega}_r$ and $\tilde{\kappa}$ are shown in figure 7.16, along with their fit with equation (7.4). Table 7.4 reports the collective spin-photon coupling $(G_N)_{\alpha\beta}$ and spin decoherence rate $\gamma_{\perp,\alpha\beta}$ of transitions $1 \leftrightarrow 2$ ($\alpha = 1$, $\beta = 2$) and $2 \leftrightarrow 3$ ($\alpha = 2$, $\beta = 3$) to LERs 4 and 5. Figure 7.16 also compares these values with those obtained from continuous wave experiments (see section 7.2.2).

LER 4, 2% [Yb(trensal)], pulse transmission

Transition (temperature)	$1 \leftrightarrow 2$ (10 mK)	$2 \leftrightarrow 3$ (10 mK)
$(G_N)_{\alpha\beta}$ / 2π (kHz)	67 ± 6	29 ± 9
$\gamma_{\perp,\alpha\beta}$ / 2π (MHz)	3.0 ± 0.4	0.8 ± 0.4
$(G_N)_{\alpha\beta}$ / $\gamma_{\perp,\alpha\beta}$	0.022 ± 0.004	0.035 ± 0.022
$C_{\alpha\beta}$	0.39 ± 0.09	0.30 ± 0.24

LER 5, 8% [Yb(trensal)], pulse transmission

Transition (temperature)	$1 \leftrightarrow 2$ (10 mK)	$2 \leftrightarrow 3$ (10 mK)
$(G_N)_{\alpha\beta}$ / 2π (kHz)	244 ± 17	62 ± 9
$\gamma_{\perp,\alpha\beta}$ / 2π (MHz)	2.5 ± 0.3	0.4 ± 0.1
$(G_N)_{\alpha\beta}$ / $\gamma_{\perp,\alpha\beta}$	0.097 ± 0.015	0.16 ± 0.05
$C_{\alpha\beta}$	4.4 ± 1.1	2.7 ± 1.3

Table 7.4: Collective spin-photon coupling $(G_N)_{\alpha\beta}$ of LERs 4 and 5 to transitions $1 \leftrightarrow 2$ ($\alpha = 1$, $\beta = 2$) and $2 \leftrightarrow 3$ ($\alpha = 2$, $\beta = 3$), with spin decoherence rates $\gamma_{\perp,\alpha\beta}$, obtained from pulse transmission experiments. The difference in population in equilibrium, $(\Delta P)_{e,\,\alpha\beta}$, is included here in $(G_N)_{\alpha\beta}$: $(G_N)_{\alpha\beta} \propto \sqrt{(\Delta P)_{e,\,\alpha\beta}}$. These are the fit parameters of the fits of the values of $\tilde{\omega}_r$ and $\tilde{\kappa}$ in figure 7.16 (solid and dashed lines).

Overall, there is a good agreement between the collective couplings and decoherence rates obtained with continuous wave and pulse transmission experiments, confirming the high cooperativity regime of LERs coupled to nuclear transitions in [^{173}Yb(trensal)]b. The main difference between the two techniques is that the resonator frequency ω_r in pulse experiments is a few kHz above that observed in continuous measurements. There is also a jump in $\tilde{\omega}_r$ in figure 7.16a, which I attribute to a sudden change in ω_r due to the formation of vortices in the superconducting material as the magnetic field is swept [13]. These jumps are also visible in the field sweeps of figures 7.7c and 7.7d (in addition to the coupling to transitions in [Yb(trensal)]).

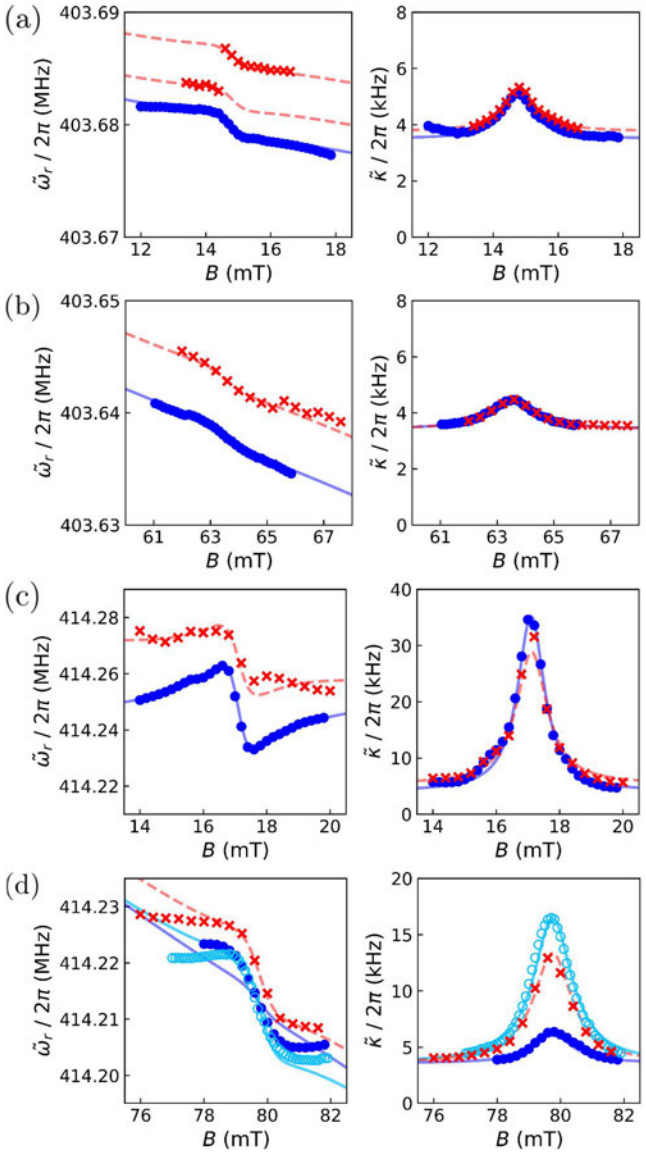

Figure 7.16: Effective resonance frequency $\tilde{\omega}_r$ and effective decay rate $\tilde{\kappa}$ of LER 4 coupled to nuclear spin transitions $1 \leftrightarrow 2$ (a) and $2 \leftrightarrow 3$ (b), and of LER 5 coupled to these same transitions (c, d). Blue dots are the fit parameters from continuous wave experiments at 10 mK, while red crosses are the fit parameters from pulse transmission experiments at this same temperature. The solid blue lines and red dashed lines are fits of these parameters based on equation (7.4). The continuous wave measurement of LER 5 coupled to the $2 \leftrightarrow 3$ transition were repeated at 50 mK. The fit parameters of this measurement are cyan dots in (d), with the cyan solid line being the fit to equation (7.4).

These results show that the decay rate of the resonator is maximum when-

ever the photons become hybridized with the nuclear spins. Besides, the characteristic ensemble coherence time $(T_2^*)_{\alpha\beta} = 1/\gamma_{\perp,\alpha\beta}$ obtained near resonance is about ten times higher for nuclear spin transitions than for electronic ones, and agrees well with the value derived from continuous wave measurements. This enhanced coherence compensates for the lower spin-photon coupling of nuclear spin transitions: $(G_N)_{\alpha\beta}(T_2^*)_{\alpha\beta} = (G_N)_{\alpha\beta}/\gamma_{\perp,\alpha\beta} \sim 0.1$–$0.2$ is achieved for both electronic and nuclear spin transitions.

7.4 Pump-probe experiments with isotopically purified samples

In pump-probe experiments, the spin-photon coupling of resonators to transitions in [Yb(trensal)] must be as large as possible, as it limits how fast the qudit can be operated. For this, the experimental setup in the previous section may be not enough. A large gap of ~ 50 μm between the chip surface and the [Yb(trensal)] crystals is reported [4]. This means that the spins do not couple to the mode volume just above the inductor, where the microwave magnetic field of the resonator is strongest. Furthermore, the number of [Yb(trensal)] molecules is reduced by diluting them in a diamagnetic matrix, and of these only a 16% has ^{173}Yb in a crystal with natural isotopical abundances.

Several improvements were carried out for the next experiments. A new chip, *Yb-pulsed* (figure 7.3b), was used instead of *Yb-cw*. The low-inductance design of LERs in *Yb-pulses* enhances the microwave magnetic field close to the inductor, which is just a narrow superconducting strip close to the transmission line. The mode volume of the LER is much smaller than before. Microscopic ($V \sim 10^{-13}$ m^3) [Yb(trensal)] crystals were placed by David Rodríguez (CAB, Madrid) on top of the inductor of LERs in *Yb-pulses* using a micro-manipulator. The crystal size matches the mode volume (see figure 7.17). Besides, these crystals were synthesized with isotopically purified ^{173}Yb, optimizing the number of [^{173}Yb(trensal)] molecules close to the inductor. The crystals have a 5% of [^{173}Yb(trensal)] molecules in a diamagnetic [Lu(trensal)] matrix. This section describes experiments aimed at measuring the spin-photon couplings to the different electronic spin transitions in these crystals, and at performing the first attempts to dispersively read out the spin states.

7.4.1 Characterization of electronic spin transitions

The resonators in *Yb-pulsed* are designed to coupled to the six allowed electronic transitions of [^{173}Yb(trensal)] (see figure 7.2c). In order to characterize

the collective spin-photon coupling of the six transitions, the transmission of the chip for driving frequencies close to the resonance frequency of LER 6 was measured for magnetic fields between 0 an 105 mT and at six different temperatures: 11, 25, 50, 100, 150 and 250 mK.

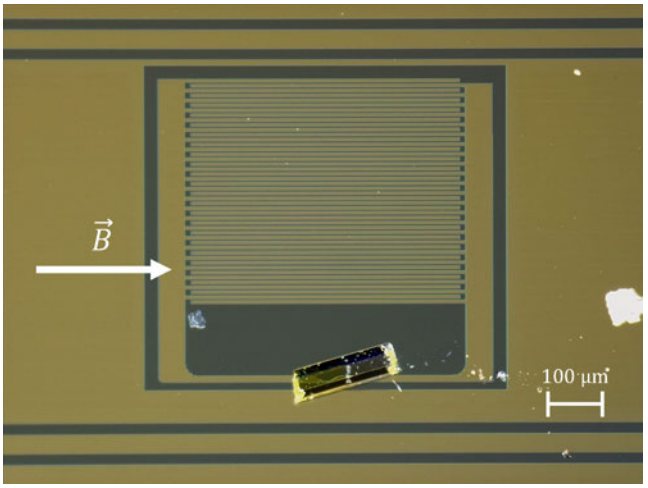

Figure 7.17: [Yb(trensal)] crystal on top of the inductor of LER 3 of *Yb-pulsed*. The crystal size matches the inductor size. The magnetic field $\boldsymbol{B}$ was applied parallel to the the inductor and transmission lines.

Figure 7.18 shows the results of these experiments, with six clear features in the resonance of LER 6 corresponding to the coupling of the resonator to the six electronic spin transitions (one for each nuclear spin proyection $m_S = -5/2$, $-3/2$, $-1/2$, $+1/2$, $+3/2$ and $+5/2$). These couplings happen approximately at $B_{\text{res}} = 23.4$, 35.0, 48.7, 64.4, 82.0 and 101.0 mT. As temperature increases, the effect of the couplings on the resonance of LER 6 is less prominent, as is expected from the decrease in the population difference between the low energy ($m_S = -1/2$) and high energy ($m_S = +1/2$) subsets of spin states. The highest measured temperature is of the same order as the energy difference (in temperature units) between the subsets up to ∼100 mT, see figure 7.2a)).

Close-ups of the measurement at 11 mK around these fields are shown in figure 7.19). The maximum collective spin-photon coupling (∼ 12.3 MHz) at 11 mK is obtained for $m_I = -5/2$. This corresponds to the $0 \leftrightarrow 11$ transition between the ground state and the highest excited, that is, the transition with the largest population difference in thermal equilibrium. For higher m_I, the electronic spin transition is between excited states. The fact that a change in the coupling is observed means that the temperature of the system is low enough to generate significant population differences between the nuclear states in each of the two subsets with $m_S = \pm 1/2$. This condition holds for temperatures

below 100 mK (see figure 7.2a).

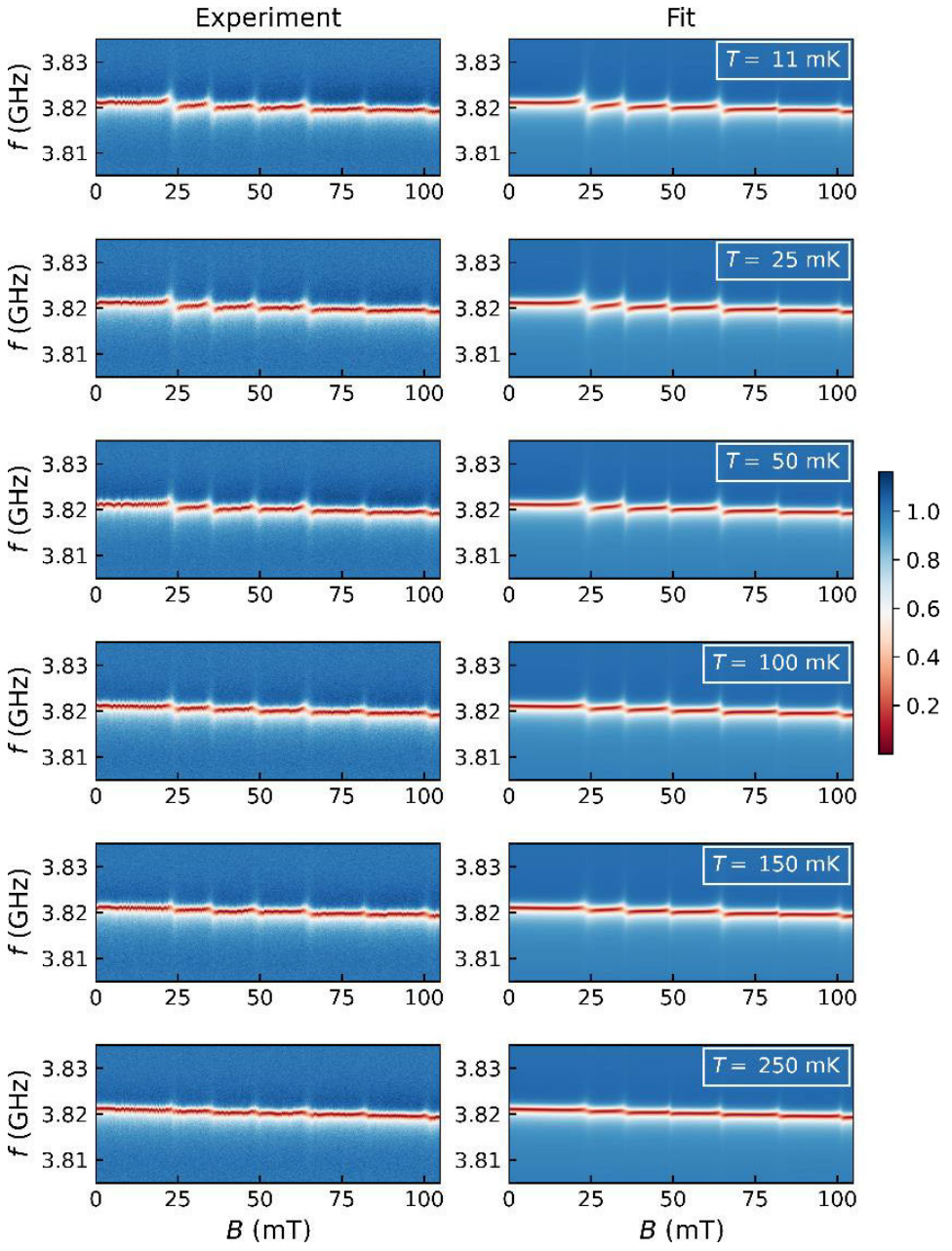

Figure 7.18: Normalized transmission of *Yb-pulsed* for driving frequencies close to the resonance frequency of LER 6, measured for magnetic fields between 0 an 105 mT at six different temperatures: 11 mK, 25 mK, 50 mK, 100 mK, 150 mK and 250 mK. Experimental data is compared to the fit of the coupling of LER 6 to the six electronic spin transitions of [^{173}Yb(trensal)] with equation (7.3).

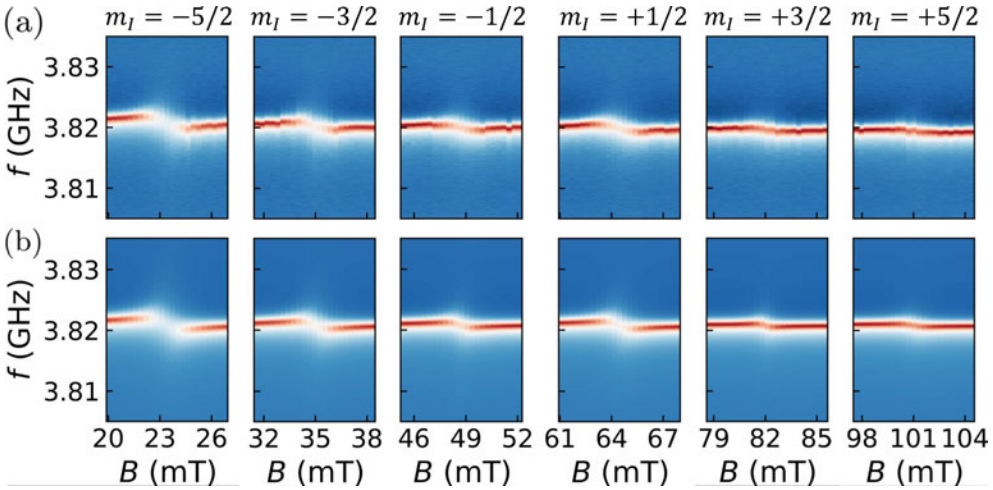

Figure 7.19: Close up of the experimental (a) and simulated (b) transmission of *Yb-pulsed* around each field where LER 6 resonates with an electronic spin transition (B_{res} = 23.4, 35.0, 48.7, 64.4, 82.0 and 101.0 mT) associated to a different nuclear spin proyection m_I, measured at T = 11 mK.

The experimental maps in figures 7.18 and 7.19 were fitted with the transmission of the resonator coupled to each of the electronic spin transitions, given by equation (7.3). The same LER parameters were used to fit the coupling to all transitions: $\omega_r = 3.821314 \pm 1.6 \cdot 10^{-5}$ GHz, $|\kappa_c| \simeq \kappa = 1.04 \pm 0.03$ MHz, $\phi_c = 15.9° \pm 0.7°$, and small drift of ω_r with magnetic field (-15.6 ± 0.3 MHz / T).

Figures 7.20a-b show the temperature dependence of the collective spin-photon coupling $(G_N)_{\alpha\beta}$ and the decoherence rate $\gamma_{\perp,\alpha\beta}$ associated to each electronic spin transition. The collective spin-photon coupling is not much higher that the one obtained for transition $1 \leftrightarrow 10$ ($m_I = -3/2$) in sections 7.2.1 and 7.3.1. Note, however, that the isotopically purified crystals are much smaller ($V \sim 10^{-13}$ m^3, , 10^{13}–10^{14} [^{173}Yb(trensal)] molecules) than those with natural abundances ($V \sim 10^{-10}$ m^3, 10^{15}–10^{16} [^{173}Yb(trensal)] molecules): figure 7.17 shows how the former fit in the resonator inductor line. Therefore, a similar collective spin-photon coupling is achieved with a smaller number of spins thanks to having the microwave field generated by the resonator localized in a volume around the inductor matching the crystal size.

The inhomogeneous broadenings $\gamma_{\perp,\alpha\beta}$ derived from these experiments are significantly higher than in crystals with natural abundances. In the latter, [^{173}Yb(trensal)] molecules were both diamagnetically diluted in a [Lu(trensal)] matrix and isotopically diluted by their natural abundance. Most Yb nuclei have zero nuclear spin ($I = 0$), which leads to a distinct different energy spectrum from that of [^{173}Yb(trensal)], where the large hyperfine coupling plays

an import role. This can hinder the exchange of spin excitations between [^{173}Yb(trensal)] and other [Yb(trensal)] molecules with $I = 0$. In the isotopically purified crystals, however, the density of [^{173}Yb(trensal)] molecules is higher, which have identical spin excitations. This might lead to the observed broadening.

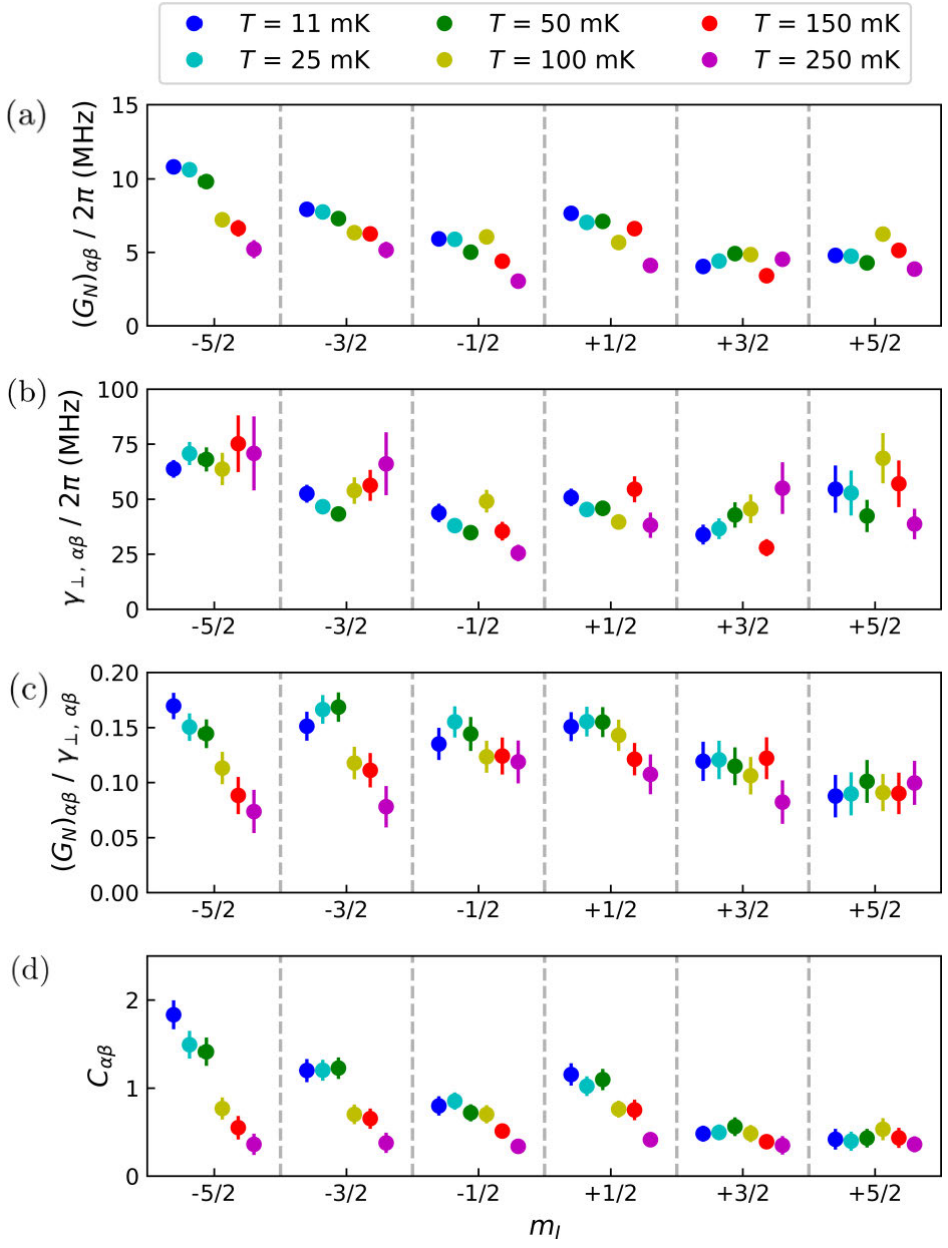

Figure 7.20: Collective spin photon coupling $(G_N)_{\alpha\beta}$ (a), decoherence rate $\gamma_{\perp,\alpha\beta}$ (b), $(G_N)_{\alpha\beta}/\gamma_{\perp,\alpha\beta}$ ratio (c) and cooperativity $C_{\alpha\beta} = (G_N)^2_{\alpha\beta}/\kappa\gamma_{\perp,\alpha\beta}$ for each electronic spin transition in [^{173}Yb(trensal)] at 11, 25, 50, 100, 150 and 250 mK.

The couplings of all six electronic spin transitions to LER 6 are in the weak coupling regime, while high cooperativity is achieved for the $0 \leftrightarrow 11$ ($m_I = -5/2$) and $1 \leftrightarrow 10$ ($m_I = -3/2$) transitions below 100 mK (see figures 7.20c-d). Again, these values have been obtained with a number of spins much smaller than in previous sections and in spite of the larger $\gamma_{\perp,\alpha\beta}$ values.

7.4.2 Dispersive readout in an electro-nuclear qudit

The theory of a qudit in the dispersive regime is detailed in seciton 3.4.3. In the case of the electro-nuclear qudit encoded in [^{173}Yb(trensal)], with $d = 12$ states, the shift in the resonator frequency is:

$$\omega_r \rightarrow \omega_r + \sum_{\alpha=0}^{11} \chi'_\alpha \langle \hat{X}^{\alpha,\alpha} \rangle, \tag{7.6}$$

where $\langle \hat{X}^{\alpha,\alpha} \rangle$ is the expectation value of the Hubbard operator $\hat{X}^{\alpha,\alpha}$ associated to each state $|\alpha\rangle$, with a dispersive shift:

$$\chi'_\alpha := \sum_{\beta \neq \alpha} \frac{|\Lambda_{\alpha\beta}|^2}{\Delta'_{\alpha\beta}}. \tag{7.7}$$

Here $\Delta'_{\alpha\beta}$ is a modified detuning, related to the actual detuning $\Delta_{\alpha\beta} = \omega_{\alpha\beta} - \omega_r$ between the frequency of transition $\alpha \leftrightarrow \beta$ and the resonator frequency ω_r by:

$$\Delta'_{\alpha\beta} := \frac{1 + \dfrac{\Delta_{\alpha\beta}}{2\omega_r}}{1 + \dfrac{\Delta_{\alpha\beta}}{\omega_r}}. \tag{7.8}$$

The resonators in *Yb-pulsed* are tuned to the electronic spin transitions. This means that the detuning between ω_r and the electronic spin transitions is much smaller than that between ω_r and the nuclear spin transitions. In addition, sections 7.2 and 7.3 showed how the collective coupling of nuclear spin transitions to the resonator is at least one order of magnitude smaller than with electronic spin transitions. The result is that the dispersive shift associated to the nuclear spin transitions is negligible compared to the one induced by electronic spin transitions, and equation (7.6) can be approximated by:

$$\omega_r \rightarrow \omega_r + |\Lambda_{\text{el}}|^2 \sum_{\alpha=0}^{5} \left(\frac{\langle \hat{X}^{\alpha,\alpha} \rangle}{\Delta'_{\alpha,11-\alpha}} + \frac{\langle \hat{X}^{11-\alpha,11-\alpha} \rangle}{\Delta'_{11-\alpha,\alpha}} \right), \tag{7.9}$$

where Λ_{el} is the coupling of the resonator to the electronic spin transitions.

In an ensemble of [^{173}Yb(trensal)] molecules at very low temperatures, the populations of the states in the high energy subset ($\langle \hat{X}^{11-\alpha,\alpha} \rangle_e$) in thermal equilibrium can be neglected. Then, the reference frequency ω_{ref} for pump-probe experiments is:

$$\omega_{\text{ref}} := \omega_r + |\Lambda_{\text{el}}|^2 \sum_{\alpha=0}^{5} \frac{\langle \hat{X}^{\alpha,\alpha} \rangle_e}{\Delta'_{\alpha,11-\alpha}}. \tag{7.10}$$

There are two types of pump-probe experiments that can be performed in this setup, depending on whether electronic or nuclear spin transitions are driven (see figure 7.21). The simpler experiment consists on pumping at the frequency of one of the electronic spin transitions, say $\beta \leftrightarrow 11-\beta$, as if it were the transition between the two states of a qubit, then measuring the resonator coupled to that same transition. The shift $\delta\omega_r$ from ω_{ref} after pumping at the frequency $\omega_{\beta,11-\beta}$ of the $\beta \leftrightarrow 11-\beta$ transition is:

$$\begin{aligned} \delta\omega_r =& |\Lambda_{\text{el}}|^2 \left(\frac{\langle \hat{X}^{\beta,\beta} \rangle - \langle \hat{X}^{\beta,\beta} \rangle_e}{\Delta'_{\beta,11-\beta}} + \frac{\langle \hat{X}^{11-\beta,11-\beta} \rangle}{\Delta'_{11-\beta,\beta}} \right) \\ \simeq& \frac{|\Lambda_{\text{el}}|^2}{\Delta_{11-\beta,\beta}} \left[\langle \hat{X}^{\beta,\beta} \rangle_e + \left(\langle \hat{X}^{11-\beta,11-\beta} \rangle - \langle \hat{X}^{\beta,\beta} \rangle \right) \right]. \end{aligned} \tag{7.11}$$

In the last step, the modified detuning $\Delta'_{11-\beta,\beta}$ was approximated to $\Delta_{11-\beta,\beta}$, and $\Delta'_{\beta,11-\beta}$ to $-\Delta_{11-\beta,\beta}$. This is valid if the transition frequency $\omega_{\beta,11-\beta}$ of the $\beta \leftrightarrow 11-\beta$ transition is set close enough to ω_r ($|\Delta_{11-\beta,\beta}| \ll \omega_r$), while still being in the dispersive regime ($|\Delta_{11-\beta,\beta}| \gg |\Lambda_{\text{el}}|$).

This experiment, sketched in figure 7.21b, is similar to the experiments that were carried out in the previous chapter with molecular spin qubits. The difference $\langle \hat{X}^{11-\beta,11-\beta} \rangle - \langle \hat{X}^{\beta,\beta} \rangle$ plays the role of $\langle \hat{\sigma}_z \rangle \equiv \langle \hat{X}^{1,1} \rangle - \langle \hat{X}^{0,0} \rangle$ in a qubit. The constant $\langle \hat{X}^{\beta,\beta} \rangle_e$ includes the effect of a not complete initialization in the ground state if the different nuclear spin states for $m_S = -1/2$ are slightly populated by temperature.

The other type of pump-probe experiments involves controlling the nuclear state by driving the nuclear spin transitions, with the magnetic field set at a value where the LER resonance frequency ω_r sits in between the electronic spin transitions associated to the different m_I states (see figure 7.21c). This is the method that is proposed to read the nuclear spin qudit state coupled to an electronic spin ancilla [14].

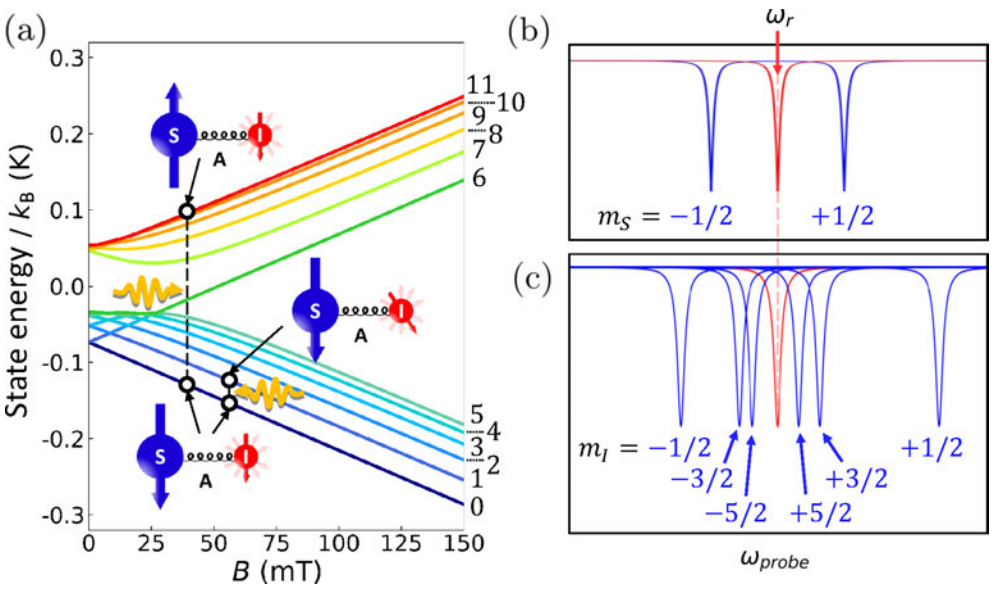

Figure 7.21: (a) The two types of pump-probe measurement are associated to whether electronic or nuclear spin transitions are driven with the pump pulse. (b) If an electronic spin transition is set close to ω_r with magnetic field, while keeping the spin-LER system in the dispersive regime, the dispersive shift of ω_r depends on the state of the electronic spin (blue solid lines). The electronic spin state can be changed by driving the electronic spin transition. In this case, a transition frequency above ω_r is assumed (positive detuning). As reference, the red solid line is the resonance of the uncoupled resonator. (c) In the alternative pump-probe experiment, the pump pulses control the nuclear spin state. The resonance of the uncoupled resonator (red solid line) is shifted differently depending on the nuclear spin state (blue solid lines). The magnetic field is chosen to have the electronic spin transitions associated to a negative m_I above ω_r and those associated to a positive m_I below ω_r.

The shift $\delta\omega_r$ after pumping the nuclear transition $\beta \leftrightarrow \gamma$ is:

$$\delta\omega_r = |\Lambda_{\mathrm{el}}|^2 \left(\frac{\langle \hat{X}^{\beta,\beta} \rangle - \langle \hat{X}^{\beta,\beta} \rangle_e}{\Delta'_{\beta,11-\beta}} + \frac{\langle \hat{X}^{\gamma,\gamma} \rangle - \langle \hat{X}^{\gamma,\gamma} \rangle_e}{\Delta'_{\gamma,11-\gamma}} \right), \tag{7.12}$$

which depends on the difference in population between nuclear states induced by pulses. Measuring this shift requires a good initialization of the system by lowering the temperature in order to see an appreciable change in $\delta\omega_r$. Here the modified detunings can not be approximated by $\Delta_{\beta,11-\beta}$ and $\Delta_{\gamma,11-\gamma}$, as in general it is not possible to simultaneously set both associated electronic spin transition frequencies $\omega_{\beta,11-\beta}$ and $\omega_{\gamma,11-\gamma}$ close to ω_r.

7.4.3 First pump-probe experiments

The first pump-probe experiments were carried out pumping the $0 \leftrightarrow 11$ electronic spin transition, which has the largest population difference in the system in thermal equilibrium. Thus, this transition provides the closest analogue of the pump-probe experiments with qubits. The magnetic field was set to 25.5 mT, which places the $0 \leftrightarrow 11$ transition frequency 123 MHz above the resonance frequency ω_r of LER 6 (see figure 7.22). This value was chosen to be ten times the coupling obtained for this transition at 11 mK, $(G_N)_{0,11} = 12.3$ MHz, so that the dispersive regime condition $\Delta_{0,11} \gg (G_N)_{0,11}$ is fulfilled.

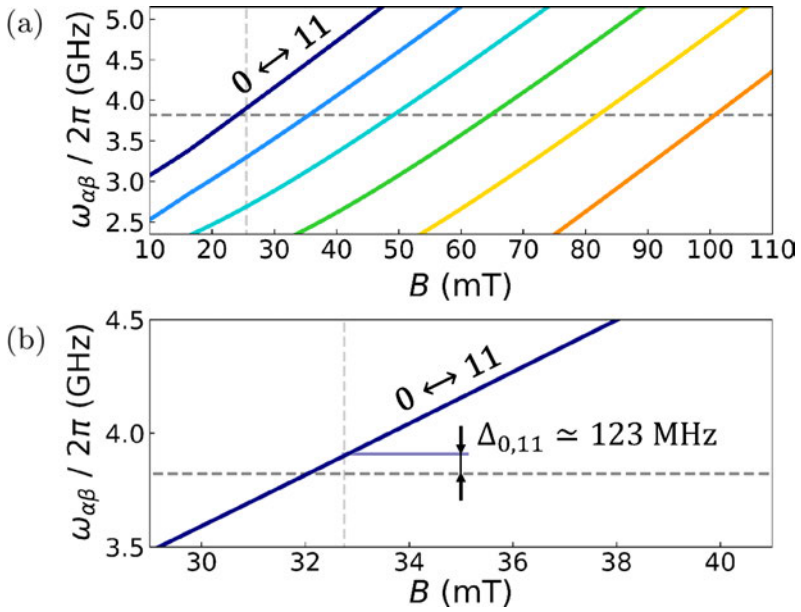

Figure 7.22: (a) Electronic spin transitions in [^{173}Yb(trensal)]. The horizontal dashed line marks the resonance frequency ω_r of LER 6, while the vertical line marks the magnetic field, $B = 25.5$ mT, at which pump-probe experiments were carried out. (b) Close-up of the range of magnetic fields for which the $0 \leftrightarrow 11$ transition frequency is close to ω_r. At $B = 25.5$ mT, the detuning between the transition frequency and ω_r is $\Delta_{0,11} = 123$ mT.

Pump pulses with lengths up to 500 μs were sent at the frequency of the $0 \leftrightarrow 11$ electronic spin transition at 25 mT. Figure 7.23 shows the resonance measured after the longest pump pulse was applied, compared to the reference. The shift $\delta\omega_r$ between the two is small compared to what was expected ($\delta\omega_r \sim (G_N)^2_{0,11}/\Delta_{0,11} \sim (G_N)_{0,11}/10 \sim 1$ MHz), and its only detected for very long pulses. Note that this was obtained with a non-attenuated excitation line, so it is not a power limitation as in the first pump-pulse experiments with PTM_r.

The main difference between these experiments and those in the previous chapter is how the sample is interfaced with superconducting chip. PTM_r/PS deposits were directly on top of the resonator, in particular its inductor. This produced high spin-photon couplings in a small set of PTM_r spins, which were responsible for most of the shift $\delta\omega_r$. Here, [^{173}Yb(trensal)] samples were crystals, which are susceptible to a small chip-sample gap due to any irregularities in the sample surface. The subsequent loss of the spins that would have the highest spin-photon couplings is probably the main limitation for producing a higher shift $\delta\omega_r$.

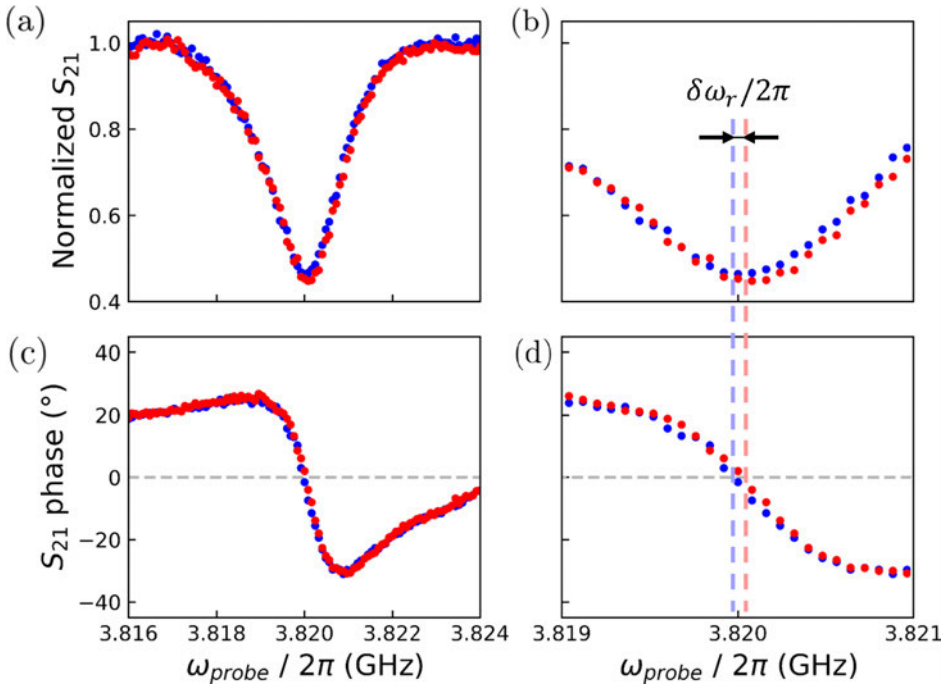

Figure 7.23: (a) Normalized module of the complex-valued transmission S_{21} of *Yb-pulsed* for probe frequencies close to the LER 6 resonance frequency ω_r, measured at $B = 25.5$ mT. Two situations are compared: red dots show the resonance after driving the $0 \leftrightarrow 11$ electronic spin transition, blue dots show the same resonance without any previous pump pulse. (b) Close-up centered at ω_r, showing the shift $\delta\omega_r$ of the center frequency of the resonance. Figures (c, d) illustrate more clearly this shift with the measurement of the phase of S_{21}.

7.5 Conclusions

High cooperativity has been observed in both electronic and nuclear transitions in [^{173}Yb(trensal)]. Reaching this regime the nuclear spin transitions was, a priori, much more demanding than with electronic ones due the very small

nuclear magnetic moment. Although the collective spin-photon couplings and cooperativities for nuclear transitions are indeed smaller than for electronic transitions in this same molecular system (about one order of magnitude), they are nevertheless remarkably high compared to the coupling of isolated nuclear spins to electromagnetic radiation, which would be three order of magnitude ($\sim \mu_N/\mu_\mathrm{B}$) than for electronic spin. The presence of the electronic spin, and its high hyperfine coupling to the nuclear spin, introduces an efficient path to couple nuclear transitions to the microwave magnetic field generated by the LER. Here the coupling is mediated by the *electronic* Zeeman interaction, which drives the nuclear transition due to the mixing of the electronic and nuclear spin wavefunctions through the hyperfine coupling.

The coupling of LERs to electronic spin and nuclear spin transitions was studied independently with continuous wave experiments and with pulse transmission, the latter unveiling the dynamics of the hybrid spin-LER system. The experimental results obtained with these two types of measurement are consistent with each other. This shows that the theory for the measurement of resonators coupled to molecular spins is not only valid in the driven steady state ($t \gg 1/\kappa, 1/\tilde{\kappa}$), but also for all the dynamics of the system.

The lower coupling to nuclear spin transitions compared to electronic ones is compensated by their longer ensemble coherence times T_2^*. Thus, both can be used in almost equal terms to define the states of a qudit. This opens prospects for QEC withing a hybrid a circuit QED hybrid scheme.

Finally, additional experiments were carried out with isotopically purified [^{173}Yb(trensal)] crystals. The coupling of a resonator to the six electronic spin transitions was measured at different temperatures. The purification gives higher couplings to these transitions, but also an increases their decoherence rate due to the higher concentration of ^{173}Yb nuclear spins ($I = 5/2$). The first pump-probe experiments with qudits were performed in these samples, giving a shift $\delta\omega_r$ smaller than expected, which could be due to the presence of a sample-gap.

References

[1] E. Tancini, M. J. Rodriguez-Douton, L. Sorace, A.-L. Barra, R. Sessoli, and A. Cornia, Chemistry: A European Journal **16(34)**, 10482 (2010).

[2] L. Vergnani, A.-L. Barra, P. Neugebauer, M. J. Rodriguez-Douton, R. Sessoli, L. Sorace, W. Wernsdorfer, and A. Cornia, Chemistry: A European Journal **18(11)**, 3390 (2010).

[3] K. Masatoshi and Y. Toshiro, Journal of the American Chemical Society **140**, 9814 (2018).

[4] V. Rollano, M. C. de Ory, C. D. Buch, M. Rubín-Osanz, D. Zueco, C. Sánchez-Azqueta, A. Chiesa, D. Granados, S. Carretta, A. Gomez, et al., Communications Physics **5**, 246 (2022).

[5] K. Masatoshi and Y. Toshiro, Chemistry Letters **28(2)**, 137 (1999).

[6] P. V. Bernhardt, B. M. Flanagan, and M. J. Riley, Australian Journal of Chemistry **53**, 229 (2000).

[7] P. V. Bernhardt, B. M. Flanagan, and M. J. Riley, Australian Journal of Chemistry **54**, 229 (2001).

[8] T. Fujito, Inorganic Chemistry **41**, 5024 (2002).

[9] M. Chizzini, L. Crippa, L. Zaccardi, E. Macaluso, S. Carretta, A. Chiesa, and P. Santini, Physical Chemistry Chemical Physics **24(34)**, 19979 (2022).

[10] J. A. Jones, V. Vlatko, A. Ekert, and G. Castagnoli, Nature **403**, 869 (2000).

[11] L. M. K. Vandersypen, M. Steffen, G. Breyta, C. S. Yannoni, M. H. Sherwood, and I. L. Chuang, Nature **414**, 883 (2001).

[12] A. Blais, R.-S. Huang, A. Wallraff, S. M. Girvin, and R. J. Schoelkopf, Physical Review A **69**, 062320 (2004).

[13] D. Bothner, T. Gaber, M. Kemmler, D. Koelle, R. Kleiner, S. Wünsch, and M. Siegel, Physical Review B **86**, 014517 (2012).

[14] A. Gómez-León, F. Luis, and D. Zueco, Physical Review Applied **17**, 064030 (2022).

Chapter 8

Circuit QED beyond non-interacting magnetic molecules

The experiments in previous chapters were carried out with large ensembles of N magnetic molecules in order to enhance the ensemble-resonator coupling G_N, which scales with $\sqrt{N}$. Molecules were considered to be close to equivalent and non-interacting, with the same effective spin Hamiltonian for each molecule. In this situation, the microwave magnetic field generated resonator couples to Dicke or Dicke-like states that are completely symmetric in the excitation of any of the N identical molecular spins.

As the temperature of the spin system is decreased, spin-spin interactions may play an important role on the physics of the ensemble. The question then arises of whether these intrinsic collective states affect the coupling to the circuit and, then, if this allows detecting the onset of magnetic correlations. Besides, the spin-photon coupling can be seen as a source of correlations that eventually leads to phase transition known as as photon condensation [1]. It is therefore interesting to study the competition between these two interactions.

This chapter studies the effect of spin-spin interactions on transmission experiments performed with spin 1/2 and spin 1 ensembles. The step up from spin 1/2 to spin 1 is quite relevant. The two-fold energy degeneracy at zero magnetic field in a spin 1/2 can not be split by magnetic anisotropy (see section 3.1.2 from chapter 3), while in the spin 1 case its three spin states are non-degenerate in energy if there is some magnetic anisotropy in the ion. An additional competition is then expected between spin-spin interactions and magnetic anisotropy, which is not present in a spin 1/2.

8.1 Competition between spin-photon and spin-spin interactions in DPPH organic free radicals coupled to a superconducting transmission line

The collective character of the coupling of an ensemble of qubits to photons in a waveguide reflects itself in an enhanced superradiant emission of light and in the broadening of the absorption lines [2, 3]. The underlying mechanism is the light-mediated interaction among emitters, leading to the formation of collective spin states known as Dicke states [4, 5]. So far, the focus in waveguide QED (w-QED) has been mainly on non-interacting emitters, where all interactions occur through photons. Exploring the competition of this photon-mediated interactions and intrinsic spin-spin interactions in the material remains rather unexplored.

A sample of organic free radicals (DPPH) was chosen for this purpose. DPPH is a free radical with spin $1/2$ and a g-factor $g_S = 2.004$ close to that of a free electron [6]. At low temperatures, it forms antiferromagnetic (AF) dimers and one-dimensional AF spin-chains. Figure 8.1a shows the increase of the spin-spin correlations (in absolute value) generated by the antiferromagnetic exchange interactions, as estimated from magnetic susceptibility data al ready discussed in chapter 5.

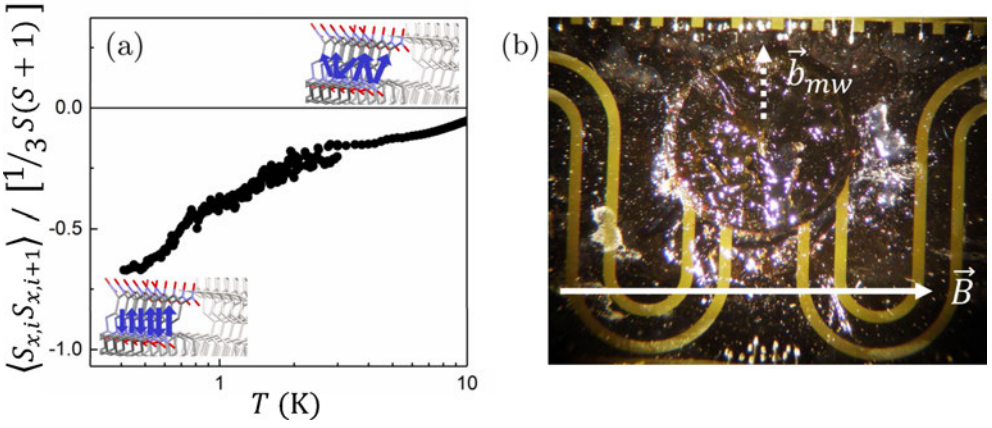

Figure 8.1: (a) Steady increase (in absolute value) in the spin-spin correlation $\langle S_{x,\,i}S_{x,\,i+1}\rangle$ between nearest neighbor type-B DPPH sites as temperature is lowered. The negative correlations reflect the formation of antiferromagnetic spin chains. They are computed from the dc-magnetic susceptibility of type-B DPPH molecules in figure 5.11, following the relation $\chi T/C \simeq 1 - |\langle S_{x,\,i}S_{x,\,i+1}\rangle/(1/3)\,[S(S+1)]\,|$ given in [7]. Here, C is the Curie constant of the type-B sublattice. (b) DPPH sample on top of a meandering transmission line. The static magnetic field $\boldsymbol{B}$ is applied horizontally. Only the top part of the sample, where the microwave magnetic field $\boldsymbol{b_{mw}}$ generated by the line is perpendicular to $\boldsymbol{B}$, is coupled to the line.

A powder sample of DPPH was deposited on top of a superconducting coplanar waveguide (CPW) to measure how these correlations influence the interaction to photons travelling via the CPW (see figure 8.1b). The CPW was fabricated by optical lithography on a 100 nm thin film of Nb deposited on a crystalline sapphire wafer. The central line of the CPW had a width of 400 μm in order to match the DPPH sample size. The sample was glued to the CPW with apiezon grease, ensuring proper thermalisation. The powder DPPH pellets used here for broadband transmission experiments are similar to the ones measured in chapter 5, where the full characterization of DPPH samples is detailed. The broadband nature of waveguides provides a distinct advantage, allowing the exploration of the transmission of DPPH in a wide range of frequencies [8–11] and the different phases of DPPH (paramagnetic / AF chains) within a single experiment. However, this advantage comes with a trade-off of a reduced sensitivity compared to that of a resonator ($(G_N)_{line} \ll G_N$).

8.1.1 Paramagnetic phase: spin-photon coupling enhancement

The broadband transmission of the CPW coupled to a DPPH powder sample was measured below 4.25 K. The device was thermally coupled to the mixing chamber of a 'wet' ^{3}He-^{4}He dilution refrigerator giving access to the temperature region between 130 mK and 4.2 K. Additional experiments were carried out with the dilution refrigerator described in section 2.2, which gives access to lower temperatures. Well above $T = 0.65$ K, half of the DPPH molecules are forming dimers with $S = 0$ (type-A DPPH, see section 5.2.2 in chapter 5), while the other half remain in a paramagnetic phase (type-B DPPH). Only the latter can couple to the microwave photon magnetic field generated by the CPW.

Normalized transmission data, measured at 2 K from 10 MHz up to 14 GHz and for fields up to 500 mT are shown in figure 8.2a. A field-dependent resonant absorption of photons by the paramagnetic ensemble is observed, matching the transition frequency $\omega_q = \mu_B g_S B/\hbar$ of a spin $S = 1/2$ with $g_S = 2.004$. The transmission shows close to Lorentzian absorption minima. A nearly constant $\gamma_\perp \ / \ 2\pi \simeq 20$ MHz is measured at 2 K. The collective spin-photon coupling $G_N^{(\mathrm{line})}$ increases with magnetic field B (and therefore with frequency). This leads to a coupling visibility that also increases with B, as shown in figure 8.2b. These measurements were fitted using the theory for an ensemble of non-interacting spins 1/2 coupled to a transmission line (see section 4.5.3 in chapter 4):

$$S_{21}(\omega_d) = 1 - \frac{G_N^{(\mathrm{line})}(\Delta P)_e}{i(\omega_q - \omega_d) + \gamma_\perp + G_N^{(\mathrm{line})}(\Delta P)_e}, \tag{8.1}$$

where $G_N^{(\mathrm{line})}$ is the collective coupling of the spins to photons travelling via the line and $\gamma_\perp$ is the decoherence rate of the spin ensemble. In what follows, the population difference in thermal equilibrium, $(\Delta P)_e$, between the down ($m_S = -1/2$) and up ($m_S = +1/2$) spin states is included in $G_N^{(\mathrm{line})}$: $G_N^{(\mathrm{line})} \propto (\Delta P)_e$. This population difference alone encodes the temperature dependence of the intensity of the absorption signal in the paramagnetic phase:

$$(\Delta P)_e := \tanh\left(\frac{\hbar\omega_q}{2k_\mathrm{B}T}\right) = \tanh\left(\frac{\mu_\mathrm{B} g_S B}{2k_\mathrm{B}T}\right). \tag{8.2}$$

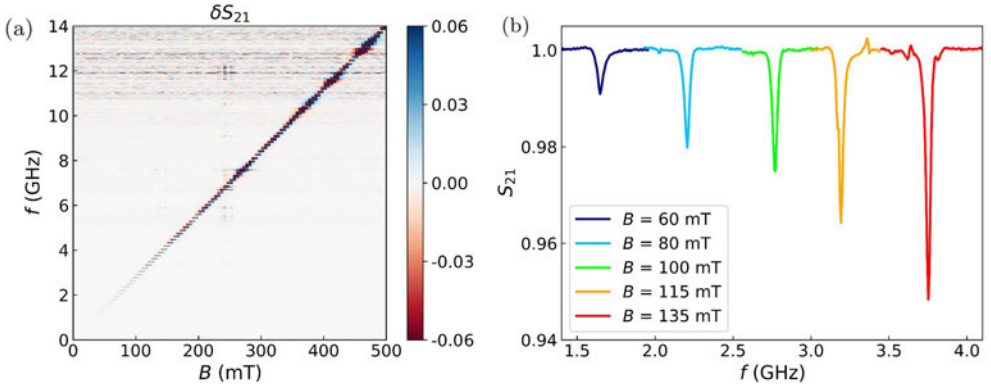

Figure 8.2: (a) Normalized transmission difference (δS_{21}) of a DPPH sample coupled to a transmission line at $T = 2$ K. This difference is computed at each field B as $\delta S_{21}(B) = [S_{21,\,\mathrm{exp}}(B) - S_{21,\,\mathrm{exp}}(B + \delta B)]\,/S_{21,\,\mathrm{exp}}(B + \delta B)$, effectively removing the baseline of the transmission signal. δB is a small field, but large enough so that the spin resonance signals at B and $B + \delta B$ do not overlap in frequency. A large increase in visibility is observed at some specific frequencies due to the coupling of spins to resonant modes in the transmission line. (b) Normalized transmission $S_{21} = 1 + \delta S_{21}$ at four selected fields, avoiding the coupling with line resonant modes. The visibility of the resonance increases with frequency, as expected for spin-photon coupling in a one-dimensional waveguide.

Figure 8.3 shows the field and temperature dependence of $G_N^{(\mathrm{line})}$ and $\gamma_\perp$. $G_N^{(\mathrm{line})}$ is proportional to the spectral density $J(\omega_d)$, which in turn is proportional to the input frequency $\omega_d = 2\pi f$ in a one-dimensional waveguide (Ohmic bath). Close to the spin resonance ($\omega_d \simeq \omega_q$), and $G_N^{(\mathrm{line})}$ can be written as:

$$G_N^{(\mathrm{line})} := \alpha\omega_q(\Delta P)_e = \alpha\frac{\mu_\mathrm{B} g_S B}{\hbar}\tanh\left(\frac{\mu_\mathrm{B} g_S B}{2k_\mathrm{B}T}\right), \tag{8.3}$$

where α is a temperature- and field-independent dimensionless scaling factor. $\alpha = 0.00441 \pm 6 \cdot 10^{-5}$ is the only free parameter in the fit of $G_N^{(\mathrm{line})}$ in figure 8.3.

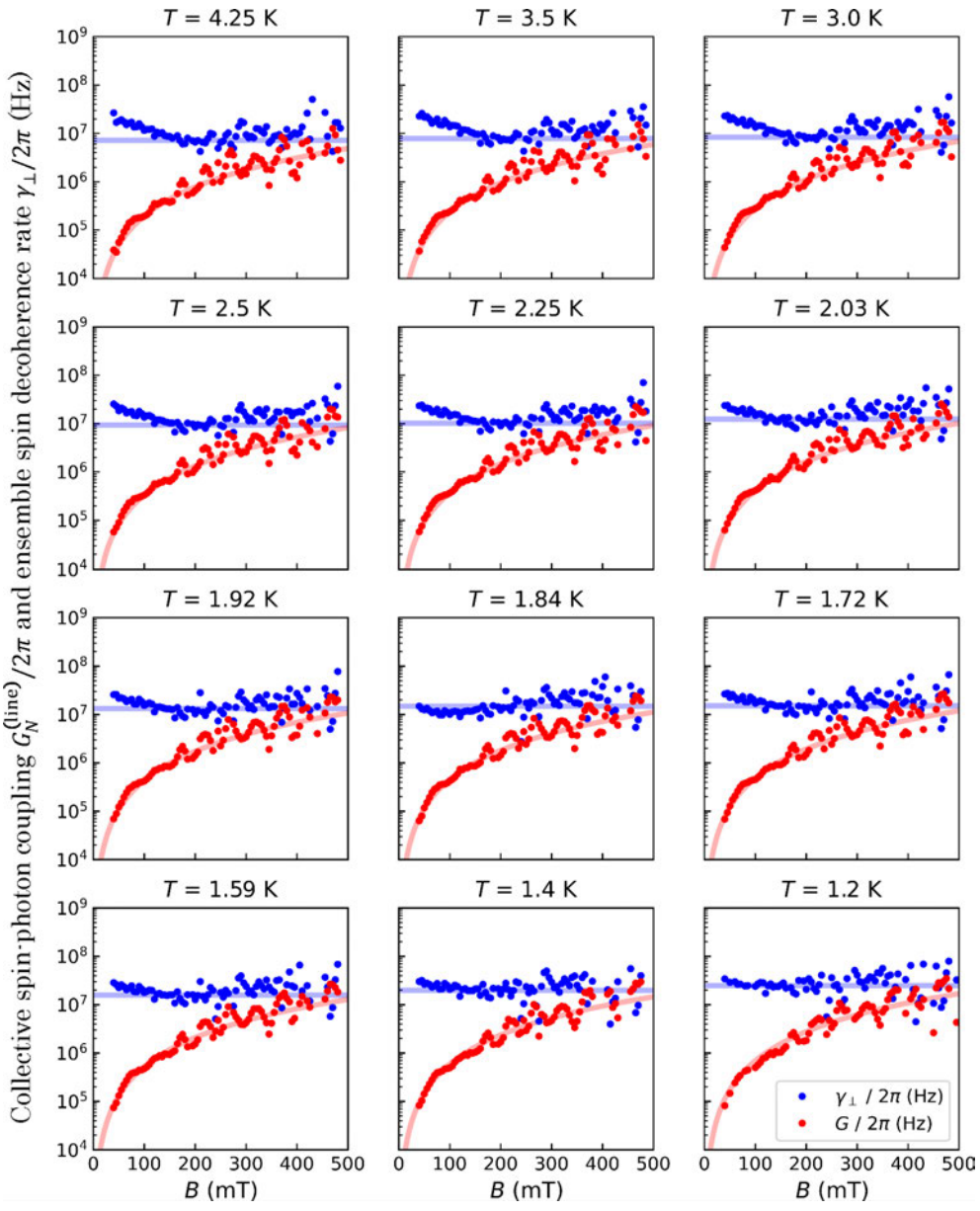

Figure 8.3: Magnetic field dependence of $G_N^{(\mathrm{line})}$ and $\gamma_\perp$ for several temperatures in the paramagnetic phase. Experimental values are shown as dots. The solid blue line is the average $\gamma_\perp$ at intermediate fields. The solid red line is the fit of $G_N^{(\mathrm{line})}$ to equation (8.3), with only α as a free parameter to fit all temperatures. Oscillations with magnetic field (and therefore frequency) in the the experimental $G_N^{(\mathrm{line})}$ values are associated to modes in the waveguide.

The coupling enhancement by $N_{\mathrm{eff}} = N(\Delta P)_e$, where N is the number of spins in the DPPH sample coupled to the microwave magnetic field generated

by the waveguide, signifies the increase in the radiative rate decay in superradiant collective states. In the single-photon limit and at zero temperature, this serves as a signature of the formation of Dicke states. Here, at finite temperature, the system forms thermal collective states that also emit in a superradiant manner.

The decoherence rate $\gamma_\perp$ is found to be fairly temperature- and field-independent, except for the slight increase at lower temperatures as the model of the paramagnetic phase starts to fail. I associate it to a homogeneous broadening $\gamma_\perp = T_2^{-1}$. The observed $\gamma_\perp/2\pi \cong 8$ MHz at $T = 4.2$ K is compatible with the value measured for DPPH samples coupled to coplanar resonators ([12, Ch.7] and [13]) and to lumped-element resonators (see chapter 5). Remarkably, for magnetic fields $B > 400$ mT, $G_N^{(\mathrm{line})}$ becomes of the same order of $\gamma_\perp$. This yields a signal visibility:

$$\eta := \max(|\delta \mathrm{S}_{21}|) = \frac{\mathrm{G}_\mathrm{N}^{(\mathrm{line})}}{\mathrm{G}_\mathrm{N}^{(\mathrm{line})} + \gamma_\perp} \tag{8.4}$$

close to unity. Therefore, the spins are then in a regime that resembles the strong coupling limit ($G_N \geq \gamma_\perp$) that is often me for cavities, but in this case with a transmission line ($G_N^{(\mathrm{line})} \geq \gamma_\perp$).

8.1.2 Breakdown of superradiance by magnetic correlations

Below $T_\mathrm{N} = -\theta = 0.65$ K, B-type DPPH molecules tend to form AF chains (see section 5.2.2). Temperature controls the extension of spin correlations along these chains in a continuous and monotonic manner (see figure 8.1a). In order to explore how these correlations modify the transmission of the CPW, the CPW + DPPH device was thermally coupled to the mixing chamber of a different ^{3}He-^{4}He dilution refrigerator giving access to the temperature region down to 10 mK.

Figure 8.4a shows transmission data measured at a fixed magnetic field $B = 125$ mT as function frequency and (decreasing) temperature. At this field, the transmission of the waveguide is relatively 'clean', in the sense that the oscillations in $G_N^{(\mathrm{line})}$ (8.3) are not present. The spin resonance first gets enhanced on cooling below 2 K, as a result of the higher spin polarization (higher $(\Delta P)_e$), but then it broadens out by an order of magnitude upon cooling from 2 K to 100 mK. This broadening is significantly larger than the broadening associated with the weak anisotropy, less than 1 in 1000, between the principal g-factors of DPPH [6]. Concurrently, the average resonance frequency ω_q increases by about 7 % and the visibility decreases. Below 100 mK, the resonance becomes temperature independent.

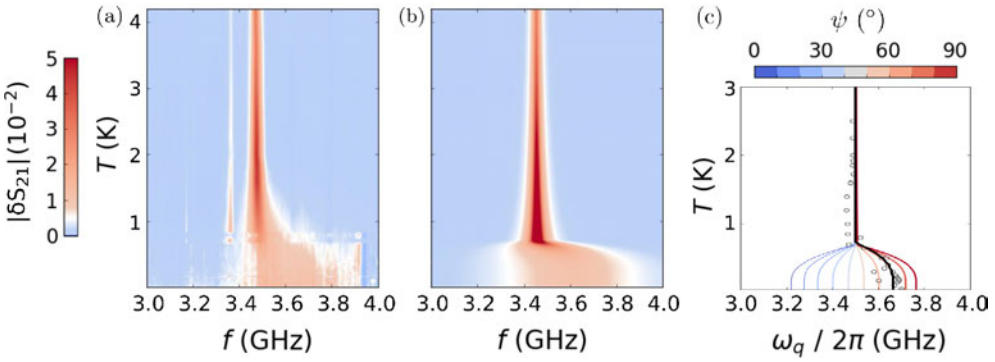

Figure 8.4: (a) Temperature dependence of the visibility of the resonance, given by δS_{21} at a magnetic field $B = 125$ mT. A large broadening of the resonance signal is observed below 1 K, marking the breakdown of superradiance due to the onset of antiferromagnetic correlations between type-B DPPH molecules. (b) Simulation of the experimental visibility with an antiferromagnetic mean-field model for type-B DPPH molecules with an imposed temperature independent visibility below T_{N} due to the formation of spin waves (see main text). (c) Dependence of the antiferromagnetic resonance frequency, ω_{res}, of each chain with the angle ψ between the anisotropy axis $\boldsymbol{\epsilon}$ of the chain and the applied magnetic field $\boldsymbol{B}$. The solid angle distribution favours the presence of larger angles (thicker solid lines) and therefore, larger frequencies, which is reflected in the transmission. The central frequency of the resonance, ω_q obtained from (b) is represented by the solid black line, which fits quite well the experimental data (grey open dots).

These features can not be explained anymore as just the transmission of an ensemble non-interacting spins. They are a consequence of the growing 1D spin correlations between DPPH molecules from sublattice B shown in figure 8.1a. A theory for the transmission of a waveguide coupled to 1D antiferromagnetic chains was developed by collaborators Sebastián Roca and David Zueco from the Q-MAD group at INMA. Using short chains does not suffice to describe the transmission, as longer chains have larger contributions. Unfortunately, a description of the coupling of arbitrarily long chains is computationally unaffordable. Therefore, a mean field (MF) theory was developed as a first approximation to describe the antiferromagnetism of the sample.

In antiferromagnetic MF theory, spins are split into two sublattices with magnetization $\boldsymbol{M_1}$ and $\boldsymbol{M_2}$:

$$H = -\boldsymbol{B} \cdot (\boldsymbol{M_1} + \boldsymbol{M_1}) + \boldsymbol{M_1} \cdot \boldsymbol{J} \cdot \boldsymbol{M_2}, \tag{8.5}$$

where $\boldsymbol{J}$ is a tensor encoding the anisotropy of the spin-spin exchange interactions. This anisotropy is defined by an axis $\boldsymbol{\epsilon}$ that depends on the orientation of the chains, introducing small corrections on the antiferromagnetic exchange constant J fixed via the Curie-Weiss law: $J/k_{\mathrm{B}} = 4T_{\mathrm{N}} = -4\theta = 0.65$ K (see

section 5.2.2). The module of $\boldsymbol{\epsilon}$ is the anisotropy exchange energy ϵ. With this model, the $k = 0$ spin wave frequency or *antiferromagnetic resonance* frequency ω_{res} is computed by solving Landau-Lifshitz-Gilbert (LLG) equation with equation (8.5) in the linear regime [14]. This is the frequency at which each chain resonates with microwave light, provided that the photon wavelength λ is much longer than the size of the spin chains. Here this is a valid assumption, as the sample size is smaller than the smallest photon wavelengths ($\lambda = 4.4$ mm) for which the spin-photon coupling was measured ($\omega_d \leq 14$ GHz).

The presence of a weak anisotropy in the interactions along the chain is key to explain the observed shift in the resonance frequency ω_q. Each DPPH crystallite acquires a different resonance frequency depending on the angle ψ between the anisotropy axis $\boldsymbol{\epsilon}$ and the magnetic field. In a powder, the anisotropy introduces a distribution of resonance frequencies ω_{res} with a larger contribution for angles $\psi \sim \pi/2$ (see figure 8.4c). The ensuing inhomogeneous broadening makes different DPPH molecules 'distinguisable' and breaks down the Dicke state. The resonance frequency ω_q is computed as the central frequency of this broadened signal.

This simple model is therefore able to account for the change in the 'average resonance frequency' $\bar{\omega_q}$ (figure 8.4c) and the resonance broadening (figure 8.5b) that are observed experimentally. $\bar{\omega_q}$ is computed as the centre frequency of the average of the resonances for all solid angles. The only fit parameter is the magnitude ϵ of the anisotropy in $\boldsymbol{J}$:

$$\epsilon := \frac{J_\perp - J_\parallel}{J_\parallel}, \tag{8.6}$$

where $J_\parallel \equiv J$ and $J_\perp$ are the components of $\boldsymbol{J}$ parallel and perpendicular to the anisotropy axis $\boldsymbol{\epsilon}$, respectively. Therefore, a reasonably good fit of $\bar{\omega}_q$ gives a measure of the exchange coupling anisotropy, giving $\epsilon \simeq -1/10$.

There is, however, an important limitation inherent to MF models: it overestimates the sharpness of the transition and predicts a phase transition towards an AF phase, which does not occur in 1D (see the dashed line in figure 8.5a). Besides, it does not properly account for the elementary excitations of the AD chains, i.e. the spins waves. The temperature insensitivity of $\max(|\delta S_{21}|)$ in figure 8.5a is indeed obtained by imposing the appearance of the spin-wave dynamics below T_{N}, which gives the solid line. This insensitivity provides direct evidence for a change in the statistics governing the elementary excitations of the spin system that interact with the microwave photons, from that of individual spin 1/2 angular momenta (fermions) to the bosonic commutation relations of spin waves.

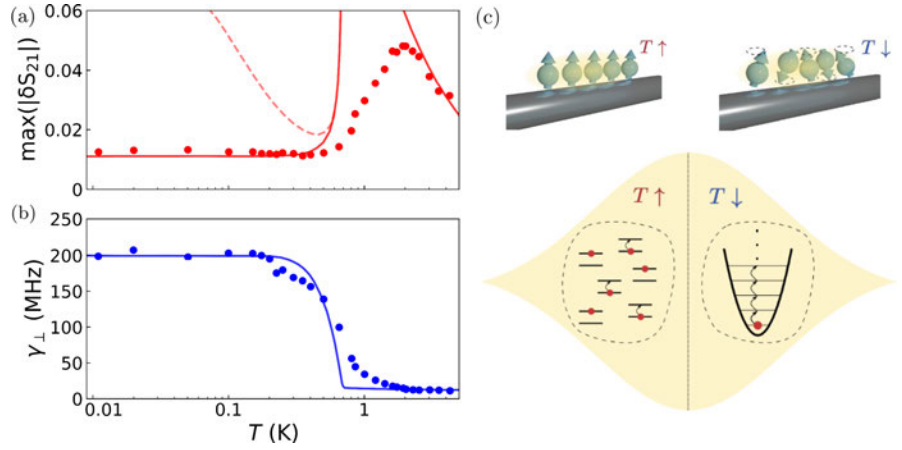

Figure 8.5: (a) Temperature dependence of the maximum visibility, $\max(|\delta S_{21}|)$, extracted from figures 8.4a (red dots) and 8.4b (solid red line). As a comparison, the dashed line shows the expected visibility in the absence of spin waves below T_N. (b) Temperature dependence of $\gamma_\perp$. Blue dots represent the experimental values extracted from figure 8.4a. The blue solid line is the prediction from mean field theory, scaled to include the 'inhomogeneous' broadening that arises from exchange anisotropy in a powder sample. (c) Picture of the competition between spin-photon and spin-spin interactions. At high temperatures, type-B spins are in the paramagnetic phase and superradiant emission is observed. When the temperature is low enough, spins form chains, and spin waves appear. This is a change in the fundamental statistics of the system, from fermions (paramagnetic phase) to bosons (AF chains).

8.2 On-chip magnetic spectroscopy across a magnetic phase transition

8.2.1 Qubits based on spin clock states

The main source of decoherence in molecular spin qubits is the interaction of the spin with magnetic noise in the environment. Typical sources of these magnetic fields are other neighbouring spins (as in the previous section), or even nuclear spins from atoms in the same molecule. A straightforward strategy to achieve long coherence times (T_2) is, therefore, to use molecules with effective spin 1/2 and nuclear spin-free ligands in dilution. The best coherence times are obtained with solvents which are also nuclear spin-free, like CS_2 (see figure 8.6 for some milestones).

A radically different strategy is inspired by so-called 'clock transitions' that are used in atomic clocks, and which appear in the anti-crossings between quantum states. In a magnetic molecule, these avoided crossings appear between superposition spin states with opposite symmetry (symmetric/antisymmetric)

that form at certain magnetic fields. These 'spin clock transitions' have a remarkable stability against magnetic field fluctuations, as dipolar decoherence vanishes at first order [15].

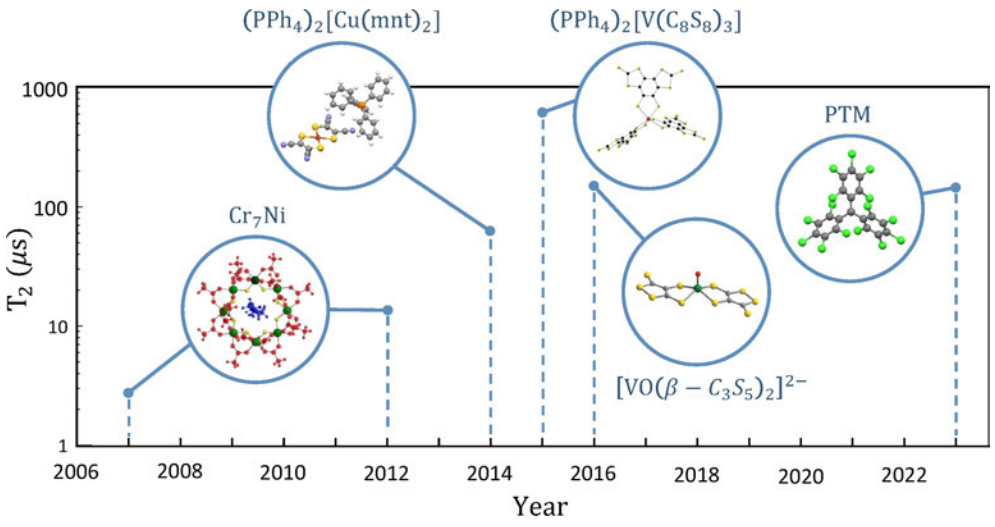

Figure 8.6: Beating decoherence in molecular spin qubits. These systems have effective spin 1/2, with nuclear spin-free ligands and in solution with nuclear spin-free solvents. References: Cr_7Ni [16, 17], $(PPh_4)_2\,[Cu(mnt)_2]$ [18], $(PPh_4)_2\,[V(C_8S_8)_3]$ [19], $[VO(\beta - -C_3S_5)_2]^{2-}$ [20], PTM [21].

Examples of these transitions have been found among molecular materials. A paradigmatic example is provided by the HoW_10 complex. EPR experiments performed on diamagnetically diluted $Ho_xY_{1-x}W_10$ crystals show that spin coherence times increase sharply near each clock transition as the spin-photon coupling becomes maximum [11, 22]. However, the presence of sizeable hyperfine interactions turns them into non-ideal qubit candidates. First, getting to the clock transition requires the application of an external magnetic field and second and, probably more important, the two levels involved in the clock transition might not include the actual ground spin state, thus hindering a simple qubit initialization by cooling.

The ideal situation is a clock transition between the ground and the first excited spin states. The simplest system that can achieve this is a spin 1 with tetragonal and orthorhombic distortions (only if $D < 0$), which is described by the following Hamiltonian:

$$H = D\hat{S}_z^2 + E\left(\hat{S}_x^2 - \hat{S}_y^2\right) + \mu_B g\left(B_x\hat{S}_x + B_y\hat{S}_y + B_z\hat{S}_z\right), \qquad (8.7)$$

where a constant term in the magnetic anisotropy has been dropped.

8.2.2 Molecular design of the simplest system with spin-clock states: the case of [Ni(2-Imdipa)]

The metallorganic compounds [Ni(Me_6tren)] and [Ni(2-imdipa)(NCS)]-(NCS) provide a physical realization of the system described by Hamiltonian (8.7) [23]. Here I focus on [Ni(2-imdipa)(NCS)]-(NCS), shortened as [Ni(2-Imdipa)] in what follows, which has a clock transition frequency of roughly 6 GHz suitable for the frequency range of on-chip broadband experiments and for coupling to superconducting resonators. [Ni(2-Imdipa)] is composed of an organic ligand (2-imdipa) hosting a Ni^{2+} ion with spin 1 (see figure 8.7).

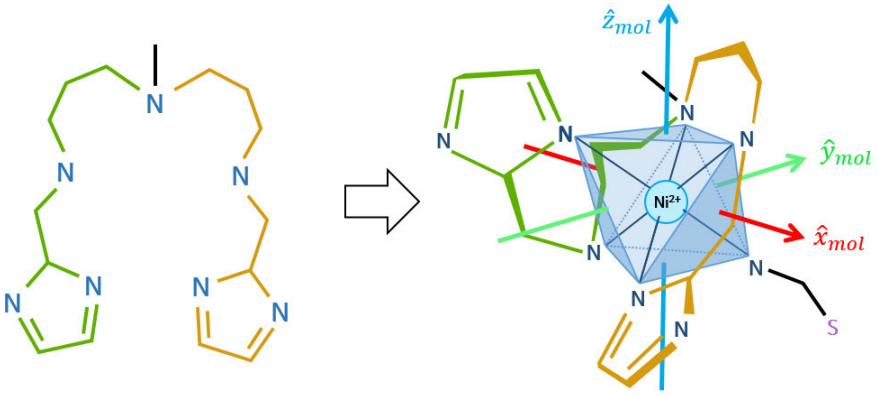

Figure 8.7: 2-imdipa pentadentate ligand (left) and its encasing of the Ni^{2+} ion in the Ni(2-Imdipa)(NCS) complex. Together with the NCS group, 2-imdipa forms an octahedral coordination site for Ni^{2+}. Only $\boldsymbol{y_{mol}}$ is completely determined from previous experiments, with two possible solutions for $\boldsymbol{x_{mol}}$ and $\boldsymbol{z_{mol}}$. A guess of these axes, based on the symmetry of the coordination site, is shown here: the $\boldsymbol{z_{mol}}$ is perpendicular to a face of the octahedron (not exactly in practice, as it is a distorted octahedron).

The energy spectrum of [Ni(2-imdipa)] was calculated from the experimental results of heat capacity experiments [23]. Figure 8.8a shows the temperature dependence of the specific heat of a [Ni(2-imdipa)] crystal for fields in the range between 0 and 3 T applied along the longer dimension of the crystal. The specific heat measured at zero field has two peaks related to D and E, and giving $D/k_B = -3.9$ K and $E/k_B = 0.15$ K. The Zeeman term is considered to be isotropic with $g_S = 2.34$, as the effect of magnetic anisotropy in the g-factor is negligible compared to the large D and E parameters. The evolution of the energy gap between the ground and first excited states with magnetic field is tracked by following the position of the low temperature peak in the specific heat (8.8b). The non-linear increase of the gap with the magnetic field is a signature of a clock transition. The results are consistent with the magnetic field being applied at 52.6° from the molecular z axis.

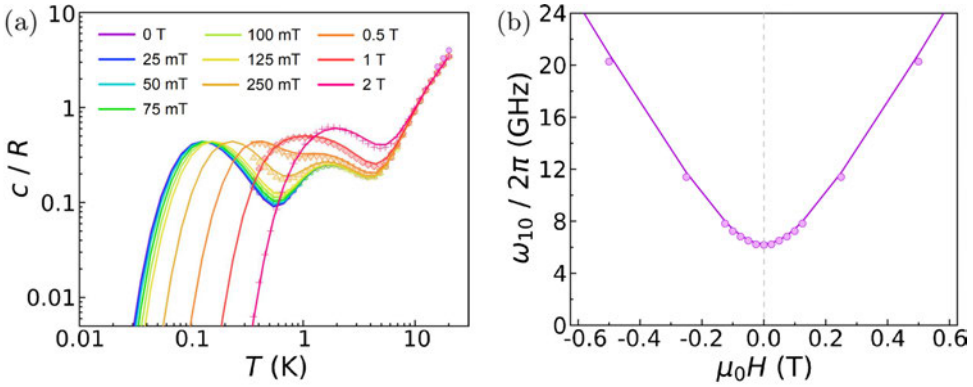

Figure 8.8: (a) Temperature dependence of the specific heat of a [Ni(2-imdipa)] crystal for magnetic fields in the range between 0 and 3 T applied along the longer dimension of the crystal. Solid lines show the simulated specific heat of a [Ni(2-imdipa)] molecule with its molecular z axis at 52.6° from the magnetic field. (b) Magnetic field dependence of the energy gap between the lowest lying energy spin states of this Ni complex, extracted form the position of the low temperature peak in the specific heat at each measured field. The solid line is the expected evolution of the gap for this relative orientation of the magnetic field and the molecular z axis.

Figure 8.9 energy spectrum of [Ni(2-imdipa)] as a function of magnetic field using the parameters reported above, assuming the same relative orientation of the magnetic field to the molecular z axis. The orthorhombic term $D\hat{S}_z^2$ splits the $m_S = 0$ state from the $m_S = \pm 1$ doublet by $|D|$, while the orthorhombic term $E\left(\hat{S}_x^2 - \hat{S}_y^2\right)$ opens a gap $2E$ between the two levels associated with symmetric and antisymmetric superpositions of the $m_S = \pm 1$ states. For $D < 0$, $E \ll |D|$ and $|\mu_B g B_j| \ll |D|$ $(j = x, y, z)$, perturbation theory gives a simple formula for the energy gap Δ as a function of the static magnetic field:

$$\Delta \simeq 2\sqrt{E^2 + (\mu_B g B_z)^2} + \frac{(\mu_B g B_y)^2 - (\mu_B g B_x)^2}{|D|}. \tag{8.8}$$

The two lowest lying energy spin states of this Ni complex can encode a qubit with frequency of operation $\omega_q := \omega_{10} = \Delta/\hbar$. However, the fact that it has an integer total spin introduces significant differences with respect to a simple $S = 1/2$ system. The orthorhombic distortion gives ω_q stability against fluctuations in B_z ($\mu_B g B_z$ against E), while the longitudinal distortion gives it stability against fluctuations in B_x and B_y ($\mu_B g B_x$ and $\mu_B g B_y$ against $|D|$)). The large $|D|$ of [Ni(2-imdipa)] makes ω_q almost insensitive to B_x and B_y. All these features make the transition between the ground and first excited states of [Ni(2-imdipa)] at zero-field a textbook example of a 'clock transition'. This transition has a frequency that is protected against small magnetic field fluctuations, as is evident from equation (8.8): the leading order in a perturbation

of the gap Δ at zero-field is of second order, while the first order contribution vanishes.

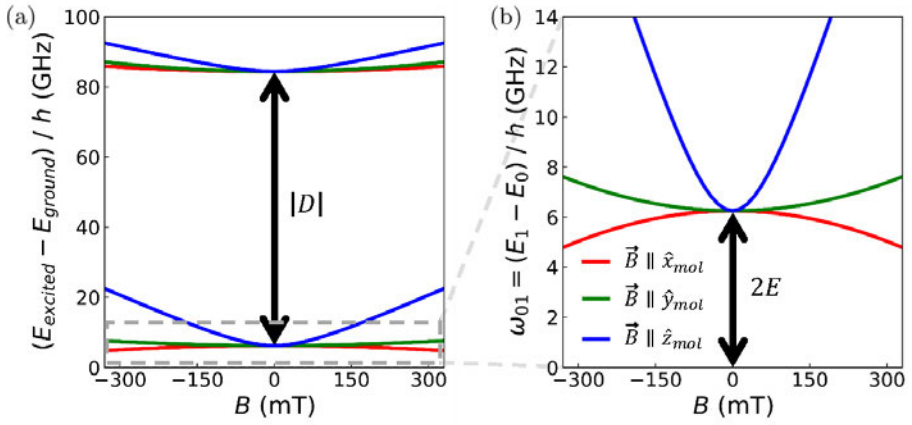

Figure 8.9: Magnetic field dependence of the transition frequencies between the ground and the excited spin states in [Ni(2-imdipa)] (a). A close up of the $0 \leftrightarrow 1$ transition between the ground and first excited states is shown in (b). $|D|$ is large enough to consider these two states as an isolated pair. The gap is easily tuned with the magnetic field parallel to the molecular z-axis $\hat{z}_{mol}$, while is more less insensitive to small fields parallel to $\hat{x}_{mol}$ and $\hat{y}_{mol}$.

At the clock transition, two superposition states with opposite symmetry appear:

$$|\pm\rangle = \frac{1}{\sqrt{2}} \left(|m_S = +1\rangle \pm |m_S = -1\rangle \right). \tag{8.9}$$

The nature of these superposition states encoding the qubit states determines the coupling of the qubit to photons. The transition between $|-\rangle$ and $|+\rangle$ is only addressable with the S_z spin operator, that is, with microwave magnetic fields $\boldsymbol{b_{mw}}$ parallel to the molecular z axis $\hat{z}_{mol}$. This is shown in figure 8.10. If the static magnetic field is increased in the direction of $\hat{z}_{mol}$, the coupling to $b_{mw,z}$ decreases. This is due to the increase in the magnetic field transforming the $|\pm\rangle$ superposition states into the $|m_S = \pm 1\rangle$ states, with the transition between the latter being forbidden. Conversely, the effect of magnetic fields of the same magnitude oriented perpendicular to $\hat{z}_{mol}$ on $|\pm\rangle$ is negligible, yielding a coupling to $b_{mw,z}$ that remains close to its maximum value at zero field.

In view of this strong dependence of the coupling on the orientation of the molecules with respect to the static magnetic field $\boldsymbol{B}$ and the microwave field $\boldsymbol{b_{mw}}$, it is important how [Ni(2-imdipa)] crystals are placed onto the chips. Figure 8.11a shows a [Ni(2-imdipa)] crystal in the form of a hexagonal prism. The axis going through the two hexagonal faces is the unit cell $\hat{c}$ axis. The $\hat{a}$

and $\hat{b}$ axes are parallel to the hexagonal faces.

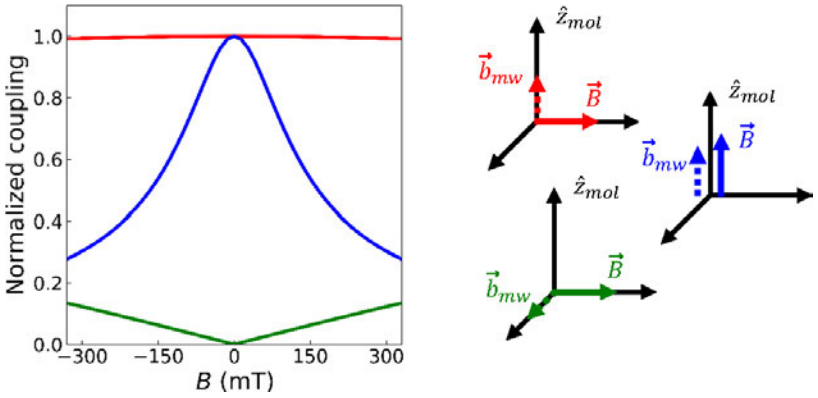

Figure 8.10: Single-spin photon coupling in [Ni(imdipa)], normalized by the maximum coupling. This maximum is located at the clock transition. Three cases are shown. In red, the microwave magnetic field $\boldsymbol{b_{mw}}$ parallel to $\hat{z}_{mol}$ ($\boldsymbol{b_{mw}} \parallel \hat{z}_{mol}$) and the static magnetic field $\boldsymbol{B}$ perpendicular to both ($\vec{B} \perp \hat{z}_{mol}$). In green, $\boldsymbol{b_{mw}}$, $\boldsymbol{B} \perp \hat{z}_{mol}$ and $\boldsymbol{b_{mw}} \perp \vec{B}$. In blue, $\boldsymbol{b_{mw}}$, $\boldsymbol{B} \parallel \hat{z}_{mol}$.

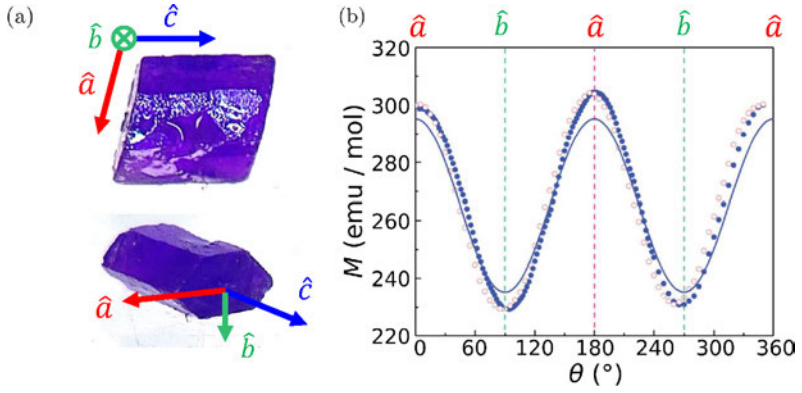

Figure 8.11: (a) A [Ni(2-imdipa)] crystal, showing the relation between the hexagonal prism and the unit cell axes. (b) Magnetization of the crystal at $B = 0.1$ T and $T = 5$ K as a function of rotation angle θ around an axis perpendicular to the $\hat{a}$-$\hat{b}$ unit cell plane. The difference between data measured while increasing (blue solid dots) and decreasing (red open symbols) angles is due to a mechanical hysteresis of the rotation system and provides a measure of the angular uncertainties. The crystal was placed so that the magnetic field aligned with $\hat{b}$ at $\theta = 90$, 270°. The solid line shows the simulation of the magnetization with the parameters from heat capacity experiments and assuming that the molecular z axis lies in the $\hat{a}$-$\hat{c}$ plane.

The specific heat measurements in figure 8.8a were performed with the magnetic field applied along the longer dimension of the crystal, that is, parallel to the $\hat{c}$ axis. These measurements, combined with the measurement of the

magnetization of the crystal for magnetic fields applied at different orientations in the $\hat{a}$-$\hat{b}$ plane shown in figure 8.11b, are consistent with the molecular z axis, $\hat{z}_{mol}$, being in the $\hat{a}$-$\hat{c}$ plane, at 52.6° from the $\hat{c}$ axis.

Each unit cell contains eight [Ni(2-imdipa)] molecules (see figure 8.12a), giving a spin density of $1.76 \cdot 10^{27}$ spins/m^3 in the crystal. These eight molecules related by an inversion centre, a 2-fold screw axis along $\hat{b}$ and a glide plane spanned by $\hat{a}$ and $\hat{c}$. This means that the $\hat{z}_{mol}$ axes of all 8 molecules are aligned. The tentative solution shown in figure 8.7 is compared with the cell axes in figure 8.12b.

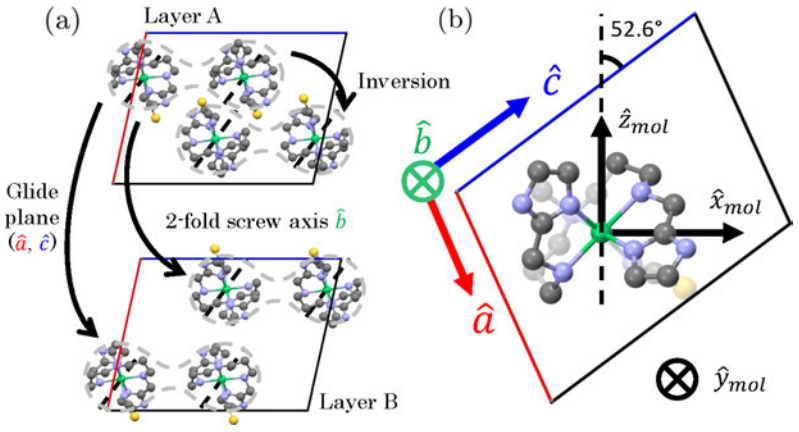

Figure 8.12: (a) The 8 [Ni(2-imdipa)] molecules in the unit cell, with their symmetry relations. They are distributed in two layers, labeled A and B. (c) Relation between the tentative solution for the molecular axes given in figure 8.7 and the unit cell axes.

8.2.3 Determination the molecular axes of [Ni(2-imdipa)] with transmission experiments

Measuring a molecular spin qubit encoded in the states of a spin clock transition coupled to a resonator is not as simple as with a qubit encoded in a spin 1/2. First, the latter can be easily tuned with the applied field ($\omega_q = \mu_B g B/\hbar$) to the match frequency of a resonator, ω_r. On the other hand, the anti-crossing of the spin clock transition makes the frequency of operation more insensitive to magnetic field, that is, more difficult to tune. For that reason, the first experiments of [Ni(2-imdipa)] samples coupled to superconducting circuits were carried out with a CPW, where a wide frequency range between 10 MHz and 14 GHz can be explored.

A [Ni(2-imdipa)] crystal was deposited on top of the waveguide, with the cell $\hat{c}$ axis parallel to the CPW (see figure 8.12), inside a dilution refrigerator mounting a superconducting vector magnet. This ensures that the microwave

magnetic field generated by the line, which here is perpendicular to $\hat{c}$ has a component along the molecular z axis. The transmission of the CPW was measured at 128 mK and magnetic fields between -300 and +300 mT for two magnetic field orientations, one for each of the two possible molecular z axis, which lie at 52.6° from $\hat{c}$ in the $\hat{a}$-$\hat{c}$ plane. The temperature could not be lowered further in this experiments due to a thermalisation problem in the cryostat. Figure 8.13 shows the transmission of the CPW for the two orientations.

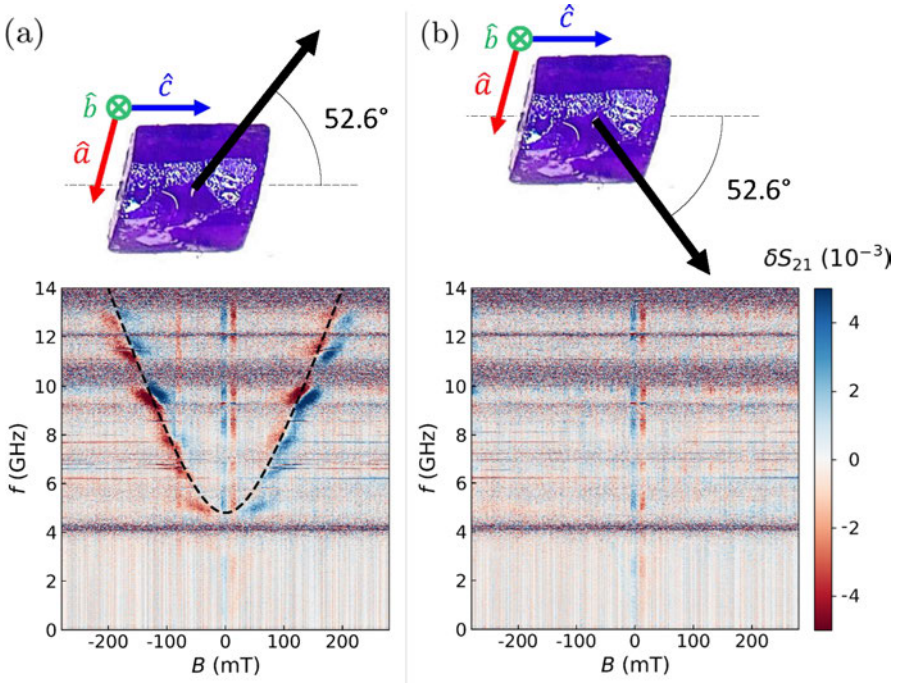

Figure 8.13: (a,b) Normalized transmission difference (δS_{21}) of a CPW coupled to a [Ni(2-imdipa)] crystal, for two magnetic field orientations that lie at 52.6° from $\hat{c}$ in the $\hat{a}$-$\hat{c}$ plane. This difference is computed at each field B as $\delta S_{21}(B) = [S_{21,\,\mathrm{exp}}(B) - S_{21,\,\mathrm{exp}}(B+\delta B)]\,/S_{21,\,\mathrm{exp}}(B+\delta B)$, effectively removing the baseline of the transmission signal. Here, δS_{21} is calculated with $\delta B = 10$ mT. The transmission measured for the orientation in (a) is consistent with the magnetic field applied along the molecular z axis, $\hat{z}_{mol}$.

The absorption signal in figure 8.13a shows the non-linear dependence with magnetic field that is associated to clock transitions. The minimum resonance frequency is found at zero field and is associated with a magnetic anisotropy gap $\Delta = 2E = 5$ GHz. This value is lower than the gap of ~ 6 GHz that was expected from heat capacity experiments. The magnetic field dependence is consistent with the magnetic field applied along the molecular z axis, $\hat{z}_{mol}$ (compare with figure 8.9b). This confirms the choice of $\hat{z}_{mol}$ in previous sections. The orientation of the magnetic field in figure 8.13b corresponds then

to the magnetic field along $\hat{x}_{mol}$. In this case, no absorption signal is observed. The transition frequency between the ground and first excited states in [Ni(2-imdipa)] is more insensitive to magnetic fields applied along $\hat{x}_{mol}$ than to magnetic fields applied along $\hat{z}_{mol}$ (see figure 8.9b). The normalized transmission difference δS_{21} defined in figure 8.13 tends to lower the visibility of transitions that vary slowly with magnetic field, as is the case here for the magnetic field along $\hat{x}_{mol}$. These results highlight how the relative orientation of the applied field and the magnetic anisotropy axes plays a crucial role in the coupling of the spin clock transitions to microwave photons.

8.2.4 Coupling spin-clock states to superconducting transmission lines

The experiment in the previous section was repeated in order to have access to the temperature range below 128 mK. This time, a DPPH powder sample was also placed on top of the CPW. The low temperature results of DPPH coupled to a CPW discussed in section 8.1.2 come from this experiment. Figure 8.14 shows how this setup allows a direct comparison between the standard electronic Zeeman transition in a $S = 1/2$ system (DPPH) and the clock transition in a $S = 1$ system ([Ni-(2-imdipa)]).

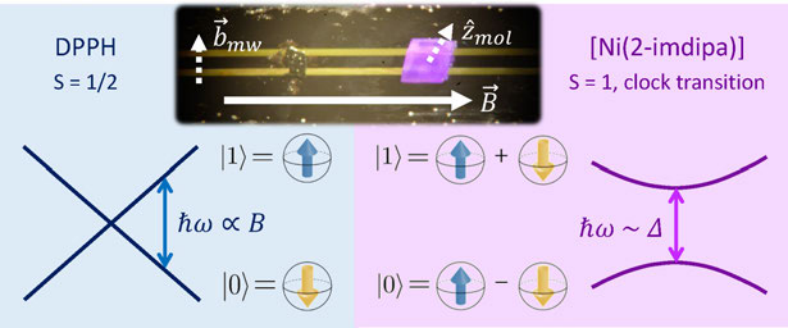

Figure 8.14: Comparison between the expected transmission for two samples deposited on the same CPW: DPPH (black powder pellet, $S = 1/2$) and [Ni-(2-imdipa)] (indigo-purple crystal, $S = 1$ with a clock transition). In DPPH, the transition frequency is proportional to the magnetic field, and therefore easy to tune. Conversely, the superposition states that arise at the clock transition of [Ni(2-imdipa)] makes the transition frequency more insensitive to the magnetic field. This property makes clock transitions difficult to tune, but also more robust against magnetic field fluctuations.

The transmission of the CPW was measured in the temperature range between 10 mK and 800 mK, with magnetic fields between -300 mT and +300 mT applied parallel to the waveguide. The results are shown in figure 8.15.

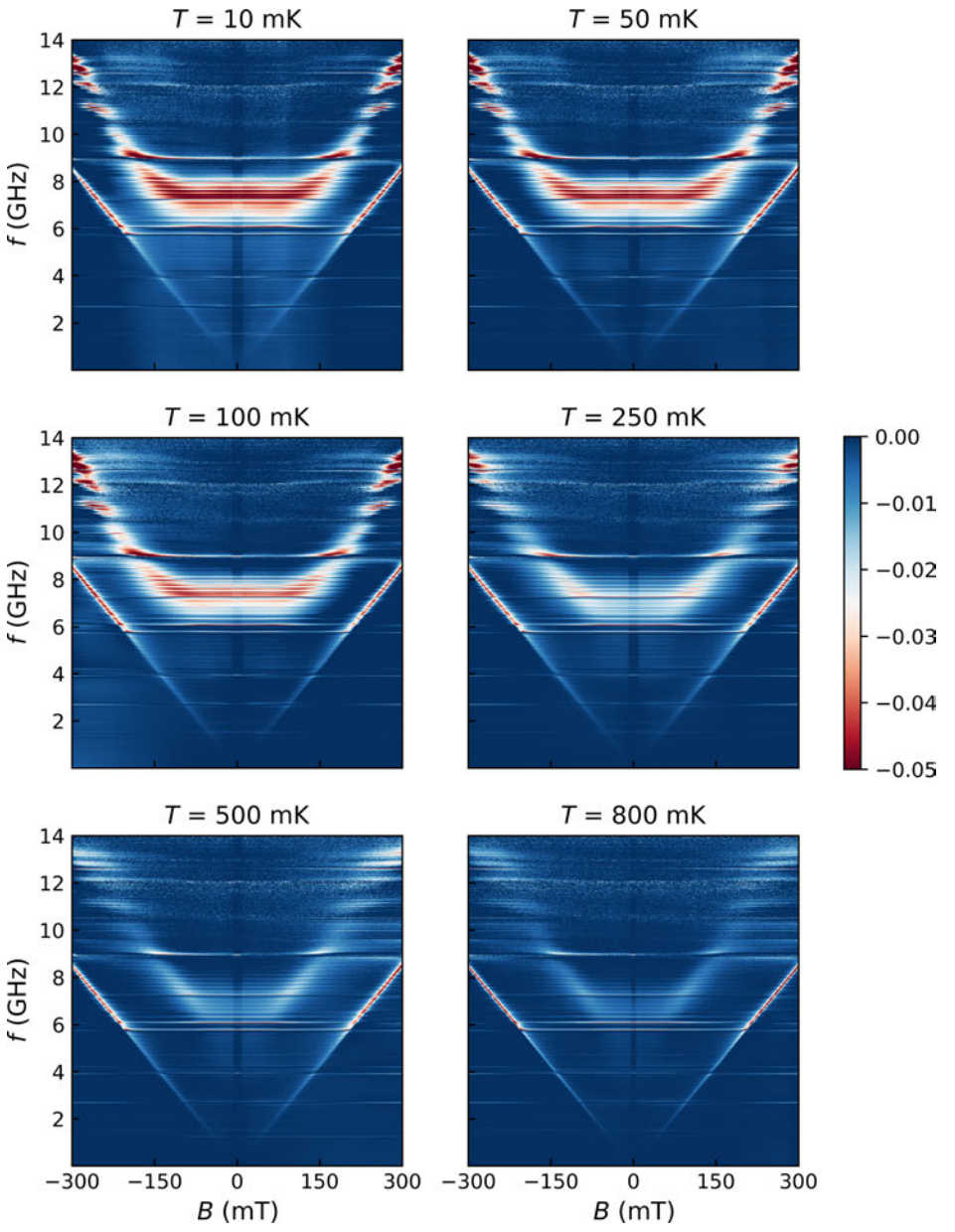

Figure 8.15: Normalized transmission of a CPW coupled to a a [Ni(2-imdipa)] crystal and a DPPH powder sample as a function of magnetic field and input microwave frequency, for six selected temperatures in the range between 10 and 800 mK. The complete set of measurements includes also the transmission at 20, 150, 175, 200, 225, 300, 350 and 400 mK.

Two resonance signals are observed, one with a linear dependence with field (DPPH, $S = 1/2$), and the non-linear dependence of the clock transition of [Ni(2-imdipa)] ($S = 1$). The transmission data was normalized by the trans-

mission of the uncoupled CPW, which was estimated by taking the values at those fields and frequencies that were sufficiently far from any of these signals. The minimum resonance frequency of the [Ni(2-imdipa)], as in the previous section, appears at zero field and is associated with a magnetic anisotropy gap $\Delta = 2E > 6$ GHz. At each field and temperature, the absorption resonance of [Ni(2-imdipa)] is fitted with:

$$S_{21}(\omega_d \simeq \omega_{10}) = \frac{\gamma_{\perp,10} + i\,(\omega_{10} - \omega_d)}{\gamma_{\perp,10} + (G_N^{(\mathrm{line})})_{01}(\Delta P_{10})_e + i\,(\omega_{10} - \omega_d)}. \tag{8.10}$$

This equation is the combination of equations (4.127) and (4.128), assuming that $(G_1^{(\mathrm{line})})_{01} \sim (G_N^{(\mathrm{line})})_{01}/N \ll \gamma_{\perp,10}$. Here, ω_{10} is the frequency of the transition $0 \leftrightarrow 1$ between the ground and first excited states, with collective spin-photon coupling $(G_N^{(\mathrm{line})})_{01}$ and decoherence rate $\gamma_{\perp,10}$.

The population difference $(\Delta P_{10})_e$ between the two states of the clock transition is given by:

$$(\Delta P_{10})_e = \frac{1 + e^{-\hbar\omega_{10}/k_\mathrm{B}T}}{Z} \simeq \tanh\left(\frac{\hbar\omega_{10}}{2k_\mathrm{B}T}\right), \tag{8.11}$$

as in a two-level system. The thermal population of the second excited state has been neglected in the approximation of the partition function Z, as $|D|$ is large enough to make this population less than 1% in the measured temperature range. In what follows, the collective spin-photon coupling $(G_N^{(\mathrm{line})})_{01}$ is redefined to include the population difference:

$$(G_N^{(\mathrm{line})})_{01} := \alpha\omega_{10}(\Delta P_{10})_e \simeq \alpha\omega_{10}\tanh\left(\frac{\hbar\omega_{10}}{2k_\mathrm{B}T}\right), \tag{8.12}$$

where the linear dependence of the coupling in a 1D waveguide has been included. α is a dimensionless proportionality constant.

Figure 8.16a shows the fitted magnetic field-dependent transition frequency ω_{10} for all the measured temperatures. In the higher end of measured temperatures (500–800 mK), the magnetic field dependence of the [Ni(2-imdipa)] signal is compatible with the behaviour expected for a a paramagnetic two-level system described by equation (8.8) with the magnetic field $\boldsymbol{B}$ applied at in the $(\hat{x}_{mol}, \hat{z}_{mol})$ plane at ∼52.6° from the molecular z axis $\hat{z}_{mol}$.

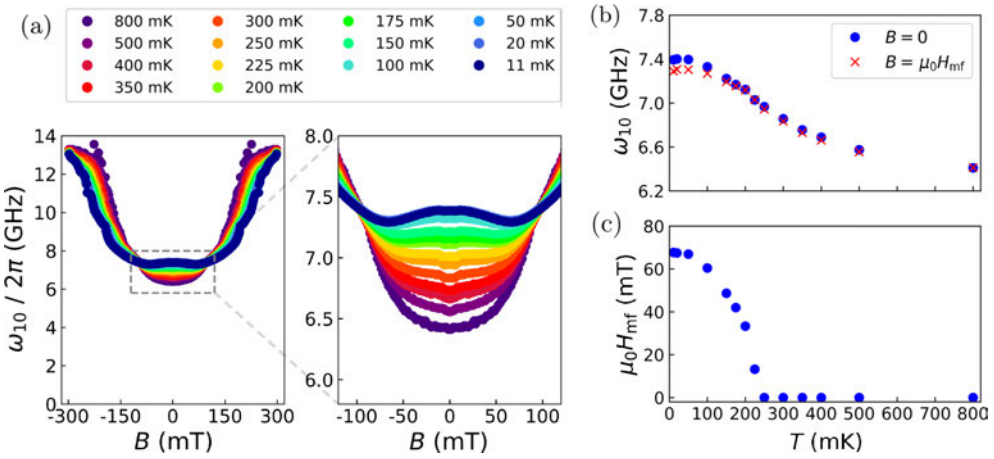

Figure 8.16: (a) Magnetic field dependence of the transition frequency ω_{10} for temperatures between 10 and 800 mK. A close-up of the area inside the dashed line is also shown. The gap at zero-field increases as temperature is lowered, while two minima appear at $B = \pm\mu_0 H_{\mathrm{mf}}$. (b) Temperature dependence of the zero-field gap (ω_{10} at $B = 0$, blue dots) and the minimum ω_{10} (ω_{10} at $B = \mu_0 H_{\mathrm{mf}}$, red crosses). ω_{10} increases steadily from ∼6.4 GHz at 800 mK to ∼7.4 GHz at 10 mK as temperature is lowered. (c) Temperature dependence of $\mu_0 H_{\mathrm{mf}}$, the magnetic field with minimum ω_{10}. Below 250 mK, two symmetric minima appear at $\pm\mu_0 H_{\mathrm{mf}} \neq 0$, with $\mu_0 H_{\mathrm{mf}}$ increasing sharply until it settles to ∼70 mT at the lowest measured temperatures.

However, as T decreases, the dependence of ω_{10} on B undergoes significant changes and deviates from this simple picture. First, below ∼ 350 mK the zero-field gap of the clock transition increases. Besides, the magnetic dependence near $B = 0$ flattens. This modulation of the gap, represented in figure 8.16b, suggests that there is a phase transition to a magnetically ordered state due to spin-spin interactions. The net interaction magnetic field stabilizes the ground stat, lowering its energy with respect to the excited states. That is, the energies associated to the elemental excitations of the ground state are higher, thereby increasing ω_{10} at zero field. The steady increase of ω_{10} also suggests the presence of short range magnetic order at the higher measured temperatures. The extent of this order then grows as the temperature is lowered.

In addition to its increase at zero field, ω_{10} develops two minima at two magnetic fields with the same magnitude $\mu_0 H_{\mathrm{mf}}$ but opposite signs below 250 mK (see figure 8.16c). $\mu_0 H_{\mathrm{mf}}$ appears sharply at this temperature, indicating the onset of long range interactions. This can be seen as the different magnetization orientations of small parts of the sample with short range order aligning to generate a 'mean field' $\mu_0 H_{\mathrm{mf}}$.

In order to illustrate how spin-spin interactions modify the main features of the transmission spectrum, I used a simple toy model of a dimer of [Ni(2-

imdipa)] molecules with a $\hat{S}_{z,i} \otimes \hat{S}_{z,j}$ exchange interaction:

$$\begin{aligned} H = &\left[D\hat{S}_{z,1}^2 + E\left(\hat{S}_{x,1}^2 - \hat{S}_{y,1}^2\right) + \mu_B g_S \boldsymbol{B}\cdot\hat{\boldsymbol{S}}_1\right] \otimes \mathbb{I}_2 \\ &+ \mathbb{I}_1 \otimes \left[D\hat{S}_{z,2}^2 + E\left(\hat{S}_{x,2}^2 - \hat{S}_{y,2}^2\right) + \mu_B g_S \boldsymbol{B}\cdot\hat{\boldsymbol{S}}_2\right] \\ &+ J\hat{S}_{z,1} \otimes \hat{S}_{z,2}. \end{aligned} \tag{8.13}$$

Keeping only the $\hat{S}_{z,1}\hat{S}_{z,2}$ term to describe the interaction between the spins is justified by the insensibility of energy of the gap to magnetic fields perpendicular to the molecular z axis. The spin-spin interaction can be seen as the interaction of a spin with a 'mean field' generated by the surrounding spins, then the z-axis Zeeman term of this field dominates against the other two axes.

At very low temperatures ($T \ll 2E/k_B$) and for small $|J|$, only one allowed transition of the dimer has non-negligible thermal population difference. Figure 8.17 compares the experimental ω_{10} at 10 mK with the frequency of this transition. The fit with the dimer model gives a zero-field gap $\Delta/h = 5.921 \pm 0.003$ GHz and an antiferromagnetic exchange constant $J\ /\ k_B = 63.6 \pm 0.2$ mK. The two symmetric minima in the experimental ω_{10} are only possible with an antiferromagnetic coupling. The angle between the magnetic field and molecular z axis was slightly reduced to 47.7° for the fit.

Figure 8.18a shows the magnetic field and temperature dependence of the other two fit parameters of the resonance, the decoherence rate $\gamma_{\perp,10}$ and the collective spin-photon coupling $(G_N^{(\mathrm{line})})_{01}$. Both $\gamma_{\perp,10}$ and $(G_N^{(\mathrm{line})})_{01}$ decrease with increasing (absolute) magnetic field. On top, a small dip shows in $\gamma_{\perp,10}$ around the clock transition (close to zero magnetic field). The magnetic field dependence of $(G_N^{(\mathrm{line})})_{01}$ is a combination of the prediction in figure 8.10, with the maximum coupling at the clock transition, and the decrease in $(\Delta P_{10})_e$ due to the increase of the transition frequency ω_{10} with magnetic field.

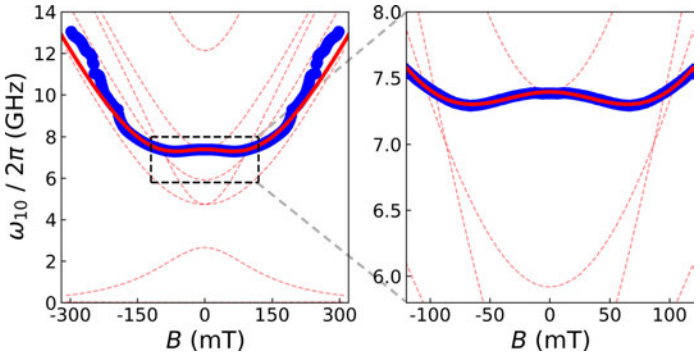

Figure 8.17: Comparison of ω_{10} measured at 10 mK (blue dots) with the only relevant transition of the dimer at 10 mK (red solid line). Red dashed lines are forbidden transition or with negligible population difference at 10 mK.

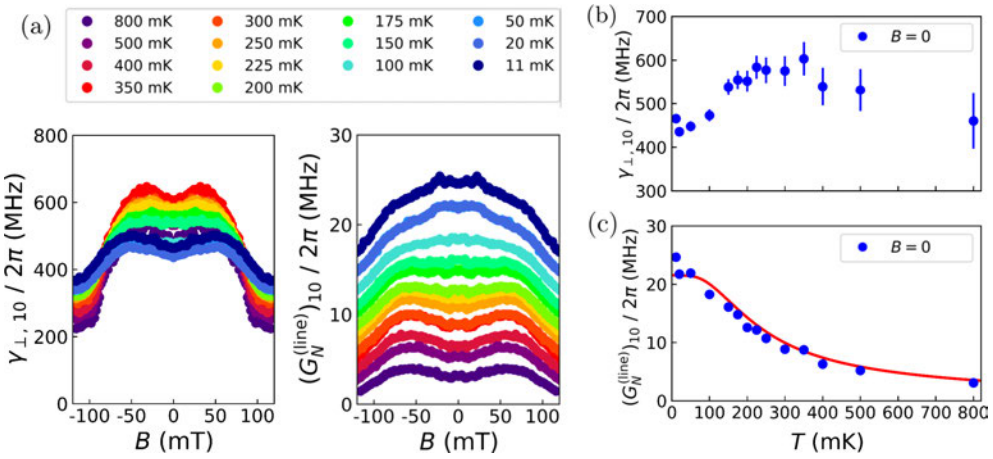

Figure 8.18: (a) Magnetic field dependence of the decoherence rate $\gamma_{\perp,10}$ and the collective spin-photon coupling $(G_N^{(\text{line})})_{01}$ for temperatures between 10 and 800 mK and fields between -100 and +100 mT. (b) Temperature dependence of $\gamma_{\perp,10}$ at zero magnetic field. A maximum in $\gamma_{\perp,10}$ is observed as the transition temperature is crossed ($\sim$ 200–300 mK). (c) Temperature dependence of $(G_N^{(\text{line})})_{01}$. Blue dots are the values from the fit of the experimental resonance, while the red solid line is the fit to equation (8.12).

The temperature dependence of $\gamma_{\perp,10}$ and $(G_N^{(\text{line})})_{01}$ at the clock transition (zero magnetic field) is shown in figures 8.18b and 8.18c respectively. As the transition temperature is crossed, a maximum in $\gamma_{\perp,10}$ is observed. Conversely, $(G_N^{(\text{line})})_{01}$ is fitted to equation (8.12), which assumes non-interacting spins, with a proportionality constant $\alpha \sim 0.0029$.

8.2.5 Coupling spin-clock states to lumped-element resonators

The coupling of spin-clock states in [Ni(2-imdipa)] to photons travelling through a waveguide has been characterized in the previous sections. The next step is then to enhance the spin-photon coupling by coupling [Ni(2-imdipa)] crystals to superconducting lumped-element resonators (LERs). A chip, labeled *Ni-cw*, was designed with ten LERs with frequencies slightly above the zero-field gap $2E/h \sim 6$ GHz of [Ni(2-imdipa)]. The chip design is shown in figure 8.19a. [Ni(2-imdipa)] crystals of different sizes were placed on top of each resonator with different orientations in order to see the effect of the number of spins and magnetic anisotropy on the coupling (see figure 8.19b). Unfortunately, most of the crystals in this experiment fell or broke into pieces during cooldown, as it can be seen in figure 8.19c. I decided then to focus the experiments on the sample on LER 9, which is the crystal that matches the size of the resonators (see figure 8.20).

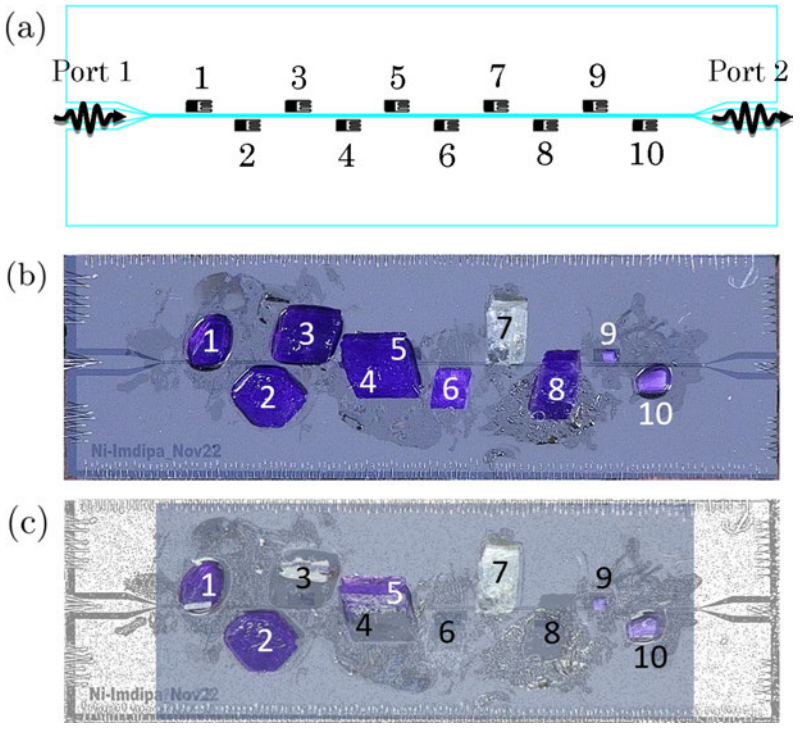

Figure 8.19: (a) Chip *Ni-cw*, hosting ten LERs (black) coupled to a single transmission line (cyan). (b) Superconducting chip with [Ni(2-imdipa)] crystals (indigo crystals) on top of *Ni-cw* LERs. One of the crystals is on top of two resonators, and also on top of the transmission line. White crystal is a sample of spin defects on ZnO, measurements with this sample are out of the scope of this work. (c) Remaining crystals after the experiments (color) superimposed over (b) in greyscale. Note that some of them fell from the chip at some point (crystals on top of LERs 3, 6 and 8) or even broke into pieces (half of a crystal on top LER 4).

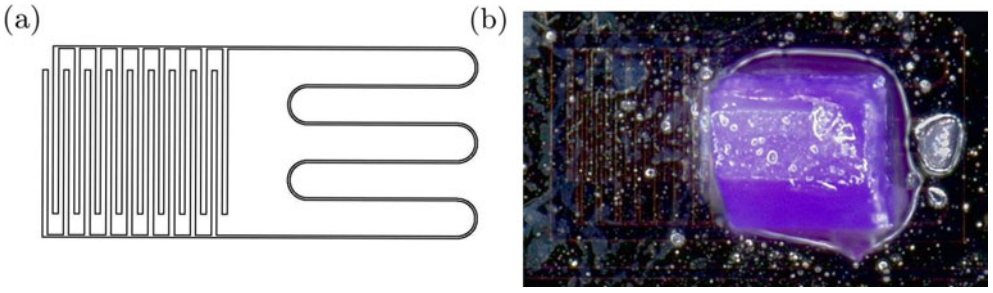

Figure 8.20: (a) Design of LER 1. The size of the resonator is smaller than in other chips, as they are aiming for a higher resonance frequency ω_r: smaller size $\rightarrow$ lower capacitance C and inductance L $\rightarrow$ higher $\omega_r = 1/\sqrt{LC}$. (b) [Ni(2-imdipa)] crystal on top of LER 9, matching the inductor size.

The transmission of *Ni-cw* with driving frequencies $\omega_d = 2\pi f$ close to the resonance frequency of LER 9 was measured for magnetic fields between -300 and +300 mT applied along the transmission line. The experiment was carried out at two temperatures: $T = 440$ mK (figure 8.21a) and $T = 128$ mK (figure 8.21b). A very large collective spin-photon coupling is observed, with the LER resonance almost vanishing completely for fields $|B| < 200$ mT. Note that an effect on the resonator is observed at zero field even if the resonance frequency $\omega_r \simeq 8.2$ GHz of LER 9 is far from the zero field gap of [Ni(2-imdipa)] ($\Delta/h =$ 6–7 GHz). This proves difficult for finding the LER resonances. The resonance of LER 9 was found by comparing the transmission data for $B = 0$ and $B = 300$ mT.

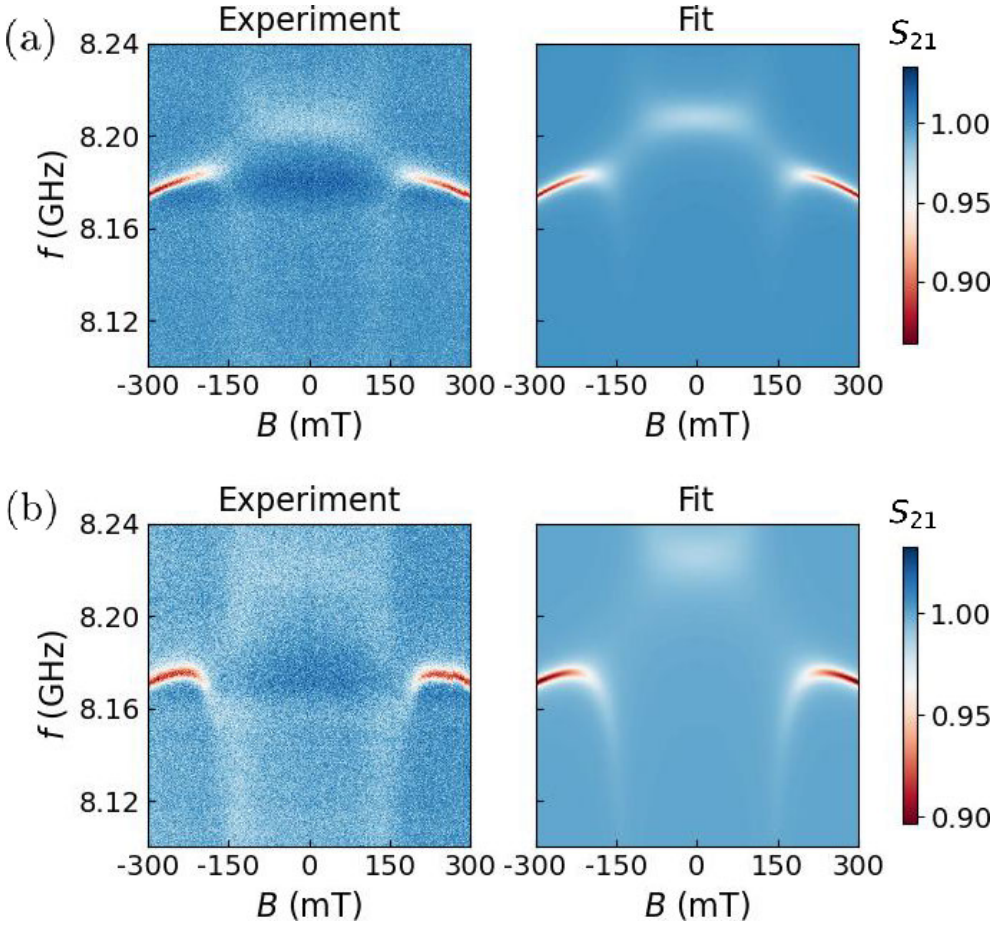

Figure 8.21: Normalized transmission of *Ni-cw* for driving frequencies ω_d close to the resonance frequency of LER 9, measured for magnetic fields between -300 mT and +300 mT along the transmission line and at two temperatures: 440 mK (a) and 128 mK (b). The resonator couples to the clock transition of [Ni(2-imdipa)].

The experimental data are fitted with the model for the resonance of a LER with frequency ω_r coupled to a qubit of frequency ω_q. The second excited state of [Ni(2-imdipa)] is neglected, as it lies ∼80 GHz above the measured range. The expression for the transmission parameter S_{21} is reproduced here:

$$S_{21}(\omega_d \simeq \omega_{10}) = 1 - \frac{\kappa_c}{i(\omega_r - \omega_d) + \kappa + \dfrac{(G_N)_{10}^2 \Delta P_{10}}{i(\omega_{10} - \omega_d) + \gamma_{\perp,10}}}. \tag{8.14}$$

Here the qubit frequency $\omega_q := \omega_{10} = \Delta/\hbar$ is defined by the evolution of the energy gap Δ between the ground and first excited states of [Ni(2-imdipa)], which is given in equation (8.8). The collective spin-photon coupling $(G_N)_{10}$ is also field dependent (see figure 8.10). In what follows, $(G_N)_{10}$ refers to the spin-photon coupling at zero field, which is scaled at other fields following the expected evolution of the coupling for a magnetic field at 52.6° from the molecular z axis. The fit parameters are listed in table 8.1 for both measured temperatures.

	$T = 440$ mK	$T = 128$ mK
ω_r / 2π (GHz)	$8.196611 \pm 9 \cdot 10^{-6}$	$8.194578 \pm 1.7 \cdot 10^{-5}$
κ / 2π (MHz)	1.135 ± 0.008	1.261 ± 0.011
κ_c / κ	0.1487 ± 0.0009	0.1346 ± 0.0011
$(G_N)_{10}$ / 2π (MHz)	192.8 ± 0.2	279.1 ± 0.3
$\gamma_{\perp,10}$ / 2π (MHz)	831 ± 4	460 ± 3
$(G_N)_{10}$ / $\gamma_{\perp,10}$	0.232 ± 0.001	0.606 ± 0.003
C_{10} (MHz)	39.3 ± 0.3	134.1 ± 1.5
$\omega_{10}(B = 0)$ (GHz)	6.442 ± 0.004	6.801 ± 0.003

Table 8.1: Parameters of the fit of the transmission maps in figure 8.21 with equation 8.14.

The transition frequency at zero field, $\omega_{10}(B = 0)$ and the decoherence rate $\gamma_{\perp,10}$ obtained for both temperatures are of the same order of the values reported in the previous section for [Ni(2-imdipa)] coupled to a CPW. However, here it is assumed the same $\gamma_{\perp,10}$ for all fields, while figure 8.18a showed a magnetic field dependent $\gamma_{\perp,10}$. The change in both $\omega_{10}(B = 0)$ and $\gamma_{\perp,10}$ with temperature is consistent with previous results: $\omega_{10}(B = 0)$ increases with decreasing temperature, while $\gamma_{\perp,10}$ is higher at 440 mK (which is close to the temperature with maximum $\gamma_{\perp,10}$ in figure 8.18b).

The collective spin-resonator coupling is enhanced compared to the couplings to the CPW in figure 8.18a. A large coupling $(G_N)_{10} = 192.8$ MHz is observed at $T = 440$ mK, with an even higher $(G_N)_{10} = 279.1$ MHz. These couplings are not in the strong coupling regime $(G_N)_{10}/\gamma_{\perp,10} > 1$, but they

are not far from it, with $(G_N)_{10}/\gamma_{\perp,10} > 0.6$ at 128 mK. In fact, the increase of $(G_N)_{10}$ between 440 mK and 128 mK, combined with the decrease in $\gamma_{\perp,10}$, suggests that the strong coupling regime might be reached at base temperature ($T \sim 10$ mK). Unfortunately, the temperature region below 128 mK could not be explored in these experiments due to a thermalization problem in the cryostat. Similarly, it could be argued that the strong coupling regime could be achieved using a LER with resonance frequency ω_r closer to $\omega_{10}(B = 0)$.

The high cooperativity regime $C_{10} = (G_N)^2_{10}/\kappa\gamma_{\perp,10} \gg 1$ is reached at both $T = 440$ mK and $T = 128$ mK, with a remarkably large $C_{10} = 134.1$ at the lower temperature. This is more than four times the cooperativity of electronic spin transitions in [Yb(trensal)] at $T = 10$ mK, e.g. $C_{1\,10} = 32.5$ for the electronic spin transition $1 \leftrightarrow 10$ with $m_I = -3/2$ (see chapter 7). Note, however, that the [Yb(trensal)] crystals were diamagnetically diluted, while here the [Ni(2-imdipa)] crystal is fully concentrated. That is, the protection of the clock transition against decoherence is enough to obtain high cooperativity even without improving its coherence time by diamagnetically diluting the [Ni(2-imdipa)] molecules in a diamagnetic matrix. In comparison, the increase of the concentration of [^{173}Yb(trensal)] molecules in isotopically purified [Yb(trensal)] samples decreased significantly the cooperativity.

8.3 Conclusions

Powder samples of DPPH deposited on top of a CPW, an organic free radical molecule with spin 1/2, provided a platform to study the competition between spin-spin and spin-photon interactions. Above $T_{\rm N} = -\theta = 0.65$ K, the DPPH ensemble is in the paramagnetic regime, and the superradiant emission of thermal collective spin states is observed. Below T_N, type-B DPPH molecules form antiferromagnetic (AF) chains. The insensitivity of the absorption signal in this temperature range is a signature of a change in the statistics of the elementary excitations of the spin system due to the formation of spin-waves. The coupling of the AF chains in a powder sample to a CPW allows estimating the weak anisotropy in the antiferromagnetic exchange interactions in the chains.

[Ni(2-imdipa)], a metallorganic compound with a Ni^{2+} ion with spin 1, adds a third element, spin clock transitions, to the competition between spin-spin and spin-photon interactions. The superposition spin states that form in this transitions are more robust against spin-spin interactions, and have also distinct geometrical properties concerning their interaction with microwave magnetic fields. The effect of spin-spin interaction on the properties of the coupling of the spin clock transition of [Ni(2-imdipa)] to a CPW has been studied with transmission measurements down to 10 mK, which suggest the

presence of antiferromagnetic interactions below 200-300 mK. [Ni(2-imdipa)] crystals have been also coupled to lumped-element resonators, achieving a remarkably high cooperativity regime ($C > 100 \gg 1$).

References

[1] J. Román-Roche, F. Luis, and D. Zueco, Physical Review Letters **127**, 167201 (2021).

[2] M. O. Scully and A. A. Svidzinsky, Science **325**, 1510 (2009).

[3] M. O. Scully, Physical Review Letters **102**, 143601 (2009).

[4] R. H. Dicke, Physical Review **93**, 99 (1954).

[5] R. G. DeVoe and R. G. Brewer, Physical Review Letters **76(12)**, 2049 (1996).

[6] D. Z. Žilić, D. Pajić, M. Jurić, K. Molčanov, B. Rakvin, P. Planinić, and K. Zadro, Journal of Magnetic Resonance **207**, 34 (2010).

[7] L. J. de Jongh and A. R. Miedema, Advances in Physics **23(1)**, 1 (1974).

[8] C. Clauss, D. Bothner, D. Koelle, R. Kleiner, L. Bogani, M. Scheffler, and M. Dressel, Applied Physics Letters **102**, 162601 (2013).

[9] Y. Wiemann, J. Simmendinger, C. Clauss, L. Bogani, D. Bothner, D. Koelle, R. Kleiner, M. Dressel, and M. Scheffler, Applied Physics Letters **106**, 193505 (2015).

[10] I. Gimeno, A. Urtizberea, a. J. Romáan-Roche, D. Zueco, A. Camón, P. J. Alonso, O. Roubeau, and F. Luis, Chemical Science **12**, 5621 (2021).

[11] I. Gimeno, V. Rollano, D. Zueco, Y. Duan, M. C. de Ory, A. Gomez, A. Gaita-Ariño, C. Sánchez-Azqueta, T. Astner, D. Granados, et al., Physical Review Applied **20**, 044070 (2023).

[12] M. D. Jenkins Sánchez, Ph.D. thesis, Universidad de Zaragoza (2015).

[13] I. Gimeno, W. Kersten, M. C. Pallarés, P. Hermosilla, M. J. Martínez-Pérez, M. D. Jenkins, A. Angerer, C. Sánchez-Azqueta, D. Zueco, J. Majer, et al., Physical Review Applied **20**, 044070 (2020).

[14] F. Keffer and C. Kittel, Physical Review **85(2)**, 329 (1952).

[15] G. Wolfowicz, A. M. Tyryshkin, R. E. George, H. Riemann, N. V. Abrosimov, P. Becker, H.-J. Pohl, M. L. W. Thewalt, S. A. Lyon, and J. J. L. Morton, Nature Nanotechnology **8**, 561 (2013).

[16] A. Ardavan, O. Rival, J. J. L. Morton, S. J. Blundell, A. M. Tyryshkin, G. A. Timco, and R. E. P. Winpenny, Physical Review Letters **98**, 057201 (2007).

[17] C. J. Wedge, G. A. Timco, E. T. Spielberg, R. E. George, F. Tuna, S. Rigby, E. J. L. McInnes, R. E. P. Winpenny, S. J. Blundell, and A. Ardavan, **108**, 107204 (2012).

[18] K. Bader, D. Dengler, S. Lenz, B. Endeward, S.-D. Jiang, P. Neugebauer, and J. van Slageren, Nature Communications **5**, 5304 (2014).

[19] J. M. Zadrozny, J. Niklas, O. G. Poluektov, and D. E. Freedman, ACS Central Science **1**, 488 (2015).

[20] C.-J. Yu, M. J. Graham, J. M. Zadrozny, J. Niklas, M. D. Krzyaniak, M. R. Wasielewski, O. G. Poluektov, and D. E. Freedman, Journal of the American Chemical Society **138**, 14678 (2016).

[21] D. Schüfter, J. Wischnat, L. Tesi, J. A. D. Sousa, E. Little, J. McGuire, M. Mas-Torrent, C. Rovira, J. Veciana, F. Tuna, et al., Advanced Materials **35(38)**, 2302114 (2023).

[22] M. Shiddiq, D. Komijani, Y. Duan, A. Gaita-Ariño, E. Coronado, and S. Hill, Nature **531**, 348 (2016).

[23] M. Rubín-Osanz, F. Lambert, F. Shao, E. Rivière, R. Guillot, N. Suaud, N. Guihéry, D. Zueco, A.-L. Barra, T. Mallah, et al., Chemical Science **12**, 5123 (2021).

Chapter 9

Conclusions

- Superconducting lumped-element resonators (LERs) have been studied as an alternative to coplanar resonators. They are interesting due to their property of frequency multiplexing and the possibility to fabricate low-impedance resonators. This allows having LERs with very small inductance, which enhances the spin-photon coupling in a small volume around it. The experiments with DPPH powder samples coupled to LERs confirm that the strong coupling regime, defined by a collective spin-photon coupling G_N greater than the decoherence rate $\gamma_\perp$, can be achieved with LERs. The results also highlight the importance of minimizing the gap between the sample and the surface of the superconducting surface in order to have the largest collective spin-photon coupling.

- A low-inductance LER design was used to perform the control and dispersive readout of molecular spin qubits based on PTM_r organic radicals. The absorption spectrum and the relaxation time T_1 of the spin ensemble were measured. These measurements also showcased the effect of the resonator on spin relaxation, obtaining an estimation of the highest single spin-photon couplings and their distribution through their role in the dynamics of the spin ensemble. In addition, experiments with short pulses (10–500 ns) showed the first signs of coherent manipulation of a ensemble of molecular spin qubits in this platform.

- The step of going from qubits to qudits is explored in the [^{173}Yb(trensal)] complex, a magnetic molecule encoding an electro-nuclear qudit with $d = 12$ states coming from its electronic spin $S = 1/2$ and the nuclear spin $I = 5/2$ of the ^{173}Yb isotope. High cooperativity has been observed in both electronic and nuclear transitions in [^{173}Yb(trensal)], which puts electronic and nuclear states almost on equal footing in this system. The presence of the electronic spin, and its high hyperfine coupling to the

nuclear spin, introduces an efficient path to couple nuclear transitions to the microwave magnetic field generated by the LER.

- The effect of spin-spin interactions in molecular ensembles on their coupling to superconducting has been studied with molecular systems with spin 1/2 and spin 1. These interactions are unavoidable until the limit of measuring a single molecular spin qubit is achieved. DPPH powder samples coupled to superconducting coplanar waveguides (CPW) provide a platform to study the competition between spin-spin and spin-photon interactions in spin 1/2 ensembles. As the temperature is lowered, the characteristics of the coupling of the sample to the waveguide change, marking the formation of spin waves in antiferromagnetic DPPH chains. [Ni(2-imdipa)], a metallorganic compound with a Ni^{2+} ion with spin 1, adds a third ingredient, spin clock transitions. The effect of spin-spin interactions on the spin clock transition in [Ni(2-imdipa)] can be detected via the changes in the spin-photon interaction of the clock transition spin superposition states with photons propagating through the waveguide. [Ni(2-imdipa)] crystals have been also coupled to LERs, achieving a remarkably high cooperativity regime ($C > 100 \gg 1$)

Conclusiones

- Los resonadores de parámetros concentrados (LERs) son una alternativa interesante a los resonadores coplanares para integrar qubits de espín molecular en circuitos superconductores. A diferencia de los resonadores coplanares, varios LERs de distintas frecuencias pueden fabricarse en un chip y medir su resonancia con una única línea de transmisión. Además, estos resonadores pueden diseñarse con una inductancia muy baja, generando campos magnéticos de microondas muy intensos en volúmenes pequeños. Una propiedad importante que quedaba por comprobar era si los LERs pueden alcanzar el régimen de acoplo fuerte a muestras de qubits de espín molecular. Este régimen está definido por un acoplo espín-fotón colectivo mayor que la tasa de decoherencia del conjunto de espines en la muestra. Este régimen se ya se había alcanzado previamente con resonadores coplanares. Los experimentos de transmisión de microondas de LERs acoplados a muestras en polvo de DPPH, un radical libre con espín $1/2$, confirman que también es posible alcanzar el régimen de acoplo fuerte en estos resonadores. Los resultados de los experimentos también destacan la importancia que el espacio que queda entre la muestra y la superficie del resonador tiene en el acoplo obtenido.

- Se ha construido un montaje experimental de generación y detección de pulsos de microondas para realizar experimentos de control y lectura de estados de qubits de espín molécular acoplados a LERs de baja inductancia. Con esta técnica se ha medido el espectro de absorción de una muestra de $\mathrm{PTM_r}$, otro radical libre con espín $1/2$, así como su tiempo de relajación T_1. Los resultados de estos últimos experimentos muestran el efecto que tiene el resonador en la dinámica de los espínes. Experimentos con pulsos más cortos (10–500 ns) muestran los primeros indicios de una manipulación coherente de estados de qubits de espín molecular basada en una plataforma basada en circuitos superconductores.

- Se ha estudiado el complejo molecular [^{173}Yb(trensal)] como un ejem-

plo qudit de espín molecular, con d estados cuánticos. La molécula de [^{173}Yb(trensal)] es un qudit electronuclear con $d = 12$ estados provinientes de su espín electrónico $1/2$ y el espín nuclear $5/2$ del isótopo ^{173}Yb. Se ha conseguido alta cooperatividad en este sistema tanto para transiciones de espín electrónico como para transiciones de espín nuclear, lo que permite utilizar los estados de espín nuclear de manera similar a los estados de espín electrónicos. La alta cooperatividad de las transiciones nucleares se debe al alto acoplo hiperfino del espín nuclear del ^{173}Yb al espín electrónico en esta molécula. Esto permite acoplar de manera eficiente el estado nuclear a campos magnéticos de microondas a través del espín electrónico.

- Se ha medido el efecto de las interacciones entre espínes en el acoplo de muestras de qubits moleculares a fotones propagándose por una línea de transmisión. Las muestras en polvo de DPPH, con espín $1/2$, acopladas a líneas de transmisión ofrecen una plataforma para estudiar la competición que existe entre las interacciones espín-espín y las interacciones espín-fotón. Al bajar la temperatura, las propiedades del acoplo de la muestra a la línea de transmisión cambian, señalando la formación de ondas de espín en cadenas antiferromagnéticas de DPPH. El complejo [Ni(2-imdipa)], con un ion Ni^{2+} ion con espín 1, introduce un nuevo ingrediente: una transición de reloj de espín entre su estado fundemental y su primer estado excitado. Estos dos estados son superposiciones de estados de espín que forman un qubit de espín molecular protegido frente a ruido magnético. El efecto de las interacciones entre espínes en la transición de reloj a muy baja temperatura se ha detectado midiendo el acoplo de ésta a fotones propagándose por una línea de transmisión. También se han acoplado cristales de [Ni(2-imdipa)] a LERs, consiguiendo una cooperatividad muy alta ($C > 100 \gg 1$).

List of publications

- E. Macaluso, M. Rubín, D. Aguilà, A. Chiesa, L. A. Barrios, J. I. Martínez, P. J. Alonso, O. Roubeau, F. Luis, G. Aromí and S. Carretta, Chemical Science **11**, 10337-10343 (2020)
- M. Rubín-Osanz, F. Lambert, F. Shao, Eric Rivière, R. Guillot, N. Suaud, N. Guihéry, D. Zueco, A. Barra, T. Mallah and F. Luis, Chemical Science **12**, 5123-5133 (2021)
- V. Rollano, M. C. de Ory, C. D. Buch, M. Rubín-Osanz, D. Zueco, C. Sánchez-Azqueta, A. Chiesa, D. Granados, S. Carretta, A. Gomez, S. Piligkos and F. Luis, Communications Physics **5**, 246 (2022)

Appendix A - Tables

LER	$\omega_r/2\pi$ (GHz)	$\kappa/2\pi$ (kHz)	$\kappa_c/2\pi$ (kHz)
1	1.8246150	48.4	47.4
2	1.8264478	49.3	48.3
3	1.8559130	26.4	25.3
4	1.8572975	26.5	25.4
5	2.2679124	18.8	17.4
6	2.2714567	19.2	17.8
7	2.4125265	3.5	1.7
9	3.7892397	13.2	9.8
10	–	–	–
11	4.1887260	19.5	15.7
12	4.1955763	19.5	15.7

Table A.1: Parameters from the simulation with Sonnet of the lumped-element resonators in chip *Test 1*.

LER	$\omega_r/2\pi$ (GHz)	$\kappa/2\pi$ (kHz)	$\lvert\kappa_c\rvert/2\pi$ (kHz)	ϕ_c (°)
1	$1.6696529 \pm 3 \cdot 10^{-7}$	254.7 ± 0.2	76.1 ± 0.1	0.19 ± 0.03
3	$1.7144528 \pm 4 \cdot 10^{-7}$	206.1 ± 0.2	26.64 ± 0.04	2.1 ± 0.1
5	$2.116451 \pm 1 \cdot 10^{-6}$	415.5 ± 0.8	30.4 ± 0.1	23.2 ± 0.1

Table A.2: Parameters from the fit of the resonances of LERs 1, 3 and 5 in chip *Test 1* measured at $T = 4.2$ K and $B \simeq B_{\text{res}}$, as defined in tables **??** and 5.1. We placed the same DPPH sample on top of each of the three resonators (see Fig. 5.17).

LER	$\omega_r/2\pi$ (GHz)	$\kappa/2\pi$ (kHz)	$\lvert\kappa_c\rvert/2\pi$ (kHz)	ϕ_c (°)
1	$1.595572 \pm 1 \cdot 10^{-6}$	138.6 ± 1.3	13.4 ± 0.2	-10.6 ± 0.4
2	$1.598124 \pm 2 \cdot 10^{-6}$	199.0 ± 1.6	18.6 ± 0.2	-17.5 ± 0.3
3	$1.6537159 \pm 9 \cdot 10^{-7}$	167.1 ± 0.9	23.0 ± 0.2	-11.2 ± 0.2
4	$1.657256 \pm 1 \cdot 10^{-6}$	150.4 ± 1.1	16.3 ± 0.2	-14.7 ± 0.3
5	$1.723823 \pm 2 \cdot 10^{-6}$	219.4 ± 1.9	114.8 ± 1.2	-6.7 ± 0.4
6	$1.725325 \pm 2 \cdot 10^{-6}$	196.61 ± 1.99	94.7 ± 1.1	-13.5 ± 0.4
7	$1.806576 \pm 2 \cdot 10^{-6}$	206.1 ± 2.3	8.4 ± 0.1	10.8 ± 0.5
8	$1.811397 \pm 3 \cdot 10^{-6}$	212.1 ± 2.9	7.0 ± 0.1	-3.9 ± 0.6
9	$1.9589596 \pm 9 \cdot 10^{-7}$	149.0 ± 0.9	28.3 ± 0.2	6.4 ± 0.3
10	$1.964212 \pm 1 \cdot 10^{-6}$	179.7 ± 1.3	27.7 ± 0.2	-4.9 ± 0.3
11	$2.063403 \pm 1 \cdot 10^{-6}$	181.9 ± 1.4	32.5 ± 0.3	10.9 ± 0.3
12	$2.065999 \pm 2 \cdot 10^{-6}$	172.8 ± 1.5	27.2 ± 0.3	-6.1 ± 0.4

Table A.3: Parameters from the fit of the transmission of the lumped-element resonators in chip *Test 2* at 4 K and zero field, as defined in tables **??** and 5.1.

LER	$\omega_r/2\pi$ (GHz)	$\kappa/2\pi$ (kHz)	$\lvert\kappa_c\rvert/2\pi$ (kHz)	ϕ_c (°)
1	$1.5848946 \pm 9 \cdot 10^{-7}$	98.3 ± 0.9	17.0 ± 0.2	-0.5 ± 0.4
2	$1.5904145 \pm 8 \cdot 10^{-7}$	95.0 ± 0.8	15.6 ± 0.2	-1.4 ± 0.3
3	$1.6511598 \pm 6 \cdot 10^{-7}$	110.9 ± 0.6	22.5 ± 0.2	-1.4 ± 0.2
4	$1.6326271 \pm 6 \cdot 10^{-7}$	101.0 ± 0.6	16.0 ± 0.1	7.4 ± 0.3
5	$1.719468 \pm 2 \cdot 10^{-6}$	210.1 ± 1.8	115.7 ± 1.2	-0.5 ± 0.3
6	$1.722812 \pm 2 \cdot 10^{-6}$	154.3 ± 2.1	61.94 ± 1.01	0.0 ± 0.6
7	$1.802034 \pm 3 \cdot 10^{-6}$	121.9 ± 2.9	6.2 ± 0.2	-0.08 ± 0.98
8	$1.777309 \pm 2 \cdot 10^{-6}$	107.9 ± 1.8	6.1 ± 0.1	-3.3 ± 0.7
9	$1.9096160 \pm 7 \cdot 10^{-7}$	126.3 ± 0.7	24.5 ± 0.2	13.0 ± 0.2
10	$1.8715570 \pm 7 \cdot 10^{-7}$	122.5 ± 0.7	22.0 ± 0.2	12.9 ± 0.2
11	$2.0267752 \pm 9 \cdot 10^{-7}$	131.4 ± 0.9	29.8 ± 0.2	13.3 ± 0.3
12	$1.9992826 \pm 8 \cdot 10^{-7}$	121.4 ± 0.8	21.9 ± 0.2	6.3 ± 0.3

Table A.4: Parameters from the fit of the transmission of the lumped-element resonators in chip *Test 2* at 4 K and zero field, as defined in tables **??** and 5.1, with DPPH samples on top of LERs 1, 4, 5, 8, 10 and 12.

LER	$\omega_r/2\pi$ (GHz)	$\kappa/2\pi$ (kHz)	$\lvert\kappa_c\rvert/2\pi$ (kHz)	ϕ_c (°)
1	$1.5843312 \pm 2 \cdot 10^{-7}$	141.3 ± 0.1	16.07 ± 0.02	2.49 ± 0.03
2	$1.5898394 \pm 2 \cdot 10^{-7}$	140.2 ± 0.1	14.84 ± 0.02	-0.86 ± 0.03
3	$1.6502776 \pm 9 \cdot 10^{-7}$	181.1 ± 0.6	23.5 ± 0.1	-5.4 ± 0.1
4	$1.631767 \pm 2 \cdot 10^{-6}$	134.5 ± 1.6	13.6 ± 0.2	4.3 ± 0.2
5	$1.7185818 \pm 4 \cdot 10^{-7}$	232.0 ± 0.3	94.7 ± 0.1	6.18 ± 0.04
8	$1.7761841 \pm 9 \cdot 10^{-7}$	187.5 ± 0.5	5.19 ± 0.02	0.0 ± 0.1
10	$1.8712407 \pm 8 \cdot 10^{-7}$	252.5 ± 0.4	20.89 ± 0.05	20.27 ± 0.05
12	$1.9979448 \pm 5 \cdot 10^{-7}$	219.4 ± 0.3	19.39 ± 0.03	6.28 ± 0.04

Table A.5: Parameters from the fit of the transmission of the lumped-element resonators in chip *Test 2* at 4 K. The values of ω_r here are those of the resonators at their corresponding resonance fields B_{res} (between 56 and 72 mT, depending on the resonator). They are slightly shifted to lower frequencies compared to the values reported in table A.4 due to the effect of the static field on the resonators (see section 5.4.1).

LER	$\omega_r/2\pi$ (GHz)	$\kappa/2\pi$ (kHz)	$\lvert\kappa_c\rvert/2\pi$ (kHz)	ϕ_c (°)
1	$1.5897023 \pm 1 \cdot 10^{-7}$	99.3 ± 0.1	15.78 ± 0.01	-13.83 ± 0.03
2	$1.5782930 \pm 3 \cdot 10^{-7}$	142.5 ± 0.2	14.92 ± 0.02	-3.51 ± 0.04
7	$1.7796599 \pm 9 \cdot 10^{-7}$	203.2 ± 0.5	11.70 ± 0.04	19.7 ± 0.1
8	$1.7994068 \pm 5 \cdot 10^{-7}$	153.4 ± 0.3	9.09 ± 0.02	-1.3 ± 0.1
11	$1.9605984 \pm 3 \cdot 10^{-7}$	167.8 ± 0.2	35.02 ± 0.05	6.65 ± 0.03
12	$1.9733963 \pm 2 \cdot 10^{-7}$	155.1 ± 0.1	27.83 ± 0.03	1.43 ± 0.03

Table A.6: Parameters from the fit of the transmission of the lumped-element resonators in chip *Test 2* at 4 K.

LER	$\omega_r/2\pi$ (GHz)	$\kappa/2\pi$ (kHz)	$\kappa_c/2\pi$ (kHz)
1	2.8308	14.0 ± 1	2.0 ± 1
2	2.6597	11.0 ± 1	3.0 ± 1
3	2.5194	13.0 ± 1	4.0 ± 1
4	2.3896	17.0 ± 1	4.0 ± 1
5	2.2800	13.0 ± 1	4.0 ± 1
6	2.1756	23.0 ± 1	4.0 ± 1
7	2.0870	13.0 ± 1	5.0 ± 1
8	2.0059	10.0 ± 1	10.0 ± 1
9	1.9331	10.0 ± 1	5.0 ± 1
10	1.8585	11.0 ± 1	8.0 ± 1

Table A.7: Parameters from the characterization, just after fabrication at CAB, of the lumped-element resonators in chip *Test 3* at 12 mK.